Numerical Investigation of Sedimentation in Viscoelastic Fluids using Spectral Element Methods

Ross Kynch
Supervised by Prof. T. N. Phillips

A thesis submitted for the degree of Doctor of Philosophy

June 2013

Cardiff University
School of Mathematics
Senghennydd Road, Cardiff

Firstly, I wish to thank my supervisor Prof. Tim Phillips for his excellent guidance, support and patience throughout the course of this thesis. I cannot thank you enough for everything you've done over the last few years. It has been an absolute honour to work with you.

I would also like to thank my examiners, Prof Mike Webster and Dr. John Pryce, for agreeing to take part in my viva and for their feedback.

I am very grateful to the EPSRC for funding me as well as to the School of Maths at Cardiff University for allowing me to undertake this research.

I'd like to thank all the members (past and present) of the Fluids group at Cardiff for the wonderful atomosphere and simulating discussion throughout my time here. In particular I'd like to thank Steve, Chris and Susanne for the many discussions about our work. I'd also like to thank the friends I've made during my time here, especially Gareth and Stu. To the OR lot, thanks for making me feel welcome on your floor, despite me not being one of you!

To Rachel, thank you for putting up with me for the past year and I hope it was worth the struggle. You kept me going through the hardest part and kept me sane.

Finally, to my parents: thank you for proof-reading my thesis and spotting many mistakes that I hadn't. I may not show it all of the time but I truly appreciate the support and encouragement you've both given me throughout my life. I am very happy to leave my dad as the only non-Dr. in the family!

DECLARATION

This work has not previously been accepted in substance for any degree and is not being concurrently submitted in candidature for any other degree.

Signed .....
Date .....

STATEMENT 1

This thesis is the result of my own investigations, except where otherwise stated. Other sources are acknowledged and explicit references given. A reference section is appended.

Signed .....
Date .....

STATEMENT 2

I hereby give consent for my thesis, if accepted, to be available for photocopying and for inter-library loan, and for the title and summary to be made available to outside organisations.

Signed .....
Date .....

Summary

In this thesis we consider the problem of a falling sphere within a fluid. We are primarily interested in incompressible fluids exhibiting so-called viscoelastic properties in which a range of phenomena have been observed experimentally. These phenomena are typically manifest in the presence of a negative wake, an overshoot of the velocity of the falling sphere and drag reduction as well as enhancement in some cases. We consider fluid models which have been designed to capture these effects and use them to simulate the flow numerically with the intention of gaining an insight into the observed phenomena.

We begin with the most basic fluid models in order to validate our scheme, considering both Stokes and Newtonian fluids before progressing to viscoelastic fluid models in a range of problems to ensure the robustness of our solver. Our scheme ultimately utilises the Spectral Element Method(SEM) combined with a Discontinuous Galerkin(DG) treatment of the constituitive equation along with a DEVSS-G stabilisation term in the momentum equation. We employ an Arbitrary Lagrangian Eulerian(ALE) scheme when simulating a falling sphere.

Our simulations successfully capture the drag reduction when moving fluid past a fixed sphere as well as velocity overshoot for the sedimenting sphere, although we have failed to capture the presence of a negative wake thus far. Excellent agreement with the literature is demonstrated for the benchmarks considered in both planar and axisymmetric geometries.

Contents

Chapter 1

Introduction

This thesis is concerned with the sedimentation of a spherical particle in a viscoelastic fluid. This chapter contains a brief history of considerations of the problem, beginning with the initial efforts in the field, followed by experimentally observed phenomena as well as efforts to capture them.

Subsequent chapters follow our efforts to understand the problem. Chapter 2 deals with the mathematical formulation of the equations we shall be considering to model the fluid, ranging from Stokes flow, Newtonian flow and more complicated viscoelastic models such as Oldroyd B. Chapter 3 details our numerical methods with which we shall attempt to compute an approximate solution to these models. Chapter 4 details our efforts to validate our scheme for Stokes flow and compute solutions to the benchmark of a fixed sphere in uniform flow which serves as validation of our spatial discretisation. Chapter 5 is concerned with the Newtonian fluid and provides further validation of our scheme with the introduction of time-dependence.

In Chapter 6 we consider viscoelastic flows for fixed domains. Validation on the scheme is performed using available analytical solutions and we continue with the benchmarks used for Stokes and Newtonian flow. The viscoelastic models considered are the Oldroyd B and Giesekus fluids. Finally, Chapter 7 introduces our scheme for the falling sphere problem and details some results from initial numerical experiments using the scheme.

1.1 Motivation

The study of fluid flow past a sphere is of great interest in fluid dynamics. The problem has a long history and the problem of flow past a sphere fixed inside a cylinder is a useful benchmark problem for numerical schemes. It also has applications in the settling of suspensions and in sedimentation. In industrial settings, the transport of particles in mineral and chemical processing, for example, may be modelled by a sphere in motion through an incompressible fluid. Particles are also present in processes such as engine combustion. This makes the understanding of the effect of the sphere's presence on the flow important in the study of these processes.

1.2 History

Flow past a sphere (in particular at a low Reynolds number) has a long history in fluid dynamics, dating back to at least 1845 when work was published (and later in 1851) by G. G. Stokes. Stokes studied the problem of a sphere moving at some constant velocity, V, in an infinite expanse of fluid [56]. Taking a frame of reference which follows the sphere, he was able to find a steady solution to the equations of motion he had formulated a few years earlier [55]. We follow the essay of Lindgren [31] who explored the history of the problem beginning with Stokes' work. Stokes started with what are now known as the Navier-Stokes equations for an incompressible viscous fluid,

$$(\mathbf{u} \cdot \nabla)\,\mathbf{u} = -\frac{\nabla p}{\rho} + \nu \nabla^2 \mathbf{u}, \tag{1.1}$$

$$\nabla \cdot \mathbf{u} = 0 \tag{1.2}$$

where $\mathbf{u}$ is the flow velocity, p the pressure, ρ the density and $\nu = \frac{\eta}{\rho}$ the kinematic viscosity (η being the dynamic viscosity). Also note that (1.2) is the continuity equation for incompressible fluids.

Stokes' analysis was performed under the assumption that inertial forces may be neglected as they are dominated by the viscous forces. He argued that this assumption holds as long as the motion of the sphere is relatively slow. This meant that $\rho\,(\mathbf{u} \cdot \nabla)\,\mathbf{u}$

is assumed to be zero in an inertial frame of reference. The result is that (1.1) becomes,

$$0 = -\nabla p + \eta \nabla^2 \mathbf{u}. \tag{1.3}$$

The solution is obtained in terms of what is now known as Stokes' stream function, given in spherical co-ordinates by

$$\psi(r,\theta) = \pm \frac{V}{2} r^2 \sin^2\theta \left(1 - \frac{3a}{2r} + \frac{a^3}{2r^3}\right) \tag{1.4}$$

for a uniform velocity V past a fixed sphere of radius a so that $u_r = -V\cos\theta$ and $u_\theta = V\sin\theta$ at $r = \infty$. One may extract a velocity field from the stream function using

$$u_r = \frac{1}{r^2 \sin\theta} \frac{\partial \psi}{\partial \theta}, \tag{1.5}$$

$$u_\theta = -\frac{1}{r \sin\theta} \frac{\partial \psi}{\partial r} \tag{1.6}$$

giving,

$$\begin{aligned} u_r(r,\theta) &= V\cos\theta \left(1 - \frac{3}{2}\frac{a}{r} + \frac{1}{2}\frac{a^3}{r^3}\right), \\ u_\theta(r,\theta) &= -V\sin\theta \left(1 - \frac{3a}{4r} - \frac{1}{4}\frac{a^3}{r^3}\right). \end{aligned} \tag{1.7}$$

An example of the steady flow field at low Reynolds number can be seen in Figure 1.1(a). The flow is both axisymmetric and laterally symmetric about the sphere.

By superimposing a uniform velocity field of $-V$, the "unsteady" solution may be found which corresponds to the physical problem of a sphere moving through an otherwise stationary fluid, rather than a fixed sphere with fluid moving around it. The stream function is given by

$$\psi(r,\theta) = \frac{3}{4} V a r \sin^2\theta \left(1 - \frac{1}{3}\frac{a^2}{r^2}\right) \tag{1.8}$$

with the corresponding velocity solution given by

$$\begin{aligned} u_r(r,\theta) &= V\cos\theta \left(\frac{3}{2}\frac{a}{r} - \frac{1}{2}\frac{a^3}{r^3}\right), \\ u_\theta(r,\theta) &= -V\sin\theta \left(\frac{3}{4}\frac{a}{r} + \frac{1}{4}\frac{a^3}{r^3}\right). \end{aligned} \tag{1.9}$$

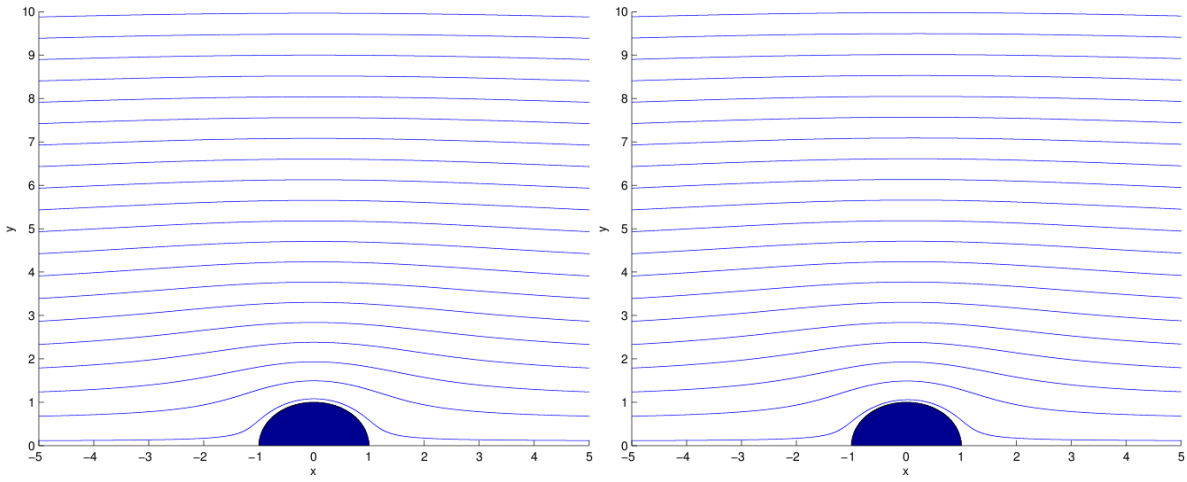

(a) Stokes(laterally symmetric) (b) Oseen/Lamb

Figure 1.1: Streamlines for the stationary sphere problem, $Re = 0.01$. The flow is from left to right.

An example of the unsteady flow field at both short and long distances may be seen in Figure 1.2. As with the stationary sphere case, the flow is axially and laterally symmetric. One can see that at a increasing distance from the sphere its presence is still clearly influencing the flow which demonstrates that the validity of the solution is restricted to some radial distance from the sphere. The conditions for the validity of Stokes' approximation is that the Reynolds number $Re = \frac{Va}{\nu} \ll 1$.

Finally, Stokes found that the drag force upon the sphere while travelling through an otherwise undisturbed fluid under the above assumptions is

$$F = 6\pi\eta aV. \tag{1.10}$$

An objection to Stokes' analysis was made by Oseen [40, 41] and independently by Noether [38]. Their objections were based on the arguement that the inertial forces at long distances from the sphere were not negligible. Further to this, it was argued that Stokes' approximation produced an inertia term which reaches arbitrarily large values as r increases. These objections of long-range dependence are valid, not for the above reasons, however, but related to a transformation between inertial frames.

Oseen's work also introduced an innovation in the formulation of the problem. Specifying the velocity components of the flow as the addition of the uniform velocity field (of

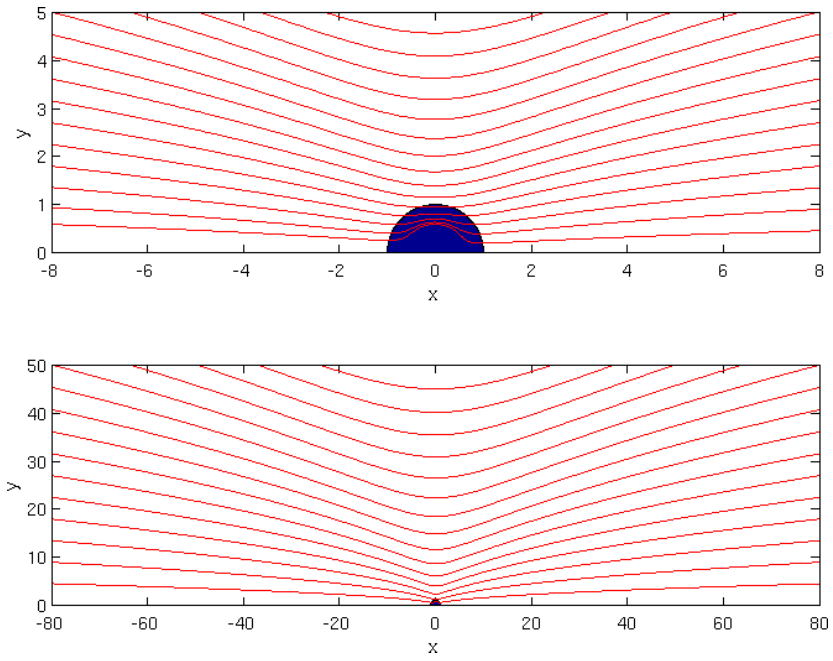

Figure 1.2: Streamlines at small and large scales of Stokes' solution for the moving sphere problem at $Re = 0.01$. The sphere is moving from right to left, although the flow is laterally symmetric.

speed V) and the velocity perturbations, due to the sphere's presence, one can reformulate the problem. By neglecting second order quantities in the perturbed variables, Oseen introduced linearised inertia terms via a partial convective acceleration, for the force equations. The result is a system of PDEs in only the perturbed variables,

$$V\frac{\partial \mathbf{u}}{\partial x_1} = -\frac{\nabla p}{\rho} + \nu\nabla^2\mathbf{u}, \tag{1.11}$$
$$\nabla \cdot \mathbf{u} = 0$$

where $\frac{\partial \mathbf{u}}{\partial x_1}$ is the partial convective acceleration.

The transformation into an equation in only the perturbed variables allows the unsteady flow problem to be solved in the format of a steady solution if the boundary conditions are satisfied. This transformation can also be made for Stokes' formulation and is equivalent to setting the left-hand side to be zero in (1.11).

A further contribution was made by Lamb [28] who presented a more condensed, clearer analysis using Oseen's equations in 1911. Lamb noted that the conditions on the validity of Oseen's model were the same as Stokes' theory, $Re = \frac{Va}{\nu} \ll 1$. Oseen did

not extract a stream function from his analysis, but his calculations allow a prediction of the general character of the flow field which differs from Stokes' flow field considerably - this was in agreement with Lamb's own findings for the flow field. The stream function extracted by Lamb for the steady case is given by,

$$\Psi(r,\theta) = \frac{3}{2}\nu a(1+\cos\theta)\left(1-e^{-(Vr/2\nu)(1-\cos\theta)}\right) - \frac{V}{2}\left(1+\frac{1}{2}\frac{a^3}{r^3}\right)r^2\sin^2\theta \tag{1.12}$$

which results in the flow field,

$$v_r = V\cos\theta\left(1+\frac{1}{2}\frac{a^3}{r^3}\right) + \frac{3}{2}\frac{a}{r}\nu\left[\frac{1}{r}-\left(\frac{v}{2\nu}(1+\cos\theta)+\frac{1}{r}\right)e^{-(Vr/2\nu)(1-\cos\theta)}\right], \tag{1.13}$$

$$v_\theta = -V\sin\theta\left[1-\frac{1}{4}\frac{a^3}{r^3}-\frac{3}{4}\frac{a}{r}e^{-(Vr/2\nu)(1-\cos\theta)}\right]. \tag{1.14}$$

The unsteady velocity field may be found by superimposing the uniform velocity field V on the above solutions. Figures 1.1(b) and 1.3 show the steady and unsteady streamlines respectively. At short distances the difference is not so apparent, but at long distances however, the effect of the inertia terms is seen. The lateral symmetry of the solution is broken and the sphere is seen to have a large impact on the flow at long range. Lamb also concluded that Oseen and Stokes' models must result in the same drag force (1.10). Oseen's own work agreed with this view at the time, and the same conclusion was reached by Noether.

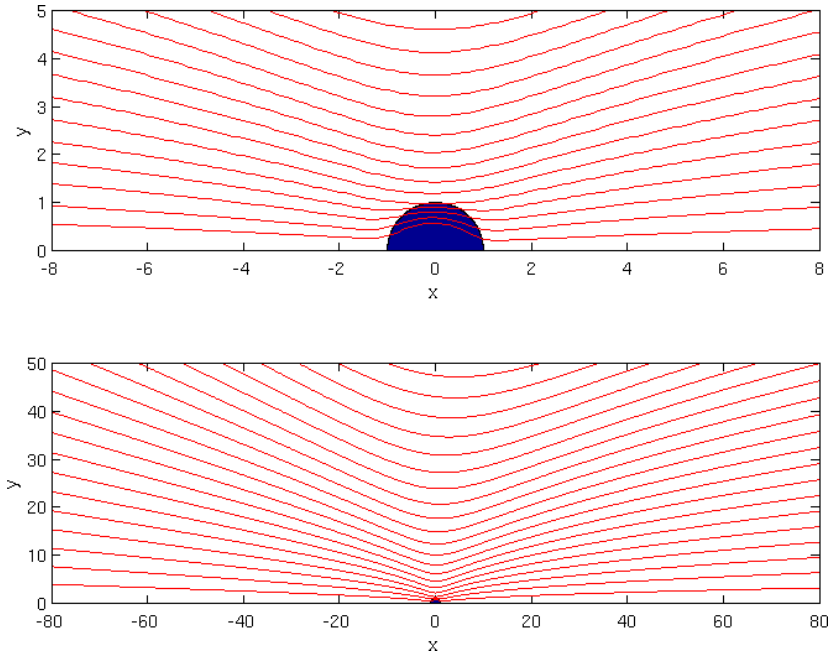

Figure 1.3: Streamlines at small and large scales found by Lamb using Oseen's formulation for the moving sphere problem, $Re = 0.01$. The flow is from right to left.

Chapter 2

Mathematical Formulation

In the following chapter we dicuss the mathematical formulation governing our fluid models. In Section 2.1 we outline the general framework of the models used and in Section 2.2 we outline some specified models for viscoelastic fluids. An alternative formulation of one of the governing equations is covered in Section 2.3. We discuss the boundary conditions applied to our equations in Section 2.5. A statement of our final equations is found in Section 2.6.

2.1 Governing Equations

The equations which govern fluid flow are based upon simple principles, viz.

- Momentum is conserved,
- Mass is conserved,
- Energy is conserved.

However, in this thesis we consider only isothermal flows so do not consider the conservation of energy. Using the first two of these principles, the Navier-Stokes equations

for an incompressible fluid may be derived, and stated as

$$\rho_F \left(\frac{\partial \mathbf{u}}{\partial t} + \mathbf{u} \cdot \nabla \mathbf{u} \right) = \nabla \cdot \boldsymbol{\sigma} + \mathbf{f} \tag{2.1}$$

$$\nabla \cdot \mathbf{u} = 0 \tag{2.2}$$

in some domain Ω with boundary $\partial\Omega$. Here $\mathbf{u}$ is the flow velocity, ρ_F is the fluid density, $\boldsymbol{\sigma}$ is the Cauchy stress tensor and $\mathbf{f}$ represents external forces (per unit volume). This system is closed by boundary conditions and a so-called constitutive equation relating the Cauchy stress to the rate-of-deformation tensor, $\mathbf{d} = \frac{1}{2}\left(\nabla \mathbf{u} + (\nabla \mathbf{u})^T\right)$. This relationship effectively defines the characteristics of the fluid being modelled. Boundary conditions will be discussed in Section 2.5. We define the gradient of a vector field, $\mathbf{u}$, as

$$(\nabla \mathbf{u})_{ij} = \frac{\partial u_j}{\partial x_i}, \tag{2.3}$$

and the divergence of a tensor field, $\boldsymbol{\sigma}$, as

$$(\nabla \cdot \boldsymbol{\sigma})_i = \sum_j \frac{\partial \sigma_{ji}}{\partial x_j}. \tag{2.4}$$

It is standard to split the Cauchy stress tensor into pressure, p, and extra-stress tensor, $\mathbf{T}$, parts

$$\boldsymbol{\sigma} = -p\mathbf{I} + \mathbf{T}. \tag{2.5}$$

This allows the constitutive relationship to be defined which relates the tensors $\mathbf{T}$ and $\mathbf{d}$. We also define the material derivative of a general tensor $\mathbf{G}$ by

$$\frac{D\mathbf{G}}{Dt} = \frac{\partial \mathbf{G}}{\partial t} + \mathbf{u} \cdot \nabla \mathbf{G}. \tag{2.6}$$

Substituting these definitions, equations (2.1)-(2.2) become

$$\rho_F \frac{D\mathbf{u}}{Dt} = -\nabla p + \nabla \cdot \mathbf{T} + \mathbf{f} \tag{2.7}$$

$$\nabla \cdot \mathbf{u} = 0 \tag{2.8}$$

2.1.1 Newtonian Fluids

A range of constitutive relationships will be discussed in Section 2.2 but for now we shall focus on the model for a Newtonian fluid. A Newtonian fluid is characterised by a

linear, isotropic relation between extra-stress and strain rate (or rate of deformation). The constitutive relation is given by

$$\mathbf{T} = 2\eta_0 \mathbf{d} \tag{2.9}$$

where η_0 is the zero shear rate viscosity of the fluid.

We may eliminate $\mathbf{T}$ by substituting (2.9) into (2.7). We apply the definition of $\mathbf{d}$ and then use the fact that $\nabla \cdot (\nabla \mathbf{u})^T = \nabla (\nabla \cdot \mathbf{u})$. Finally, we use (2.8) to obtain the velocity-pressure formulation for a Newtonian fluid

$$\begin{aligned} \rho_F \frac{D\mathbf{u}}{Dt} &= -\nabla p + \eta_0 \nabla^2 \mathbf{u} + \mathbf{f} \\ \nabla \cdot \mathbf{u} &= 0 \end{aligned} \tag{2.10}$$

Dimensionless Equation

It is standard to define dimensionless variables in order to allow comparisons between studies. We define our length, velocity and time scales as, L, U and L/U, respectively, and pressure and stress by $\eta_0 U/L$. We typically choose a length and velocity scale according to the characteristics of a given problem such as the width of a channel or terminal velocity of a falling sphere. The dimensionless equations corresponding to (2.10) are then

$$\begin{aligned} Re \frac{D\mathbf{u}}{Dt} &= -\nabla p + \nabla^2 \mathbf{u} + \mathbf{f} \\ \nabla \cdot \mathbf{u} &= 0 \end{aligned} \tag{2.11}$$

where the non-dimensional group,

$$Re = \frac{\rho_F U L}{\eta_0} \tag{2.12}$$

is called the Reynolds number. This dimensionless group gives a measure of the ratio of inertial forces to viscous forces. At low Reynolds numbers, viscous forces dominate and the flow tends to be laminar and smooth. Conversely, at high Reynolds numbers, inertial forces dominate and the flow tends to be turbulent with instabilities occurring. The range of Reynolds numbers for laminar or turbulent flow depend on the geometry in which the fluid is flowing. In the context of the present work, we are interested in laminar flow past a sphere and so only low Reynolds numbers, $Re < 50$, are considered.

In the special case of $Re = 0$ we obtain the steady-state Stokes' problem. Fluid flows with $Re \ll 1$ are referred to as creeping flows for which the governing equations are

$$\begin{aligned} \nabla^2 \mathbf{u} - \nabla p &= \mathbf{f} \\ \nabla \cdot \mathbf{u} &= 0 \end{aligned} \tag{2.13}$$

We shall use the Stokes' problem as a means of validating part of our numerical scheme (see Chapter 4).

2.2 Constitutive Models

So far we have considered the model for a Newtonian fluid, which features purely viscous fluid behaviour. Now we will build upon the Newtonian model and include other types of behaviour. A fluid which does not obey the linear relation between stress and strain rate is termed Non-Newtonian. This term covers a wide range of different fluids. For example, one may be interested in fluids which show an increase (shear-thickening) or decrease (shear-thinning) in viscosity as the shear rate experienced by the fluid is increased. We are particularly interested in viscoelastic fluids where, along with viscous effects, elastic behaviour is exhibited by the fluid, which may manifest itself in a variety of observable traits.

Viscoelastic fluids typically have two different characteristic times associated with them. Firstly, the time taken for the fluid to reach a state of equilibrium after a stress has been applied. This is termed the relaxation time, λ_1. The second is the time taken for at least partial elastic recovery to be felt by the fluid after a deformation. This is termed the retardation time, λ_2. In the case of a Newtonian fluid, these times are equal and so effectively their effects are cancelled out.

Viscoelastic fluids also tend to have a non-zero first, and sometimes second, normal stress difference. For a Newtonian fluid, both are zero-valued. These properties will be investigated for our viscoelastic models in Section 2.2.3.

Treating a fluid as containing both viscous and elastic contributions to its properties we separate the zero shear rate viscosity, η_0, into solvent(η_s) and polymeric(η_p)

contributions so that

$$\eta_0 = \eta_s + \eta_p. \tag{2.14}$$

We may define the retardation time in terms of these viscosities and the relaxation time by the relationship

$$\lambda_2 = \frac{\eta_s \lambda_1}{(\eta_p + \eta_s)}. \tag{2.15}$$

We may also apply the same concept of solvent and polymeric contributions to the extra-stress tensor, so that

$$\mathbf{T} = 2\eta_s \mathbf{d} + \boldsymbol{\tau} \tag{2.16}$$

where $\boldsymbol{\tau}$ is called the elastic stress tensor.

We substitute this expression into (2.7) to obtain the conservation equations for a general incompressible viscoelastic fluid

$$\rho_F \frac{D\mathbf{u}}{Dt} = -\nabla p + \eta_s \nabla^2 \mathbf{u} + \nabla \cdot \boldsymbol{\tau} + \mathbf{f} \tag{2.17}$$

$$\nabla \cdot \mathbf{u} = 0 \tag{2.18}$$

since $\nabla \cdot (2\mathbf{d}) = \nabla^2 \mathbf{u}$, using $\nabla \cdot \nabla \mathbf{u}^T = 0$ from the continuity equation.

Dimensionless Equation

For the dimensionless form of these equations we introduce a dimensionless parameter, β, defined by

$$\beta = \frac{\eta_s}{\eta_s + \eta_p} \tag{2.19}$$

which is termed the viscosity ratio. Using this alongside our previous dimensionless variables, (2.16) becomes

$$\mathbf{T} = 2\beta \mathbf{d} + \boldsymbol{\tau}. \tag{2.20}$$

and we obtain the dimensionless conservation equations for a general incompressible viscoelastic fluid

$$Re \frac{D\mathbf{u}}{Dt} = -\nabla p + \beta \nabla^2 \mathbf{u} + \nabla \cdot \boldsymbol{\tau} + \mathbf{f},$$

$$\nabla \cdot \mathbf{u} = 0. \tag{2.21}$$

We note that this system is not closed, since we still require a constitutive equation as we did for a Newtonian fluid. We define this through the relationship between the elastic-stress, $\boldsymbol{\tau}$, and the rate-of-deformation, $\mathbf{d}$. The choice of model will dictate the fluid properties which may be captured.

At this point, it is also convenient to define the upper-convected derivative of a general tensor field, $\mathbf{G}$, by

$$\overset{\triangledown}{\mathbf{G}} = \frac{D\mathbf{G}}{Dt} - \mathbf{G} \cdot \nabla\mathbf{u} - (\nabla\mathbf{u})^T \cdot \mathbf{G}. \tag{2.22}$$

2.2.1 Oldroyd B Model

The constitutive equation for the Oldroyd B model [39] is given by

$$\mathbf{T} + \lambda_1 \overset{\triangledown}{\mathbf{T}} = 2\eta_0 \left(\mathbf{d} + \lambda_2 \overset{\triangledown}{\mathbf{d}} \right) \tag{2.23}$$

However if we substitute (2.16) into (2.23), then we obtain the Oldroyd B constitutive equation for the elastic stress tensor

$$\boldsymbol{\tau} + \lambda_1 \overset{\triangledown}{\boldsymbol{\tau}} = 2\eta_p \mathbf{d} \tag{2.24}$$

Dimensionless Form

Applying the previous dimensionless scales, we arrive at a dimensionless constitutive equation for the Oldroyd B model,

$$\boldsymbol{\tau} + We \overset{\triangledown}{\boldsymbol{\tau}} = 2\left(1 - \beta\right)\mathbf{d} \tag{2.25}$$

where the dimensionless group, We, is termed the Weissenberg number, and is defined by

$$We = \frac{\lambda_1 U}{L} \tag{2.26}$$

This dimensionless group may be interpreted as a measure of the amount of recoverable strain in the fluid [64] or more simply (and crudely) as a measure of the elasticity in the fluid.

The Oldroyd B model does not capture all the features of a general viscoelastic fluid and in fact displays some very unphysical behaviour under certain conditions, as we shall see in section 2.2.3. However, it has been used to reproduce a wide range of experimentally observed phenomena and is therefore a good starting point when attempting to model viscoelastic fluids.

Upper-Convected Maxwell (UCM)

In the case of a purely elastic fluid, with no solvent contribution to the stress or viscosity, then we may take the limiting case of $\eta_s \to 0$. This means that $\mathbf{T} \equiv \boldsymbol{\tau}$ for (2.24). This leads to the Upper-Convected Maxwell model. It is considered to be the simplest model capable of capturing viscoelastic behaviour. We shall not be considering this model in the current work.

2.2.2 Giesekus Model

There are many models which involve the addition of extra terms to the Oldroyd B constitutive equation, but they may all be captured in the following general formulation

$$\boldsymbol{\tau} + \lambda_1 \overset{\triangledown}{\boldsymbol{\tau}} + \mathbf{f}\left(\boldsymbol{\tau}, \mathbf{d}\right) = 2\eta_p \mathbf{d} \tag{2.27}$$

where $\mathbf{f}$ is a function specific to the particular model in question.

One such model which fits this form is the Giesekus model [18]. Using a kinetic theory description of the polymer dynamics, Giesekus [18] introduced the idea of an anisotropic drag on the beads. Introducing a tensor drag coefficient, the constitutive equation for the elastic stress is given by

$$\boldsymbol{\tau} + \lambda_1 \overset{\triangledown}{\boldsymbol{\tau}} + \frac{\alpha\lambda_1}{\eta_p}\boldsymbol{\tau}^2 = 2\eta_p \mathbf{d} \tag{2.28}$$

with $\alpha > 0$ being known as the mobility parameter and where $\boldsymbol{\tau}^2 = \boldsymbol{\tau} \cdot \boldsymbol{\tau}$. For this model, the second normal stress difference is non-zero (negative) in shear and the extensional viscosity asymptotes to a constant value for large $\lambda_1\dot{\eta}$.

Applying our usual dimensionless scales, we obtain a dimensionless constitutive equation for the Giesekus model,

$$\boldsymbol{\tau} + We\left(\overset{\triangledown}{\boldsymbol{\tau}} + \frac{\alpha}{(1-\beta)}\boldsymbol{\tau}^2\right) = 2\,(1-\beta)\,\mathbf{d} \tag{2.29}$$

The value of the mobility parameter is restricted to values in the range $0 \leq \alpha \leq 0.5$ in order for the model to remain physically realistic. Its value determines the extent of the behaviour captured by the model. In particular, α has an impact on both the shear and extensional behaviour of the model. It plays a significant role in extension hardening and shear-thinning as well as the convergence of both first and second normal stress differences with increasing shear-rate. A detailed look at the change with variation of the mobility parameter can be seen in Section 2.2.3.

An alternative non-dimensionalisation uses $\frac{\eta_p U}{L}$ as the characteristic scale for the elastic stress. In this case the dimensionless form of the Giesekus constitutive equation is

$$\boldsymbol{\tau} + We\left(\overset{\triangledown}{\boldsymbol{\tau}} + \alpha\boldsymbol{\tau}^2\right) = 2\mathbf{d}. \tag{2.30}$$

The corresponding conservation equations are,

$$Re\frac{D\mathbf{u}}{Dt} = -\nabla p + \beta\nabla^2\mathbf{u} + (1-\beta)\,\nabla\cdot\boldsymbol{\tau} + \mathbf{f} \tag{2.31}$$

$$\nabla\cdot\mathbf{u} = 0. \tag{2.32}$$

2.2.3 Viscometrics

When investigating the suitability of a model for a fluid, it is important to look at its behaviour under simple types of flow. These flows enable one to compare characteristics of models against each other. The shear viscosity (or shear-rate dependent viscosity), $\eta_{shear}(\dot{\gamma})$, is given by the ratio of the shear stress to the shear rate, $\dot{\gamma}$, i.e.

$$\eta_{shear}\,(\dot{\gamma}) = \frac{\sigma_{xy}}{\dot{\gamma}}. \tag{2.33}$$

The zero shear-rate viscosity is given by

$$\eta_0 = \lim_{\dot{\gamma}\to 0}\eta_{shear}\,(\dot{\gamma})\,. \tag{2.34}$$

The shear viscosity for many non-Newtonian fluids is observed to be monotonically decreasing for increasing shear-rate, $\dot{\gamma}$, to some limit, η_∞, as the shear-rate gets very large.

This behaviour is known as shear-thinning, as mentioned earlier. There are examples of fluids which display the opposite behaviour, known as shear-thickening. Further, yielding fluids exist which only begin to deform after a threshold of shear stress is reached, after which it may display any of the properties previously mentioned. Another type would be rheopectic and thixotropic fluids, where there is a time-dependence on the shear viscosity with respect to the shear stress. Our focus shall be on fluids exhibiting shear-thinning behaviour.

The first and second normal stress differences are the independent differences

$$N_1(\dot{\gamma}) := \sigma_{xx} - \sigma yy \tag{2.35}$$

$$N_2(\dot{\gamma}) := \sigma_{yy} - \sigma zz. \tag{2.36}$$

The presence of (non-zero) normal stress differences is very important in viscoelastic fluids and experimental evidence suggests that they are responsible for many of the observed distinctive phenomena. It is generally expected that N_1 is positive and larger in magnitude than N_2. Experimental evidence suggests that N_2 is negative, especially in polymeric liquids [45].

The extensional viscosity at some extension rate, $\dot{\epsilon}$, is given by

$$\eta_{ext}(\dot{\epsilon}) = \frac{\sigma_{xx} - \sigma_{yy}}{\dot{\epsilon}}, \tag{2.37}$$

which is the contribution to viscosity as a result of the material being stretched and is an important feature in many flows involving non-Newtonian fluids. For polymeric fluids η_{ext} is typically seen to increase with increasing extension rate. This is termed extension-hardening with the reverse (decreasing extensional viscosity with increasing extension rate) is termed extension-softening. It has been noted that the extensional properties of a fluid may turn what is otherwise a relatively simple problem into one which is incredibly complex and difficult to model. Choosing a model which behaves well under extension is therefore a consideration when studying flows where regions of extensional flow are to be expected.

The Trouton ratio is the ratio between the extensional viscosity and the zero-shear-rate viscosity, so it is dependent on the The reason for a fluid having a large Trouton ratio may come from the effect of shear-thinning (polymer melts for example) or from extensional viscosities which increase greatly with the extension rate, $\dot{\epsilon}$.

Simple Steady Shear Flow

Consider a shearing flow with a constant shear rate, $\dot{\gamma}$ in the Cartesian x-direction. The resulting flow field is $\mathbf{u} = (\dot{\gamma}y, 0, 0)$ which gives a pressure, $p = C$ (where C is some constant). By substituting the velocity field into the constitutive equation we find that the stress tensor, $\boldsymbol{\sigma}$, has components which satisfy the following

$$\sigma_{xy} = \eta_{shear}(\dot{\gamma})\,\dot{\gamma} \tag{2.38}$$

$$\sigma_{xx} - \sigma_{yy} = N_1(\dot{\gamma}) \tag{2.39}$$

$$\sigma_{yy} - \sigma_{zz} = N_2(\dot{\gamma}) \tag{2.40}$$

$$\sigma_{xz} = \sigma_{yz} = 0 \tag{2.41}$$

which gives us the means to calculate the shear viscosity and first and second normal stress differences for this simple flow.

The Newtonian model predicts a constant shear viscosity (i.e. $\eta_{shear}(\dot{\gamma}) = \eta_0$) and zero first and second normal stress differences, as is clear from (2.9).

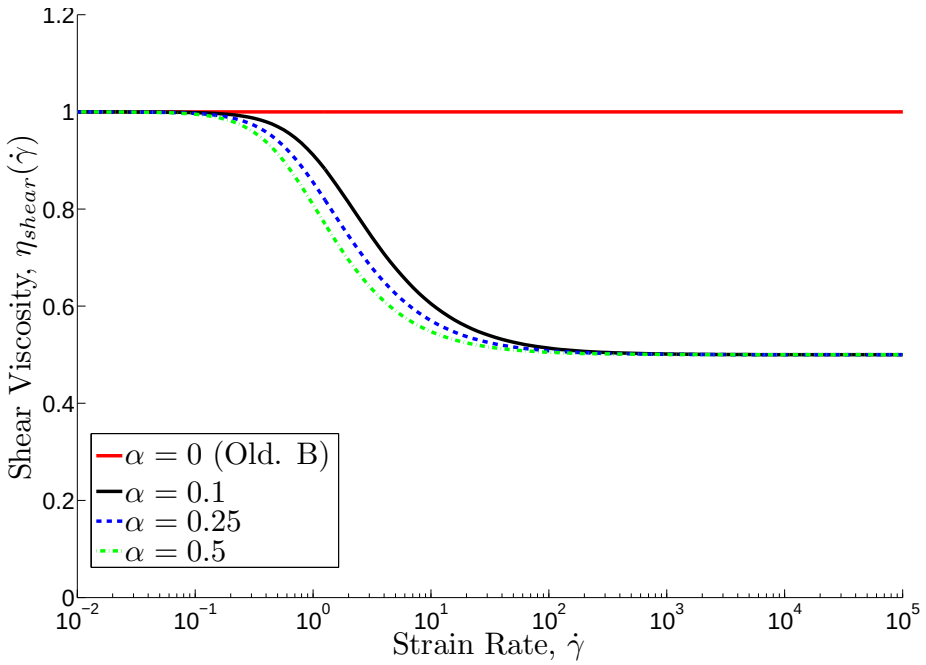

Figure 2.1: Shear viscosity behaviour for the Oldroyd B and Giesekus models. Parameters: $\lambda = 1$, $\eta_p = \frac{1}{2}$, $\eta_0 = 1$

Figure 2.1 and Figures 2.2(a)- 2.2(b) show graphs of the shear viscosity and normal stress differences as a function of shear rate, respectively, for the Oldroyd B and Giesekus models. Like the Newtonian case, the Oldroyd B model predicts a constant shear viscosity and therefore would not be a suitable choice of constitutive equation in modelling a shear-thinning fluid. However, they do capture a non-zero first normal stress difference, given by

$$N_1\left(\dot{\gamma}\right) = 2\lambda\eta_0\dot{\gamma}^2, \tag{2.42}$$

which is a common viscoelastic property, although neither model predicts a non-zero second stress difference.

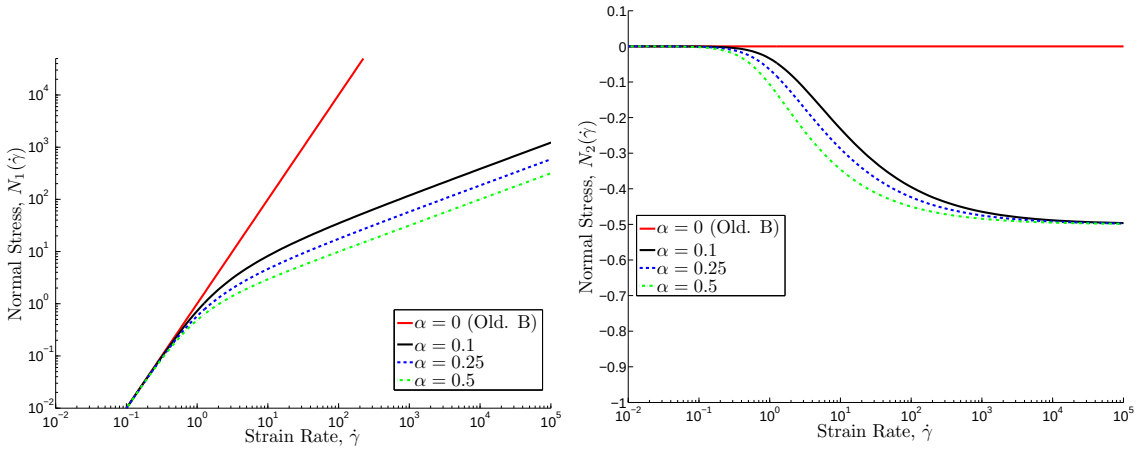

(a) N_1 (b) N_2

Figure 2.2: Normal stress difference behaviour Oldroyd B and Giesekus models. Parameters: $\lambda_1 = 1$, $\eta_p = \frac{1}{2}$, $eta_0 = 1$.

Finally, the Giesekus model predicts shear-thinning behaviour as well as non-zero first and second normal stress differences. We may refer to Renardy [49], where a detailed analysis of the flow is found, to obtain the shear behaviour in the limits of large and small shear rates

$$\dot{\gamma} \to 0, \quad \eta_{shear}\left(\dot{\gamma}\right) = \eta_0, \quad N_1\left(\dot{\gamma}\right) = 0, \quad N_2\left(\dot{\gamma}\right) = 0, \tag{2.43}$$

$$\dot{\gamma} \to \infty, \quad \eta_{shear}\left(\dot{\gamma}\right) = \eta_s, \quad N_1 \sim \sqrt{\dot{\gamma}}, \quad N_2\left(\dot{\gamma}\right) = -\frac{\eta_p}{\lambda}. \tag{2.44}$$

The second normal stress difference takes a negative value and is smaller in magnitude than the first, which matches experimentally observed results [45]. The choice of α

plays a role in the each of the viscometric functions for this flow where we observe that the model becomes increasingly shear-thinning with increasing α and that both the first and second normal stress differences decrease. However, the large shear rate behaviour is not dependent upon α with the exception of N_1 which decreases with α at a fixed shear rate.

Uniaxial Extensional Flow

We now consider a fluid being extended in opposite directions along a chosen axis. For this case, uniaxial extensional flow, we have the velocity field, $\mathbf{u} = \left(\dot{\epsilon}x, -\frac{\dot{\epsilon}y}{2}, -\frac{\dot{\epsilon}z}{2}\right)$. Solving the Navier-Stokes equations for this velocity field gives $p = -\frac{\rho}{8}\dot{\epsilon}^2\left(4x^2 + y^2 + z^2\right) + C$ (where C is some constant) and the following form for the stress tensor,

$$\sigma_{xx} - \sigma_{yy} = \dot{\epsilon}\eta_{ext}(\dot{\epsilon}) \tag{2.45}$$

$$\sigma_{xx} - \sigma_{zz} = \dot{\epsilon}\eta_{ext}(\dot{\epsilon}) \tag{2.46}$$

$$\sigma_{ij} = 0, \quad i \neq j \tag{2.47}$$

which gives us the means to calculate the extensional viscosity.

The Newtonian model predicts a linearly increasing extensional viscosity with increasing extension rate

$$\eta_{ext}\left(\dot{\gamma}\right) = 3\eta_0. \tag{2.48}$$

Figure 2.3 shows the extensional viscosity for the Oldroyd B model for a chosen set of parameters. The extensional viscosity is given by

$$\eta_{ext}\left(\dot{\gamma}\right) = \frac{3\eta_0\left(1 - \lambda_2\dot{\epsilon} - 2\lambda\lambda_2\dot{\epsilon}^2\right)}{\left(1 - 2\lambda\dot{\epsilon}\right)\left(1 + \lambda\dot{\epsilon}\right)}. \tag{2.49}$$

where $\lambda_2 = \frac{\eta_s\lambda}{\eta_0}$. It is clear from both the figure and the expression above that the Oldroyd B model predicts a infinitely large extensional viscosity at a finite extension rate $\dot{\epsilon} = \frac{1}{2\lambda}$. This is certainly not a desirable feature and is a result of the underlying

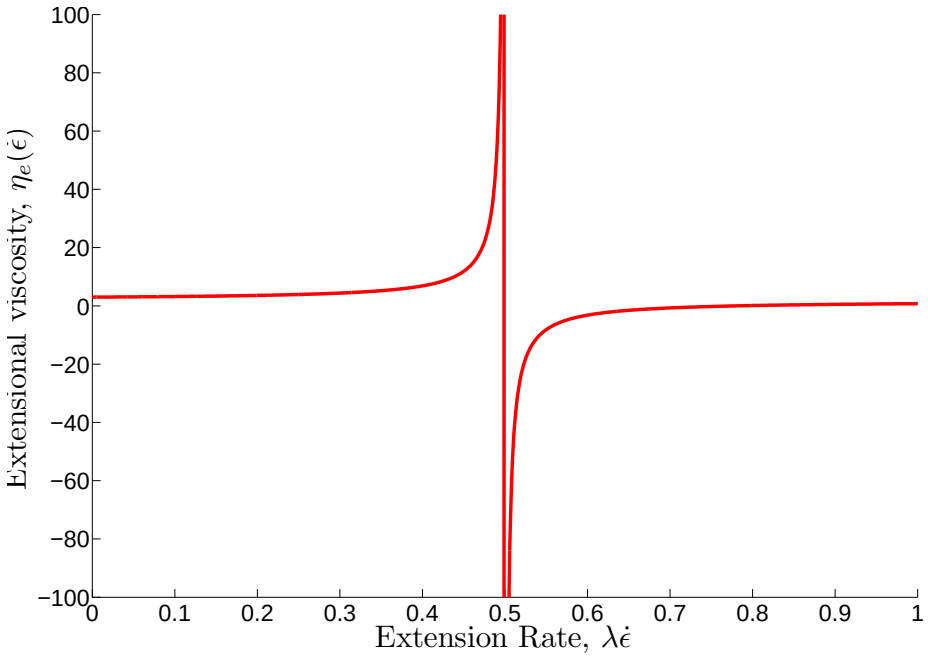

Figure 2.3: Extensional viscosity, $\eta_{ext}(\dot{\epsilon})$ for the Giesekus model. Parameters: $\lambda = 1$, $\eta_p = \frac{1}{2}$, $\eta_0 = 1$.

assumption of a Hookean spring. This means that Oldroyd B models are a not sound choice for flows involving extension.

The Giesekus model, however, does not suffer from this problem and predicts finite values of η_{ext} at all extension rates. Figure 2.4 show the extensional viscosity for the model at selected values of α where we can see that extension hardening is predicted. We see that a constant value is reached as the extension rate is increased and we find reaching a limiting value [49] of

$$\eta_{ext}(\dot{\epsilon}) = 3\eta_s + 2\frac{\eta_p}{\alpha} \tag{2.50}$$

as $\dot{\epsilon} \to \infty$, meaning that the extensional viscosity decreases with increasing α. At values of $\alpha > 0.5$ the model exhibits non-monotonic behaviour of the extensional viscosity and so it may be considered to be unphysical. Other authors have limited their range to $0 < \alpha \leq 0.5$ [36] and we shall consider values in this range too.

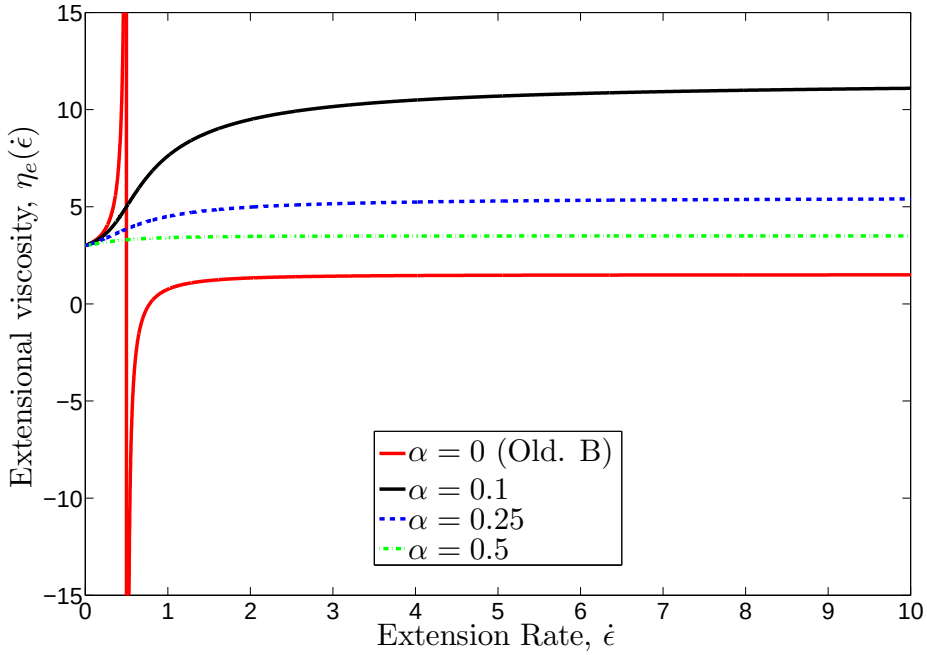

Figure 2.4: Extensional viscosity, $\eta_{ext}(\dot{\epsilon})$ for the Giesekus model. Parameters: $\lambda = 1$, $\eta_p = \frac{1}{2}$, $\eta_0 = 1$.

2.3 Alternative Continuity Equation

In the previous sections, we have considered the usual continuity equation for an incompressible fluid, $\nabla \cdot \mathbf{u} = 0$. In 2006, Gwynllyw and Phillips [50] considered an alternative formulation of the Stokes' problem where the continuity equation is replaced by

$$\nabla \cdot \mathbf{u} = -\mu \int_{\Omega} p d\Omega \tag{2.51}$$

where μ is some positive constant.

The statement remains equivalent to the original equation because the pressure has a vanishing mean over the domain, Ω. This may be seen by integrating (2.51) over Ω and applying Green's theorem. The benefit is that the vanishing mean property is not guaranteed to be satisfied within a single element of the domain, but this alternative formulation guarantees that the pressure possesses the vanishing mean over the domain and so we can be sure that $p \in L_0^2(\Omega)$. That is to say that we may determine a unique solution for the pressure, rather than a solution up to a constant for the traditional formulation. While this formulation was originally used for the Stokes' problem, the

alternative formulation is clearly valid for the Navier-Stokes equations.

There is also an additional benefit for the spectral element method, in that there is some improvement in the conditioning of the linear system arising from the spatial discretisation. This will be investigated further in the results chapters.

From this point on, we use the alternative form of the continuity equation, (2.51), with the knowledge that we may recover the original formulation by setting $\mu = 0$.

2.4 Expression for Drag

We shall be considering flows where we wish to calculate the drag which is found by integrating $\boldsymbol{\sigma} \cdot \mathbf{n}$ over the surface of the body we wish to calculate the drag upon. For a cylinder in planar co-ordinates, the drag is given by

$$D = 2\int_0^\pi \Big(\big(p - 2\beta\nabla\mathbf{u}_{xx} - \tau_{xx}\big)\cos\theta + \big(\beta(\nabla\mathbf{u}_{xy} + \nabla\mathbf{u}_{yx}) + \tau_{xy}\big)\sin\theta \Big) d\theta, \tag{2.52}$$

and for a sphere in an axisymmetric geometry

$$D = 2\pi R_S^2 \int_0^\pi \Big(\big(p - 2\beta\nabla\mathbf{u}_{zz} - \tau_{zz}\big)\cos\theta + \big(\beta(\nabla\mathbf{u}_{rz} + \nabla\mathbf{u}_{zr}) + \tau_{rz}\big)\sin\theta \Big) \sin\theta d\theta. \tag{2.53}$$

2.5 Boundary Conditions

To solve the governing equations we require boundary conditions. The choice of boundary conditions determines the flow, so they are extremely important. We must first consider the geometry of the problem. We denote the boundary of some bounded domain, Ω, as Γ, and further we split the boundary into sections so that

$$\Gamma = \Gamma^- \cup \Gamma^+ \cup \Gamma^W \cup \Gamma^C \cup \Gamma^S \tag{2.54}$$

where Γ^- and Γ^+ are inflow and outflow boundaries, Γ^W and Γ^C are wall and circular wall boundaries and Γ^S is a boundary on the axis of symmetry.

We prescribe a velocity at inflow and outflow, apply no-slip conditions on wall boundaries and axisymmetric boundary conditions along the axis of symmetry

$$\mathbf{u} = \mathbf{u_{in}} \text{ on } \Gamma^-, \tag{2.55}$$

$$\mathbf{u} = \mathbf{u_{out}} \text{ on } \Gamma^+, \tag{2.56}$$

$$\mathbf{u} = \mathbf{0} \text{ on } \Gamma^W, \tag{2.57}$$

$$\mathbf{u} = \mathbf{0} \text{ on } \Gamma^C, \tag{2.58}$$

$$\mathbf{u} \cdot \mathbf{n} = \mathbf{0} \text{ on } \Gamma^S. \tag{2.59}$$

where $\mathbf{u_{in}}$ and $\mathbf{u_{out}}$ are known and are chosen according to the geometry and problem of interest.

Further, we must prescribe a boundary condition on the elastic stress at inflow

$$\boldsymbol{\tau} = \boldsymbol{\tau_{in}} \text{ on } \Gamma^-, \tag{2.60}$$

where $\boldsymbol{\tau_{in}}$ is typically found by substituting the known velocity solution into the constitutive equation and solving for $\boldsymbol{\tau}$. This is fairly trivial for the majority of boundary conditions we shall be considering. There are solutions available for a limited range of complicated boundary conditions, such as transient pipeflow.

2.5.1 Types of boundary on Subdomains

Suppose we have Ω_e, some subdomain of Ω, with boundary Γ_e. We define an inflow boundary, Γ_e^- of this subdomain with respect to a given velocity, $\mathbf{u}$, as,

$$\Gamma_e^- = \{\mathbf{x} \in \Gamma \mid \mathbf{u}(\mathbf{x}) \cdot \mathbf{n}(\mathbf{x}) < 0\}, \tag{2.61}$$

where $\mathbf{n}$ is the outward normal to Γ_e. We define the outflow boundary on this subdomain to be $\Gamma_e^+ \equiv \Gamma_e \backslash \Gamma_e^-$.

2.6 Statement of Equations

Before continuing, we restate the final system of dimensionless equations which we use to model fluids in the subsequent chapters. The most general form of this system is

$$Re\frac{D\mathbf{u}}{Dt} = -\nabla p + \beta\nabla^2\mathbf{u} + \nabla\cdot\boldsymbol{\tau} + \mathbf{f}, \tag{2.62}$$

$$\nabla\cdot\mathbf{u} = -\mu\int_\Omega p d\Omega, \tag{2.63}$$

$$\boldsymbol{\tau} + We\left(\overset{\triangledown}{\boldsymbol{\tau}} + \frac{\alpha}{(1-\beta)}\boldsymbol{\tau}^2\right) = 2\left(1-\beta\right)\mathbf{d}. \tag{2.64}$$

We may recover the Oldroyd B model (2.25) by setting the mobility parameter, $\alpha = 0$. Following this, we recover the UCM model by setting $\beta = 0$. Alternatively to UCM, we recover the Newtonian model (2.11) by setting $\beta = 1$ and $We = 0$. Finally, we arrive at the Stokes' problem (2.13) by setting $Re = 0$.

We may choose to use the alternative formulation of the continuity equation, or the original form by setting the parameter, $\mu = 0$.

2.6.1 Strong Component Form of Equations

In the coming section, we state our equations in component form for the co-ordinate systems of interest, namely 2-D Cartesian and 3-D axisymmetric cylindrical polar co-ordinates.

First we state the components of the velocity gradient in Cartesian co-ordinates

$$\left(\nabla\mathbf{u}\right)_{xx} = \frac{\partial u_x}{\partial x}, \tag{2.65}$$

$$\left(\nabla\mathbf{u}\right)_{xy} = \frac{\partial u_y}{\partial x}, \tag{2.66}$$

$$\left(\nabla\mathbf{u}\right)_{yx} = \frac{\partial u_x}{\partial y}, \tag{2.67}$$

$$\left(\nabla\mathbf{u}\right)_{yy} = \frac{\partial u_y}{\partial y}, \tag{2.68}$$

where $\mathbf{u} = (u_x, u_y)$ and the non-zero components of the velocity gradient in axisym-

metric cylindrical polar co-ordinates

$$(\nabla \mathbf{u})_{rr} = \frac{\partial u_r}{\partial r}, \tag{2.69}$$

$$(\nabla \mathbf{u})_{rz} = \frac{\partial u_z}{\partial r}, \tag{2.70}$$

$$(\nabla \mathbf{u})_{zr} = \frac{\partial u_r}{\partial z}, \tag{2.71}$$

$$(\nabla \mathbf{u})_{zz} = \frac{\partial u_z}{\partial z}, \tag{2.72}$$

$$(\nabla \mathbf{u})_{\theta\theta} = \frac{u_r}{r}. \tag{2.73}$$

where $\mathbf{u} = (u_r, 0, u_z)$.

Momentum and Continuity Equations

We state the strong formulation of the conservation of momentum and mass for an incompressible viscoelastic fluid, (2.18)-(2.17), in both (2-D) Cartesian co-ordinates

$$Re\left(\frac{\partial u_x}{\partial t} + u_x\frac{\partial u_x}{\partial x} + u_y\frac{\partial u_x}{\partial y}\right) = \beta\left(\frac{\partial^2 u_x}{\partial x^2} + \frac{\partial^2 u_x}{\partial y^2}\right) - \frac{\partial p}{\partial x} + \frac{\partial \tau_{xx}}{\partial x} + \frac{\partial \tau_{yx}}{\partial y} + f_x, \tag{2.74}$$

$$Re\left(\frac{\partial u_y}{\partial t} + u_x\frac{\partial u_y}{\partial x} + u_y\frac{\partial u_y}{\partial y}\right) = \beta\left(\frac{\partial^2 u_y}{\partial x^2} + \frac{\partial^2 u_y}{\partial y^2}\right) - \frac{\partial p}{\partial x} + \frac{\partial \tau_{xy}}{\partial x} + \frac{\partial \tau_{yy}}{\partial y} + f_y, \tag{2.75}$$

$$\frac{\partial u_x}{\partial x} + \frac{\partial u_y}{\partial y} = -\mu\int_\Omega p d\Omega. \tag{2.76}$$

and given in axisymmetric cylindrical polar coordinates

$$Re\left(\frac{\partial u_r}{\partial t} + u_r\frac{\partial u_r}{\partial r} + u_z\frac{\partial u_r}{\partial z}\right) = \beta\left(\frac{1}{r}\frac{\partial}{\partial r}\left(r\frac{\partial u_r}{\partial r}\right) + \frac{\partial^2 u_r}{\partial z^2} - \frac{u_r}{r^2}\right) - \frac{\partial p}{\partial r} + \frac{1}{r}\frac{\partial}{\partial r}(r\tau_{rr}) + \frac{\partial \tau_{zr}}{\partial z} - \frac{\tau_{\theta\theta}}{r} + f_r, \tag{2.77}$$

$$Re\left(\frac{\partial u_z}{\partial t} + u_r\frac{\partial u_z}{\partial r} + u_z\frac{\partial u_z}{\partial z}\right) = \beta\left(\frac{1}{r}\frac{\partial}{\partial r}\left(r\frac{\partial u_z}{\partial r}\right) + \frac{\partial^2 u_z}{\partial z^2}\right) - \frac{\partial p}{\partial z} + \frac{1}{r}\frac{\partial}{\partial r}(r\tau_{rz}) + \frac{\partial \tau_{zz}}{\partial z} + f_z, \tag{2.78}$$

$$\frac{1}{r}\frac{\partial}{\partial r}(ru_r) + \frac{\partial u_z}{\partial z} = -\mu\int_\Omega p d\Omega. \tag{2.79}$$

and note that in the axisymmetric cylindrical polar coordinates, $d\Omega = rdrdz$.

Constitutive Equation

We state the strong formulation of the Giesekus model in both (2-D) Cartesian coordinates

$$\begin{aligned}
\tau_{xx} + We\Bigg(&\frac{\partial \tau_{xx}}{\partial t} + u_x\frac{\partial \tau_{xx}}{\partial x} + u_y\frac{\partial \tau_{xx}}{\partial y} \\
&-2\left(\tau_{xx}\frac{\partial u_x}{\partial x} + \tau_{xy}\frac{\partial u_x}{\partial y}\right) \quad = 2(1-\beta)\frac{\partial u_x}{\partial x} \\
&+\frac{\alpha}{1-\beta}\left(\tau_{xx}^2 + \tau_{xy}^2\right)\Bigg) \qquad (2.80)\\
\tau_{xy} + We\Bigg(&\frac{\partial \tau_{xy}}{\partial t} + u_x\frac{\partial \tau_{xy}}{\partial x} + u_y\frac{\partial \tau_{xy}}{\partial y} \\
&-\tau_{xx}\frac{\partial u_y}{\partial x} - \tau_{xy}\left(\frac{\partial u_x}{\partial x} + \frac{\partial u_y}{\partial y}\right) - \tau_{yy}\frac{\partial u_x}{\partial y} \quad = (1-\beta)\left(\frac{\partial u_x}{\partial y} + \frac{\partial u_y}{\partial x}\right) \\
&+\frac{\alpha}{1-\beta}\tau_{xy}\left(\tau_{xx} + \tau_{yy}\right)\Bigg) \qquad (2.81)\\
\tau_{yy} + We\Bigg(&\frac{\partial \tau_{y}}{\partial t} + u_x\frac{\partial \tau_{yy}}{\partial x} + u_y\frac{\partial \tau_{yy}}{\partial y} \\
&-2\left(\tau_{xy}\frac{\partial u_y}{\partial x} + \tau_{yy}\frac{\partial u_y}{\partial y}\right) \quad = 2(1-\beta)\frac{\partial u_y}{\partial y} \\
&+\frac{\alpha}{1-\beta}\left(\tau_{xy}^2 + \tau_{yy}^2\right)\Bigg) \qquad (2.82)
\end{aligned}$$

and in axisymmetric cylindrical polar co-ordinates

$$\begin{aligned}\tau_{zz} + We\Bigg(&\frac{\partial \tau_{zz}}{\partial t} + u_z\frac{\partial \tau_{zz}}{\partial z} + u_r\frac{\partial \tau_{zz}}{\partial r}\\ &-2\left(\tau_{zz}\frac{\partial u_z}{\partial z} + \tau_{zr}\frac{\partial u_z}{\partial r}\right) \qquad = 2\left(1-\beta\right)\frac{\partial u_z}{\partial z}\\ &+\frac{\alpha}{1-\beta}\left(\tau_{zz}^2 + \tau_{zr}^2\right)\Bigg)\end{aligned} \tag{2.83}$$

$$\begin{aligned}\tau_{zr} + We\Bigg(&\frac{\partial \tau_{zr}}{\partial t} + u_z\frac{\partial \tau_{zr}}{\partial z} + u_r\frac{\partial \tau_{zr}}{\partial r}\\ &-\tau_{zz}\frac{\partial u_r}{\partial z} - \tau_{zr}\left(\frac{\partial u_z}{\partial z} + \frac{\partial u_r}{\partial r}\right) - \tau_{rr}\frac{\partial u_z}{\partial r} \qquad = \left(1-\beta\right)\left(\frac{\partial u_z}{\partial r} + \frac{\partial u_r}{\partial z}\right)\\ &+\frac{\alpha}{1-\beta}\tau_{zr}\left(\tau_{zz} + \tau_{rr}\right)\Bigg)\end{aligned} \tag{2.84}$$

$$\begin{aligned}\tau_{rr} + We\Bigg(&\frac{\partial \tau_{rr}}{\partial t} + u_z\frac{\partial \tau_{rr}}{\partial z} + u_r\frac{\partial \tau_{rr}}{\partial r}\\ &-2\left(\tau_{zr}\frac{\partial u_r}{\partial z} + \tau_{rr}\frac{\partial u_r}{\partial r}\right) \qquad = 2\left(1-\beta\right)\frac{\partial u_r}{\partial r}\\ &+\frac{\alpha}{1-\beta}\left(\tau_{zr}^2 + \tau_{rr}^2\right)\Bigg)\end{aligned} \tag{2.85}$$

$$\tau_{\theta\theta} + We\left(\frac{\partial \tau_{\theta\theta}}{\partial t} + u_z\frac{\partial \tau_{\theta\theta}}{\partial z} + u_r\frac{\partial \tau_{\theta\theta}}{\partial r} - 2\tau_{\theta\theta}\frac{u_r}{r} + \frac{\alpha}{1-\beta}\tau_{\theta\theta}^2\right) = 2\left(1-\beta\right)\frac{u_r}{r} \tag{2.86}$$

Chapter 3

Numerical Method

We are interested in solving both steady and transient problems. Therefore the equations are discretised in both time and space. This chapter will describe this process in detail. The temporal discretisation is covered in Section 3.1 and the spatial discretisation is covered in Section 3.2. Details of the spectral element method used for the spatial discretisation are given in Section 3.3.

3.1 Temporal Discretisation

3.1.1 Timestepping

We choose a uniform discretisation in time with timestep Δt so that $t^n = n\Delta t$. When referring to our outer timesteps, or solutions to the problem at particular timesteps, this is the time between any two consecutive steps. However, we may also employ intermediate timesteps for the various methods to deal with temporal derivatives. Further, we decouple the solution of the velocity and pressure part of our system from the elastic stress. This is achieved by solving the velocity-pressure problem at timestep t^{n+1} with an approximation of elastic stress using information from previous timesteps. The elastic stress at timestep t^{n+1} is then calculated using this velocity solution.

Coefficient	$J=1$	$J=2$	$J=3$
γ_0	1	3/2	11/6
α_0	1	2	3
α_1	-	$-1/2$	$-3/2$
α_2	-	-	1/3
β_0	1	2	3
β_1	-	-1	-3
β_2	-	-	1

Table 3.1: Table of coefficients for both J^{th}-order linear multistep approximations, such as the backward difference formula and Adams-Bashforth, and extrapolation methods.

Typically, if we have a function defined in both space and time, $\mathbf{f}(\mathbf{x}, t)$, then we denote the function at a particular timestep t^n by,

$$\mathbf{f}^n = \mathbf{f}(\mathbf{x}, t^n)\,. \tag{3.1}$$

3.1.2 Backward Difference Formula (BDF) Approximation

We need to approximate the temporal derivative at a particular timestep, t^{n+1}. One suitable scheme is to use the family of implicit linear multistep methods known as the backward differentiation formula (BDF). The J^{th}-order approximation of the temporal derivative of some arbitrary function, $\mathbf{f}$, at timestep t^{n+1} is,

$$\left.\frac{\partial \mathbf{f}}{\partial t}\right|^{n+1} \approx \frac{1}{\Delta t}\left(\gamma_0 \mathbf{f}^{n+1} - \sum_{q=0}^{J-1} \alpha_q \mathbf{f}^{n-q}\right) \tag{3.2}$$

where γ_0 and $\{\alpha_q\}_{q=0}^{J-1}$ are the BDF coefficients chosen such that the method achieves the prescribed order, J. Table 3.1 contains the coefficients for $J = 1, 2, 3$. We typically use $J = 2$.

3.1.3 Extrapolation (EX) of Explicit Terms

When we treat terms within our equations explicitly, using values computed at previous timesteps to approximate a value at the current timestep, we may improve accuracy

by using an extrapolation. As in Section 3.1.2, if we let the order of extrapolation be some integer, J, then we may write the J^{th} order extrapolation of some variable $\mathbf{x}$ as,

$$\mathbf{x}^{n+1} \approx \sum_{q=0}^{J-1} \beta_q \mathbf{x}^{n-q}, \tag{3.3}$$

where $\{\beta_q\}_{q=0}^{J-1}$ are the extrapolation coefficients. Table 3.1 contains the coefficients for $J = 1, 2, 3$ [27].

3.1.4 BDF/EX Approximation

We combine the BDF and EX approximations from Sections 3.1.2- 3.1.3 to discretise a differential equation of the form

$$\frac{\partial \mathbf{X}}{\partial t} = \mathbf{F}(\mathbf{X}), \tag{3.4}$$

with an arbitrary function $\mathbf{F}(\mathbf{X}) = \mathbf{F}_1(\mathbf{X}) + \mathbf{F}_2(\mathbf{X})$, where $\mathbf{F}_1(\mathbf{X})$ is explicitly known at timestep t^{n+1} and $\mathbf{F}_2(\mathbf{X})$ is known only at timesteps t^n and below. We may approximate this function as

$$\frac{\gamma_0 \mathbf{X}^{n+1} - \sum_{q=0}^{J-1} \alpha_q \mathbf{X}^{n-q}}{\Delta t} = \mathbf{F}_1\left(\mathbf{X}^{n+1}\right) + \sum_{q=0}^{J-1} \beta_q \mathbf{F}_2\left(\mathbf{X}^{n-q}\right) \tag{3.5}$$

3.1.5 Operator-Integration-Factor Splitting Scheme

Rather than approximate the temporal and convective derivatives separately, we may use the Operator-Integration-Factor Splitting (OIFS) method [35] to calculate an approximation for the material derivative. In general, the J^{th}-order OIFS (OIFSJ) approximation is given by

$$\frac{D\mathbf{G}}{Dt} = \frac{\partial \mathbf{G}}{\partial t} + \mathbf{u} \cdot \nabla \mathbf{G} \approx \frac{1}{\Delta t} \left(\gamma_0 \mathbf{G}^{n+1} - \sum_{q=0}^{J-1} \alpha_q \tilde{\mathbf{G}}_q^{n+1} \right), \tag{3.6}$$

where the coefficients, γ_0 and α_q, are the same as those given in the BDFJ approximation and $\tilde{\mathbf{G}}_q$ is the solution to the pure-advection initial value problem,

$$\frac{\partial \tilde{\mathbf{G}}_q}{\partial t} = -\mathbf{u}^* \cdot \nabla \tilde{\mathbf{G}}_q, \qquad t \in \left[t^{n-q}, t^{n+1}\right], \qquad \tilde{\mathbf{G}}_q\left(\mathbf{x}, t^{n-q}\right) = \mathbf{G}^{n-q}\left(\mathbf{x}\right), \tag{3.7}$$

and where $\mathbf{u}^*$ is the piecewise linear approximation of velocity given by

$$\mathbf{u}^*(t) = \left(\frac{t-t^{i-1}}{\Delta t}\right)\mathbf{u}^i + \left(1-\left(\frac{t-t^{i-1}}{\Delta t}\right)\right)\mathbf{u}^{i-1}, \qquad \mathbf{u}^i = \mathbf{u}\big(\mathbf{x}, t^i\big)\,, \tag{3.8}$$

where $i = n$ for $t \in [t^{n-1}, t^{n+1}]$ and $i = n-q$ for $t \in [t^{n-q-1}, t^{n-q}]$, $q > 1$.

We solve these advection problems numerically using a 4^{th}-order Runge-Kutta (RK4) method with M inner timesteps. Typically a value $M = 4$ or 8 is used.

For example, at second-order (OIFS2) the material derivative of some arbitrary function, $\mathbf{G}$, is approximated at time $t = t^{n+1}$ by,

$$\frac{D\mathbf{G}}{Dt} = \frac{\partial \mathbf{G}}{\partial t} + \mathbf{u}\cdot\nabla\mathbf{G} \approx \frac{1}{2\Delta t}\left(3\mathbf{G}^{n+1} - 4\tilde{\mathbf{G}}_0^{n+1} + \tilde{\mathbf{G}}_1^{n+1}\right) \tag{3.9}$$

where $\tilde{\mathbf{G}}$ and $\tilde{\mathbf{G}}$ are the solutions of the two pure-advection initial value problems,

$$\frac{\partial \tilde{\mathbf{G}}_0}{\partial t} = -\mathbf{u}^*\cdot\nabla\tilde{\mathbf{G}}_0, \qquad t \in \left[t^n, t^{n+1}\right], \qquad \tilde{\mathbf{G}}_0\left(\mathbf{x}, t^n\right) = \mathbf{G}^n\left(\mathbf{x}\right), \tag{3.10}$$

$$\frac{\partial \tilde{\mathbf{G}}_1}{\partial t} = -\mathbf{u}^*\cdot\nabla\tilde{\mathbf{G}}_1, \qquad t \in \left[t^{n-1}, t^{n+1}\right], \qquad \tilde{\mathbf{G}}_1\left(\mathbf{x}, t^{n-1}\right) = \mathbf{G}^{n-1}\left(\mathbf{x}\right). \tag{3.11}$$

3.1.6 Semi-Discrete System

Using the previously described approximations in time we present our semi-discrete equations. For the momentum and continuity equations, (2.62)-(2.63), we use the OIFS approximation for the material derivative of velocity and EX on the explicitly treated elastic stress terms, both at order J. This results in the following OIFSJ/EXJ semi-discrete velocity-pressure system,

$$\frac{Re\gamma_0}{\Delta t}\mathbf{u}^{n+1} - \beta\nabla^2\mathbf{u}^{n+1} + \nabla p^{n+1} = \mathbf{f}^{n+1} + \sum_{q=0}^{J-1}\left(\frac{Re}{\Delta t}\alpha_q\tilde{\mathbf{u}}_q^{n+1} + \beta_q\nabla\cdot\boldsymbol{\tau}^{n-q}\right), \tag{3.12}$$

$$\nabla\cdot\mathbf{u}^{n+1} + \mu\int_\Omega p^{n+1}d\Omega = 0. \tag{3.13}$$

The spatial discretisation of this system of equations will be discussed in the following Section 3.2.

For the constitutive equation, (2.64), we use an explicit treatment of the velocity and velocity gradients, using the previously computed solution from the velocity-pressure

system. We apply the BDF approximation at order J to the temporal derivative and treat the convective terms explicitly using EX, also at order J. The resulting BDFJ/EXJ semi-discrete constitutive equation is,

$$\begin{aligned}\left(1+We\frac{\gamma_0}{\Delta t}\right)\boldsymbol{\tau}^{n+1} - \boldsymbol{\tau}^{n+1}\cdot\nabla\mathbf{u}^{n+1} - \left(\nabla\mathbf{u}^{n+1}\right)^T\cdot\boldsymbol{\tau}^{n+1} \\ = 2\left(1-\beta\right)\mathbf{d}^{n+1} + We\sum_{q=0}^{J-1}\left(\frac{\alpha_q}{\Delta t}\boldsymbol{\tau}^{n-q} - \beta_q\mathbf{u}^{n+1}\cdot\nabla\boldsymbol{\tau}^{n-q}\right) \\ - We\frac{\alpha}{(1-\beta)}\sum_{q=0}^{J-1}\beta_q\left(\boldsymbol{\tau}^{n-q}\right)^2. \end{aligned} \tag{3.14}$$

The spatial discretisation of the constitutive equation will be discussed in Section 3.5.

Semi-Implicit Fixed Point Iteration Scheme

The explicit treatment of the convection terms within (3.14) could prove to be a cause of numerical instability. An alternative method is to use a fixed-point iteration (FPI) in the solution of the constitutive equation to replace the explicit (EX) terms with the goal of achieving a semi-implicit treatment of them. Further, we may include the non-linear Giesekus term in this iteration.

For this scheme we use the BDF treatment, at order J, of the temporal derivative combined with an iterative scheme to determine, $\boldsymbol{\tau}$. We set $\widetilde{\boldsymbol{\tau}}^0 = \boldsymbol{\tau}^n$ and then repeatedly solve the following BDFJ/FPI semi-discrete system for $\widetilde{\boldsymbol{\tau}}^{i+1}$,

$$\begin{aligned}\left(1+We\frac{\gamma_0}{\Delta t}\right)\widetilde{\boldsymbol{\tau}}^{i+1} - \widetilde{\boldsymbol{\tau}}^{i+1}\cdot\nabla\mathbf{u}^{n+1} - \left(\nabla\mathbf{u}^{n+1}\right)^T\cdot\widetilde{\boldsymbol{\tau}}^{i+1} \\ = 2\left(1-\beta\right)\mathbf{d}^{n+1} + We\left(\sum_{q=0}^{J-1}\left(\frac{\alpha_q}{\Delta t}\boldsymbol{\tau}^{n-q}\right) - \mathbf{u}^{n+1}\cdot\nabla\widetilde{\boldsymbol{\tau}}^{i}\right) \\ - We\frac{\alpha}{1-\beta}\left(\widetilde{\boldsymbol{\tau}}^{i}\right)^2. \end{aligned} \tag{3.15}$$

until $|\widetilde{\boldsymbol{\tau}}^{i+1} - \widetilde{\boldsymbol{\tau}}^{i}| < \delta$, where δ is some chosen tolerance. Once the tolerance is reached, we set $\boldsymbol{\tau}^{n+1} = \widetilde{\boldsymbol{\tau}}^{i+1}$.

3.1.7 Stopping Criteria

When computing numerical time-dependent solutions we must set the criteria terminating the simulation. The choice will depend on the flow being simulated. For example, when comparing to a known solution one set of criteria will be used whereas a benchmark will have another.

For known solutions, we have a good idea of the behaviour of the flow, and when a steady state might be reached, so we set absolute time-limits on the simulations. For the Newtonian flows, this is set at 10 time units and for viscoelastic flows this is set to 40 time units, which for all problems considered, is more than adequate to reach a steady state solution. In some cases this may be more time than required, but the additional time to run is a test of longer term stability of the scheme. This allows us to test that once the steady state solution has been reached, the numerical scheme does not diverge from that state.

For the other simulations where the time to reach a steady state is unknown, we employ a different criterion, although we do impose an absolute time limit of 50 time units. At any timestep we store the values of the field variables, at least, at the previous timestep, so it is easy to measure the point-wise (on the GLL grid, detailed in Section 3.3) change of a variable between timesteps. However to be useful we require a way of quantifying these differences using a single measure. A suitable measure for this is the L^2-norm, which we also use for error quantification. Details on how this is computed are given in Section 3.4.

For a Newtonian flow, the quantity, S_{newt}, is calculated via the following

$$S_{newt}(p, \mathbf{u}) = \sqrt{\frac{\|p^n - p^{n-1}\|^2_{L^2(\Omega)} + \|\mathbf{u}^n - \mathbf{u}^{n-1}\|^2_{L^2(\Omega)}}{\|p^n\|^2_{L^2(\Omega)} + \|\mathbf{u}^n\|^2_{L^2(\Omega)}}}, \tag{3.16}$$

and for a viscoelastic flow, the quantity, S_{velast}, is calculated via the following

$$S_{velast}(p, \mathbf{u}, \boldsymbol{\tau}) = \sqrt{\frac{\|p^n - p^{n-1}\|^2_{L^2(\Omega)} + \|\mathbf{u}^n - \mathbf{u}^{n-1}\|^2_{L^2(\Omega)} + \|\boldsymbol{\tau}^n - \boldsymbol{\tau}^{n-1}\|^2_{L^2(\Omega)}}{\|p^n\|^2_{L^2(\Omega)} + \|\mathbf{u}^n\|^2_{L^2(\Omega)} + \|\boldsymbol{\tau}^n\|^2_{L^2(\Omega)}}}. \tag{3.17}$$

This quantity is compared to a threshold value, S_{crit}, and if it is less, and meets any other criteria set, the simulation is stopped. The value of S_{crit} is typically set at 10^{-7}.

A final criteria set on simulations involving the calculation of the drag, D, is that the change in drag must also meet the S_{crit} criteria. So

$$D_{change} = \left| \frac{D^n - D^{n-1}}{D^n} \right| \tag{3.18}$$

must be less than S_{crit} too.

3.2 Spatial Discretisation

To solve the field equations in space we use the spectral element method (SEM) which requires their weak formulation. We solve the constitutive equation spatially in strong form. In the following section we shall detail the steps required before applying the SEM to the momentum and continuity equations. The spectral element method itself is detailed in Section 3.3.

3.2.1 Weak Form of Equations

We consider equations (2.62)-(2.63), the general dimensionless equations for a viscoelastic fluid. Firstly, we define the following spaces of functions

$$L^2(\Omega) := \left\{ u \colon \Omega \to \mathbb{R} \mid \int_\Omega u^2 \, d\Omega < \infty \right\}, \tag{3.19}$$

$$L_0^2(\Omega) := \left\{ p \in L^2(\Omega) \mid \int_\Omega p \, d\Omega = 0 \right\}, \tag{3.20}$$

$$H^1(\Omega) := \left\{ u \colon \Omega \to \mathbb{R} \mid u, \nabla u \in L^2(\Omega) \right\}. \tag{3.21}$$

We define so-called trial and test spaces,

$$V := \left\{ \mathbf{v} \in \left[H^1(\Omega) \right]^2 \mid \mathbf{v} = \mathbf{w} \ \text{ on } \partial\Omega_{\mathrm{D}} \right\} \tag{3.22}$$

$$W := \left\{ \mathbf{v} \in \left[H^1(\Omega) \right]^2 \mid \mathbf{v} = \mathbf{0} \ \text{ on } \partial\Omega_{\mathrm{D}} \right\} \tag{3.23}$$

where a trial function is one satisfying the prescribed boundary conditions which may be used to make up the solution we seek and a test function is one which takes a zero value on Dirichlet boundaries.

Multiplying the momentum equation in (2.62) by some velocity test function $\mathbf{v} \in W$, integrating over Ω and applying Green's 2^{nd} identity we obtain an expression containing contributions from the boundary. For our sphere in a cylinder geometry all of these boundary terms are zero valued due to a combination of the zero value of $\mathbf{v}$ on $\partial\Omega_D$ and that our boundary conditions are the equivalent of $\mathbf{u}\cdot\mathbf{n} = 0$ on $\partial\Omega_N$. We multiply the continuity equation in (2.63) by some pressure test function $q \in L_0^2(\Omega)$ and again integrate over Ω. The resulting weak form is,

Find $\mathbf{u} \in V$ and $p \in L_0^2(\Omega)$ such that,

$$Re\int_\Omega \mathbf{v}\cdot\frac{D\mathbf{u}}{Dt}\,d\Omega + \beta\int_\Omega \nabla\mathbf{u}\colon\nabla\mathbf{v}\,d\Omega - \int_\Omega p\nabla\cdot\mathbf{v}\,d\Omega = \int_\Omega \mathbf{f}\cdot\mathbf{v}\,d\Omega - \int_\Omega \boldsymbol{\tau}\colon\nabla\mathbf{v}\,d\Omega \quad \forall\ \mathbf{v}\in W \tag{3.24}$$

$$\int_\Omega q\nabla\cdot\mathbf{u}\,d\Omega = -\mu\int_\Omega q\,d\Omega\int_\Omega p\,d\Omega \quad \forall\ q\in L_0^2(\Omega). \tag{3.25}$$

We write equations (3.24)-(3.25) in component form for 2-D Cartesian coordinates,

$$Re\int_\Omega v\frac{D\mathbf{u}}{Dt}_x\,dxdy - \int_\Omega p\frac{\partial v}{\partial x}\,dxdy + \beta\int_\Omega\left(\frac{\partial u_x}{\partial x}\frac{\partial v}{\partial x}+\frac{\partial u_x}{\partial y}\frac{\partial v}{\partial y}\right)\,dxdy = \int_\Omega vf_x\,dxdy - \int_\Omega \boldsymbol{\tau}_{xx}\frac{\partial v}{\partial x}+\boldsymbol{\tau}_{yx}\frac{\partial v}{\partial y}\,dxdy, \tag{3.26}$$

$$Re\int_\Omega v\frac{D\mathbf{u}}{Dt}_y\,dxdy - \int_\Omega p\frac{\partial v}{\partial y}\,dxdy + \beta\int_\Omega\left(\frac{\partial u_y}{\partial x}\frac{\partial v}{\partial x}+\frac{\partial u_y}{\partial y}\frac{\partial v}{\partial y}\right)\,dxdy = \int_\Omega vf_y\,dxdy - \int_\Omega \boldsymbol{\tau}_{xy}\frac{\partial v}{\partial x}+\boldsymbol{\tau}_{yy}\frac{\partial v}{\partial y}\,dxdy, \tag{3.27}$$

$$\int_\Omega q\left(\frac{\partial u_x}{\partial x}+\frac{\partial u_y}{\partial y}\right)dxdy + \mu\int_\Omega q\,dxdy\int_\Omega p\,dxdy = 0. \tag{3.28}$$

and for the axisymmetric cylindrical polar coordinate case

$$Re\int_\Omega v\frac{D\mathbf{u}}{Dt}_r\,r\,drdz - \int_\Omega p\left(r\frac{\partial v}{\partial r}+v\right)\,drdz + \beta\int_\Omega\left[r\left(\frac{\partial u_r}{\partial r}\frac{\partial v}{\partial r}+\frac{\partial u_r}{\partial z}\frac{\partial v}{\partial z}\right)+\frac{vu_r}{r}\right]\,drdz = \int_\Omega vf_r r\,drdz - \int_\Omega\left[r\left(\boldsymbol{\tau}_{rr}\frac{\partial v}{\partial r}+\boldsymbol{\tau}_{zr}\frac{\partial v}{\partial z}\right)+v\boldsymbol{\tau}_{\theta\theta}\right]\,drdz, \tag{3.29}$$

$$Re\int_\Omega v\frac{D\mathbf{u}}{Dt}_z\,r\,drdz - \int_\Omega p\frac{\partial v}{\partial z}r\,drdz + \beta\int_\Omega\left(\frac{\partial u_z}{\partial r}\frac{\partial v}{\partial r}+\frac{\partial u_z}{\partial z}\frac{\partial v}{\partial z}\right)r\,drdz = \int_\Omega vf_z r\,drdz - \int_\Omega\left(\boldsymbol{\tau}_{rz}\frac{\partial v}{\partial r}+\boldsymbol{\tau}_{zz}\frac{\partial v}{\partial z}\right)r\,drdz, \tag{3.30}$$

$$\int_\Omega rq\left(\frac{\partial u_r}{\partial r}+\frac{\partial u_z}{\partial z}\right)+qu_r\,drdz + \mu\int_\Omega qr\,drdz\int_\Omega pr\,drdz = 0. \tag{3.31}$$

3.2.2 Bilinear Forms

It is common to define bilinear forms for the terms within the weak form for ease of notation. We define them as follows

$$m(\mathbf{u}, \mathbf{v}) := \int_\Omega \mathbf{u} \cdot \mathbf{v} \; d\Omega \tag{3.32}$$

$$a(\mathbf{u}, \mathbf{v}) := \int_\Omega \nabla \mathbf{u} \colon \nabla \mathbf{v} \; d\Omega \tag{3.33}$$

$$b(p, \mathbf{v}) := \int_\Omega p \nabla \cdot \mathbf{v} \; d\Omega \tag{3.34}$$

$$b^*(\mathbf{u}, q) := \int_\Omega q \nabla \cdot \mathbf{u} \; d\Omega \tag{3.35}$$

$$c(p, q) := z(p)\, z(q) \tag{3.36}$$

$$e(\boldsymbol{\tau}, \mathbf{v}) := \int_\Omega \boldsymbol{\tau} \colon \nabla \mathbf{v} \; d\Omega \tag{3.37}$$

where

$$z(q) := \int_\Omega q \; d\Omega. \tag{3.38}$$

We also introduce the subscript notation, $m_i(\mathbf{u}, \mathbf{v})$, to indicate when we are referring to the i^{th} component of a bilinear form assuming that there is more than one. For example, in axisymmetric cylindrical polar co-ordinates, the r-component of (3.33), would be

$$a_r(\mathbf{u}, \mathbf{v}) = \int_\Omega \left[r \left(\frac{\partial u_r}{\partial r} \frac{\partial v}{\partial r} + \frac{\partial u_r}{\partial z} \frac{\partial v}{\partial z} \right) + \frac{v u_r}{r} \right] \; dr dz. \tag{3.39}$$

We use these definitions to rewrite our weak form, (3.24)-(3.25), as

Find $\mathbf{u} \in V$ and $p \in L^2_0(\Omega)$ such that,

$$Re \; m\left(\mathbf{v}, \frac{D\mathbf{u}}{Dt} \right) + \beta a(\mathbf{u}, \mathbf{v}) - b(p, \mathbf{v}) = m(\mathbf{f}, \mathbf{v}) - e(\boldsymbol{\tau}, \mathbf{v}) \quad \forall \; \mathbf{v} \in W \tag{3.40}$$

$$b^*(\mathbf{u}, q) + \mu c(p, q) = 0 \quad \forall \; q \in L^2_0(\Omega). \tag{3.41}$$

where we may set $\mu = 0$ to use the standard continuity equation, or a non-zero value for the alternative continuity equation. This is done under the condition that we instead seek a pressure solution $p \in L^2(\Omega)$.

3.2.3 Semi-Discrete Weak Formulation

Applying the temporal discretisation as described in Section 3.1 to our final weak formulation, (3.40)-(3.41), we arrive at the semi-discrete weak formulation for our field equations, which for some $n = 1, 2, 3, ..$ is given by

Find $\mathbf{u}^{n+1} \in V$ and $p^{n+1} \in L_0^2(\Omega)$ such that,

$$Re\frac{\gamma_0}{\Delta t}m\big(\mathbf{u}^{n+1}, \mathbf{v}\big) + \beta a\big(\mathbf{u}^{n+1}, \mathbf{v}\big) - b\big(p^{n+1}, \mathbf{v}\big)$$
$$= m\big(\mathbf{f}^{n+1}, \mathbf{v}\big) + \sum_{q=0}^{J-1}\Big(Re\frac{\alpha_q}{\Delta t}m\big(\mathbf{u}^{n-q}, \mathbf{v}\big) - \beta_q e\big(\boldsymbol{\tau}^{n-q}, \mathbf{v}\big)\Big) \quad \forall\ \mathbf{v} \in W, \quad (3.42)$$

$$b^*\big(\mathbf{u}^{n+1}, q\big) + \mu c\big(p^{n+1}, q\big) = 0 \quad \forall\ q \in L_0^2(\Omega), \quad (3.43)$$

It remains to discretise the variables in space and perform the integration numerically using quadrature. The method for this is described in Section 3.3.

3.3 Spectral Element Method

The weak formulation of the governing equations is discretised using the Spectral Element Method (SEM), which is similar in many respects to the Finite Element Method (FEM). However, the basis functions are carefully chosen polynomials which have useful properties when combined with an appropriately chosen mesh within each spectral element. The ultimate goal of the SEM, like most numerical methods of this type, is to obtain a linear system of equations from the discrete approximations made, which can then be solved via available numerical linear algebra techniques.

As a basic overview of the method, the premise is to decompose the physical domain into a finite number of elements (as one would do in the FEM). These elements are then mapped onto a parent domain such that, via this mapping, every local point within the parent domain is associated with a global point within a particular element. Within this parent domain the field variables are then discretised using a polynomial representation. The discrete versions of the weak form are then approximated using a Gauss-Lobatto-

Legendre(GLL) quadrature rule. This results in a linear system of equations which is solved using standard numerical linear algebra methods. The method is detailed in the following sections.

3.3.1 Domain Decomposition

Suppose we have a physical domain, Ω. We decompose Ω into K non-overlapping spectral elements such that $\Omega = \bigcup_{k=1}^{K} \Omega^k$. We may write a general integral of some arbitrary function $f(\mathbf{x})$ over Ω as,

$$\int_{\Omega} f(\mathbf{x})\, d\Omega = \sum_{k=1}^{K} \int_{\Omega_k} f(\mathbf{x})\, d\Omega. \tag{3.44}$$

Contrary to the FEM, elements are chosen to be relatively large with refinement performed within the element on a mesh-level by "polynomial enrichment". We gain higher mesh resolution by choosing smaller spectral elements in areas of the domain where, for example, high velocity gradients are expected. We choose to restrict our spectral elements to quadrilaterals, although triangles are also a suitable choice.

When considering variables, integrals, etc. within the whole domain, we typically refer to these as "global" and conversely refer to variables, integrals, etc. within a single spectral element as "local". For example, we could consider an integral over the whole domain as a global integral or we could consider a sum of contributions from local integrals over all spectral elements.

We make use of this domain decomposition within the bilinear forms, defined in Section 3.2.2. Local versions of the bilinear forms are identified by a superscript, k. For example, (3.32) on the local spectral element, Ω_k, is denoted by,

$$m^k(\mathbf{u}, \mathbf{v}) := \int_{\Omega_k} \mathbf{u} \cdot \mathbf{v}\ d\Omega. \tag{3.45}$$

Further, we define a restriction operator, R_k for each element, Ω_k. This so-called global-to-local map which acts as a means of restricting from a global integral over Ω to one over the local spectral element, Ω_k. We use this restriction operator to write (3.45) as

$$m^k(\mathbf{u}, \mathbf{v}) = R_k m(\mathbf{u}, \mathbf{v})\,. \tag{3.46}$$

is serving as link between local and global integrals. Note that the action of the restriction operator is explicitly on the bilinear form and shorten $(R_k m)(\mathbf{u}, \mathbf{v})$ to $R_k m(\mathbf{u}, \mathbf{v})$ for ease of notation. This notation is continued for the reverse mapping below.

We denote the reverse mapping R_k^T, and call it a prolongation operator which is used to take a local integral to one over the global domain. This is referred to as the local-to-global map. For example, we may write (3.32) as a sum of contributions from the local bilinear form as follows

$$m(\mathbf{u}, \mathbf{v}) = \sum_{k=1}^{K} R_k^T m^k(\mathbf{u}, \mathbf{v}) = \sum_{k=1}^{K} \int_{\Omega_k} \mathbf{u} \cdot \mathbf{v} \; d\Omega \tag{3.47}$$

While these maps essentially serve as an alternative way of writing the decomposition in (3.44), their use at a discrete level becomes important in a practical sense when implementing the method computationally. Details of the construction of the map are given in Section 3.3.7

3.3.2 Transfinite Element Mapping

The physical domain has now been decomposed into K quadrilateral elements, although, depending on the geometry of the domain and the problem to be solved, they will not necessarily be uniform. It is useful to define a reference element in which computational work is performed. This requires a mapping between the computational and physical domain. As we are dealing with quadrilateral elements it is typical for the reference element, D to be the square occupying $[-1, 1] \times [-1, 1]$. An integral in an arbitrarily chosen element is transformed in the following way,

$$\int_{\Omega_k} f(\mathbf{x}) \, d\Omega = \int_D f\big(\mathbf{x}^k(\xi, \eta)\big) \det(\mathbf{J}^k) d\xi d\eta, \tag{3.48}$$

for some function $f(\mathbf{x})$, with $\mathbf{x}^k(\xi, \eta)$ the global co-ordinate mapped from the local variables and where $\mathbf{J}^k$ is the Jacobian of the transformation for that element,

$$\mathbf{J}^k(\xi, \eta) = \begin{pmatrix} \dfrac{\partial x}{\partial \eta}^k & \dfrac{\partial x}{\partial \xi}^k \\ \dfrac{\partial y}{\partial \eta}^k & \dfrac{\partial y}{\partial \xi}^k \end{pmatrix}. \tag{3.49}$$

$\mathbf{J}^k$ can be used to determine expressions for a spatial derivative within an element with respect to the global variables in terms of derivatives of the transformed variables as,

$$\begin{aligned}\frac{\partial}{\partial x}^k &= \frac{1}{\det(\mathbf{J}^k)}\left(\frac{\partial y}{\partial \eta}^k \frac{\partial}{\partial \xi} - \frac{\partial y}{\partial \xi}^k \frac{\partial}{\partial \eta}\right), \\ \frac{\partial}{\partial y}^k &= \frac{1}{\det(\mathbf{J}^k)}\left(\frac{\partial x}{\partial \xi}^k \frac{\partial}{\partial \eta} - \frac{\partial x}{\partial \eta}^k \frac{\partial}{\partial \xi}\right)\end{aligned} \tag{3.50}$$

where the factors involving the partial derivatives of x and y with respect to ξ and η come from the entries of the Jacobian matrix of the mapping operator which is discussed below.

We now are looking for continuous transformations which map the reference square one-to-one onto an arbitrary, simply connected and bounded region $\Omega_k \in \mathbb{R}^2$. We assume that the determinant of the Jacobian, $\det(\mathbf{J})$ is finite and non-zero, and secondly, that the transformation maps the boundary of D onto the boundary of Ω. Further, while it is possible to choose transformations which result in $\det(\mathbf{J})$ being negative, we do not choose to use them for the purposes of this thesis.

A suitable means to achieve this (see [45]) is to use the transfinite element mappings introduced by Gordon and Hall [19], which use a parametric representation of the boundaries. These methods were first introduced into SEM by Schneidesch and Deville [54] combined with domain decomposition. They introduced a general transfinite operator which allows for varying orders of the polynomial spaces used in the mapping. The one chosen for the current work is the bi-linear transfinite element mapping, which we will term $\mathbf{U}$.

Firstly, we define the so-called blending functions, ϕ_1 and ϕ_2

$$\phi_1(s) = \frac{1}{2}(1-s), \qquad \phi_2(s) = \frac{1}{2}(1+s), \qquad -1 \leq s \leq 1. \tag{3.51}$$

Using these blending functions, we may build the transfinite element mapping. Firstly the four edges of the quadrilateral need to be parameterized in the ranges of the reference square

$$\begin{aligned}\mathbf{F}_1^k(s) &= \phi_1(s)\mathbf{V}_1^k + \phi_2(s)\mathbf{V}_2^k \\ \mathbf{F}_2^k(s) &= \phi_1(s)\mathbf{V}_2^k + \phi_2(s)\mathbf{V}_3^k \\ \mathbf{F}_3^k(s) &= \phi_2(s)\mathbf{V}_3^k + \phi_1(s)\mathbf{V}_4^k \\ \mathbf{F}_4^k(s) &= \phi_2(s)\mathbf{V}_4^k + \phi_1(s)\mathbf{V}_1^k\end{aligned} \tag{3.52}$$

where $\mathbf{F}_i^k$ is the i^{th} edge and $\mathbf{V}_i^k$ is the co-ordinate of the i^{th} corner of the spectral element Ω_k.

If we create a function which uses all of these edge functions and blends them, then every point within the quadrilateral may be mapped into the parent square, however there will be a double counting of the vertices themselves, therefore we must remove these in the final transfinite element mapping,

$$\begin{aligned}\mathbf{X}^k(\xi,\eta) =&\phi_1(\xi)\mathbf{F}_1^k(\eta) + \phi_2(\xi)\mathbf{F}_2^k(\eta)\\ &+ \phi_1(\eta)\mathbf{F}_3^k(\xi) + \phi_2(\eta)\mathbf{F}_4^k(\xi)\\ &- \phi_1(\xi)\phi_1(\eta)\mathbf{V}_1^k - \phi_1(\xi)\phi_2(\eta)\mathbf{V}_2^k\\ &- \phi_2(\xi)\phi_1(\eta)\mathbf{V}_3^k - \phi_2(\xi)\phi_2(\eta)\mathbf{V}_4^k\end{aligned} \tag{3.53}$$

This is the general form of this type of mapping, the choice of edge parametrisation generates the desired map. Substutiting (3.52) into (3.53), we obtain the bi-linear transfinite element mapping for a general quadrilateral with straight edges,

$$\begin{aligned}\mathbf{X}^k(\xi,\eta) =&\phi_1(\xi)\phi_1(\eta)\mathbf{V}_1^k + \phi_2(\xi)\phi_1(\eta)\mathbf{V}_2^k\\ &+ \phi_2(\xi)\phi_2(\eta)\mathbf{V}_3^k + \phi_1(\xi)\phi_1(\eta)\mathbf{V}_4^k\end{aligned} \tag{3.54}$$

where $\mathbf{X}^k(\xi,\eta)$ is the global spatial co-ordinate corresponding to the local co-ordinates (ξ,η) in the spectral element Ω_k.

Using these definitions we apply partial differentiation to find the Jacobian of the transfinite map

$$\mathbf{J}^k(\xi,\eta) = \frac{1}{4}\begin{pmatrix} (1-\eta)(x_2^k - x_1^k) & (1-\eta)(y_2^k - y_1^k)\\ +(1+\eta)(x_3^k - x_4^k) & +(1+\eta)(y_3^k - y_4^k)\\ & \\ (1-\xi)(x_4^k - x_1^k) & (1-\xi)(y_4^k - y_1^k)\\ +(1+\xi)(x_3^k - x_2^k) & +(1+\xi)(y_3^k - y_2^k)\end{pmatrix} \tag{3.55}$$

where the x_i^k and y_i^k refer to the x and y co-ordinates of the i^{th} vertex in the spectral element Ω_k.

Using this mapping together with the elemental decomposition of the physical domain, we are able to solve for each spectral element on the same reference square.

Circular Transfinite Mapping

If we include circular boundaries for the global domain we will need to include the possibility of circular edges. These must be mapped onto the parent square too, so the appropriate $\mathbf{F}_i^k$ must be defined for the general transfinite map (3.53).

By replacing the parametrisation of a straight edge with an arc, we may include a circular edge for any given element. We adopt the convention that the first and second vertices of a particular element will always contain the circular edge, which simplifies the implementation in computer code due to a reduction in possible scenarios. The parametrisation of the arc may be performed using two angles associated with element Ω_k, θ_1^k and θ_2^k. We define θ_1^k to be the angle between $\mathbf{V}_2^k$ and the horizontal line passing through the origin of the circle of which the arc is a part and θ_2 is defined to be angle between the vertex $\mathbf{V}_2^k$ and the same line.

This allows us to parametrise the arc between the two vertices with position vectors $\mathbf{V}_1^k$ and $\mathbf{V}_2^k$ as follows,

$$\lambda^k(s) = \theta_1^k \phi_1(s) + \theta_2^k \phi_2(s) \tag{3.56}$$

Using this we may modify the previously defined $\mathbf{F}_1^k(s)$ in (3.52) so that

$$\mathbf{F}_1^k(s) = \begin{pmatrix} a + R\cos(\lambda^k(s)) \\ b + R\sin(\lambda^k(s)) \end{pmatrix} \tag{3.57}$$

where R is the radius of the circle of which the arc is a part and (a, b) are the co-ordinates of the centre of that circle.

Substituting (3.57) into (3.53) and simplifying, we obtain the transfinite element mapping for a quadrilateral with a single circular edge

$$\mathbf{X}^k(\xi,\eta) = \begin{pmatrix} \phi_1(\eta)\left(a + R\cos(\lambda^k(\xi))\right) + \phi_2(\xi)\phi_2(\eta)x_3^k + \phi_1(\xi)\phi_2(\eta)x_4^k \\ \phi_1(\eta)\left(b + R\sin(\lambda^k(\xi))\right) + \phi_2(\xi)\phi_2(\eta)y_3^k + \phi_1(\xi)\phi_2(\eta)y_4^k \end{pmatrix} \tag{3.58}$$

where the x_i^k and y_i^k refer to the x and y co-ordinates of the i^{th} vertex. The resulting

Jacobian evaluated using (3.58) is

$$\mathbf{J}^k(\xi,\eta) = \frac{1}{2}\begin{pmatrix} \phi_2(\eta)(x_3^k - x_4^k) & \phi_2(\eta)(y_3^k - y_4^k) \\ -R\phi_1(\eta)(\theta_2^k - \theta_1^k)\sin(\lambda^k(\xi)) & +R(\theta_2^k - \theta_1^k)\phi_1(\eta)\cos(\lambda^k(\xi)) \\ \\ \phi_2(\xi)x_3^k + \phi_1(\xi)x_4^k & \phi_2(\xi)y_3^k + \phi_1(\xi)y_4^k \\ -\big(a + R\cos(\lambda^k(\xi))\big) & -\big(b + R\sin(\lambda^k(\xi))\big) \end{pmatrix} \tag{3.59}$$

3.3.3 Parametrisation of Boundary Integrals

Suppose that we wish to map a boundary integral of some function $f(\mathbf{x})$, over the spectral element Ω_k onto a boundary integral over the parent element, D. We use the edge parametrisations defined in (3.52) so that a boundary integral becomes,

$$\int_{\Gamma_k} f(\mathbf{x})\, d\Omega = \sum_{i=1}^{4} \int_{-1}^{1} f\big(\mathbf{F}_i^k(\xi)\big) \det\big(\mathbf{J}\big(\mathbf{F}_i^k\big)\big)\, d\xi, \tag{3.60}$$

where the set of Jacobians resulting from the transformation of variables is given by

$$\begin{aligned} \mathbf{J}\big(\mathbf{F}_1^k\big) &= \frac{1}{2}\left(\mathbf{V}_2^k - \mathbf{V}_1^k\right), \\ \mathbf{J}\big(\mathbf{F}_2^k\big) &= \frac{1}{2}\left(\mathbf{V}_3^k - \mathbf{V}_2^k\right), \\ \mathbf{J}\big(\mathbf{F}_3^k\big) &= \frac{1}{2}\left(\mathbf{V}_3^k - \mathbf{V}_4^k\right), \\ \mathbf{J}\big(\mathbf{F}_4^k\big) &= \frac{1}{2}\left(\mathbf{V}_4^k - \mathbf{V}_1^k\right), \end{aligned} \tag{3.61}$$

3.3.4 Spectral Representation

The unknown variables, velocity, stress and pressure, in (2.21) are approximated within the parent domain (mapped from a particular spectral element) using Lagrange interpolants based on a chosen set of nodal points, called Gauss-Lobatto-Legendre (GLL) points. Inside any element, in 2-D (or equally for axisymmetric 3-D), we may write

[20],

$$u_a^k(\xi,\eta) = \sum_{i=0}^{N}\sum_{j=0}^{N}\left(u_{ij}^k\right)_a h_i(\xi)\, h_j(\eta)\,, \tag{3.62}$$

$$p^k(\xi,\eta) = \sum_{i=1}^{N-1}\sum_{j=1}^{N-1} p_{\widetilde{ij}}^k \widetilde{h}_i(\xi)\, \widetilde{h}_j(\eta)\,, \tag{3.63}$$

$$\tag{3.64}$$

where a denotes the component of velocity and $\left(u_{ij}^k\right)_a$ and $p_{\widetilde{ij}}^k$ are approximations to the field variables, $u_a(\xi,\eta)$ and $p(\xi,\eta)$ at the GLL node point (ξ_i,η_j) within the spectral element Ω_k. The subscript notation ij refers to a single GLL node point referenced via the formula,

$$ij = i + j\,(N+1)\,, \quad \text{for } 0 \le i,j \le N, \tag{3.65}$$

and for the internal GLL nodes for the pressure via the formula

$$\widetilde{ij} = i + (j-1)\,(N-1)\,, \quad \text{for } 1 \le i,j \le N-1. \tag{3.66}$$

The velocity basis functions, $h_i(\xi)$ are the set of Lagrange interpolants of the GLL points given by

$$h_i(\xi) = -\frac{(1-\xi^2)L_N'(\xi)}{N(N+1)L_N(\xi_i)(\xi-\xi_i)}, \qquad 0 \le i \le N, \tag{3.67}$$

and the pressure basis functions are given by

$$\widetilde{h}_i(\xi) = -\frac{(1-\xi_i^2)L_N'(\xi)}{N(N+1)L_N(\xi_i)(\xi-\xi_i)}, \qquad 1 \le i \le N-1, \tag{3.68}$$

where $L_N(x)$ is the Legendre polynomial of degree N, and ξ_p is the p^{th} GLL point in any one grid direction.

Note that there are no pressure basis functions associated with GLL points lying on the boundary of the spectral elements. This is because we must ensure that the Ladyzhenskaya-Babuška-Brezzi (LBB) compatibility condition is satisfied by our approximation spaces for the problem to be well-posed. This has been shown [34] to be satisfied if the velocity test space is contained in the space of polynomials of order N, while the pressure test space is contained in the space of polynomials of order $N-2$.

For the pressure representation, the choice of the Lagrange interpolant $\widetilde{h}_i(\xi)$, while meeting the LBB condition, also ensures that the discrete pressure nodes lie on the

internal nodes of the whole GLL grid as they do for the velocity nodes. The pressure value on an element boundary may be extrapolated from the internal element nodes. Continuity of pressure between elements is not guaranteed, but in practice this does not cause problems.

We introduce the notation, $h_{pi} = h_i(\xi_p)$ and $\widetilde{h}_{pi} = \widetilde{h}_i(\xi_p)$. These Lagrange interpolants, by design, satisfy the Kronecker-Delta property on the whole GLL grid for the velocity basis functions and on the internal grid points for the pressure. That is,

$$h_{pi} = \delta_{pi} = \begin{cases} 0, & p \neq i \\ 1, & p = i \end{cases} \tag{3.69}$$

for $i = 0, .., N$ and $p = 0, .., N$. For ease of notation we also define

$$\widetilde{\delta}_{pi} = \begin{cases} \delta_{pi}, & i = 1, .., N-1, \quad p = 1, .., N-1 \\ \widetilde{h}_{pi}. & i = 1, .., N-1, \quad p = 0 \text{ or } p = N \end{cases} \tag{3.70}$$

for $i = 1, .., N-1$ and $p = 0, .., N$.

For the pressure test functions, while we do not have a test function corresponding directly to a node on the boundary of a spectral element as we would for the velocity, we must still evaluate the internal test functions on this boundary and it does not necessarily take the values 0 or 1. We must take these additional boundary values into account when discretising operators on the pressure or involving the pressure test function.

We introduce the notation, $d_{pi} = h_i'(\xi_p)$. One may use the properties of Legendre polynomials to show that,

$$d_{pi} = \begin{cases} \dfrac{L_N(\xi_p)}{L_N(\xi_i)} \dfrac{1}{\xi_p - \xi_i}, & p \neq i, \\ -\dfrac{N(N+1)}{4}, & p = i = 0, \\ \dfrac{N(N+1)}{4}, & p = i = N, \\ 0, & p = i, \quad 1 \leq i, j \leq N-1. \end{cases} \tag{3.71}$$

This is known as the Legendre pseudospectral differentiation matrix.

From our spectral representations, we can define the velocity and pressure test functions in terms of the Lagrange interpolants within any particular spectral element. Assuming that the grid point does not correspond to a Dirichlet boundary node (in which case an associated test function is identically zero), we choose our set of test functions to be associated with a particular GLL node point, (ξ_i, η_j) ,

$$v_{ij}(\xi,\eta) = h_i(\xi)\, h_j(\eta), \qquad i,j = 0,..,N, \tag{3.72}$$

$$q_{ij}(\xi,\eta) = \widetilde{h}_i(\xi)\, \widetilde{h}_j(\eta), \qquad i,j = 1,..,N-1. \tag{3.73}$$

where $v_{ij}(\xi,\eta)$ is a velocity test function (for both components) and $q_{ij}(\xi,\eta)$ is a pressure test function.

In applying our approximations to the weak form of our field equations, we note that the derivatives with respect to the global spatial variables are required. By applying (3.50) to the partial derivatives, with respect to x and y, of a velocity test function we obtain expressions in terms of local spatial variables

$$\frac{\partial v_{ij}}{\partial x}^k(\xi,\eta) = \frac{1}{\det(\mathbf{J}^k)}\left(\frac{\partial y}{\partial \eta}^k h_i'(\xi)\, h_j(\eta) - \frac{\partial y}{\partial \xi}^k h_i(\xi)\, h_j'(\eta)\right), \tag{3.74}$$

$$\frac{\partial v_{ij}}{\partial y}^k(\xi,\eta) = \frac{1}{\det(\mathbf{J}^k)}\left(\frac{\partial x}{\partial \xi}^k h_i(\xi)\, h_j'(\eta) - \frac{\partial x}{\partial \eta}^k h_i'(\xi)\, h_j(\eta)\right). \tag{3.75}$$

Evaluating these derivatives at GLL points (ξ_p, η_q) and using the previously defined notation, we denote the partial derivatives of a velocity test function at a particular GLL node point as

$$\left(D_x^k\right)_{ij,pq} = \frac{\partial v_{ij}}{\partial x}^k(\xi_p,\eta_q) = \frac{1}{\det(\mathbf{J}^k)_{pq}}\left(\frac{\partial y}{\partial \eta}^k_{pq} d_{pi}\delta_{qj} - \frac{\partial y}{\partial \xi}^k_{pq} \delta_{pi} d_{qj}\right), \tag{3.76}$$

$$\left(D_y^k\right)_{ij,pq} = \frac{\partial v_{ij}}{\partial y}^k(\xi_p,\eta_q) = \frac{1}{\det(\mathbf{J}^k)_{pq}}\left(\frac{\partial x}{\partial \xi}^k_{pq} \delta_{pi} d_{qj} - \frac{\partial x}{\partial \eta}^k_{pq} d_{pi}\delta_{qj}\right), \tag{3.77}$$

with the subscript denoting which global spatial variable the derivative is with respect to.

When considering axisymmetric cylindrical polar co-ordinates we use the equivalent expressions for D_r^k and D_z^k to represent the partial derivatives of a velocity test function with respect to r and z. Under the assumption that the axes are chosen so that they coincide, we consider that the r-direction is equivalent to the Cartesian y-direction and that the z-direction is equivalent to the x-direction.

By substituting the spectral representation of velocity into (2.65)-(2.68) or (2.70)-(2.73) and using the above notation we get the following expressions for the ab-component of the local velocity gradient at the GLL point (ξ_p, η_q)

$$\left(\nabla \mathbf{u}^k(\xi_p, \eta_q)\right)_{ab} = \sum_{i=0}^{N}\sum_{j=0}^{N} \left(u_{ij}^k\right)_b \left(D_a^k\right)_{ij,pq}, \tag{3.78}$$

for $a = x, y$ and $b = x, y$ in Cartesian co-ordinates and $a = r, z$ and $b = r, z$ in axisymmetric cylindrical polar co-ordinates with the additional component,

$$\left(\nabla \mathbf{u}^k(\xi_p, \eta_q)\right)_{\theta\theta} = \frac{\left(u_{pq}^k\right)_r}{r_{pq}}. \tag{3.79}$$

We note here that if $r_{pq} = 0$ then we have a division by zero. However, we see that in the axisymmetric case, $r = 0$ corresponds to an axisymmetric boundary, where $u_r = 0$. This allows us to use L'Hôpital's rule to write,

$$\lim_{r\to 0} \frac{u_r}{r} = \lim_{r\to 0} \frac{\partial u_r}{\partial r}, \tag{3.80}$$

so we may allow for the calculation of the gradient on the axis of symmetry by instead using

$$\left(\nabla \mathbf{u}^k(\xi_p, \eta_q)\right)_{\theta\theta} = \begin{cases} \dfrac{\left(u_{pq}^k\right)_r}{r_{pq}} & \text{if } r_{pq} \neq 0, \\ \left(\nabla \mathbf{u}^k(\xi_p, \eta_q)\right)_{rr} & \text{if } r_{pq} = 0. \end{cases} \tag{3.81}$$

3.3.5 Numerical Quadrature

Given the choice of grid points within the reference element where the computational work is performed, we use Gauss-Lobatto(GL) quadrature to perform the numerical integration. For a 1-D integral of some function $f(\xi)$ defined on $[-1, 1]$ such as we see in the parametrised boundary integral in (3.60) the the GL integration is given by

$$\int_{-1}^{1} f(\xi)\, d\xi \approx \sum_{p=0}^{N} f(\xi_p)\, w_p. \tag{3.82}$$

where $\{w_i\}_{i=0}^{N}$ are the numerical weights which are calculated by integrating the Lagrange interpolants of the GLL points over $[-1, 1]$, $w_i = \int_{-1}^{1} h_i(\xi)\, d\xi$, which gives

$$w_i = \frac{2}{N(N+1)\, L_N(\xi_i)^2}, \tag{3.83}$$

for the GLL points. This rule is exact when f is a polynomial of order $\leq 2N-1$ in each independent variable. This may be extended to 2-D, with the general Gauss-Lobatto integration over the reference square of some function $f(\xi,\eta)$ defined on D given by

$$\int_{-1}^{1}\int_{-1}^{1} f(\xi,\eta)\,d\xi d\eta \approx \sum_{p=0}^{N}\sum_{q=0}^{N} f(\xi_p,\eta_q)\,w_p w_q, \tag{3.84}$$

with the weights given as in the 1-D case.

3.3.6 Discretised Bilinear Forms

In Section 3.2.2 we defined bilinear forms for the weak formulation of the governing equations. We apply the SEM to these bilinear forms to obtain a discrete approximation. Through use of the domain decomposition introduced in Section 3.3.1 we need only consider the bilinear forms on a single, locally labelled, spectral element, Ω_e (note switch of element index to e). We may reassemble the global integral using the local-to-global mapping discussed in the same section.

We apply the transfinite element mapping for the integral as in (3.48) and the spectral representations of our variables, (3.62)-(3.63), and using the defined test functions, (3.72)-(3.73). After approximating the integral according to the Gauss-Lobatto quadrature, (3.84), we obtain the following local spectral element approximations of the bilinear operators. We write the approximations as a matrix-vector multiplication. The entries of each matrix for 2-D Cartesian co-ordinates are given by

$$\left(M^e\right)_{kl,ij} = \delta_{ik}\delta_{jl}\det\left(\mathbf{J}^e\right)_{kl} w_k w_l, \tag{3.85}$$

$$\left(A^e\right)_{kl,ij} = \sum_{p=0}^{N}\sum_{q=0}^{N}\left(\left(D_x^e\right)_{ij,pq}\left(D_x^e\right)_{kl,pq} + \left(D_y^e\right)_{ij,pq}\left(D_y^e\right)_{kl,ij}\right)\det\left(\mathbf{J}^e\right)_{pq} w_p w_q, \tag{3.86}$$

$$\left(E_x^e\right)_{kl,ij} = \left(D_x^e\right)_{kl,ij}\det\left(\mathbf{J}^e\right)_{ij} w_i w_j, \tag{3.87}$$

$$\left(E_y^e\right)_{kl,ij} = \left(D_y^e\right)_{kl,ij}\det\left(\mathbf{J}^e\right)_{ij} w_i w_j, \tag{3.88}$$

for $0 \leq i, j, k, l \leq N$, and,

$$\left(B_x^e\right)_{kl,\widetilde{ij}} = \sum_{p=0}^{N}\sum_{q=0}^{N} \widetilde{\delta}_{pi}\widetilde{\delta}_{qj} \left(D_x^e\right)_{kl,pq} \det\left(\mathbf{J}^e\right)_{pq} w_p w_q, \tag{3.89}$$

$$\left(B_y^e\right)_{kl,\widetilde{ij}} = \sum_{p=0}^{N}\sum_{q=0}^{N} \widetilde{\delta}_{pi}\widetilde{\delta}_{qj} \left(D_y^e\right)_{kl,pq} \det\left(\mathbf{J}^e\right)_{pq} w_p w_q, \tag{3.90}$$

$$\left(Z^e\right)_{\widetilde{ij}} = \sum_{p=0}^{N}\sum_{q=0}^{N} \widetilde{\delta}_{pi}\widetilde{\delta}_{qj} \det\left(\mathbf{J}^e\right)_{pq} w_p w_q, \tag{3.91}$$

for $1 \leq i, j \leq N-1$ and $0 \leq k, l \leq N$. We then write the SEM approximation of each bilinear operator as a matrix-vector product as follows,

$$m_x^e(\mathbf{u}, \mathbf{v}) \approx M^e \mathbf{u}_x^e, \qquad m_y^e(\mathbf{u}, \mathbf{v}) \approx M^e \mathbf{u}_y^e, \tag{3.92}$$

$$a_x^e(\mathbf{u}, \mathbf{v}) \approx A^e \mathbf{u}_x^e, \qquad a_y^e(\mathbf{u}, \mathbf{v}) \approx A^e \mathbf{u}_y^e, \tag{3.93}$$

$$b^e(p, \mathbf{v}) \approx B_x^e \mathbf{p}^e + B_y^e \mathbf{p}^e, \tag{3.94}$$

$$b^{e*}(\mathbf{u}, q) \approx \left(B_x^e\right)^T \mathbf{u}_x^e + \left(B_y^e\right)^T \mathbf{u}_y^e, \tag{3.95}$$

$$z^e(p) \approx Z^e \mathbf{p}^e, \tag{3.96}$$

$$e_x^e(\boldsymbol{\tau}, \mathbf{v}) \approx E_x^e \boldsymbol{\tau}_{xx}^e + E_y^e \boldsymbol{\tau}_{xy}^e \qquad e_y^e(\boldsymbol{\tau}, \mathbf{v}) \approx E_x^e \boldsymbol{\tau}_{xy}^e + E_y^e \boldsymbol{\tau}_{yy}^e \tag{3.97}$$

where $\mathbf{u}_i^e$ is the vector of velocity values for the i^{th}-component at local GLL points, $\boldsymbol{\tau}_{ij}^e$ is the vector of stress values for the ij^{th}-component at local GLL points and $\mathbf{p}^e$ is the vector of pressure values at the internal GLL points all within the spectral element Ω_e. The lengths of the vectors $\mathbf{u}_i^e$ and $\boldsymbol{\tau}_{ij}^e$ are $(N+1)$ whereas the length of the vector $\mathbf{p}^e$ is $(N-1)^2$.

The approximation of the bilinear form (3.36) is not constructed in the same way as the others, as it requires two integrations across the whole domain, Ω. The construction of this approximation is detailed in the last subsection of Section 3.3.7.

Axisymmetric Cylindrical Polar Co-ordinates

By comparison, we can see that the component-wise weak forms in 2-D Cartesian co-ordinates, (3.26)-(3.28), and axisymmetric 3-D co-ordinates, (3.29)-(3.31) have many terms in common except that in the latter case are multiplied by $r(\xi, \eta)$. Under the assumption that the axes are chosen so that they coincide, we consider that the r-direction

is equivalent to the Cartesian y-direction and that the z-direction is equivalent to the x-direction. The resulting matrices for axisymmetric cylindrical polar co-ordinates are,

$$(M^e)_{kl,ij} = \delta_{ik}\delta_{jl} \det(\mathbf{J}^e)_{kl} \, r_{kl} w_k w_l, \tag{3.98}$$

$$(A_r^e)_{kl,ij} = \sum_{p=0}^{N}\sum_{q=0}^{N} \left(\left((D_z^e)_{ij,pq} (D_z^e)_{kl,pq} + (D_r^e)_{ij,pq} (D_r^e)_{kl,ij} \right) \det(\mathbf{J}^e)_{pq} \, r_{pq} w_p w_q \right), \tag{3.99}$$

$$(A_\theta^e)_{kl,ij} = \frac{1}{r_{kl}} \delta_{ik}\delta_{jl} \det(\mathbf{J}^e)_{kl} \, w_k w_l, \tag{3.100}$$

$$(A_z^e)_{kl,ij} = \sum_{p=0}^{N}\sum_{q=0}^{N} \left((D_z^e)_{ij,pq} (D_z^e)_{kl,pq} + (D_r^e)_{ij,pq} (D_r^e)_{kl,ij} \right) \det(\mathbf{J}^e)_{pq} \, r_{pq} w_p w_q, \tag{3.101}$$

$$(E_r^e)_{kl,ij} = (D_r^e)_{kl,ij} \det(\mathbf{J}^e)_{ij} \, r_{ij} w_i w_j, \tag{3.102}$$

$$(E_\theta^e)_{kl,ij} = \delta_{ik}\delta_{jl} \det(\mathbf{J}^e)_{kl} \, w_k w_l, \tag{3.103}$$

$$(E_z^e)_{kl,ij} = (D_z^e)_{kl,ij} \det(\mathbf{J}^e)_{ij} \, r_{ij} w_i w_j, \tag{3.104}$$

$$\tag{3.105}$$

for $0 \leq i, j, k, l \leq N$, and,

$$(B_r^e)_{kl,\widetilde{ij}} = \sum_{p=0}^{N}\sum_{q=0}^{N} \left(\widetilde{\delta}_{pi}\widetilde{\delta}_{qj} (D_r^e)_{kl,pq} \det(\mathbf{J}^e)_{pq} \, r_{pq} w_p w_q \right) \tag{3.106}$$

$$(B_\theta^e)_{kl,\widetilde{ij}} = \widetilde{\delta}_{ki}\widetilde{\delta}_{lj} \det(\mathbf{J}^e)_{kl} \, w_k w_l, \tag{3.107}$$

$$(B_z^e)_{kl,\widetilde{ij}} = \sum_{p=0}^{N}\sum_{q=0}^{N} \widetilde{\delta}_{pi}\widetilde{\delta}_{qj} (D_z^e)_{kl,pq} \det(\mathbf{J}^e)_{pq} \, r_{pq} w_p w_q, \tag{3.108}$$

$$(Z^e)_{\widetilde{ij}} = \sum_{p=0}^{N}\sum_{q=0}^{N} \widetilde{\delta}_{pi}\widetilde{\delta}_{qj} \det(\mathbf{J}^e)_{pq} \, r_{pq} w_p w_q, \tag{3.109}$$

for $0 \leq i, j \leq N$ and $1 \leq k, l \leq N-1$ and where $r_{pq} = r(\xi_p, \eta_q)$, the r co-ordinate of the global node found via the transfinite element mapping. Similarly to the Cartesian case, we write the SEM approximation in axisymmetric polar co-ordinates of each bilinear

operator as a matrix-vector product as follows,

$$m_r^e(\mathbf{u},\mathbf{v}) \approx M^e \mathbf{u}_r^e, \qquad m_z^e(\mathbf{u},\mathbf{v}) \approx M^e \mathbf{u}_z^e, \tag{3.110}$$

$$a_r^e(\mathbf{u},\mathbf{v}) \approx \left(A_r^e + A_\theta^e\right) \mathbf{u}_r^e, , \qquad a_z^e(\mathbf{u},\mathbf{v}) \approx A_z^e \mathbf{u}_z^e, \tag{3.111}$$

$$b^e(p,\mathbf{v}) \approx \left(B_r^e + B_\theta^e\right) \mathbf{p}^e + B_z^e \mathbf{p}^e, \tag{3.112}$$

$$b^{e*}(\mathbf{u},q) \approx \left(B_r^e + B_\theta^e\right)^T \mathbf{u}_r^e + \left(B_z^e\right)^T \mathbf{u}_z^e, \tag{3.113}$$

$$z^e(p) \approx Z^e \mathbf{p}^e, \tag{3.114}$$

$$e_r^e(\boldsymbol{\tau},\mathbf{v}) \approx E_r^e \boldsymbol{\tau}_{rr}^e + E_z^e \boldsymbol{\tau}_{rz}^e + E_\theta^e \boldsymbol{\tau}_{\theta\theta}^e \qquad e_z^e(\boldsymbol{\tau},\mathbf{v}) \approx E_r^e \boldsymbol{\tau}_{rz}^e + E_z^e \boldsymbol{\tau}_{zz}^e \tag{3.115}$$

with the vectors, $\mathbf{u}_i^e$, $\boldsymbol{\tau}_{ij}^e$ and $\mathbf{p}^e$ as outlined in the Cartesian case.

Numerical Treatment of Possibly Singular Point

In (3.100) there is a potential singularity if $r_{kl} = 0$. This will occur for node points along the axis of symmetry. To deal with this, we look back at the strong formulation from which it arises from in (2.77): The problem term in this form is $\frac{u_r}{r^2}$.

We know that $u_r = 0$ when $r = 0$ from the axisymmetric boundary conditions and that $v = 0$ when $r = 0$ due to the choice of test spaces ($v = 0$ for Dirichlet boundaries). We also know that the first derivatives with respect to r exist, so we again use L'Hôpital's rule.

We apply L'Hôpital's rule twice to the strong form term to see that,

$$\lim_{r\to 0} \frac{u_r}{r^2} = \lim_{r\to 0} \frac{\partial u_r}{\partial r} \frac{1}{2r} = \frac{1}{2} \frac{\partial^2 u_r}{\partial r^2} (0,z) . \tag{3.116}$$

We expect $\frac{\partial^2 u_r}{\partial r^2}$ to exist and to be finite, so expect that this term need not be a problem and that we simply need a method to incorporate it into our numerical quadrature.

If we use the former limit from (3.116) and assume that $\frac{\partial^2 u_r}{\partial r^2}$ exists and is finite then the term is cancelled out by the multiplication by r in the integral. In this instance there is no contribution from the problem term in the sum when $r_{kl} = 0$ and so we simply set the term to be zero in this case.

Alternatively, if we consider the term arising from the weak form of $\frac{u_r}{r^2}$ then we can

also use L'Hôpital's rule to see that

$$\lim_{r\to 0}\frac{u_r v}{r}=\lim_{r\to 0}\frac{\frac{\partial}{\partial r}\left(u_r v\right)}{\frac{\partial}{\partial r}\left(r\right)}=\lim_{r\to 0}\left(v\frac{\partial u_r}{\partial r}+u_r\frac{\partial v}{\partial r}\right), \tag{3.117}$$

which gives us an idea of one way to get around the problem in (3.100) when $r_{kl}=0$.

If we let R_ϵ be a horizontal strip of height $\epsilon>0$ along the axis of symmetry then we may write the weak form of the problem term as,

$$\int_\Omega \frac{u_r v}{r}d\Omega=\int_{\Omega\setminus R_\epsilon}\frac{u_r v}{r}d\Omega+\int_{R_\epsilon}\frac{u_r v}{r}d\Omega, \tag{3.118}$$

and taking limits we get

$$\lim_{\epsilon\to 0}\left(\int_{\Omega\setminus R_\epsilon}\frac{u_r v}{r}d\Omega+\int_{R_\epsilon}\frac{u_r v}{r}d\Omega\right)=\lim_{\epsilon\to 0}\left(\int_{\Omega\setminus R_\epsilon}\frac{u_r v}{r}d\Omega+\int_{R_\epsilon}v\frac{\partial u_r}{\partial r}+u_r\frac{\partial v}{\partial r}d\Omega\right). \tag{3.119}$$

We use this to justify a change to (3.100),

$$\left(A^e_\theta\right)_{kl,ij}=\begin{cases}\frac{1}{r_{kl}}\delta_{ik}\delta_{jl}\det\left(\mathbf{J}^e\right)_{kl}w_k w_l, & \text{if } r_{kl}\ \&\ r_{ij}\neq 0\\ D^r_{ij,kl}\det\left(\mathbf{J}^e\right)_{kl}w_k w_l, & \text{if } r_{kl}=0\ \&\ r_{ij}\neq 0\\ D^r_{kl,ij}\det\left(\mathbf{J}^e\right)_{ij}w_i w_j, & \text{if } r_{kl}\neq 0\ \&\ r_{ij}=0\\ D^r_{ij,kl}\det\left(\mathbf{J}^e\right)_{kl}w_k w_l+D^r_{kl,ij}\det\left(\mathbf{J}^e\right)_{ij}w_i w_j, & \text{if } r_{kl}\ \&\ r_{ij}=0\end{cases} \tag{3.120}$$

Note that while we could consider different values of ϵ and include this approximation to any node points lying a small distance away (i.e. when $r<\epsilon$) from the axis of symmetry, in practice we only apply this approximation to points lying directly on the axis of symmetry (i.e. when $r=0$).

3.3.7 Global System Assembly

If we wish to construct the global spectral element matrix approximation we must sum over all elements and take contributions from the local matrices. We do this using the prolongation operator defined earlier in Section 3.3.1. In discrete form the map, $R^T_e(pq)$, takes the locally labelled point $\mathbf{x}^e_{pq}=(\xi_p,\eta_q)$ on a particular element Ω_e and maps it to a globally labelled point $\mathbf{x}_g$. It is possible, and intended, that this operator

may map local node points from different elements onto the same global node point. This occurs when the global point lies on a shared boundary or interface between two spectral elements. The following section details how this mapping is constructed in practice.

Discrete Mapping

In this section we detail how the global and local mapping are constructed. Examples of the global and local numbering for a domain made up of two elements are shown in Figures 3.1 and 3.2, respectively. Suppose we have a domain made up of K spectral

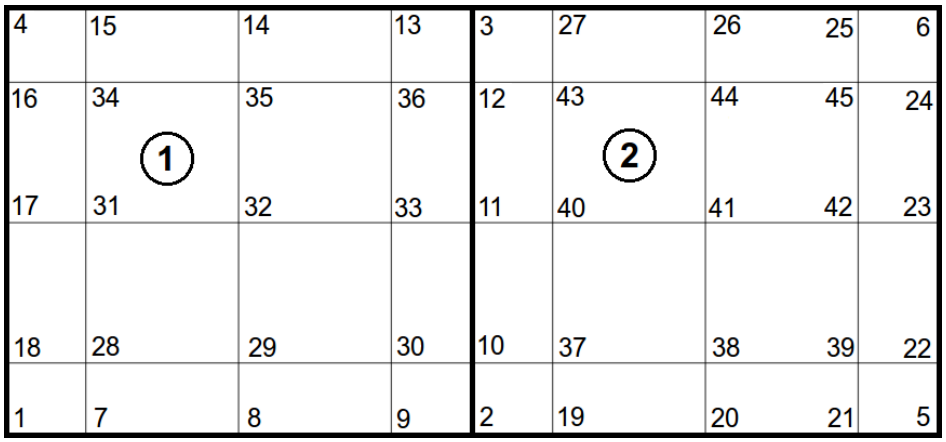

Figure 3.1: Example of the global node numbering for a domain made up of two elements. The element labels are circled.

elements as described in Section 3.3.1. We label each element from 1 to K arbitrarily. The discrete form of the local-to-global map is constructed in three stages.

1. Starting at $\mathbf{V}_1^1$ (vertex 1 of element 1), we give global labels, beginning at 1, to all vertices of Ω^1 in an anti-clockwise direction. For each locally numbered vertex, we log the global numbering to our local-to-global map.

For example: the local number of $\mathbf{V}_1^1$ is 0 (putting i=0, j=0 into (3.65)) and it has global number 1, so $R_1(1) = 0$ and $R_1^T(0) = 1$, $\mathbf{V}_3^1$ has local number $(N+1)^2 - 1$ (i=N, j=N into (3.65)) and global number 3, so $R_1(3) = (N+1)^2 - 1$ and $R_1^T\left((N+1)^2 - 1\right) = 3$ and so on. Note that from this point we will only give the global-to-local mapping, R_k,

in examples since it is now clear how to construct the local-to-global map R_k^T using R_k.

We repeat this process for all spectral elements according to the arbitrarily decided element ordering. If a vertex has already been globally labelled (due to lying on a shared boundary between elements) then we skip this vertex until we reach the next unlabelled vertex. At the end of the global labelling of all element vertices we will have labelled N_{vert} points which is dependent upon the connectivity of the spectral elements.

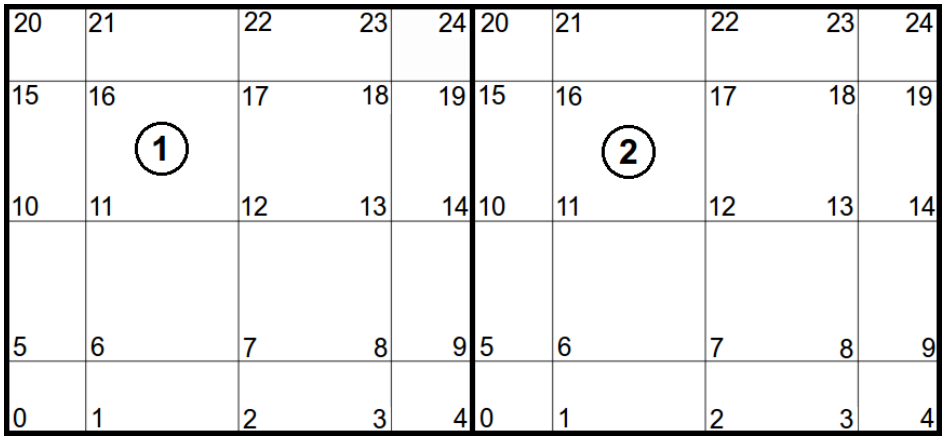

Figure 3.2: Example of the local node numbering for a domain made up of two elements. The element labels are circled.

2. We next label the edge nodes of each element starting at $\mathbf{F}_1^1$ (edge 1 on Ω^1) beginning at the first node along the edge from $\mathbf{V}_1^1$ until we reach the last non-vertex point on the edge. The local number is 1 ($i=1, j=0$ into (3.65)), so $R_1(N_{vert}+1) = 1$, $R_1(N_{vert}+2) = 2$ and so on until the local node $N-1$ ($i=N-1, j=0$ into (3.65)) is reached and labelled globally as $N_{vert}+N-1$. We then work anti-clockwise around the edges in the same manner so that $R_1(N_{vert}+N) = 2N+1$, .., $R_1(N_{vert}+2(N-1)) = N+(N-1)(N+1)$, etc.

As before, we repeat the process for each spectral element in order and similarly to the numbering of the vertices, we skip any edge points which have already been labelled due to shared boundaries. At this point, we will have labelled $N_{vert}+N_{edge}$ global points. This leaves only the internal node points.

3. We finally number each of the internal node points. This is done easily since we do not have any nodes which are shared between elements left to number. This is done by simply following the way in which local internal node points are labelled for the pressure. We fill in the rest of the local-to-global mapping using

$$R_e^T(ij) = N_{vert} + N_{edge} + (e-1)\,(N-1)^2 + \widetilde{ij}, \tag{3.121}$$

for $1 \leq i, j \leq N-1$ using the notation from (3.66). The total number of global nodes is $N_{tot} = N_{vert} + N_{edge} + N_{int}$, where $N_{int} = K\,(N-1)^2$.

The value of $g = R_e^T(ij)$ gives which global node that local node, ij, corresponds to in element Ω_e. Conversely, the discrete global-to-local map, $R_k(g)$, gives the locally numbered node in element Ω_k corresponding to global node g.

Discrete Pressure Mapping

While the pressure is approximated on the internal set of GLL points, shared with the velocity node points, we need a separate global numbering for these internal pressure nodes.

We simply offset the local-to-global mapping for these points by taking away the number of non-internal global points away from the mapping value, so an internal point ij maps to $R_e^T(ij)$ for a velocity test or trial function, but to $\tilde{R}_e^T\left(\widetilde{ij}\right) = R_e^T(ij) - (N_{vert} + N_{edge})$ for a pressure test or trial function. This means that our global numbering of internal pressure nodes begins at 1 and ends at N_{int} as desired. The discrete global-to-local map for the pressure follows the same notation and is written $\tilde{R}_e(g)$.

Construction of a Global Matrix

We assemble a global matrix from the contributions of the local matrices. For example, the global mass matrix, M, is assembled as follows,

$$M_{g_i,g_j} = \sum_{k=1}^{K} M^k_{R_k(g_i),R_k(g_j)}. \tag{3.122}$$

for $1 \leq g_i, g_j \leq N_{tot}$. The global matrix approximations of all the bilinear forms, (3.32)-(3.37), are assembled in the same manner with obvious notation. We use the appropriate velocity or pressure mapping depending on the global matrix to be assembled. For example, B_x,

$$(B_x)_{g_i,\tilde{g}_j} = \sum_{k=1}^{K} \left(B_x^k\right)_{R_k(g_i),\tilde{R}_k(\tilde{g}_j)}, \tag{3.123}$$

for $1 \leq g_i \leq N_{tot}$ and $1 \leq \tilde{g}_j \leq N_{int}$.

Zero Integral of Pressure Approximation

The one exception which requires a slightly different assembly is the construction of the global matrix representing the zero integral of pressure from the alternative formulation (3.36). Since there are two integrals over the whole domain required to compute this quantity, we cannot represent it locally. Instead we must sum both of the integrals and combine them in the global system. The global matrix is assembled using

$$C_{\tilde{g}_i,\tilde{g}_j} = \sum_{e_1=1}^{K} Z^{e_1}_{\tilde{R}_{e_1}(\tilde{g}_i)} \sum_{e_2=1}^{K} Z^{e_2}_{\tilde{R}_{e_2}(\tilde{g}_j)} \tag{3.124}$$

for $1 \leq \tilde{g}_i \leq N_{int}$ and $1 \leq \tilde{g}_j \leq N_{int}$.

We now have a means to construct the global discretised system which is detailed in Section 3.3.8. We may also write it as a linear system, which is shown in Section 3.3.9.

3.3.8 Fully Discretised Global System

With all of the global matrices assembled using the local-to-global mapping as described in Section 3.3.7 we may now write our fully discretised system of equations following from (3.43)-(3.42), as,

$$Re\frac{\gamma_0}{\Delta t}\mathbf{M}\mathbf{u}^{n+1} + \beta\mathbf{A}\mathbf{u}^{n+1} - \mathbf{B}p^{n+1} = \mathbf{M}\mathbf{f}^{n+1} + \sum_{q=0}^{J-1}\left(Re\frac{\alpha_q}{\Delta t}\mathbf{M}\tilde{\mathbf{u}}_q^{n+1} + \beta_q\mathbf{E}\boldsymbol{\tau}^{n-q}\right), \tag{3.125}$$

$$-\mathbf{B}^T\mathbf{u}^{n+1} + \mu C p^{n+1} = 0. \tag{3.126}$$

where the matrices in bold denote that they contain all components. For example the global mass matrix in Cartesian co-ordinates is constructed from the x and y components and the vector $\mathbf{u}^{n+1}$ is matched accordingly as follows

$$\mathbf{M} = \begin{pmatrix} M_x & 0 \\ 0 & M_y \end{pmatrix}, \qquad \mathbf{u}^{n+1} = \begin{pmatrix} \mathbf{u}_x^{n+1} \\ \mathbf{u}_y^{n+1} \end{pmatrix}. \tag{3.127}$$

with $\mathbf{u}_x^{n+1}$ and $\mathbf{u}_y^{n+1}$ being vectors of length equal to the number of global node points.

The elastic stress tensor, $\boldsymbol{\tau}$, is found separately via the decoupled constitutive equation using the previously computed velocity solutions from past timesteps. The method for the solution of the constitutive equation is detailed in Section 3.5.

3.3.9 Linear Global System

We may write the fully discretised velocity-pressure problem as a linear system to be solved at each timestep.

Cartesian Linear System

In the Cartesian case,

$$\begin{pmatrix} \frac{Re\gamma_0}{\Delta t} M_x + \beta A & 0 & -B_x \\ 0 & \frac{Re\gamma_0}{\Delta t} M_y + \beta A & -B_y \\ -B_x^T & -B_y^T & \mu C \end{pmatrix} \begin{pmatrix} \mathbf{u}_x^{n+1} \\ \mathbf{u}_y^{n+1} \\ \mathbf{p}^{n+1} \end{pmatrix} = \begin{pmatrix} \widehat{\mathbf{f}}_x^{n+1} \\ \widehat{\mathbf{f}}_y^{n+1} \\ \widehat{\mathbf{g}}^{n+1} \end{pmatrix} \tag{3.128}$$

with the matrices as defined in Section 3.3.7 and where $\widehat{\mathbf{f}}_i$ and $\widehat{\mathbf{g}}$ contain all the known terms from the right hand side of the discrete equations

$$\widehat{\mathbf{f}}_x^{n+1} = M\mathbf{f}_x^{n+1} + \sum_{q=0}^{J-1} \left(Re \frac{\alpha_q}{\Delta t} M \tilde{\mathbf{u}}_{x_q}^{n+1} + \beta_q \left(E_x \boldsymbol{\tau}_{xx}^{n-q} + E_y \boldsymbol{\tau}_{xy}^{n-q} \right) \right), \tag{3.129}$$

$$\widehat{\mathbf{f}}_y^{n+1} = M\mathbf{f}_y^{n+1} + \sum_{q=0}^{J-1} \left(Re \frac{\alpha_q}{\Delta t} M \tilde{\mathbf{u}}_{y_q}^{n+1} + \beta_q \left(E_x \boldsymbol{\tau}_{xy}^{n-q} + E_y \boldsymbol{\tau}_{yy}^{n-q} \right) \right), \tag{3.130}$$

$$\widehat{\mathbf{g}}^{n+1} = 0. \tag{3.131}$$

Axisymmetric Cylindrical Linear Polar System

In the axisymmetric cylindrical polar case, we have

$$\begin{pmatrix} \frac{Re\gamma_0}{\Delta t}M_r + \beta\left(A_r + A_\theta\right) & 0 & -\left(B_r + B_\theta\right) \\ 0 & \frac{Re\gamma_0}{\Delta t}M_z + \beta A_z & -B_z \\ -\left(B_r + B_\theta\right)^T & -B_z^T & \mu C \end{pmatrix} \begin{pmatrix} \mathbf{u}_r^{n+1} \\ \mathbf{u}_z^{n+1} \\ \mathbf{p}^{n+1} \end{pmatrix} = \begin{pmatrix} \widehat{\mathbf{f}}_r^{n+1} \\ \widehat{\mathbf{f}}_z^{n+1} \\ \widehat{\mathbf{g}}^{n+1} \end{pmatrix} \tag{3.132}$$

with

$$\widehat{\mathbf{f}}_r^{n+1} = M\mathbf{f}_r^{n+1} + \sum_{q=0}^{J-1}\left(Re\frac{\alpha_q}{\Delta t}M\tilde{\mathbf{u}}_{r_q}^{n+1} + \beta_q\left(E_r\boldsymbol{\tau}_{rr}^{n-q} + E_z\boldsymbol{\tau}_{rz}^{n-q} + E_\theta\boldsymbol{\tau}_{\theta\theta}^{n-q}\right)\right), \tag{3.133}$$

$$\widehat{\mathbf{f}}_z^{n+1} = M\mathbf{f}_z^{n+1} + \sum_{q=0}^{J-1}\left(Re\frac{\alpha_q}{\Delta t}M\tilde{\mathbf{u}}_{z_q}^{n+1} + \beta_q\left(E_r\boldsymbol{\tau}_{rz}^{n-q} + E_z\boldsymbol{\tau}_{zz}^{n-q}\right)\right), \tag{3.134}$$

$$\widehat{\mathbf{g}}^{n+1} = 0. \tag{3.135}$$

Application of Boundary Conditions

The final step in preparing the linear system for solution at any timestep is to apply the boundary conditions. We eliminate any rows and columns which correspond to a Dirichlet node in the global matrix. We then substitute the known values into solution at these nodes and perform the matrix-vector calculations with the corresponding rows in the global matrix, which gives a contribution to take away from the right hand side of our linear system. These are incorporated into $\widehat{\mathbf{f}}_i^{n+1}$ and $\widehat{\mathbf{g}}^{n+1}$.

Our linear system may now be solved using the numerical linear algebra methods detailed in Section 3.8.

3.4 Approximation of Spatial Measures

We will require the use of some spatial measures in various ways, such as when analysing results. The two main measures we use are the L^2-norm and the H^1-norm which are

defined as,

$$\|\mathbf{x}\|^2_{L^2(\Omega)} = \int_\Omega |\mathbf{x}|^2 \, d\Omega \tag{3.136}$$

$$\|\mathbf{x}\|^2_{H^1(\Omega)} = \|\mathbf{x}\|^2_{L^2(\Omega)} + \|\nabla\mathbf{x}\|^2_{L^2(\Omega)} = \int_\Omega |\mathbf{x}|^2 + |\nabla\mathbf{x}|^2 \, d\Omega \tag{3.137}$$

for some variable $\mathbf{x}$, which may be scalar, vector or tensor valued and the measure $|\cdot|$ is the appropriate norm analogous to the l^2 vector norm.

We decompose the domain into spectral elements as done in the SEM and perform the integration using GL quadrature so that (3.136) is approximated by

$$\|s\|^2_{L^2(\Omega)} \approx \sum_{e=1}^{K}\sum_{p=0}^{N}\sum_{q=0}^{N} \left(s^e_{pq}\right)^2 \det\left(\mathbf{J}^e\right)_{pq} w_p w_q, \tag{3.138}$$

$$\|\mathbf{v}\|^2_{L^2(\Omega)} \approx \sum_{e=1}^{K}\sum_{p=0}^{N}\sum_{q=0}^{N} \left(\left(\left(v^e_x\right)_{pq}\right)^2 + \left(\left(v^e_y\right)_{pq}\right)^2\right) \det\left(\mathbf{J}^e\right)_{pq} w_p w_q, \tag{3.139}$$

$$\begin{aligned}\|\mathbf{T}\|^2_{L^2(\Omega)} \approx \sum_{e=1}^{K}\sum_{p=0}^{N}\sum_{q=0}^{N} \Bigg(&\left(\left(T^e_{xx}\right)_{pq}\right)^2 + \left(\left(T^e_{xy}\right)_{pq}\right)^2 \\ &+ \left(\left(T^e_{yx}\right)_{pq}\right)^2 + \left(\left(T^e_{yy}\right)_{pq}\right)^2\Bigg) \det\left(\mathbf{J}^e\right)_{pq} w_p w_q,\end{aligned} \tag{3.140}$$

for a scalar, $s(\mathbf{x})$, a vector, $\mathbf{v}(\mathbf{x})$, and a second-order tensor, $\mathbf{T}(\mathbf{x})$, and where the superscript k on a variable within the sum denotes the spectral element, and the subscript pq denotes the local GLL point. These approximations of the L^2-norms can be combined to obtain to the approximation of the H^1-norm given in (3.137), noting that we do not make use of the H^1-norm for tensor valued variables.

The axisymmetric cylindrical polar co-ordinate equivalents of (3.138)-(3.140) are given by

$$\|s\|^2_{L^2(\Omega)} \approx \sum_{e=1}^{K}\sum_{p=0}^{N}\sum_{q=0}^{N} \left(s^e_{pq}\right)^2 \det\left(\mathbf{J}^e\right)_{pq} r^e_{pq} w_p w_q, \tag{3.141}$$

$$\|\mathbf{v}\|^2_{L^2(\Omega)} \approx \sum_{e=1}^{K}\sum_{p=0}^{N}\sum_{q=0}^{N} \left(\left(\left(v^e_r\right)_{pq}\right)^2 + \left(\left(v^e_z\right)_{pq}\right)^2\right) \det\left(\mathbf{J}^e\right)_{pq} r^e_{pq} w_p w_q, \tag{3.142}$$

$$\begin{aligned}\|\mathbf{T}\|^2_{L^2(\Omega)} \approx \sum_{e=1}^{K}\sum_{p=0}^{N}\sum_{q=0}^{N} \Bigg(&\left(\left(T^e_{rr}\right)_{pq}\right)^2 + \left(\left(T^e_{rz}\right)_{pq}\right)^2 + \left(\left(T^e_{zr}\right)_{pq}\right)^2 \\ &+ \left(\left(T^e_{zz}\right)_{pq}\right)^2 + \left(\left(T^e_{\theta\theta}\right)_{pq}\right)^2\Bigg) \det\left(\mathbf{J}^e\right)_{pq} r^e_{pq} w_p w_q,\end{aligned} \tag{3.143}$$

where r^e_{pq} is the radial co-ordinate at the local GLL point pq in spectral element e.

3.5 Discretisation of the Constitutive Equation

As described in Section 3.1, we have two temporal schemes, (3.14) and (3.15), both of which require spatial discretisation. If we consider an arbitrary single point within the domain, due to the decoupling from the velocity and explicit treatment of the convection and Giesekus terms in both schemes, we may rewrite the equations at timestep t^{n+1} as a linear system.

3.5.1 BDF/EX Linear System

For scheme (3.14), the linear system may be written,

$$A_\tau \boldsymbol{\tau}^{n+1} = \mathbf{b}_\tau, \tag{3.144}$$

where A_τ is a 3 by 3 matrix with non-zero entries given by

$$(A_\tau)_{11} = 1 + \frac{\gamma_0 We}{\Delta t} - 2We \left(\nabla \mathbf{u}^{n+1}\right)_{11}, \tag{3.145}$$

$$(A_\tau)_{12} = -2We \left(\nabla \mathbf{u}^{n+1}\right)_{21}, \tag{3.146}$$

$$(A_\tau)_{21} = -We \left(\nabla \mathbf{u}^{n+1}\right)_{12}, \tag{3.147}$$

$$(A_\tau)_{22} = 1 + \frac{\gamma_0 We}{\Delta t} - We\big(\left(\nabla \mathbf{u}^{n+1}\right)_{11} + \left(\nabla \mathbf{u}^{n+1}\right)_{22} \big), \tag{3.148}$$

$$(A_\tau)_{23} = -We \left(\nabla \mathbf{u}^{n+1}\right)_{21}, \tag{3.149}$$

$$(A_\tau)_{32} = -2We \left(\nabla \mathbf{u}^{n+1}\right)_{12}, \tag{3.150}$$

$$(A_\tau)_{33} = 1 + \frac{\gamma_0 We}{\Delta t} - 2We \left(\nabla \mathbf{u}^{n+1}\right)_{22} \tag{3.151}$$

and the values of the components of the elastic stress at the chosen point in the domain written in vector form,

$$\boldsymbol{\tau} = \begin{pmatrix} \tau_{11} \\ \tau_{12} \\ \tau_{22} \end{pmatrix} \tag{3.152}$$

where the subscript refer to the components of $\boldsymbol{\tau}$, with $\tau_{12} = \tau_{xy}$ in Cartesian co-ordinates and $\tau_{12} = \tau_{rz}$ in axisymmetric cylindrical polar co-ordinates. The entries of the vector, $\mathbf{b}_\tau^e$, containing all known terms from the right hand side of the equation is

given by

$$(\mathbf{b}_\tau)_1 = 2(1-\beta)\left(\nabla \mathbf{u}^{n+1}\right)_{11} + We\sum_{q=0}^{J-1}\left(\frac{\alpha_q}{\Delta t}\tau_{11}^{n-q} - \beta_q\left(\mathbf{u}^{n+1}\cdot\nabla\boldsymbol{\tau}^{n-q}\right)_{11}\right)$$
$$- We\frac{\alpha}{(1-\beta)}\sum_{q=0}^{J-1}\beta_q\left(\left(\tau_{11}^{n-q}\right)^2 + \left(\tau_{12}^{n-q}\right)^2\right), \tag{3.153}$$

$$(\mathbf{b}_\tau)_2 = (1-\beta)\left(\left(\nabla \mathbf{u}^{n+1}\right)_{12} + \left(\nabla \mathbf{u}^{n+1}\right)_{21}\right) + We\sum_{q=0}^{J-1}\left(\frac{\alpha_q}{\Delta t}\tau_{12}^{n-q} - \beta_q\left(\mathbf{u}^{n+1}\cdot\nabla\boldsymbol{\tau}^{n-q}\right)_{12}\right)$$
$$- We\frac{\alpha}{(1-\beta)}\sum_{q=0}^{J-1}\beta_q\left(\tau_{11}^{n-q}\tau_{12}^{n-q} + \tau_{12}^{n-q}\tau_{22}^{n-q}\right), \tag{3.154}$$

$$(\mathbf{b}_\tau)_3 = 2(1-\beta)\left(\nabla \mathbf{u}^{n+1}\right)_{22} + We\sum_{q=0}^{J-1}\left(\frac{\alpha_q}{\Delta t}\tau_{22}^{n-q} - \beta_q\left(\mathbf{u}^{n+1}\cdot\nabla\boldsymbol{\tau}^{n-q}\right)_{22}\right)$$
$$- We\frac{\alpha}{(1-\beta)}\sum_{q=0}^{J-1}\beta_q\left(\left(\tau_{12}^{n-q}\right)^2 + \left(\tau_{22}^{n-q}\right)^2\right) \tag{3.155}$$

Additional Equation for Axisymmetric Cylindrical Polar Co-ordinates

In the case of axisymmetric cylindrical polar co-ordinates, we have an additional component of elastic stress, $\tau_{\theta\theta}$, to be found. This component does not depend on any of the others, so we may calculate it separately via,

$$\tau_{33}^{n+1} = \frac{(\mathbf{b}_\tau)_4}{(A_\tau)_{44}} \tag{3.156}$$

where co-ordinate 3 corresponds to the θ-component and,

$$(A_\tau)_{44} = 1 + \frac{\gamma_0 We}{\Delta t} - 2We\left(\nabla \mathbf{u}^{n+1}\right)_{33}, \tag{3.157}$$

$$(\mathbf{b}_\tau)_4 = 2(1-\beta)\left(\nabla \mathbf{u}^{n+1}\right)_{33} + We\sum_{q=0}^{J-1}\left(\frac{\alpha_q}{\Delta t}\tau_{33}^{n-q} - \beta_q\left(\mathbf{u}^{n+1}\cdot\nabla\boldsymbol{\tau}^{n-q}\right)_{33}\right)$$
$$- We\frac{\alpha}{(1-\beta)}\sum_{q=0}^{J-1}\beta_q\left(\tau_{33}^{n-q}\right)^2 \tag{3.158}$$

3.5.2 Semi-Iterative BDF/FPI Linear System

When using the BDF/FPI scheme, (3.15), after the previously explained setup stage at each timestep, for each inner iteration over i we solve the linear system,

$$A_\tau \widetilde{\boldsymbol{\tau}}^{i+1} = \mathbf{b}^i_{\widetilde{\tau}}, \tag{3.159}$$

with A_τ unchanged from (3.145)-(3.151) and the entries of $\mathbf{b}^i_{\widetilde{\tau}}$ given by

$$\begin{aligned}
\left(\mathbf{b}^i_{\widetilde{\tau}}\right)_1 &= 2\left(1-\beta\right)\left(\nabla \mathbf{u}^{n+1}\right)_{11} \\
&\quad + We\left(\sum_{q=0}^{J-1}\frac{\alpha_q}{\Delta t}\tau_{11}^{n-q} - \left(\mathbf{u}^{n+1}\cdot\nabla\widetilde{\boldsymbol{\tau}}^i\right)_{11} - \frac{\alpha}{(1-\beta)}\left(\left(\widetilde{\tau}^i_{11}\right)^2 + \left(\widetilde{\tau}^i_{12}\right)^2\right)\right), \qquad (3.160)\\
\left(\mathbf{b}^i_{\widetilde{\tau}}\right)_2 &= \left(1-\beta\right)\left(\left(\nabla \mathbf{u}^{n+1}\right)_{12} + \left(\nabla \mathbf{u}^{n+1}\right)_{21}\right) \\
&\quad + We\left(\sum_{q=0}^{J-1}\frac{\alpha_q}{\Delta t}\tau_{12}^{n-q} - \left(\mathbf{u}^{n+1}\cdot\nabla\widetilde{\boldsymbol{\tau}}^i\right)_{12} - \frac{\alpha}{(1-\beta)}\left(\widetilde{\tau}^i_{11}\widetilde{\tau}^i_{12} + \widetilde{\tau}^i_{12}\widetilde{\tau}^i_{22}\right)\right), \qquad (3.161)\\
\left(\mathbf{b}^i_{\widetilde{\tau}}\right)_3 &= 2\left(1-\beta\right)\left(\nabla \mathbf{u}^{n+1}\right)_{22} \\
&\quad + We\left(\sum_{q=0}^{J-1}\frac{\alpha_q}{\Delta t}\tau_{22}^{n-q} - \left(\mathbf{u}^{n+1}\cdot\nabla\widetilde{\boldsymbol{\tau}}^i\right)_{22} - \frac{\alpha}{(1-\beta)}\left(\left(\widetilde{\tau}^i_{12}\right)^2 + \left(\widetilde{\tau}^i_{22}\right)^2\right)\right). \qquad (3.162)
\end{aligned}$$

For the axisymmetric cylindrical polar co-ordinate case then we iteratively solve

$$\widetilde{\tau}^{i+1}_{33} = \frac{\left(\mathbf{b}^i_{\widetilde{\tau}}\right)_4}{\left(A_\tau\right)_{44}} \tag{3.163}$$

with $\left(A_\tau\right)_{44}$ as in (3.157) and,

$$\begin{aligned}
\left(\mathbf{b}^i_{\widetilde{\tau}}\right)_4 &= 2\left(1-\beta\right)\left(\nabla \mathbf{u}^{n+1}\right)_{33} \\
&\quad + We\left(\sum_{q=0}^{J-1}\frac{\alpha_q}{\Delta t}\tau_{33}^{n-q} - \left(\mathbf{u}^{n+1}\cdot\nabla\widetilde{\boldsymbol{\tau}}^i\right)_{33} - \frac{\alpha}{(1-\beta)}\left(\widetilde{\tau}^i_{33}\right)^2\right) \qquad (3.164)
\end{aligned}$$

3.5.3 Spatial Discretisation of Elastic Stress

Following Sections 3.5.1 and 3.5.2 we now have a method for solving the constitutive equation at a chosen point within our domain. We are left with a choice of which set of points on which to approximate the elastic stress. The logical choice, given that we already have a method of calculating the velocity and pressure solution on it, is the global GLL grid.

We use the domain decomposition described in Section 3.3.1, and so approximate the elastic stress locally within each element on the GLL grid. Similarly to the velocity and pressure in equations (3.62)-(3.63), we adopt a spectral representation of each component, ab, of elastic stress on each spectral element, Ω_e,

$$\tau_{ab}^e(\xi,\eta) = \sum_{i=0}^{N}\sum_{j=0}^{N} (\tau_{ab}^e)_{ij}\, h_i(\xi)\, h_j(\eta)\,, \tag{3.165}$$

with $h_i(\xi)$ being the Lagrange interpolant as defined in (3.67) and where $(\tau_{ab}^e)_{ij}$ is the approximation for the elastic stress component ab at the GLL point (ξ_i, η_j). We may now use (3.144) or (3.159) to find a solution for each $1 \leq e \leq K$ and each $0 \leq i, j \leq N$ independently.

Continuity of Stress

The SEM only gives us a way of calculating derivatives with respect to global variables in a local manner which means that it is possible that for two neighbouring spectral elements, Ω^{e_1} and Ω^{e_2}, $(\nabla \mathbf{u}^{e_1})$ and $(\nabla \mathbf{u}^{e_2})$ may have different values at a shared boundary point when approximated via SEM within their respective elements. Similarly, the value of the convection term, $\mathbf{u}\cdot\nabla\boldsymbol{\tau}^{e_1}$ and $\mathbf{u}\cdot\nabla\boldsymbol{\tau}^{e_2}$ may also differ. This could lead to a loss of continuity in stress across elements.

One option is to simply allow the elastic stress to be discontinuous at these shared boundary points. An alternative is to enforce continuity across spectral elements by taking the average (or some weighting) of the two at the shared point and using it for the approximation of the elastic stress at these points. Another option is to allow for a discontinuous stress, but communicate information across the boundary in some way. A method for this last option is discussed in Section 3.6.

3.6 Discontinuous Galerkin Treatment of Constitutive Equation

The discontinuous Galerkin (DG) method was first introduced in the 1970s for use with the neutron transport equation by Lesaint and Raviart [29], but was eventually used for the simulation of viscoelastic fluid flows by Fortin and Fortin [17]. In their method, the stress approximation was made discontinuous across elements. This allowed the stress to be solved on an element-by-element basis which can heavily reduce computational costs. A further advantage, when compared to continuous Galerkin interpolations, is that the velocity-stress compatibility condition is satisfied easily. In the following description we follow Owens and Phillips [45].

3.6.1 Derivation of DG Treatment of Convection Term

Supposing we have decomposed our domain, Ω, into K non-overlapping elements, Ω_k, $k = 1, .., K$. We can then use a streamline upwinded Discontinuous Galerkin (DG) treatment of the constitutive equation. We allow stress to be discontinuous across elements. The stress between elements then only interacts in operations involving the shared elemental boundaries. We reconsider the convective derivative, multiplying by an appropriate stress test function $S \in \Sigma$ and integrating over Ω. The weak form of the convective derivative may be written in the form

$$\int_{\Omega} (\mathbf{u} \cdot \nabla \boldsymbol{\tau}) : S \; d\Omega = \sum_{k=1}^{K} \int_{\Omega_k} (\mathbf{u} \cdot \nabla \boldsymbol{\tau}) : S \; d\Omega_k, \tag{3.166}$$

which we may rewrite as

$$\sum_{k=1}^{K} \int_{\Omega_k} (\mathbf{u} \cdot \nabla \boldsymbol{\tau}) : S \; d\Omega_k = \sum_{k=1}^{K} \int_{\Omega_k} \nabla \cdot (\mathbf{u} \, (\boldsymbol{\tau} : S)) \; d\Omega_k - \sum_{k=1}^{K} \int_{\Omega_k} (\mathbf{u} \cdot \nabla S) : \boldsymbol{\tau} \; d\Omega_k. \tag{3.167}$$

Applying the divergence theorem to the first term on the right-hand side, we obtain,

$$\sum_{k=1}^{K} \int_{\Omega_k} (\mathbf{u} \cdot \nabla \boldsymbol{\tau}) : S \; d\Omega_k = \sum_{k=1}^{K} \int_{\Gamma_k} (\mathbf{n} \cdot \mathbf{u}) \, \boldsymbol{\tau} : S \; d\Gamma_k - \sum_{k=1}^{K} \int_{\Omega_k} (\mathbf{u} \cdot \nabla S) : \boldsymbol{\tau} \; d\Omega_k. \tag{3.168}$$

Considering a particular element, Ω_k, suppose that there is a point, $\mathbf{x}$, on the edge of that element, $\bar{\Omega}_k$ which is shared with the edge of a neighbouring element, $\bar{\Omega}_l$. Since our stress is allowed to be discontinuous across elements, the value of the elastic stress is not necessarily the same at $\mathbf{x}$ when evaluated within each element.

With this in mind, we denote by $\boldsymbol{\tau}^{\boldsymbol{e}}(\mathbf{x})$ the value of the elastic stress at $\mathbf{x} \in \bar{\Omega}_l$ and by $\boldsymbol{\tau}^{\boldsymbol{i}}(\mathbf{x})$ the value at $\mathbf{x} \in \bar{\Omega}_k$. We call these the external and internal stress tensors respectively. We now let

$$\boldsymbol{\tau} = \begin{cases} \alpha_{DG}\boldsymbol{\tau}^{\boldsymbol{e}} + (1-\alpha_{DG})\,\boldsymbol{\tau}^{\boldsymbol{i}} & \text{on } \Gamma_k^- \setminus \Gamma^-, \\ \alpha_{DG}\boldsymbol{\tau}^{\boldsymbol{i}} + (1-\alpha_{DG})\,\boldsymbol{\tau}^{\boldsymbol{e}} & \text{on } \Gamma_k^+ \setminus \Gamma^+, \end{cases} \tag{3.169}$$

for some upwinding parameter associated with our DG formulation, $\alpha_{DG} \in [0,1]$ where $\alpha_{DG} = 1$ corresponds to a fully upwinded formulation.

Substituting the expression(3.169) into (3.168) we obtain,

$$\begin{aligned} \sum_{k=1}^{K} \int_{\Omega_k} (\mathbf{u}\cdot\nabla\boldsymbol{\tau}) : S \; d\Omega_k = &\sum_{k=1}^{K} \int_{\Gamma_k^- \cap \Gamma^-} (\mathbf{n}\cdot\mathbf{u})\,\boldsymbol{\tau}_{inflow} : S \; d\Gamma_k \\ &+ \sum_{k=1}^{K} \int_{\Gamma_k^- \setminus \Gamma^-} (\mathbf{n}\cdot\mathbf{u}) \left(\alpha_{DG}\boldsymbol{\tau}^{\boldsymbol{e}} + (1-\alpha_{DG})\,\boldsymbol{\tau}^{\boldsymbol{i}}\right) : S \; d\Gamma_k \\ &+ \sum_{k=1}^{K} \int_{\Gamma_k^+ \setminus \Gamma^+} (\mathbf{n}\cdot\mathbf{u}) \left(\alpha_{DG}\boldsymbol{\tau}^{\boldsymbol{i}} + (1-\alpha_{DG})\,\boldsymbol{\tau}^{\boldsymbol{e}}\right) : S \; d\Gamma_k \\ &+ \sum_{k=1}^{K} \int_{\Gamma_k^+ \cap \Gamma^+} (\mathbf{n}\cdot\mathbf{u})\,\boldsymbol{\tau}^{\boldsymbol{i}} : S \; d\Gamma_k \\ &- \sum_{k=1}^{K} \int_{\Omega_k} (\mathbf{u}\cdot\nabla S) : \boldsymbol{\tau} \; d\Omega_k. \end{aligned} \tag{3.170}$$

Applying integration by parts a second time and using the divergence theorem on the last term with $\boldsymbol{\tau} \equiv \boldsymbol{\tau}^{\boldsymbol{i}}$ on $\Gamma_k \setminus \Gamma^-$ we obtain,

$$\begin{aligned} \sum_{k=1}^{K} \int_{\Omega_k} (\mathbf{u}\cdot\nabla\boldsymbol{\tau}) : S \; d\Omega_k = &\sum_{k=1}^{K} \int_{\Omega_k} (\mathbf{u}\cdot\nabla\boldsymbol{\tau}) : S \; d\Omega_k \\ &+ \alpha_{DG} \sum_{k=1}^{K} \int_{\Gamma_k^- \setminus \Gamma^-} (\mathbf{n}\cdot\mathbf{u}) \,[\![\boldsymbol{\tau}]\!] : S \; d\Gamma_k \\ &+ (1-\alpha_{DG}) \sum_{k=1}^{K} \int_{\Gamma_k^+ \setminus \Gamma^+} (\mathbf{n}\cdot\mathbf{u}) \,[\![\boldsymbol{\tau}]\!] : S \; d\Gamma_k \end{aligned} \tag{3.171}$$

where $[\![\boldsymbol{\tau}]\!] \equiv \boldsymbol{\tau}^{\boldsymbol{e}} - \boldsymbol{\tau}^{\boldsymbol{i}}$ represents the jump in stress between elements. By replacing the convected derivative in our constitutive equation with (3.171) we get the DG formulation.

3.6.2 Discretisation Of Convective Term by DG Method

Up to this point, our discretisation of the constitutive equation has been carried out in strong form, so we have not had to integrate. The DG method requires integration in order to create the jump term, so we require a way to incorporate this change without impacting on the previously described calculation of elastic stress. This can be done if we calculate the DG convection term separately. First, we introduce the notation,

$$\widehat{\boldsymbol{\tau}} = \mathbf{u} \cdot \nabla \boldsymbol{\tau}. \tag{3.172}$$

Given that, at any particular timestep, we treat the convection terms explicitly, when applying this method we do not have any other unknowns, so we calculate an approximation of $\widehat{\boldsymbol{\tau}}$ given a velocity and elastic stress field.

Following from (3.171), we set $\alpha_{DG} = 1$ and note that we may calculate $\widehat{\boldsymbol{\tau}}$ on an element-by-element basis. Dropping the summation over all elements, we write the SEM approximation of each component, ab, of the LHS of the DG system, locally, as the matrix-vector multiplication,

$$\left(\int_{\Omega_k} \widehat{\boldsymbol{\tau}}(\mathbf{x}) : S d\Omega\right)_{ab} = \left(\int_D \widehat{\boldsymbol{\tau}}^k(\xi,\eta) : S \det \mathbf{J}^k \, d\xi d\eta\right)_{ab} \approx M^k \widehat{\boldsymbol{\tau}}^k_{ab} \tag{3.173}$$

where entries corresponding to a global inflow node must be set to zero and removed from the linear system.

Next, each non-zero component of the integral on the RHS of (3.171) may be expressed locally by the matrix-vector multiplication,

$$\left(\int_{\Omega_k} (\mathbf{u} \cdot \nabla \boldsymbol{\tau}) : S \, d\Omega\right)_{ab} = \left(\int_D \left(\mathbf{u}^k \cdot \nabla \boldsymbol{\tau}^k\right) : S \det \mathbf{J}^k \, d\xi d\eta\right)_{ab} \approx \widehat{E}^k \boldsymbol{\tau}^k_{ab} \tag{3.174}$$

where

$$\left(\widehat{E}^k\right)_{kl,ij} = \left(u^k_x\right)_{kl} \left(E^k_x\right)_{ij,kl} + \left(u^k_y\right)_{kl} \left(E^k_y\right)_{ij,kl}, \tag{3.175}$$

$$\left(\widehat{E}^k\right)_{kl,ij} = \left(u^k_r\right)_{kl} \left(E^k_r\right)_{ij,kl} + \left(u^k_z\right)_{kl} \left(E^k_z\right)_{ij,kl}, \tag{3.176}$$

for the Cartesian and axisymmetric cylindrical polar co-ordinate cases, respectively.

This leaves only a term for the boundary integral, which may be expressed by,

$$\left(\int_{\Gamma_k^- \backslash \Gamma^-} (\mathbf{n}\cdot\mathbf{u}) \left[\!\left[\boldsymbol{\tau}^k\right]\!\right] \colon S \; d\Gamma\right)_{ab}$$
$$= \left(\sum_{m=1}^{4} \int_{D_m^- \backslash \Gamma^-} \left(\mathbf{n}^{k_m}\cdot\mathbf{u}^k\right) \left[\!\left[\boldsymbol{\tau}^k\right]\!\right] \colon S \; \det \mathbf{J}^{k_m} d\xi\right)_{ab} \approx \left(B_{DG}^k\right)_{ab}, \tag{3.177}$$

where the sum over m refers to the four edges of the parent element and $\mathbf{J}^{k_m}$ is the Jacobian of the edge mapping from edge m of element Ω_k to the parent edge. The entries of $\left(B_{DG}^k\right)_{ab}$ are given by

$$\left[\left(B_{DG}^k\right)_{ab}\right]_{ij}$$
$$= \sum_{(\xi_i,\eta_j)\in D_m^-} \left(\left(u_x^k\right)_{ij}\left(n_x^{k_m}\right)_{ij} + \left(u_y^{k_m}\right)_{ij}\left(n_y^{k_m}\right)_{ij}\right) \left[\!\left[\tau_{ab}^k\right]\!\right]_{ij} \det\left(\mathbf{J}^{k_m}\right)_{m_{ij}} w_{m_{ij}}, \tag{3.178}$$

$$\tag{3.179}$$

for planar co-ordinates and

$$\left[\left(B_{DG}^k\right)_{ab}\right]_{ij}$$
$$= \sum_{(\xi_i,\eta_j)\in D_m^-} \left(\left(u_z^k\right)_{ij}\left(n_z^{k_m}\right)_{ij} + \left(u_r^{k_m}\right)_{ij}\left(n_r^{k_m}\right)_{ij}\right) \left[\!\left[\tau_{ab}^k\right]\!\right]_{ij} \det\left(\mathbf{J}^{k_m}\right)_{m_{ij}} w_{m_{ij}} \tag{3.180}$$

for axisymmetric co-ordinates, with $0 \leq i,j \leq N$ for the planar and axisymmetric geometry, respectively, and where m_{ij} is the 1-D GLL edge point corresponding to the 2-D GLL grid point (ξ_i,η_j). Note that the value is zero unless the GLL node ij lies on an elemental inflow interface.

The DG contribution of each component of elastic stress, $\widehat{\boldsymbol{\tau}}_{ab}^k$ on each element Ω_k may then be calculated by solving the following linear system

$$M^k \widehat{\boldsymbol{\tau}}_{ab}^k = \widehat{E}^k \boldsymbol{\tau}_{ab}^k + \left(B_{DG}^k\right)_{ab}. \tag{3.181}$$

This system is trivial to solve for the choice of stress test function, with the matrix M^k being diagonal. The contribution of each component is then included on the appropriate right-hand side of the constitutive equation. When using the semi-iterative scheme, the DG contribution is updated at every iteration.

3.7 Elastic Viscous Split Stress (EVSS)-type Methods

When computing flows of fluids with viscoelastic properties, the constitutive equation used will typically change the elliptic problem encountered for Newtonian flows, into a set of PDEs of mixed elliptic-hyperbolic type [45]. It is important that the numerical methods used to solve the equations preserve the ellipticity of the saddle point problem formed by the momentum and continuity equations. When considering flows at medium to high Weissenberg numbers, the ellipticity of the equations reduces which can lead to numerical instabilities when computing a solution and ultimately lead to divergence of iterative techniques. The numerical instabilities have often been attributed to a solution which is under-diffused, and success has been found by introducing artificial diffusion to the momentum equation [7, 24].

One such technique to stabilise the calculations is the Elastic Viscous Split Stress(EVSS) method first introduced by Perera and Walters[46]. This technique was used for second-order fluids by Mendelson et al.[37] and with viscoelastic fluids by Beris et al.[3]. This is achieved via a change of variables involving the rate-of-strain tensor, which leads to a modification of the governing equations. Furthermore, Sun et al.[57] introduced an adaptive version of the scheme, termed AVSS, and the EVSS-G scheme of Brown et al.[8] used the velocity gradient instead of the rate-of-strain tensor as a stabilisation term. While these methods have proven to be successful in simulating flows at higher Weissenberg numbers the change of variables means that one cannot apply the technique to all constitutive equations. In addition, this technique requires second-order spatial derivatives of the velocity and time derivatives of the velocity gradients due to the need to take the upper-convected derivative of $\mathbf{D}$.

3.7.1 DEVSS Methods

DEVSS

The limitation to particular constitutive models for use with EVSS/AVSS led to Guénette and Fortin [21] to introduce the Discrete EVSS (DEVSS) method, which does not require a change of variables. Artificial diffusion is added to the momentum equation for stabilisation through an L^2-projection of the rate-of-strain tensor, which we shall denote by $\mathbf{D}$. We may rewrite the momentum and continuity equations (for some constitutive equation) as follows,

$$Re\frac{D\mathbf{u}}{Dt} - (\beta + \theta)\nabla^2\mathbf{u} + \theta\nabla\cdot\mathbf{D} + \nabla p = \nabla\cdot\boldsymbol{\tau}, \tag{3.182}$$

$$\nabla\cdot\mathbf{u} + \mu\int_\Omega p d\Omega = 0, \tag{3.183}$$

$$\mathbf{D} - \left(\nabla\mathbf{u} + (\nabla\mathbf{u})^T\right) = 0, \tag{3.184}$$

where θ is the DEVSS stabilisation parameter. At the continuous level, it is clear that (3.182)-(3.184) is equivalent to (2.17) because $\nabla\cdot\mathbf{D} = \nabla^2\mathbf{u}$ when combined with the knowledge that $\nabla\cdot\nabla\mathbf{u}^T = 0$ from the continuity equation. However, at the discrete level this is not the case, providing stabilisation to our numerical scheme. The stabilisation parameter, θ, is typically chosen to be equal to $(1-\beta)$ which fixes the multiplier of $\nabla^2\mathbf{u}$ to be 1. This increases the elliptic nature of the momentum equation for any viscosity ratio.

DEVSS-G

Similar in idea to the EVSS-G method of Brown et al. [8], Liu et al. [32] proposed an alternative option using an L^2-projection of the velocity gradient, which we denote by $\mathbf{G}$, rather than the rate-of-strain tensor. This method is known as DEVSS-G. There are two ways in which to include the stabilisation term into the momentum equation. The first, as used by Liu et al. [32] is to follow DEVSS and use $\mathbf{G}$ to form the rate-of-strain

tensor as follows

$$Re\frac{D\mathbf{u}}{Dt} - (\beta+\theta)\nabla^2\mathbf{u} + \theta\nabla\cdot\left(\mathbf{G}+\mathbf{G}^T\right) + \nabla p = \nabla\cdot\boldsymbol{\tau}, \tag{3.185}$$

$$\nabla\cdot\mathbf{u} + \mu\int_\Omega p d\Omega = 0, \tag{3.186}$$

$$\mathbf{G} - \nabla\mathbf{u} = 0. \tag{3.187}$$

Alternatively, we may stabilise the momentum equation using only the velocity gradient projection, as used in the method of Bogaerds et al. [6], so that the field equations become

$$Re\frac{D\mathbf{u}}{Dt} - (\beta+\theta)\nabla^2\mathbf{u} + \theta\nabla\cdot\mathbf{G} + \nabla p = \nabla\cdot\boldsymbol{\tau}, \tag{3.188}$$

$$\nabla\cdot\mathbf{u} + \mu\int_\Omega p d\Omega = 0, \tag{3.189}$$

$$\mathbf{G} - \nabla\mathbf{u} = 0. \tag{3.190}$$

This method complements our enforcement of $\nabla\cdot\nabla\mathbf{u}^T = 0$ in the momentum equation and we proceed with equations (3.188)-(3.190) as the basis of the stabilisation scheme for our numerical method. The differences between these two formulations of DEVSS-G are more clearly seen when written in their corresponding weak forms.

Should we wish to control the coefficient of the elliptic operator directly, we introduce an additional parameter

$$\beta_s = \beta + \theta, \tag{3.191}$$

so that (3.188) becomes

$$Re\frac{D\mathbf{u}}{Dt} - \beta_s\nabla^2\mathbf{u} + (\beta_s-\beta)\nabla\cdot\mathbf{G} + \nabla p = \nabla\cdot\boldsymbol{\tau}. \tag{3.192}$$

3.7.2 Discretisation of DEVSS-G Terms

Similarly to the elastic stress, we use a spectral representation of the velocity gradient $\mathbf{G}$ within a spectral element. However, contrary to the elastic stress we represent $\mathbf{G}$ on the internal nodes of an element in the same way as we treat the pressure. Using only the internal nodes means that we solve for $\mathbf{G}$ in each element independently and so do not need to construct the global matrix to solve for $\mathbf{G}$, reducing the computational

effort required. This treatment also means that $\mathbf{G}$ is discontinuous across elements. While improving the computational efficiency this has also been found [2] to improve stability and accuracy when used in other numerical schemes.

Therefore, the spectral representation of $\mathbf{G}$ is given by

$$\mathbf{G}^e_{ab}(\xi,\eta) = \sum_{i=0}^{N}\sum_{j=0}^{N} \left(G^e_{ij}\right)_{ab} \widetilde{h}_i\left(\xi\right)\widetilde{h}_j\left(\eta\right), \tag{3.193}$$

where ab denotes the component of the tensor and $\left(G^e_{ij}\right)_{ab} = G^e_{ab}\left(\xi_i,\eta_j\right)$.

Multiplying (3.190) by an appropriate test function, $\boldsymbol{\phi} \in \left[L^2\left(\Omega\right)\right]^4$ (or $\boldsymbol{\phi} \in \left[L^2\left(\Omega\right)\right]^5$ for axisymmetric geometries), integrating over the whole domain and applying the domain decomposition in (3.44) we get,

$$\left(\sum_{e=1}^{K}\int_{\Omega_e} \mathbf{G} : \boldsymbol{\phi}\, d\Omega\right)_{ab} = \left(\sum_{e=1}^{K}\int_{\Omega_e} \left(\nabla\mathbf{u}\right) : \boldsymbol{\phi}\, d\Omega\right)_{ab}. \tag{3.194}$$

Mapping into the parent domain, applying the spectral representation of $\mathbf{G}$ and using the GL quadrature in (3.84) yields a linear system which may be expressed locally in each component, ab,

$$\widetilde{M}^e\mathbf{G}^e_{ab} = \widehat{\mathbf{d}}^e_{ab} \tag{3.195}$$

where $\widehat{\mathbf{d}}_{ab}$ is the local vector containing the ab component of the velocity gradient at each GLL point. These velocity gradient components may be calculated using (3.78) and (3.79). The entries of $\widetilde{M}$ are those of the pressure mass matrix. By solving this linear system we obtain the local values of $\mathbf{G}$ at each internal GLL node. We then use (3.193) to extrapolate the values on the boundary of each element.

Once calculated, these values are incorporated in the current discretisation of the momentum equation by adding the following approximation of the integral of $\nabla\cdot\mathbf{G}$ to the known RHS terms given in (3.129) and (3.130),

$$\widehat{\mathbf{f}}^{n+1}_x = \widehat{\mathbf{f}}^{n+1}_x + \sum_{q=0}^{J-1}\beta_q\left(E_x\mathbf{G}^{n-q}_{xx} + E_y\mathbf{G}^{n-q}_{xy}\right), \tag{3.196}$$

$$\widehat{\mathbf{f}}^{n+1}_y = \widehat{\mathbf{f}}^{n+1}_y + \sum_{q=0}^{J-1}\beta_q\left(E_x\mathbf{G}^{n-q}_{xy} + E_y\mathbf{G}^{n-q}_{ty}\right), \tag{3.197}$$

respectively for the Cartesian case.

For the axisymmetric case, we add the following approximation to the RHS terms given in (3.133) and (3.134),

$$\widehat{\mathbf{f}}_r^{n+1} = \widehat{\mathbf{f}}_r^{n+1} + \sum_{q=0}^{J-1} \beta_q \left(E_r \mathbf{G}_{rr}^{n-q} + E_z \mathbf{G}_{rz}^{n-q} + E_\theta \mathbf{G}_{\theta\theta}^{n-q} \right), \tag{3.198}$$

$$\widehat{\mathbf{f}}_z^{n+1} = \widehat{\mathbf{f}}_z^{n+1} + \sum_{q=0}^{J-1} \beta_q \left(E_r \mathbf{G}_{rz}^{n-q} + E_z \mathbf{G}_{zz}^{n-q} \right). \tag{3.199}$$

3.8 Solution of the Linear System

The solution of the linear system arising from the temporal and spatial discretisation of the conservation of momentum and mass equations is performed using a direct method. We use the PARDISO* [53] solver, part of the Intel MKL library of mathematical functions. This is a shared-memory (OpenMP) parallel sparse solver, which we use to solve the global velocity-pressure system. In our case we are able to use the symmetric, indefinite, version of the solver. The solution is broken down into three parts. First, an analysis and re-ordering of the matrix. Second, a factorisation step, constructing an LDL^T factorisation using pivoting. Finally, the solution is found by forward and backward substution. The solver also provides iterative refinement of the solution at the final stage.

The construction of the global system is an expensive operation and we wish to avoid this in the case of a deforming mesh. Instead we set up a local element to global sparse matrix map, avoiding the need to build the global matrix at all. This map is created at a preprocessing stage and is expensive, but only needs to be performed once. This is done by scanning across each row of the global matrix via the local to global map. We then store the location of non-zero entries in each local element matrix associated with that global node. The number of non-zeroes encountered is stored, and the location within each local element matrix is then mapped to that part of the sparse storage vector.

Once this map has been constructed, the vector of values for the sparse storage may be constructed by a local element-wise operation. This also means that any nodes

not associated with deforming elements need not be updated. After the sparse matrix vector has been updated, a new factorisation may be computed for the next solving of the linear system. If there is no mesh deformation, such as when we consider flow past a fixed sphere, then the factorisation need only be computed once throughout a whole simulation. This reduces the number of operations per timestep quite considerably.

3.9 Domains and Spectral Meshes

The application of the numerical scheme will require two main sets of meshes. We define these below.

3.9.1 Infinite Channel and Cylindrical Pipe

The first set, labelled T1-T4, are used in Poiseuille flow simulations, consisting of a straight channel of length L and height H. These meshes, with a typical GLL-mesh within each spectral element, are shown in Figure 3.3. Depending on the co-ordinate system (2-D planar or 3-D axisymmetric), the bottom of the domain may be a wall boundary or a wall of symmetry. Each mesh has points A, B and C marked on the penultimate node in the positive x- or z-direction at the top, middle and bottom of the channel. These points will serve as test points when comparing numerical with analytical solutions. These meshes will be primarily used to investigate the start-up of Poiseuille flow for Newtonian and Oldroyd B. fluid models in Sections 5.1.1- 5.1.2 and 6.1.1-6.1.2.

3.9.2 Fixed Cylinder and Sphere

The second set, labelled M1-M5, are used for the benchmarks of 2-D planar flow past a fixed cylinder in an infinite channel and 3-D axisymmetric uniform flow past a fixed sphere in a cylinder. In the context of the planar benchmark, we consider a cylinder of radius R_C in a channel of height H_C giving a so-called blockage ratio defined as

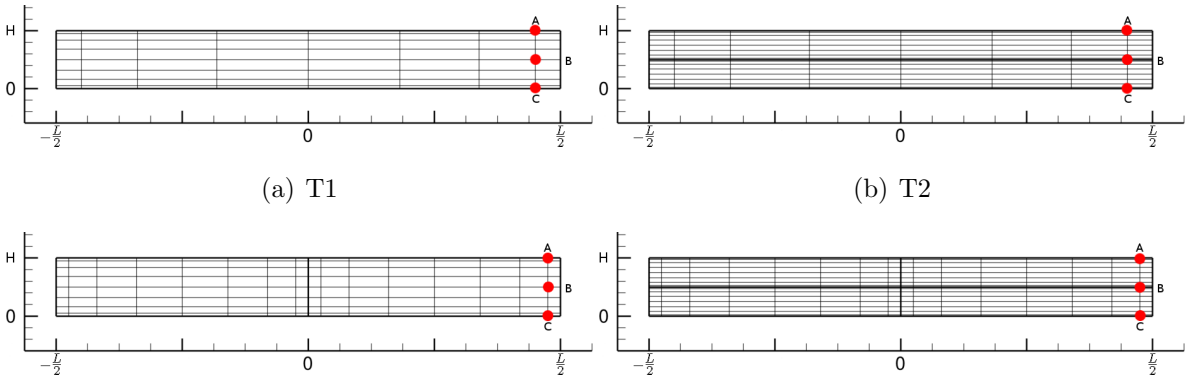

(a) T1 (b) T2

(c) T3 (d) T4

Figure 3.3: Meshes T1-T4. Test points marked with a red dot at A, B and C. Each spectral element contains the local GLL-mesh with $N = 8$.

R_C/H_C. In the context of the axisymmetric benchmark we consider a sphere of radius R_S in a cylinder of radius R_C giving a blockage ratio defined as R_S/R_C.

Each mesh, with a typical GLL-mesh within each element is shown in Figure 3.4. We focus on refinement around the surface of the cylinder/sphere as in the benchmark flows we are investigating we expect large boundary layers to form in these areas. We a refine from the very coarse M1, up to 3 progressively tighter layers around the cylinder/sphere in M4. Each mesh consists of a central section running from -4 to 4 in the horizontal direction, with additional elements added to either end in order to create a domain of the desired length. In the majority of calculations, and unless otherwise stated, we set the length to be 40 (note that the circle in the mesh of radius 1), extending the meshes to -20 and 20 in the horizontal direction.

To get from M1 to M2 we add a layer of elements at a radius of 1.25 from the centre of the circle. While the mesh appears overly thin where it nears the surface of the circle, we found that this made little difference in practice. Mesh M3 divides each element, radially from the circle, in half to produce 20 elements. Finally, for M4 we move the layer of elements out to a radius of 1.5 and add an additional layer at a radius of 1.125 to giving a total of 26 elements.

Boundary layers in the wake of the cylinder/sphere have been also been observed for viscoelastic flows so we also consider refinement in the wake, by adding an additional layer of elements with the first elemental inclined at a 15° angle from the centre of the

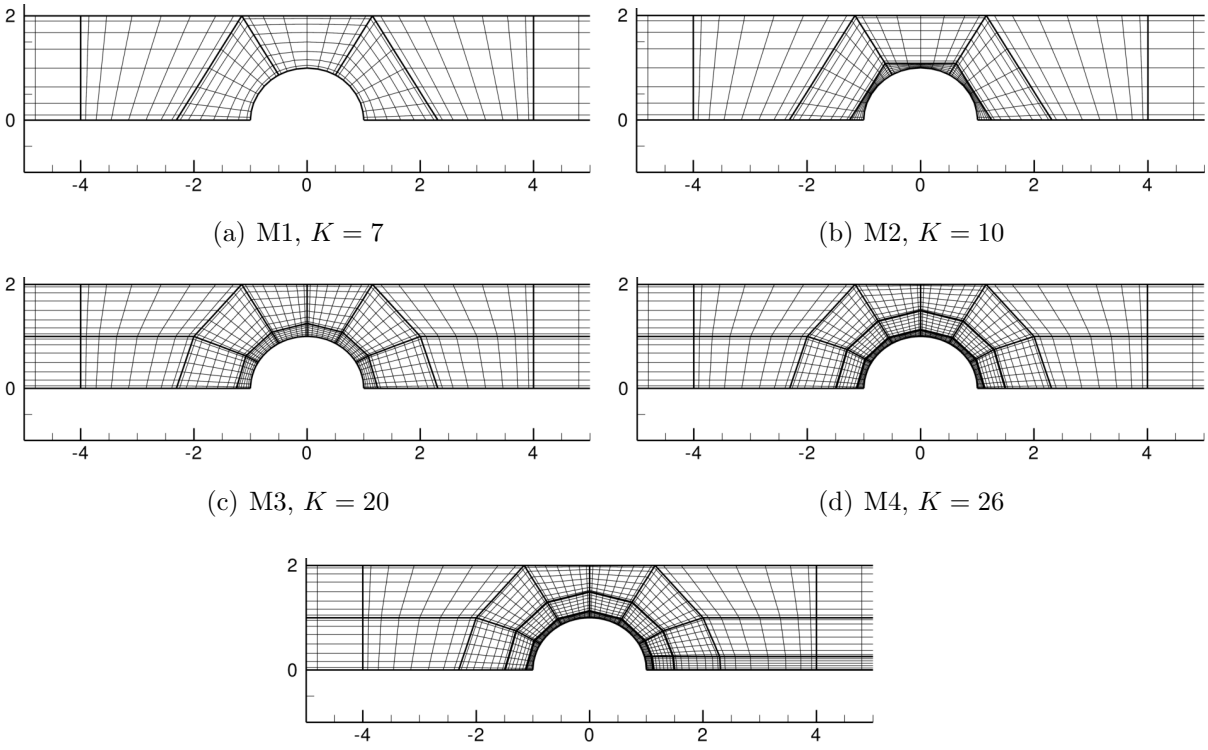

(a) M1, $K = 7$

(b) M2, $K = 10$

(c) M3, $K = 20$

(d) M4, $K = 26$

(e) M5, $K = 31$

Figure 3.4: Meshes M1-M5. Each spectral element contains the local GLL-mesh with $N = 8$.

cylinder/sphere in the downstream direction and with the remaining elements added parallel to the downstream direction until we reach the end of the domain, giving us mesh M5 with 31 elements.

Chapter 4

Stokes Flow

A very important aspect of implementing a numerical scheme is benchmarking and validation of the results it produces. We begin with the basis of our numerical solver, the steady-state Stokes problem ($Re = 0$, $We = 0$, $\beta = 1$). We validate using analytical solutions. In Section 4.1 using a velocity solution which satisfies the continuity equation along with a body force in the momentom equation which accounts for the chosen velocity and pressure solutions. In Section 4.2 we use a model solution for that of flow past a cylinder. In Sections 4.3 and 4.4 we calculate solutions to some benchmark problems which we compare with results in the literature, specifically that of flow past a cylinder in an infinite channel and uniform flow past a sphere, which are both highly relevant in the context of this thesis.

In all cases the importance of convergence with increasing order of approximation must be observed. In the case of our spectral element method, this means we must look for convergence in both mesh refinement, increasing K, and in polynomial order, increasing N.

When considering errors, we typically present these in either the H^1-norm or L^2-norm which involve integration over the domain. This integration is performed using Gauss-Lobatto quadrature as given in (3.84) on the same GLL grid as is used for the SEM itself.

4.1 Model Solution

To validate that our method converges for both increasing N and K, we seek an analytical solution which is not trivial in the sense that it is not a polynomial. If we choose functions for both the velocity and pressure fields along with the appropriate body force term, then we may find a more complex solution which should not be so easy to approximate using polynomials. We consider a solution to the Stokes problem in 2-D cartesian co-ordinates

$$\begin{aligned} u(x,y) &= \sin(\pi x)\cos(\pi y), \\ v(x,y) &= -\cos(\pi x)\sin(\pi y), \\ p(x,y) &= \sin(\pi x)\sin(\pi y). \end{aligned} \tag{4.1}$$

The resulting body force, $\mathbf{f} = (f_x, f_y)$, is given by

$$\begin{aligned} f_x(x,y) &= 2\pi^2 \sin(\pi x)\cos(\pi y) + \pi\cos(\pi x)\sin(\pi y), \\ f_y(x,y) &= -2\pi^2 \cos(\pi x)\sin(\pi y) + \pi\sin(\pi x)\cos(\pi y). \end{aligned} \tag{4.2}$$

The use of trigonometric functions is suitable as we expect a more accurate approximation with increasing polynomial order, N, as they may be expressed as an infinite sum of polynomials of increasing order.

4.1.1 Domain and Elemental Meshes

We approximate the solution to (4.1) on the parent domain $\Omega = [-1,1] \times [-1,1]$. We may exactly mesh this domain using a single spectral element. However we are interested in the convergence with increasing numbers of elements as well as with polynomial order so we make use of 5 meshes.

We begin with a single parent-sized element, and for each refinement we double the number of elements, keeping them equally-sized. The result is 4 meshes with $K = 1, 2, 4, 16$. For each of these meshes, the edges are all aligned with the co-ordinate system which means that many of the geometric factors arising from the transformation to the parent element used for SEM are zero.

To test the robustness of the solver in preparation for using non-rectangular elements, we also use a non-uniform mesh with $K = 16$ by slightly perturbing the vertex nodes of each element which are internal to the global domain. This mesh is referred to as the "non-uniform mesh" in our figures.

4.1.2 Results

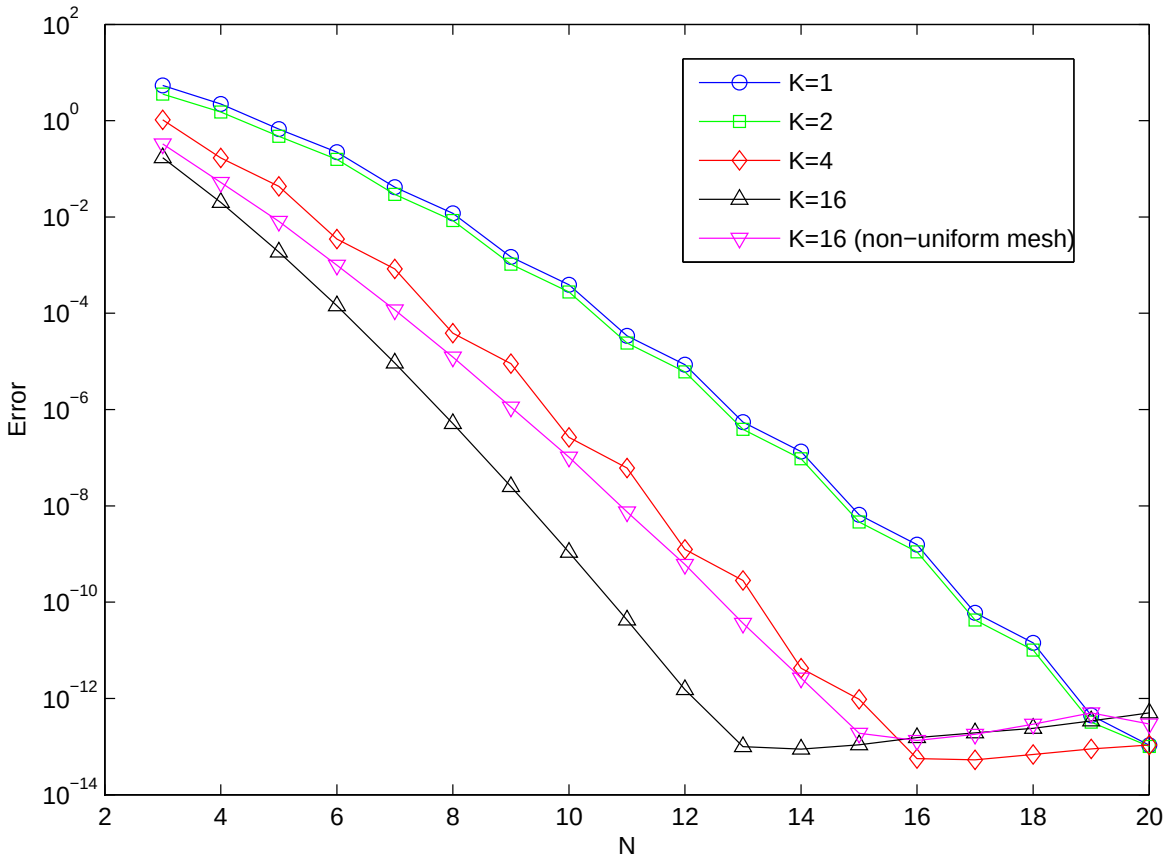

Figure 4.1: Dependence of the H^1-norm of the velocity error on N and K, for the model problem given in (4.1).

For the following results, the alternative formulation of the Stokes problem was used with $\mu = 1$.

Figures 4.1 and 4.2 show the convergence with polynomial order, N, of the log of velocity error in the H^1-norm and log of pressure error in the L^2-norm. The zig-zag pattern seen in these figures is due to the nature of the solution we are approximating. Since the trigonometric functions may be represented as sums of either odd or even polynomials it is expected that the approximation using odd or even polynomial bases will have different rates of convergence. This effect is lessened as more elements are used.

The small rise after seemingly reaching the bottom of the graph is due to the limit of machine accuracy on the computer used to compute the results. After this point, the error will always be around this order of magnitude, but due to an increased number of points within the Gauss-Lobatto quadrature for the calculation of the norm, we see a slight rise.

Spectral convergence up to machine accuracy is achieved with increasing N for each of the meshes and elemental mesh refinement results in convergence to machine accuracy at lower polynomial order, N. These results confirm that the method and solver are working as expected and that we may place confidence in the approximations it produces.

It is also worth noting that the non-uniform mesh performs far worse than the equivalent mesh which is aligned with the co-ordinate axes and in fact performs at a similar level to the uniform 4-element mesh. Convergence to machine accuracy is still reached, but not at the same rate at the aligned meshes. This is something to bear in mind when working with more complicated domains where it may not be possible to use rectangular elements.

Figure 4.3 shows the log of CPU time taken for each computation shown in the previous two figures. The function called to calculate this time only gives a time to 2 decimal places, so the lower values of N should be expected to be fairly inexact. As is intuitively obvious, more elements at equal polynomial order takes more time - roughly an order of magnitude more when doubling the number of elements. The effect of increasing the polynomial order has a more dramatic affect, although this is offset by the improvement in accuracy with increasing N.

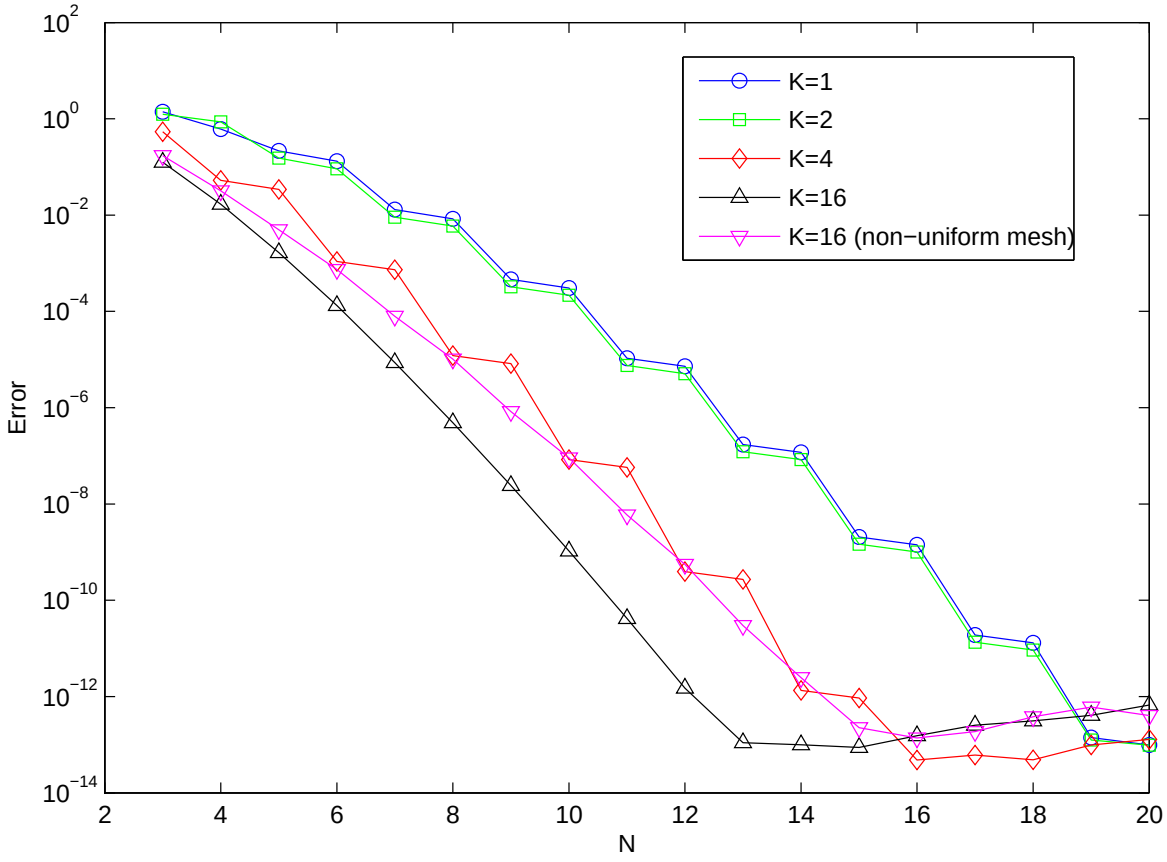

Figure 4.2: Dependence of the L^2-norm of pressure error on N and K, for the model problem given in (4.1).

4.2 Model flow past a Cylinder

To validate the accurate handling of the circular edge which will feature in our simulations involving sphere and cylinders we consider a 2-D validation problem for Stokes flow past a cylinder. We consider a problem with analytical solutions given, in polar co-ordinates by [61]:

$$\begin{aligned} u(x,y) &= \left(\frac{R_C^2}{r^2} - 1\right)\left(\frac{1}{2}\cos 2\theta\right) + \ln\left(\frac{r}{R_C}\right), \\ v(x,y) &= \left(\frac{R_C^2}{r^2} - 1\right)\cos\theta\sin\theta, \\ p(x,y) &= -\frac{2\cos\theta}{r}. \end{aligned} \tag{4.3}$$

In order to implement this solution into our 2-D code we convert from Cartesian co-ordinates where appropriate, such as when computing values for boundary conditions.

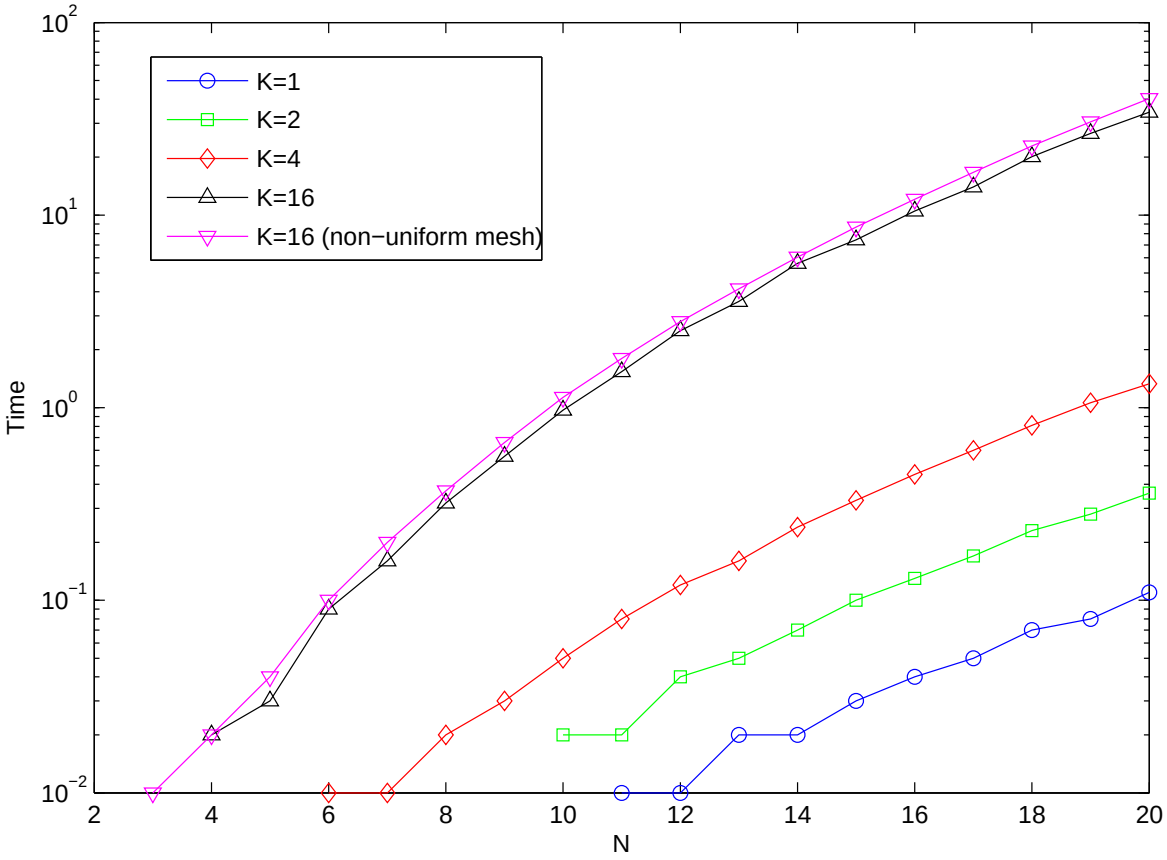

Figure 4.3: Dependence of the CPU time taken on N and K, for the model problem given in (4.1).

4.2.1 Domain and Mesh

The domain is a channel of length 8 radii and of height $H_C = 2$ radii, with a cylinder of radius $R_C = 1$ centred in the middle of the channel at $(0, 0)$. We apply the known solution on the entire boundary. There is no body force term, i.e. $\mathbf{f} = 0$.

We have 4 levels of mesh refinement for this domain. We make use of the central sections of meshes M1, M2, M3 and M4 seen in Figures 3.4(a)-3.4(d) but discard the elements which extend the length of the domain. This gives us meshes with $K = 5, 8, 10, 16$.

4.2.2 Results

Figures 4.4 and 4.5 show the convergence of velocity error in the H^1-norm and pressure error in the L^2-norm, respectively. We observe excellent agreement with the known solution as well as spectral convergence to machine precision with increasing N. We also observe higher accuracy due to elemental mesh refinement with increasing K.

However, we note that the limit of machine precision for this problem is roughly an order of magnitude higher than that of the uniform meshes in Section 4.1. We may put this down to the fact that we have non-rectangular elements making up each of our meshes in this case, due to the nature of the geometry. As such we should not expect to reach such levels of accuracy as that of our model problem on the rectangular domain due to the introduction of geometric factors in the transfinite element mapping. These are likely to degrade the accuracy of the quadrature rules employed in the discretisation of the bilinear forms.

Figure 4.6 shows the log of CPU time taken for increasing N and gives a very similar picture to that of Figure 4.3 in Section 4.1, and confirms that there is little computational impact in using the circular-edged elements over straight-edged elements.

Combined with the results found in Section 4.1, we can be confident that the Stokes solver is performing as expected and that the circular elements of our domain are being treated appropriately.

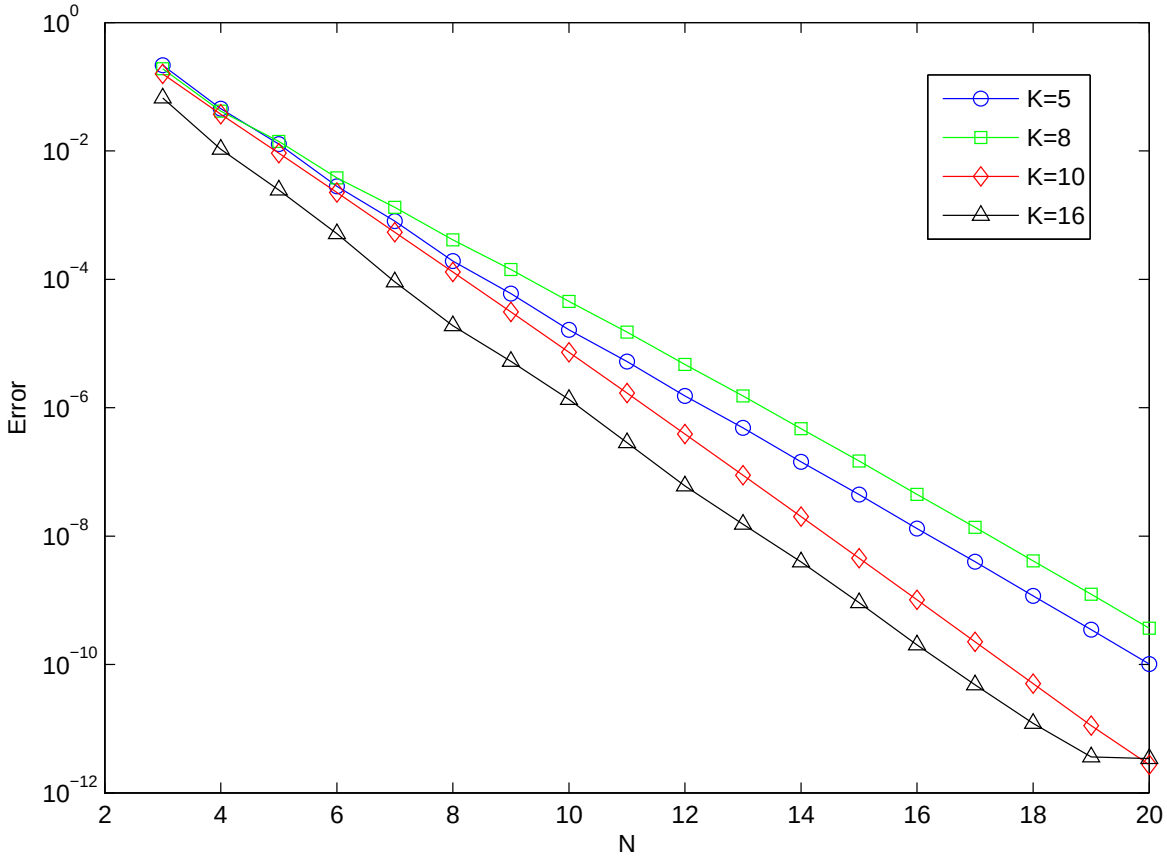

Figure 4.4: Dependence of the H^1-norm of velocity error on N and K for the model cylinder problem given in (4.3).

4.3 Flow past a Fixed Cylinder in a Channel

After confirming that our Stokes solver is working using analytical solutions, we move onto benchmarking. We begin with the benchmark of flow past a fixed cylinder in an infinite channel. Due to symmetry, this may be posed as a 2-D problem and so is appropriate for our 2-D solver.

In this benchmark, planar Poiseuille flow is applied at inflow and outflow, both of which are an appropriate distance from the cylinder. The velocity profile is given by

$$\begin{aligned} u_x &= \frac{3}{2} U_{av} \left(1 - \frac{4}{H_C^2} y^2 \right), \\ u_y &= 0, \end{aligned} \tag{4.4}$$

where U_{av} is the average velocity and H_C is the height of the channel. It is typical to

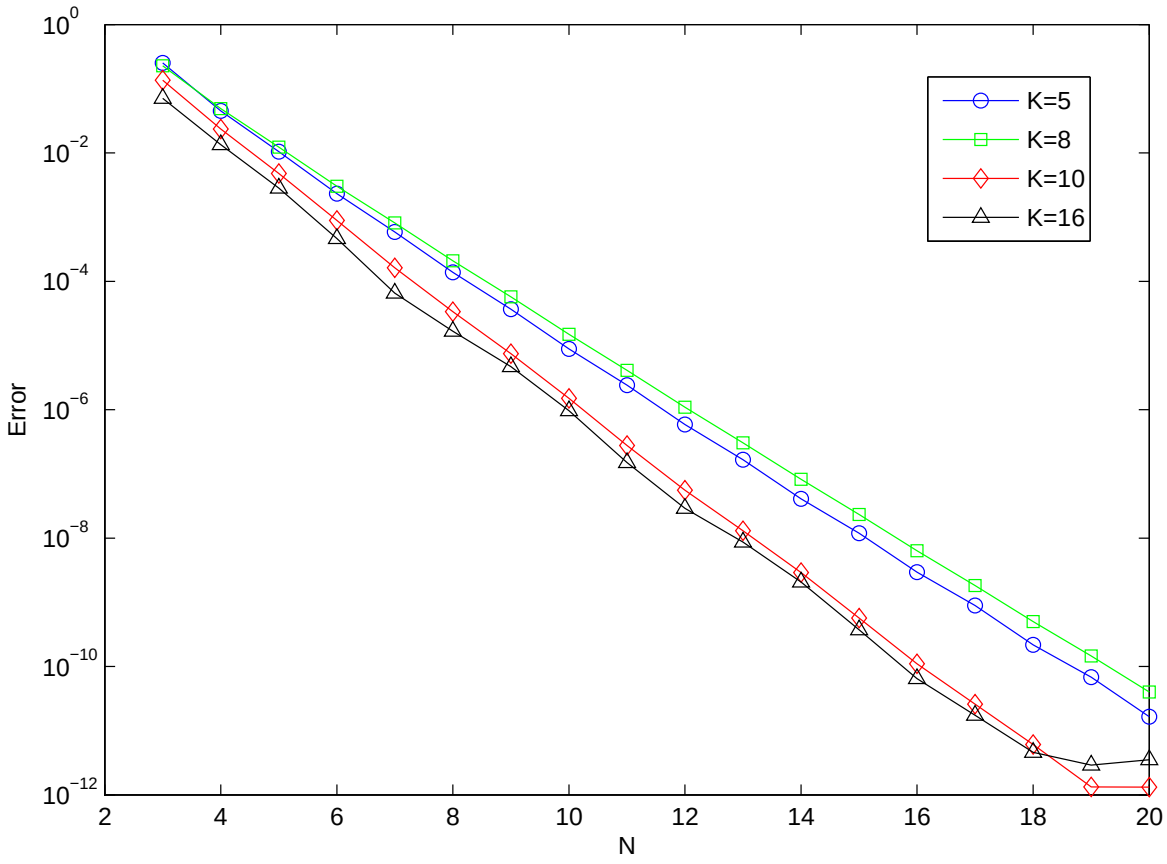

Figure 4.5: Dependence of the L^2-norm of pressure error on N and K for the model cylinder problem given in (4.3).

choose $U_{av} = 1$ for this benchmark. No-slip and no penetration conditions are applied at the top wall and on the surface of the cylinder and symmetry boundary conditions are applied along the axis of symmetry.

4.3.1 Domain and Mesh

The domain for this benchmark is a channel of length 40 radii and height $H_C = 4$ radii with the cylinder of radius $R_C = 1$ centred in the middle at $(0, 0)$, inflow at $x = -20R_C$ and outflow at $x = 20R_C$. This means that our inflow and outflow velocity profile is $u_x = \frac{3}{8}(4 - y^2)$.

We use meshes M1-M4, similarly to Section 4.2, but instead use the full length versions

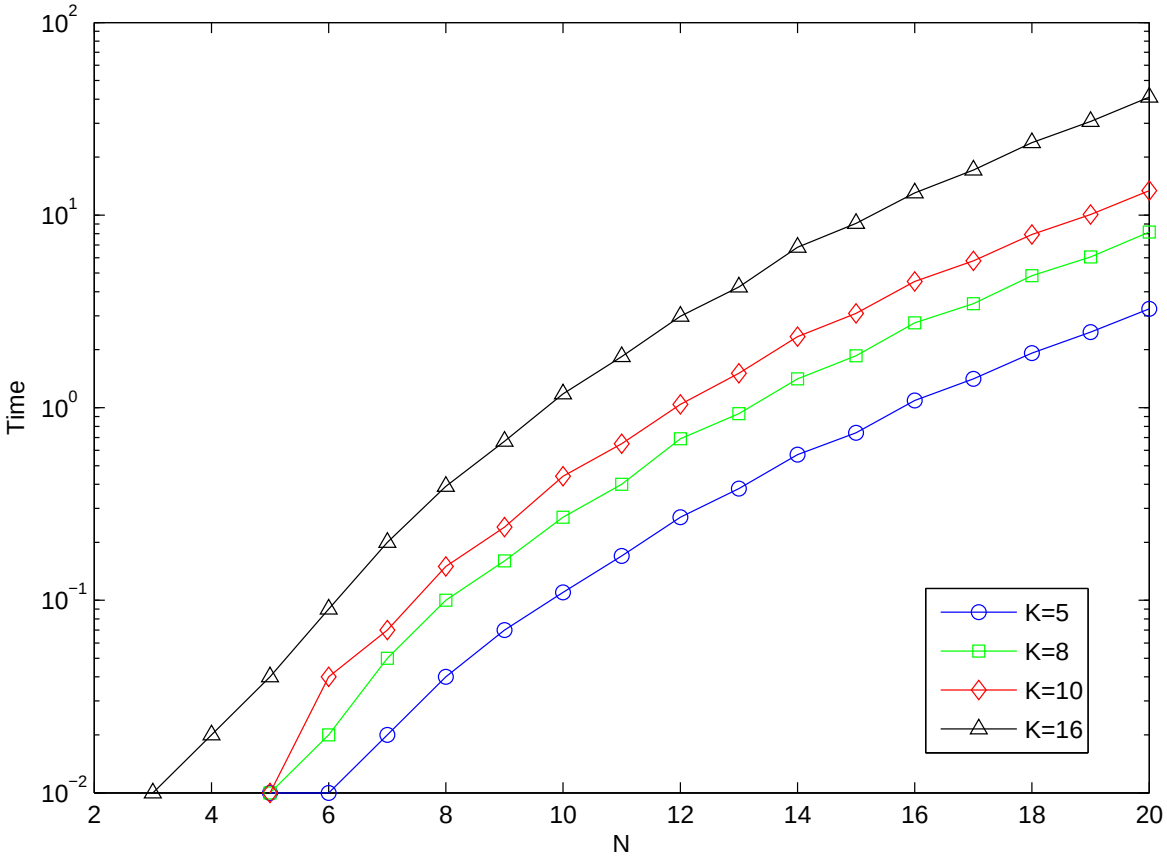

Figure 4.6: Dependence of the CPU time taken on N and K, for the model cylinder problem given in (4.3).

as seen in Figure 3.4(a)- 3.4(d) in Section 3.9.2. So our 4 meshes have $K = 7, 10, 20, 26$ with refinement concentrated around the areas where large velocity gradients are to be expected close to the surface of the cylinder. We do not expect high gradients outside of this area, so refinement in the regions away from the cylinder is kept to a minimum.

4.3.2 Results

We begin by looking at the convergence of the calculated drag with increasing N. Table 4.1 shows drag values for each value of K up to the value of N for which drag convergence had been reached for that mesh to 4 decimal places. We do indeed reach convergence for the drag in all cases and we see that elemental mesh refinement does result in convergence to that value at lower polynomial order. The converged value for

N on M1	Drag	N on M2	Drag	N on M3	Drag	N on M4	Drag
3	132.4059	3	129.2897	3	131.4683	3	131.5703
4	132.3801	4	131.3939	4	132.3226	4	132.3053
5	132.6531	5	132.3265	5	132.3538	5	132.3522
6	132.445	6	132.3509	6	132.3574	6	132.3573
7	132.381	7	132.3578	7	132.3575	7	132.3575
8	132.3636	8	132.3575	8	132.3575	8	132.3575
9	132.3592	9	132.3575	-	-	-	-
10	132.3579	-	-	-	-	-	-
11	132.3576	-	-	-	-	-	-
12	132.3575	-	-	-	-	-	-
13	132.3575	-	-	-	-	-	-

Table 4.1: Dependence of the drag on N and K for Stokes flow past a fixed cylinder in a channel. Results shown for increasing N up to the point the drag had converged to 4 decimal places.

each mesh is 132.3575 which compares favourably to the literature such as that found by Vargas et al. [60] who state a value of 132.3507 and Hulsen et al [25] who state a value of 132.3584.

Further, we also find that there is very little mesh dependence on the value to which each set of results is converging. To demonstrate this more thoroughly, Figure 4.7 shows the apparent error of the calculated drag for each value of K and N when compared to the most refined result we could reach which was $K = 26$, $N = 19$ at which point the PARDISO linear solver experienced memory allocation problems. We achieve convergence up to what seems to be the limit of machine precision (around 10^{-10}) for $K = 10, 20, 26$ by a value of $N = 14$, whereas the coarser mesh, $M1$ is nearing that point by $N = 20$. The limit of precision being slightly higher than seen previously can be explained by the use of non-rectangular shaped elements meaning that the majority of the local SEM matrices are fuller than their rectangular counterparts. However, this level of accuracy is more than acceptable.

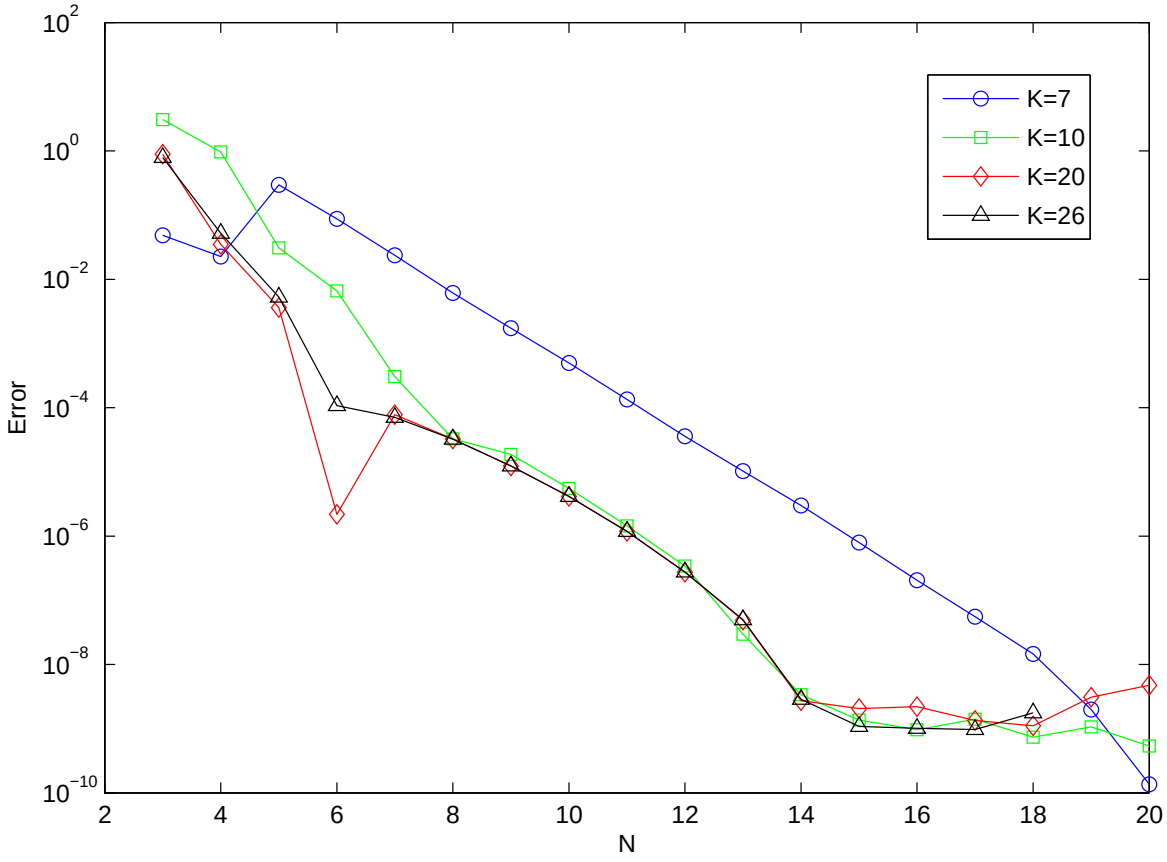

Figure 4.7: Dependence of the error in the drag calculated on N and K when compared to the converged value (result from $K = 26$, $N = 19$) for Stokes flow past a fixed cylinder.

In the context of the drag calculation, it is clear that there is very little difference between the three finest meshes used here. $K = 10$ appears to be adequate in resolving the solution and refinement with polynomial order is more important in reaching a converged solution, while $K = 7$ has a more consistent but slower rate of convergence towards machine precision. This was not observed in the convergence of the error norms for the model problems, which suggests that drag approximation may not be a definitive measure of overall convergence.

Finally, the CPU times for each calculation are given in Figure 4.8 and show that performance is largely on par with the results seen in Sections 4.1 and 4.2, as is to be expected.

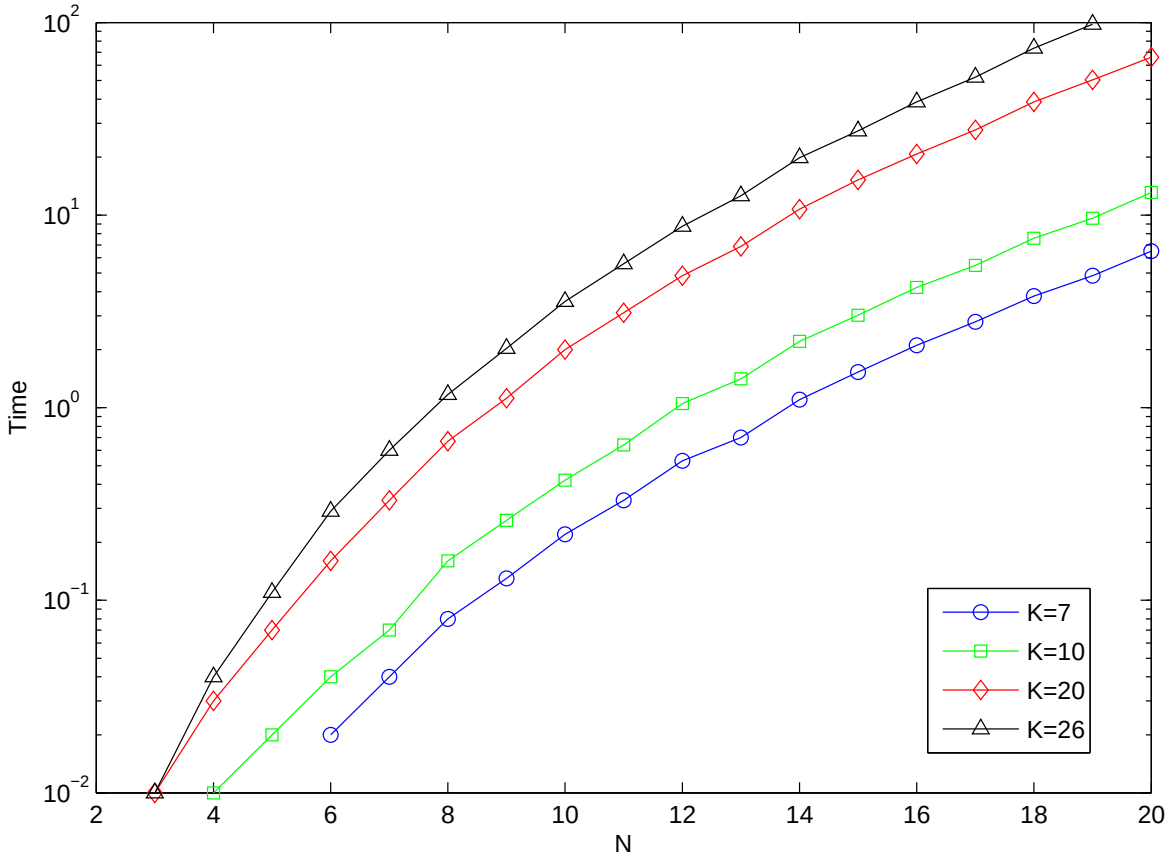

Figure 4.8: Dependence of the CPU time taken on N and K for Stokes flow past a fixed cylinder in a channel.

4.4 Flow past a Fixed Sphere

To validate within an axisymmetric 3-D domain we consider the benchmark problem of a fixed sphere in uniform flow. We use the axisymmetric geometry of a sphere on the central axis of a cylinder as given in Section 3.9. The quantity of interest, as with the fixed cylinder in a channel benchmark, is the drag force experienced by the sphere. It is generally accepted that the Drag Correction Factor, D^*, is used to normalise results for this benchmark. This is the ratio of the drag in the current flow against that which would be experienced by the same sphere in an unbounded expanse of Newtonian fluid

of the same viscosity

$$D^* = \frac{D}{6\pi\eta_0 R_S V_S}. \tag{4.5}$$

where R_S is the sphere radius and V_S is the sphere velocity, with the drag, D, calculated using (2.53)

4.4.1 Domain and Mesh

The domain for this benchmark is the axisymmetric analogue of that used in Section 4.3, with the pipe of length 20 radii and height 2 radii with the sphere of radius $R_S = 1$ centred at $(0, 0)$. As before, inflow is at $z = -20R_S$ and outflow is at $z = 20R_S$. Uniform flow in the axial direction is imposed on both of these boundaries. Axisymmetric boundary conditions are imposed along the axis of symmetry and wall boundary conditions are imposed on the surface of the sphere. Finally, moving wall boundary conditions are applied along the top wall matching the inflow and outflow velocity where a velocity $V_S = 1$ is used.

We use the same set of meshes, in cylindrical co-ordinates, as those for the cylinder benchmark as high gradients for this flow may be expected in similar areas.

4.4.2 Results

As with to the cylinder benchmark problem we are interested in the convergence of drag with mesh and polynomial refinement. Table 4.2 shows the convergence of the drag factor, D^*, with increasing N up to the point where the drag has converged to 4 decimal places for that mesh. We see convergence with lower polynomial order as the elemental mesh is refined and no evidence of mesh dependence for the Drag Factor, with convergence to the value 5.9474 for each mesh. This value agrees well with those found in the literature which are assembled in Table 4.3.

Figure 4.9 shows the apparent error when compared to the most refined results we were able to compute, again reaching memory limits with the PARDISO linear solver at $K = 26$, $N = 19$ - this comes as no surprise given that we have the same number

N on M1	D^*	N on M2	D^*	N on M3	D^*	N on M4	D^*
3	5.8037	3	5.8564	3	5.9173	3	5.9183
4	5.9353	4	5.8978	4	5.9475	4	5.9459
5	5.9695	5	5.9464	5	5.9473	5	5.9471
6	5.9567	6	5.947	6	5.9474	6	5.9474
7	5.9506	7	5.9474	7	5.9474	7	5.9474
8	5.9484	8	5.9474	-	-	-	-
9	5.9477	-	-	-	-	-	-
10	5.9475	-	-	-	-	-	-
11	5.9474	-	-	-	-	-	-
12	5.9474	-	-	-	-	-	-

Table 4.2: Dependence of the drag factor on N and K for uniform Stokes flow past a fixed sphere in a cylinder. Results shown for increasing N up to the point the drag had converged to 4 decimal places.

Authors	D^*
Present Work	5.9474
Vargas et al. (2009) [60]	5.9474
Owens and Phillips (1996) [44]	5.9474
Lunsmann et al. (2003) [33]	5.9472

Table 4.3: Comparison of computed drag factor for uniform Stokes flow past a fixed sphere in a cylinder with those found in the literature.

of degrees of freedom as in the cylinder benchmark. We find that there is, again, convergence to what appears to be machine precision of around 10^{-10} with the refined elemental meshes performing slightly better in terms of increasing polynomial order.

When considering the drag, there appears to be little difference between the $K = 20$ and $K = 26$ meshes and we may conclude that this level of elemental mesh refinement is unncessary for the solution of the Stokes problem in this geometry. The nature of the velocity gradients within this benchmark appear to not require such intense refinement around the surface of the sphere. We note that there is a gain in using the 20 element mesh over the 10 element mesh, which was not required for the cylinder benchmark problem.

Finally, the CPU times taken for each calculation are shown in Figure 4.10 and again performance is comparable to the previous simulations, although there is a slight penalty in the axisymmetric cylindrical co-ordinate system.

4.5 Summary

The main part of our computational solver has been validated thoroughly through both analytical solution and benchmarking in both the 2-D Cartesian co-ordinate system and 3-D axisymmetric cylinderical polar co-ordinate system. The use of circular edges for our spectral elements has been verified. Convergence with both mesh refinement and polynomial refinement has been observed in all cases. With all of this in mind, we may be reasonably confident in the accuracy, robustness and stability of the Stokes solver at this stage.

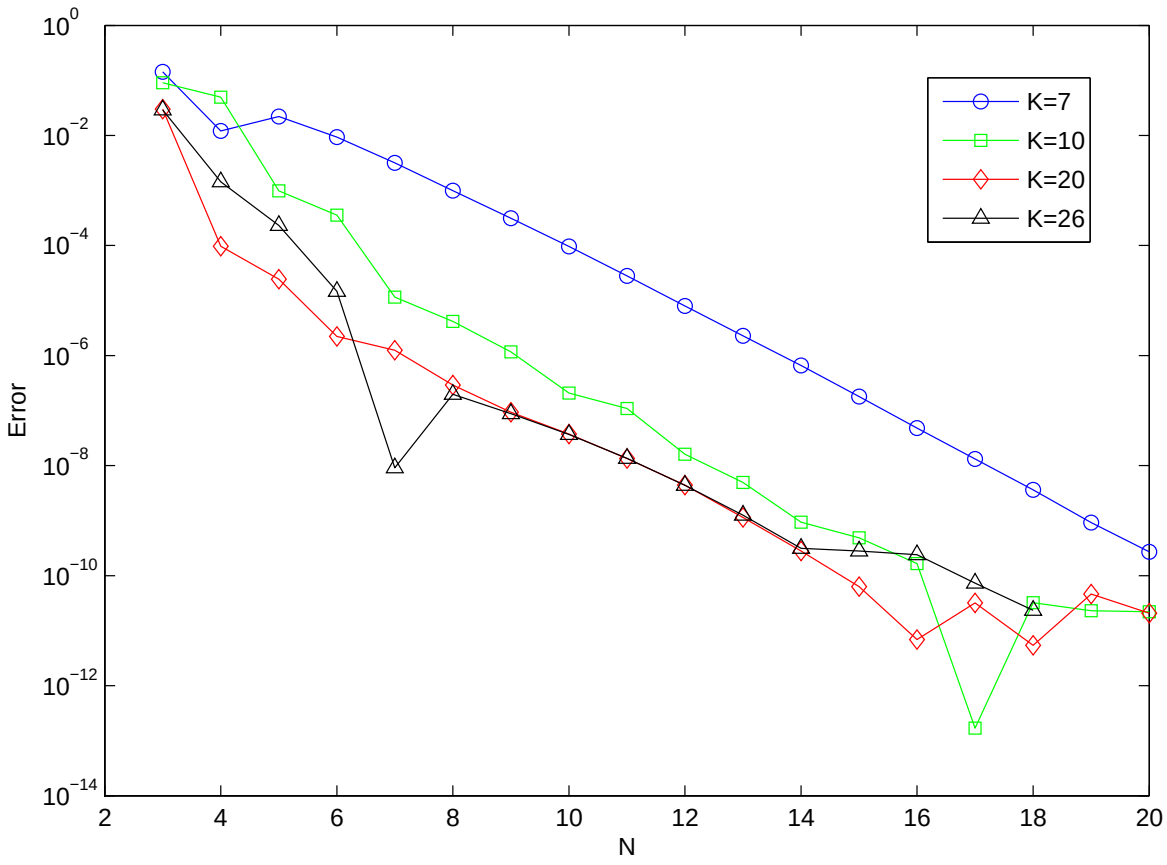

Figure 4.9: Dependence of the drag factor error on N and K when compared to the converged value (result from $K = 26$, $N = 19$) for uniform Stokes flow past a fixed sphere.

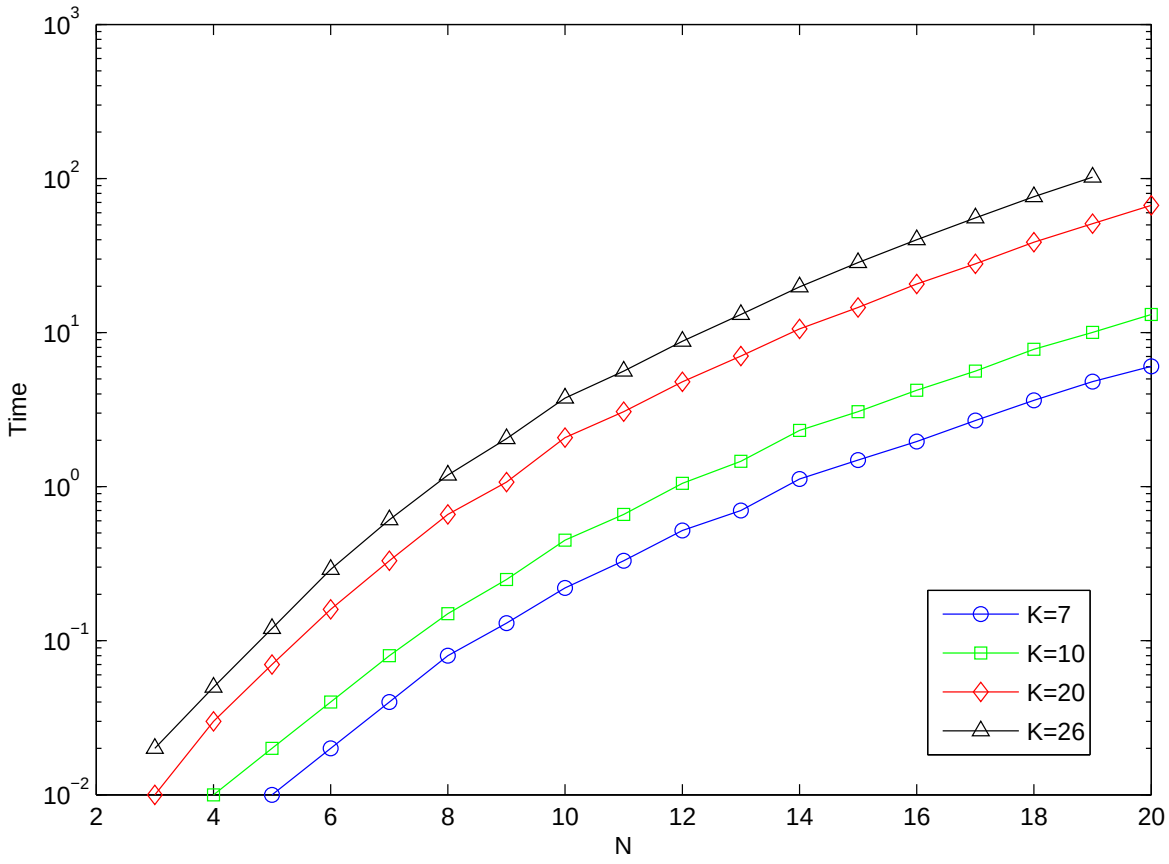

Figure 4.10: Dependence of the CPU time taken on N and K for uniform Stokes flow past a fixed sphere.

Chapter 5

Newtonian Flow

Having performed validation and benchmarking of the numerical scheme for the Stokes problem in Chapter 4, we now repeat the exercise for the incompressible Newtonian fluid flow detailed in Section 2.1.1. We begin with start-up (or transient) Poiseuille flow for which there are analytical solutions for both the planar channel flow [62] and axisymmetric pipe flow [63] cases. These solutions allow us to carefully investigate the accuracy of our numerical approximations in a time-dependent flow in Sections 5.1.1 and 5.1.2 for the 2D Cartesian and 3D axisymmetric schemes respectively.

We also continue in benchmarking our scheme using the flow past a fixed cylinder in an infinite channel for the Cartesian geometry and flow past a fixed sphere in a cylinder for the cylindrical axisymmetric geometry. These are found in Sections 5.2 and 5.3 respectively.

5.1 Transient Poiseuille Flow for an Incompressible Newtonian fluid

5.1.1 Planar Geometry

We test the validity of the numerical solution for the Cartesian Newtonian scheme using the time-dependent analytical solution for start-up of Poiseuille flow. This is achieved by prescribing a constant pressure gradient across the channel. The non-trivial parts of the solution for a channel of height H are given by,

$$u_x(\mathbf{x},t) = A(y) - 32\sum_{n=1}^{\infty}\frac{\sin(\nu y/H)}{\nu^3}\exp\left(-\nu^2 t/Re\right), \tag{5.1}$$

$$(\nabla\mathbf{u})_{yx} = A'(y) - 32\sum_{n=1}^{\infty}\frac{\cos(\nu y/H)}{\nu^2}\exp\left(-\nu^2 t/Re\right), \tag{5.2}$$

$$p(\mathbf{x},t) = -\frac{8}{H}x \tag{5.3}$$

where $\nu = \nu(n) = (2n-1)\pi$ and $A(y) = -4y(y-1)$.

We impose zero initial conditions along with boundary conditions for the velocity at inflow and outflow using the analytical solution and wall conditions at the top and bottom of the channel. No conditions are imposed on the pressure. The simulation is terminated after 10 time units.

When computing the analytical solution we must truncate the infinite sum in (5.1). We choose to use the first 20 terms when truncating this sum because for values of $t > 10^{-3}$, the terms in the sum quickly reach the limit of machine precision, and are converging to values around and below 10^{-7} for $\Delta t = 10^{-4}$, which is the lowest value of Δt used for these simulations. Note, we do not consider $t = 0$ using this solution as we know $\mathbf{u}(0) = 0$).

Domain, Mesh and Timestepping

The domain is chosen to be a channel of length L. The value of L is fixed at $L = 8$ (we saw no change in results with a change in length of the channel for the Newtonian

fluid). The height of the channel is fixed at $H = 1$. We use 4 different elemental meshes, $T1$-$T4$, which are shown in Figure 3.3 in Section 3.9.1, ranging from a single element up to 4 elements. Timesteps ranging from $\Delta t = 10^{-1}$ to $\Delta t = 10^{-4}$ are considered.

Results

Test points at the penultimate GLL-node nearest the outflow boundary are chosen in the centre of the channel (where $y = 0.5$) and on the lower wall (where $y = 0$) for the non-zero velocity and velocity gradient component, respectively. Figures 5.1(a) and 5.1(b) show a typical comparison between the actual solution and that computed by the numerical scheme at these test points. We see that even on a single element with a modest polynomial order of $N = 6$ and timestep of $\Delta t = 10^{-2}$ we obtain a numerical solution which is barely discernible from the actual solution to the eye and reaches the appropriate steady-state velocity.

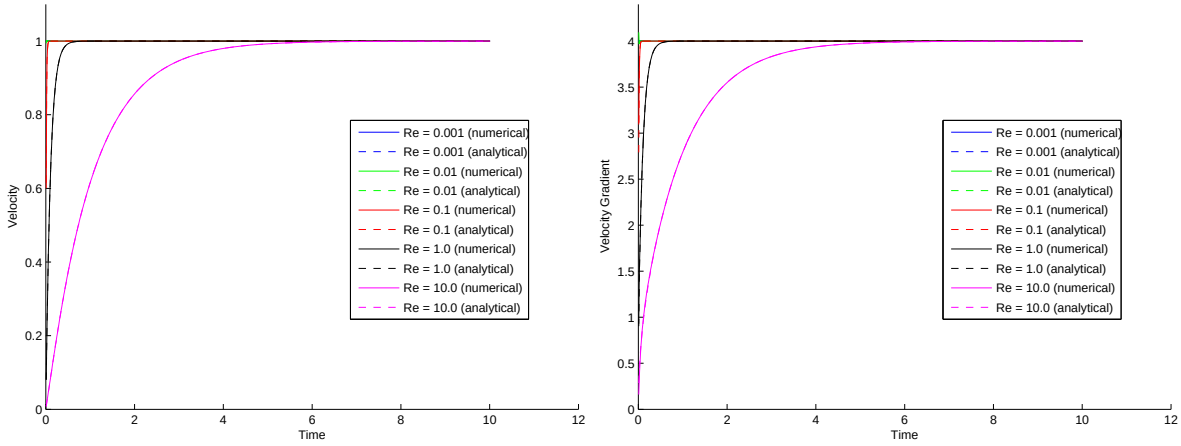

(a) u_x (b) $(\nabla \mathbf{u})_{yx}$

Figure 5.1: Comparison of numerical and analytical solutions for at the chosen test point for planar Newtonian start-up of Poiseuille flow for $Re = 0.001, 0.01, 0.1, 1.0, 10.0$. Parameters used are $\Delta t = 10^{-2}$, $K = 1$ (mesh $T1$), $N = 6$.

A more appropriate metric is a time-averaged error, given by,

$$E_u = \frac{\int |u_{numerical} - u_{analytical}| dt}{\text{Total time}}. \tag{5.4}$$

where the $u_{numerical}$ and $u_{analytical}$ are the values at the test point. We do not expect that the time-averaged error will be a smooth function so use the composite Simpson's

Mesh	Δt	$N = 4$	$N = 6$	$N = 8$	$N = 12$	$N = 16$
T1	10^{-1}	1.5712×10^{-4}	1.4424×10^{-4}	1.2775×10^{-4}	6.7742×10^{-5}	3.0286×10^{-5}
	10^{-2}	2.5887×10^{-5}	9.5223×10^{-6}	8.6610×10^{-6}	4.5430×10^{-6}	2.1020×10^{-6}
	10^{-3}	3.2371×10^{-5}	8.9735×10^{-7}	1.6314×10^{-7}	7.1161×10^{-8}	3.3383×10^{-8}
	10^{-4}	3.2442×10^{-5}	9.9041×10^{-7}	7.4702×10^{-8}	2.5366×10^{-9}	5.1796×10^{-10}
T2	10^{-1}	1.5119×10^{-4}	1.4547×10^{-4}	1.2857×10^{-4}	6.8123×10^{-5}	3.0544×10^{-5}
	10^{-2}	1.0777×10^{-5}	9.9705×10^{-6}	8.6519×10^{-6}	4.5449×10^{-6}	2.1036×10^{-6}
	10^{-3}	5.9189×10^{-7}	1.4197×10^{-7}	1.2862×10^{-7}	7.1416×10^{-8}	3.3415×10^{-8}
	10^{-4}	4.5851×10^{-7}	1.1870×10^{-8}	1.9001×10^{-9}	9.2743×10^{-10}	5.4484×10^{-10}
T3	10^{-1}	1.5747×10^{-4}	1.5560×10^{-4}	1.5567×10^{-4}	1.5207×10^{-4}	1.5194×10^{-4}
	10^{-2}	2.6240×10^{-5}	1.0428×10^{-5}	1.0786×10^{-5}	1.0529×10^{-5}	1.0515×10^{-5}
	10^{-3}	3.2845×10^{-5}	9.7822×10^{-7}	1.9424×10^{-7}	1.5320×10^{-7}	1.5312×10^{-7}
	10^{-4}	3.2918×10^{-5}	1.0706×10^{-6}	7.5230×10^{-8}	3.3606×10^{-9}	1.6351×10^{-9}
T4	10^{-1}	1.5105×10^{-4}	1.5563×10^{-4}	1.5550×10^{-4}	1.5206×10^{-4}	1.5194×10^{-4}
	10^{-2}	1.1064×10^{-5}	1.0873×10^{-5}	1.0755×10^{-5}	1.0529×10^{-5}	1.0515×10^{-5}
	10^{-3}	6.1512×10^{-7}	1.5339×10^{-7}	1.5662×10^{-7}	1.5344×10^{-7}	1.5312×10^{-7}
	10^{-4}	4.7980×10^{-7}	1.3165×10^{-8}	2.3842×10^{-9}	1.7305×10^{-9}	1.7150×10^{-9}

Table 5.1: Time-averaged velocity error, E_u, at the test point, for planar start-up flow of a Newtonian fluid, $Re = 1$.

rule to approximate the integral using the errors at the test point at each timestep, t^n. Table 5.1 shows these values for $Re = 1$ on each mesh varying Δt and N. We are especially interested in the performance of the temporal discretisation of the momentum equation.

At $N = 4$ and on meshes $T1$ and $T3$, the improvement with refinement in time is not clear, and there is little to no improvement with refinement of the mesh in the x-direction. However, we see an improvement with meshes $T2$ and $T4$, which can be explained by the refinement in the y-direction achieved by effectively doubling the number of node points in this direction. One would expect this to improve results due to the nature of the analytical solution. This also indicates that spatial error is the dominating contribution to the error at orders of $\Delta t < 10^{-2}$. To investigate the temporal discretisation we must therefore consider results which are more spatially refined. The rest of the table supports this and we see that by $N = 8$ we have largely

Mesh	Δt	time = 0.1	time = 0.2	time = 0.4	time = 0.8
T1	10^{-1}	2.8622×10^{-1}	2.8688×10^{-2}	1.6710×10^{-2}	2.0468×10^{-4}
	10^{-2}	7.5317×10^{-4}	4.1812×10^{-4}	5.8075×10^{-5}	1.1207×10^{-6}
	10^{-3}	8.0063×10^{-6}	4.0625×10^{-6}	5.6448×10^{-7}	1.0893×10^{-8}
	10^{-4}	1.3907×10^{-6}	1.1142×10^{-6}	1.5481×10^{-7}	2.9872×10^{-9}
T4	10^{-1}	2.8598×10^{-1}	2.8455×10^{-2}	1.6615×10^{-2}	2.0488×10^{-4}
	10^{-2}	7.5964×10^{-4}	4.1681×10^{-4}	5.7896×10^{-5}	1.1172×10^{-6}
	10^{-3}	7.7357×10^{-6}	3.8971×10^{-6}	5.4153×10^{-7}	1.0449×10^{-8}
	10^{-4}	9.0668×10^{-8}	4.4741×10^{-8}	6.2167×10^{-9}	1.2002×10^{-10}

Table 5.2: Velocity error in the H^1-norm of the numerical solution at selected points in time for planar start-up Poiseuille flow of a Newtonian fluid for $N = 8$.

eliminated this domination by spatial error for meshes $T3$ and $T4$ and for all meshes by $N = 12$. Continuing with the results for $N = 12$ and $N = 16$ then we can see there is a clear demonstration of the 2^{nd}-order accuracy of our temporal scheme and that the temporal error is the dominating factor up to orders of error that approach machine accuracy.

This demonstrates the accuracy of the scheme at a selected point, but it is also interesting to look at errors across the whole domain. We consider the velocity error in the H^1-norm for fixed $N = 8$ in Table 5.2 at selected points in time at $Re = 1$. The first observation is that the error in our numerical solution is higher at the beginning of the simulation. This is to be expected since the nature of the solution in time is that the rate of change in velocity is highest at these points. Furthermore, we see that the 2^{nd}-order accuracy is demonstrated at $t = 0.8$, for mesh $T1$, and for all time points for mesh $T4$, although this suggests that spatial error may still be beginning to dominate as we refine in time. Table 5.3 shows the same information for $N = 16$ where we see that 2^{nd}-order accuracy is maintained with refinement and that the spatial error no longer dominates the results generated with $\Delta t = 10^{-4}$. It is also enough refinement in the polynomial order in order to see agreement in the error measure between the single element mesh, $T1$, and the 4-element mesh, $T4$.

These results demonstrate that our numerical scheme is performing at the expected order of accuracy in terms of both spatial and temporal discretisation for a time-

Mesh	Δt	time = 0.1	time = 0.2	time = 0.4	time = 0.8
T1	10^{-1}	2.8603×10^{-1}	2.8419×10^{-2}	1.6577×10^{-2}	2.0501×10^{-4}
	10^{-2}	7.6209×10^{-4}	4.1634×10^{-4}	5.7829×10^{-5}	1.1159×10^{-6}
	10^{-3}	7.7465×10^{-6}	3.8926×10^{-6}	5.4089×10^{-7}	1.0437×10^{-8}
	10^{-4}	7.7849×10^{-8}	3.8667×10^{-8}	5.3729×10^{-9}	1.0359×10^{-10}
T4	10^{-1}	2.8608×10^{-1}	2.8504×10^{-2}	1.6589×10^{-2}	2.0620×10^{-4}
	10^{-2}	7.6186×10^{-4}	4.1636×10^{-4}	5.7832×10^{-5}	1.1159×10^{-6}
	10^{-3}	7.7463×10^{-6}	3.8928×10^{-6}	5.4092×10^{-7}	1.0438×10^{-8}
	10^{-4}	7.7897×10^{-8}	3.8669×10^{-8}	5.3733×10^{-9}	1.0376×10^{-10}

Table 5.3: Velocity error in the H^1-norm of the numerical solution at selected points in time for planar start-up Poiseuille flow of a Newtonian fluid for $N = 16$.

dependent problem for a Newtonian fluid. This has been shown for both a single point of interest and in an error measure across the whole domain. It should be noted that the convective term within the material derivative is not present in Poiseuille flow, so while the OIFS scheme dealt with this part being zero, it is essentially reduced to a BDF scheme in this type of flow.

5.1.2 Axisymmetric Geometry

Analogously to the planar problem, we test the validity of the axisymmetric scheme for a Newtonian fluid against the analytical solution for start-up of Poiseuille in a cylinder. As in Section 5.1.1 this is flow is characterised by a constant pressure gradient. The non-trivial parts of the solution for a pipe of radius R_C are given by,

$$u_z(\mathbf{x},t) = A(r) - 8\sum_{n=1}^{\infty} \frac{J_0(rZ_n/R_C)}{J_1(Z_n)\,Z_n^3} \exp\left(-Z_n^2 t/Re\right), \tag{5.5}$$

$$(\nabla\mathbf{u})_{rz} = A'(r) + 8\sum_{n=1}^{\infty} \frac{J_1(rZ_n/R_C)}{J_1(Z_n)\,Z_n^2} \exp\left(-Z_n^2 t/Re\right), \tag{5.6}$$

$$p(\mathbf{x},t) = -\frac{8}{H}x \tag{5.7}$$

where, Z_n is the n^{th} real and positive root of the Bessel function of zero order, J_0, and $A(r) = 1 - r^2$.

As before, we impose zero initial conditions along with boundary conditions for the velocity at inflow and outflow using the analytical solution, no-slip and no-penetration conditions are imposed on the wall of the pipe. Axisymmetric boundary conditions are imposed along the central axis of the pipe. No conditions are imposed on the pressure or pressure gradient. The simulation is terminated after 10 time units.

As in the analytical solution in Section 5.1.1 we must truncate the infinite sum and we include the first 20 terms, as we did in the planar solution.

Domain, Mesh and Timestepping

The domain chosen is a cylinder of radius $R_C = 1$, and length $L = 8$, analogous to the planar geometry in Section 5.1.1. We use the same meshes $T1 - T4$ shown in Figure 3.3. Timesteps ranging from $\Delta t = 10^{-1}$ to $\Delta t = 10^{-4}$ are considered.

Results

The chosen test points are the penultimate GLL-node nearest the outflow boundary in the centre of the channel (i.e. on the axis of symmetry, $r = 0$) and on the upper wall (where $r = 1$) for the velocity and velocity gradient respectively. As with the planar geometry, even on a single element with a modest polynomial order of $N = 6$ and timestep of $\Delta t = 10^{-2}$ we obtain a numerical solution which is barely discernible from the actual solution.

We continue to use the time-averaged error (5.4) as a more appropriate metric. Table 5.4 shows E_u for a each combination of mesh, N and Δt at $Re = 1$. Fixing a coarse value of Δt such as $\Delta t = 10^{-1}$ we see that there is little improvement in the numerical solution with polynomial or mesh refinement. We can conclude that temporal discretisation error is the dominating factor here. By decreasing the timestep to $\Delta t = 10^{-4}$ we see, by fixing $N = 4$ and comparing $T1$ and $T3$ with $T2$ and $T4$ that spatial error is the dominating factor, since mesh refinement in the r-direction results in a lower time-averaged error. Varying the polynomial refinement for a fixed mesh, $T4$, we see further decrease in error up to $N = 8$, by which time further spatial refinement yields

Mesh	Δt	$N = 4$	$N = 6$	$N = 8$	$N = 12$	$N = 16$
T1	10^{-1}	5.1180×10^{-4}	4.3616×10^{-4}	3.0554×10^{-4}	1.0530×10^{-4}	4.1938×10^{-5}
	10^{-2}	3.4128×10^{-5}	1.1495×10^{-5}	8.1820×10^{-6}	2.8931×10^{-6}	1.1344×10^{-6}
	10^{-3}	2.9005×10^{-5}	1.0018×10^{-6}	1.2556×10^{-7}	3.2473×10^{-8}	1.2687×10^{-8}
	10^{-4}	2.9003×10^{-5}	9.2898×10^{-7}	7.7034×10^{-8}	6.0085×10^{-9}	4.1644×10^{-9}
T2	10^{-1}	4.9704×10^{-4}	4.3563×10^{-4}	3.0569×10^{-4}	1.0543×10^{-4}	4.2066×10^{-5}
	10^{-2}	1.2870×10^{-5}	1.1506×10^{-5}	8.2313×10^{-6}	2.8936×10^{-6}	1.1350×10^{-6}
	10^{-3}	3.8246×10^{-7}	1.3195×10^{-7}	9.3387×10^{-8}	3.2797×10^{-8}	1.2733×10^{-8}
	10^{-4}	4.0177×10^{-7}	1.0350×10^{-8}	6.4100×10^{-9}	4.6189×10^{-9}	3.9967×10^{-9}
T3	10^{-1}	5.4018×10^{-4}	5.2569×10^{-4}	5.1328×10^{-4}	5.0940×10^{-4}	5.0941×10^{-4}
	10^{-2}	3.4671×10^{-5}	1.3757×10^{-5}	1.3413×10^{-5}	1.3338×10^{-5}	1.3340×10^{-5}
	10^{-3}	2.9118×10^{-5}	1.0291×10^{-6}	1.7221×10^{-7}	1.5046×10^{-7}	1.5132×10^{-7}
	10^{-4}	2.9108×10^{-5}	9.3251×10^{-7}	7.6588×10^{-8}	8.6687×10^{-9}	6.9938×10^{-9}
T4	10^{-1}	5.2187×10^{-4}	5.2497×10^{-4}	5.1325×10^{-4}	5.0939×10^{-4}	5.0941×10^{-4}
	10^{-2}	1.3571×10^{-5}	1.3770×10^{-5}	1.3464×10^{-5}	1.3338×10^{-5}	1.3340×10^{-5}
	10^{-3}	3.8717×10^{-7}	1.5755×10^{-7}	1.5270×10^{-7}	1.5134×10^{-7}	1.5136×10^{-7}
	10^{-4}	4.0917×10^{-7}	1.1494×10^{-8}	7.9906×10^{-9}	7.1496×10^{-9}	7.1789×10^{-9}

Table 5.4: Time-averaged velocity error, E_u, at the test point, for axisymmetric start-up flow of a Newtonian fluid, $Re = 1$.

no improvement, meaning that temporal discretisation error is dominating once again.

Using these observations we confirm that the temporal scheme is 2^{nd}-order as prescribed. Focusing on the results for $N \geq 8$, we see that each decrease in timestep order results in a reduction of the time-averaged error 2 orders of magnitude. This continues up to $\Delta t = 10^{-4}$ where we converge to an error of order 10^{-9}, which is approaching machine accuracy. Further to this point, we note that the truncation of the infinite sum within the first few timesteps at $\Delta t = 10^{-4}$ may be responsible for our analytical solution being prone to error of this order.

We also consider the error in the H^1-norm at select points in time in Table 5.5 for $N = 8$ with $Re = 1$. The error is higher during the transitional phase of the start-up of Poiseuille flow as is demonstrated by the order of the error being higher at $t = 0.1$

Mesh	Δt	time = 0.1	time = 0.2	time = 0.4	time = 0.8
T1	10^{-1}	1.0348×10^{-1}	5.4345×10^{-2}	8.6269×10^{-3}	1.1949×10^{-3}
	10^{-2}	1.7630×10^{-3}	9.8749×10^{-5}	7.8477×10^{-5}	7.9521×10^{-6}
	10^{-3}	1.6571×10^{-5}	8.5548×10^{-7}	7.5577×10^{-7}	7.6505×10^{-8}
	10^{-4}	5.0555×10^{-6}	2.1372×10^{-7}	1.1130×10^{-7}	1.1050×10^{-8}
T4	10^{-1}	1.0347×10^{-1}	5.4043×10^{-2}	8.6536×10^{-3}	1.1877×10^{-3}
	10^{-2}	1.7488×10^{-3}	9.9773×10^{-5}	7.8042×10^{-5}	7.9054×10^{-6}
	10^{-3}	1.5630×10^{-5}	8.5520×10^{-7}	7.4450×10^{-7}	7.5366×10^{-8}
	10^{-4}	2.9638×10^{-7}	1.3039×10^{-7}	4.0323×10^{-8}	3.9894×10^{-9}

Table 5.5: Table showing velocity error in the H^1-norm of the numerical solution at points in time for axisymmetric start-up Poiseuille flow for varying Δt on the T1 and T4 meshes at polynomial order $N = 8$.

compared to $t = 0.8$ for all values of Δt and for both meshes shown. This is to be expected due to the nature of the solution as the change in velocity and gradients are most extreme in this period. For mesh $T1$ we see an improvement in error in line with the 2^{nd}-order temporal scheme, but this breaks down between 10^{-3} and 10^{-4} when it seems that spatial error begins to dominate. There is a slight improvement in convergence with refinement in time discretisation when using mesh $T4$, which supports this.

Table 5.6 shows the same information for increased polynomial order $N = 16$. This appears to improve things slightly, at least for mesh $T1$, but there is no discernible improvement for mesh $T4$. This is an interesting result as, combined with the time-averaged error in Table 5.4, it appears to show a limit in the achievable accuracy using our numerical scheme is of order 10^{-9}. This is still a high degree of accuracy, but we were able to reach higher levels of accuracy when computing solutions for the Stokes problem. It is also slightly lower than that seen for 2D planar start-up of Poiseuille flow in a channel. The source of this additional error may be explained by the additional component of the velocity gradient, $(\nabla \mathbf{u})_{\theta\theta}$ which we must rewrite using L'Hôpital's rule in (3.81) in order to evaluate it on the axis of symmetry. Overall, however, we have demonstrated that the temporal scheme is indeed 2^{nd}-order and we see excellent agreement with an analytical solution in axisymmetric 3D.

Mesh	Δt	time = 0.1	time = 0.2	time = 0.4	time = 0.8
T1	10^{-1}	1.0351×10^{-1}	5.4001×10^{-2}	8.6456×10^{-3}	1.1873×10^{-3}
	10^{-2}	1.7474×10^{-3}	9.9722×10^{-5}	7.8014×10^{-5}	7.9022×10^{-6}
	10^{-3}	1.5618×10^{-5}	8.5557×10^{-7}	7.4429×10^{-7}	7.5341×10^{-8}
	10^{-4}	2.8090×10^{-7}	1.3490×10^{-7}	4.1896×10^{-8}	4.1450×10^{-9}
T4	10^{-1}	1.0352×10^{-1}	5.4017×10^{-2}	8.6460×10^{-3}	1.1874×10^{-3}
	10^{-2}	1.7475×10^{-3}	9.9743×10^{-5}	7.8026×10^{-5}	7.9038×10^{-6}
	10^{-3}	1.5621×10^{-5}	8.5648×10^{-7}	7.4446×10^{-7}	7.5362×10^{-8}
	10^{-4}	2.9472×10^{-7}	1.4005×10^{-7}	4.3492×10^{-8}	4.3029×10^{-9}

Table 5.6: Velocity error in the H^1-norm of the numerical solution at selected points in time for axisymmetric start-up Poiseuille flow of a Newtonian fluid for $N = 16$.

5.1.3 Summary

In both the planar 2D and axisymmetric 3D versions of our numerical scheme we have demonstrated convergence with refinement in both time and space to a high degree of accuracy. Appropriate refinement in both aspects has been demonstrated to be important since the error may become dominated by either so a balance should be reached in order to avoid wasted computational time. We also observed that the axisymmetric scheme may suffer slightly more error due to the extra terms present in the velocity gradient.

5.2 Flow past a Fixed Cylinder in a channel

In Section 4.3 we benchmarked our numerical scheme using Poiseuille flow past an infinite cylinder in an infinite channel, and continue to do so for the Newtonian scheme. While the focus of this thesis is flows at $Re < 1$, it is still worthwhile to validate the solver at moderate Reynolds numbers, $Re < 50$, but we must be wary of where the assumption of axisymmetry is valid.

As before, we prescribe the inflow and outflow velocity conditions as given in (4.4) along with no-slip wall conditions at the top and symmetric wall conditions at the bottom

of the channel. We impose zero initial conditions and stop the simulation according to the stopping criteria described in Section 3.1.7. A range of Reynolds numbers from $Re = 10^{-3}$ up to $Re = 10$, in orders of 10, are considered in detail along with additional results up to $Re = 40$.

5.2.1 Domain, Mesh and Timestepping

We make use of the fixed cylinder in an infinite channel domain and benchmarking meshes, $M1$-$M4$, seen in from Figures 3.4(a)- 3.4(d). Unlike the Stokes flow version of this benchmark, we use the full length of the meshes shown in Section 3.9.2. Timesteps ranging from $\Delta t = 10^{-1}$ to $\Delta t = 10^{-4}$ are considered.

5.2.2 Results

Table 5.7 shows the collected results up to $Re = 10$ at fixed $\Delta t = 10^{-4}$. We focus on these results, at the highest level of refinement in time, with the assumption that this would eliminate as much temporal discretisation error as possible. Convergence is seen for all meshes between $N = 12$ and $N = 16$ with the exception of $Re = 10$, which has not fully converged to a drag value with refinement in polynomial order or mesh. There is no indication that, with further refinement, convergence to a drag value would not be reached, although this is beyond the range of Reynolds numbers we are interested in and so these have not been performed. At $Re \leq 1$, we see convergence to within 4-5 decimal places which, while not confirming that the solution reached is correct, places confidence in the stability of the solution produced by our numerical scheme. A final observation is that for these calculations all of our meshes were able to reach agreement with enough polynomial refinement with the exception of mesh $M1$ at $Re = 10$, which disagrees to some degree with the drag compared to the other 3 meshes.

We now move our focus to refinement in time. Table 5.8 show the collected results up to $Re = 10$ at fixed polynomial order, $N = 16$, a value chosen to eliminate spatial discretisation error as much as possible. At the lowest timestep, $\Delta t = 10^{-1}$, some results are missing due a breakdown in the numerical scheme usually resulting in blow-

		Drag				
Mesh	N	$Re = 0.001$	$Re = 0.01$	$Re = 0.1$	$Re = 1$	$Re = 10$
M1	4	132.382481	132.403986	132.628584	135.818530	192.138158
	8	132.365687	132.384961	132.585676	135.382445	206.542116
	12	132.359612	132.378818	132.578893	135.373688	200.094315
	16	132.359576	132.378782	132.578853	135.373692	200.252481
M2	4	131.395930	131.414305	131.606066	134.319850	198.709973
	8	132.359609	132.378814	132.578885	135.373703	200.411425
	12	132.359576	132.378782	132.578853	135.373691	200.438695
	16	132.359576	132.378781	132.578853	135.373686	200.423101
M3	4	132.324715	132.343917	132.543934	135.337998	201.843848
	8	132.359609	132.378814	132.578886	135.373763	200.381844
	12	132.359576	132.378782	132.578853	135.373695	200.439184
	16	132.359576	132.378781	132.578853	135.373695	200.427622
M4	4	132.307419	132.326587	132.526259	135.316213	199.612814
	8	132.359608	132.378814	132.578886	135.373761	200.408090
	12	132.359576	132.378782	132.578853	135.373692	200.425943
	16	132.359576	132.378781	132.578853	135.373695	200.427681

Table 5.7: Dependence of computed Drag, D on each mesh on N for fixed $\Delta t = 10^{-4}$ for Newtonian flow past a fixed cylinder in a channel for different values of Re.

		Drag				
Mesh	Δt	$Re = 0.001$	$Re = 0.01$	$Re = 0.1$	$Re = 1$	$Re = 10$
M1	10^{-1}	132.359833	132.381361	132.605446	135.702159	193.997078
	10^{-2}	132.359578	132.378796	132.579010	135.377324	200.604820
	10^{-3}	132.359576	132.378785	132.578888	135.375214	200.611932
	10^{-4}	132.359576	132.378782	132.578853	135.373692	200.252481
M2	10^{-1}	-	-	-	-	-
	10^{-2}	132.359577	132.378795	132.579010	135.377323	-
	10^{-3}	132.359576	132.378784	132.578888	135.375213	200.788063
	10^{-4}	132.359576	132.378781	132.578853	135.373686	200.423101
M3	10^{-1}	-	-	-	-	-
	10^{-2}	132.359577	132.378795	132.579010	135.377324	200.832718
	10^{-3}	132.359576	132.378784	132.578888	135.375214	200.787934
	10^{-4}	132.359576	132.378781	132.578853	135.373695	200.427622
M4	10^{-1}	-	-	-	-	-
	10^{-2}	132.359577	132.378795	132.579010	135.377324	200.832890
	10^{-3}	132.359576	132.378784	132.578888	135.375214	200.787933
	10^{-4}	132.359576	132.378781	132.578853	135.373695	200.427681

Table 5.8: Convergence of Drag, D, with refinement in timestep and at $N = 16$ for Newtonian flow past a fixed cylinder in a channel.

up of the solution. The majority can be explained easily since we are using a highly refined GLL grid with very small spacing, which would require a smaller timestep in order to meet the CFL condition. The missing result for $Re = 10.0$ on mesh $M2$ at $\Delta t = 10^{-2}$ is less easily explained because on the other, more refined meshes, we were able to compute a solution - we are forced to put this down to a software glitch as it was possible to compute the solution by changing parameters in the linear solver. It serves as a warning that direct methods for solving these types of matrices require care.

In terms of convergence, we see good agreement again at low values of Re, with some change as we reach $Re = 1$. By $Re = 10$, we would need to perform further refinement to confirm whether our numerical scheme is convergent with temporal refinement, although since this is outside the focus of this thesis, we do not perform it.

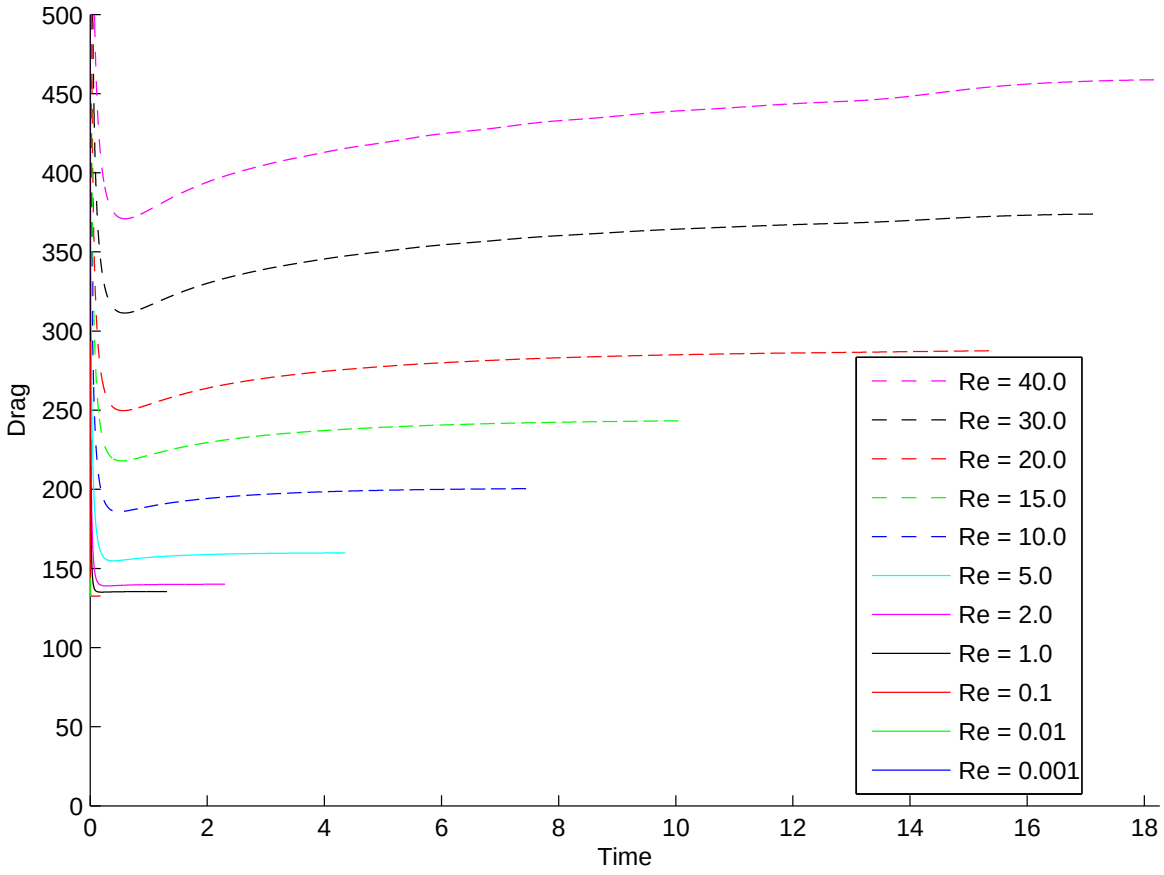

Figure 5.2: Evolution of the drag for Newtonian flow past a fixed cylinder in a channel. Calculations performed on mesh $M4$ at polynomial order $N = 16$ and timestep $\Delta t = 10^{-4}$.

Figure 5.2 shows the evolution of the drag in time for each calculation performed at the highest refinement in all of our numerical parameters for a range of Reynolds numbers. The simulation is stopped once our stopping criteria has been reached, so the smaller Reynolds number simulations complete far sooner than those at higher Re. The reason for the dip and then increase is because of the velocity profile at inflow and outflow being Poiseuille flow and, in effect, we go through the transition phase from start-up to steady flow.

The lack of convergence observed at $Re = 10$ sustained at larger Reynolds numbers

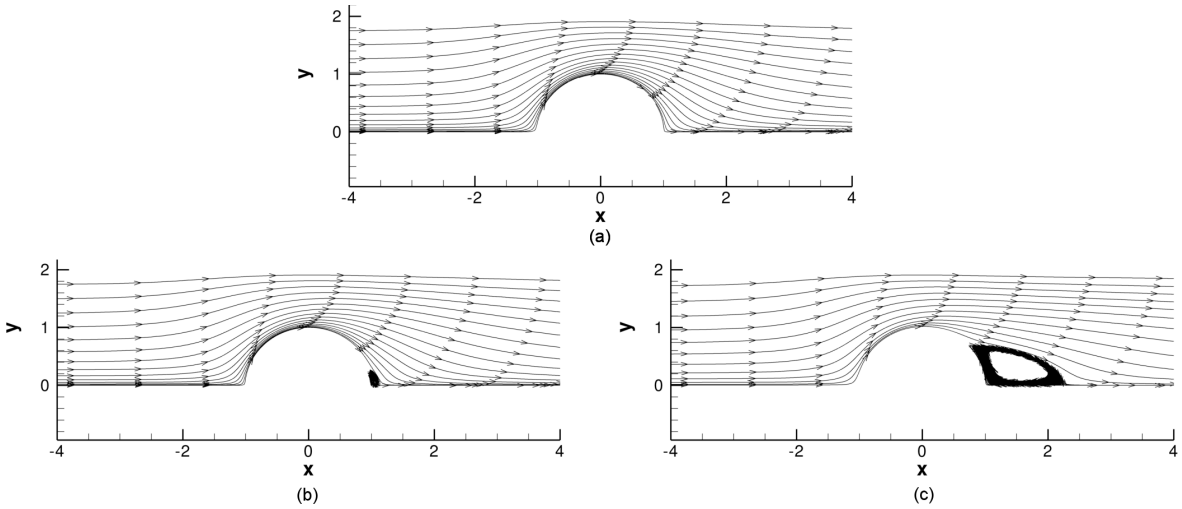

Figure 5.3: Streamlines for Newtonian flow past a fixed cylinder in a channel at (a) $Re = 10$ (b) $Re = 15$ (c) $Re = 40$. Calculation performed on mesh $M4$, $N = 16$ and $\Delta t = 10^{-4}$

where we see there is a visible increase in the drag towards the end of the simulation for both $Re = 30$ and $Re = 40$. Looking at the streamlines at the supposed steady-state solution for $Re = 40$ in Figure 5.3 (c), a possible reason for this may be the presence of a recirculation zone in the wake of the cylinder. These vortices may indicate an unsteady flow which could cause the drag value to fluctuate. Figures 5.3 (a) and (b) show the streamlines for $Re = 10$ and $Re = 15$, respectively. We see that the formation of the circulation zone happens between these two Reynolds numbers. After looking into the literature we find that this fits well with the critical value of $Re = 24.3$ as detailed by Chen et al. in 1995 [11] for this blockage ratio where the flow changes from steady to unsteady, although the assumption of symmetry is maintained for Reynolds numbers upwards of 200. At first glance our results may appear odd, but the non-dimensionalisation employed by Chen et al. [11] used the height of the channel as their length scale, whereas we use the radius of the cylinder meaning their Reynolds number is larger by a factor of 2 compared to our computations. This serves as an additional validation of our scheme for this benchmark with our results predicting a change from steady to unsteady flow between $Re = 20$ and $Re = 30$ in terms of their non-dimensionalisation. While we could push the Reynolds number higher to look for the break down in symmetry, this is far beyond the intents of our research, and we do not investigate it further.

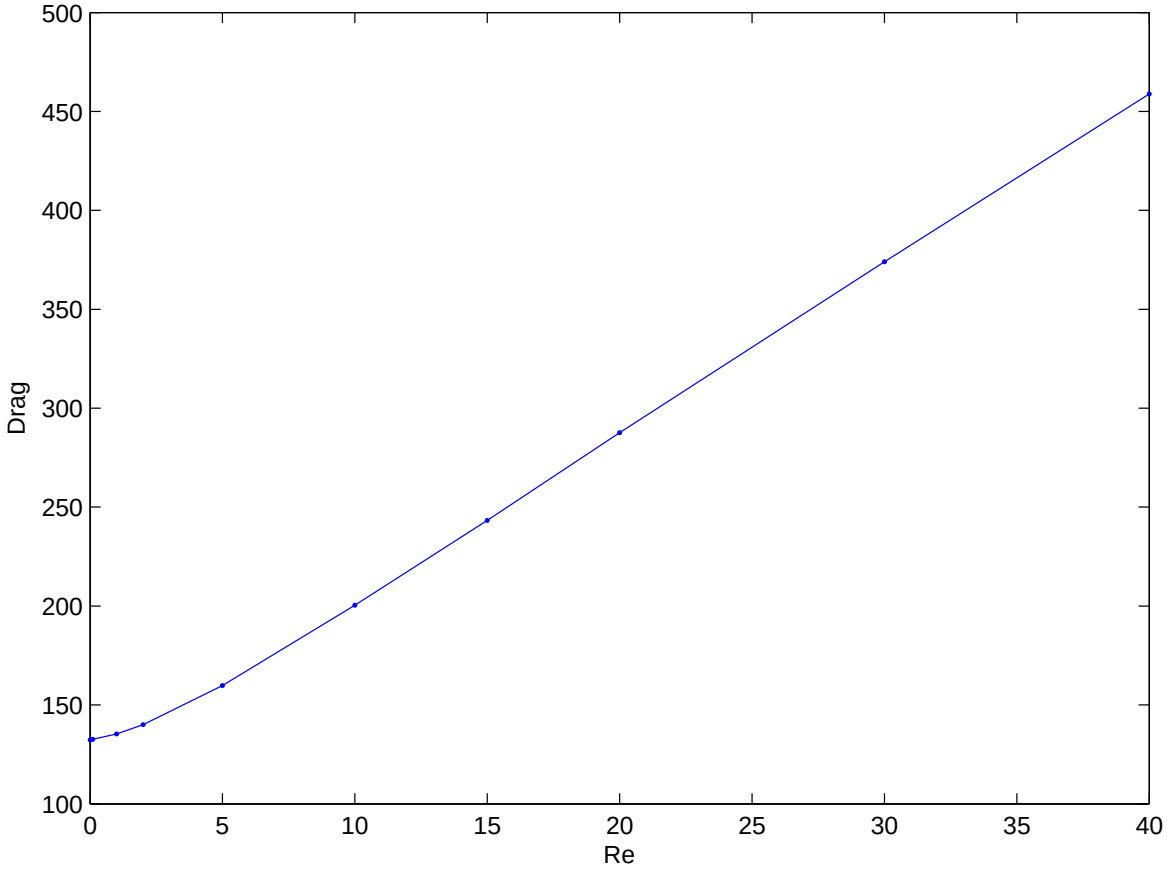

Figure 5.4: Dependence of the drag on the Reynolds Number, Re, for Newtonian flow past a fixed cylinder in a channel. Calculations performed on mesh $M4$ with $N = 16$ and $\Delta t = 10^{-4}$.

Finally, Figure 5.4 shows the steady drag value computed at all Reynolds numbers tested using our numerical scheme, although the validity of the results beyond $Re = 10$ can certainly be questioned with the breakdown of axisymmetry discussed above. The general trend is as expected with increasing Re, in that the drag increases from the Stokes limit. This is fairly intuitive since the flow rate is increased which is usually the dominating factor on the drag force experienced by the cylinder.

5.2.3 Summary

While moderate Reynolds numbers are not the focus of this thesis we have demonstrated that the 2^{nd}-order OIFS scheme performs well under these conditions and produces convergent results with refinement up to $Re = 1$. Additionally we are able to observe phenomena in our simulations which match those found by other studies in the literature on the topic.

5.3 Flow past a Fixed Sphere

We now consider the Newtonian model for a fixed sphere in uniform flow, continuing the benchmark used in Section 4.4. As with the cylinder benchmark in Section 5.2, we consider a range of low to moderate Reynolds numbers while bearing in mind our assumption of axisymmetry.

Uniform flow conditions are imposed at inflow, outflow and on wall boundaries, and symmetric wall conditions are applied along the axis of symmetry. We prescribe zero initial velocity conditions and stop the simulation according to the usual stopping criteria given in Section 3.1.7. Reynolds numbers from $Re = 10^{-3}$ up to $Re = 10$, in orders of 10, are considered in detail along with additional values up to $Re = 40$.

5.3.1 Domain, Mesh and Timestepping

We make use of the fixed sphere in a cylinder domain and benchmarking meshes, $M1$-$M4$, shown in from Figures 3.4(a)- 3.4(d). As with the cylinder benchmark problem, we use the full axial extent of the meshes in Section 3.9.2. We use the same domain and meshes, $M1$-$M4$, as used in the Stokes validation. Timesteps ranging from $\Delta t = 10^{-1}$ to $\Delta t = 10^{-4}$ are considered.

		Drag Factor				
Mesh	N	$Re = 0.001$	$Re = 0.01$	$Re = 0.1$	$Re = 1$	$Re = 10$
M1	4	5.935352	5.935777	5.940200	6.000944	7.746503
	8	5.948412	5.948800	5.952820	6.006720	7.543457
	12	5.947425	5.947808	5.951777	6.005155	7.472311
	16	5.947417	5.947800	5.951769	6.005143	7.478621
M2	4	5.897876	5.898250	5.902128	5.954719	7.442873
	8	5.947412	5.947795	5.951764	6.005136	7.478656
	12	5.947417	5.947800	5.951769	6.005143	7.478658
	16	5.947417	5.947800	5.951769	6.005144	7.478664
M3	4	5.947514	5.947897	5.951872	6.005367	7.496324
	8	5.947417	5.947800	5.951769	6.005142	7.478713
	12	5.947417	5.947800	5.951769	6.005142	7.478661
	16	5.947417	5.947800	5.951769	6.005145	7.478663
M4	4	5.945974	5.946356	5.950319	6.003622	7.463581
	8	5.947417	5.947800	5.951769	6.005142	7.478661
	12	5.947417	5.947800	5.951769	6.005143	7.478663
	16	5.947417	5.947800	5.951769	6.005142	7.478663

Table 5.9: Dependence of the computed Drag Factor, D^* on each mesh on N with $\Delta t = 10^{-4}$ for uniform Newtonian flow past a fixed sphere.

5.3.2 Results

We first look at convergence with spatial refinement. Table 5.9 shows the collected results in terms of the drag factor up to $Re = 10$ with spatial refinement at fixed timestep $\Delta t = 10^{-4}$. We choose this small timestep with the hope that it will remove as much temporal discretisation error as possible. Convergence of the drag factor is reached for each value of Re with both mesh and polynomial refinement. Looking at mesh refinement, we see that when fixing $N = 12$ we reach convergence for all values of Re on each mesh. In particular, mesh $M2$ is typically enough to resolve the drag on the sphere. At lower polynomial order, $N = 4$ we find that further elemental mesh refinement is likely needed to reach a converged drag factor value.

Moving on to polynomial order, as we increase Re, more polynomial refinement is needed to reach the converged value with mesh $M1$ not quite reaching as good agreement at $Re = 10$ and mesh $M2$ requiring $N = 16$ to agree with meshes $M3$ and $M4$ requiring $N = 12$ and $N = 8$, respectively. Generally speaking, further polynomial refinement above $N = 16$ does not appear to be required for this range of Reynolds numbers, apart from when using the coarse mesh, $M1$. Overall, these results show excellent convergence in the drag factor with spatial refinement.

We now focus on refinement in temporal discretisation. Table 5.10 shows collected results up to $Re = 10$ with varying timestep on each mesh at fixed polynomial $N = 16$, hoping to minimise spatial discretisation error. We note that for timestep $\Delta t = 10^{-1}$ a solution could only be computed on mesh $M1$ since the CFL condition was not met when using any of the finer elemental meshes at this polynomial order. Overall we see a good agreement for all timesteps, noting that the choice of mesh makes no difference until $Re \geq 1$, where the differences are spatial, as seen above.

At $Re = 0.1$ and $Re = 1$, there is a slight discrepancy between results obtained with $\Delta t = 10^{-4}$ and the other timesteps. At first this may provide a cause for concern since

		Drag Factor				
Mesh	Δt	$Re = 0.001$	$Re = 0.01$	$Re = 0.1$	$Re = 1$	$Re = 10$
M1	10^{-1}	5.947418	5.947813	5.951905	6.006850	7.479327
	10^{-2}	5.947417	5.947799	5.951758	6.005021	7.478857
	10^{-3}	5.947417	5.947799	5.951758	6.005015	7.478623
	5×10^{-4}	5.947416	5.947799	5.951759	6.005025	7.478621
	10^{-4}	5.947417	5.947800	5.951769	6.005143	7.478621
M2	10^{-1}	-	-	-	-	-
	10^{-2}	5.947417	5.947799	5.951758	6.005021	7.478875
	10^{-3}	5.947417	5.947799	5.951758	6.005015	7.478666
	5×10^{-4}	5.947416	5.947799	5.951759	6.005025	7.478664
	10^{-4}	5.947417	5.947800	5.951769	6.005144	7.478664
M3	10^{-1}	-	-	-	-	-
	10^{-2}	5.947417	5.947799	5.951758	6.005021	7.478874
	10^{-3}	5.947417	5.947799	5.951758	6.005015	7.478665
	5×10^{-4}	5.947416	5.947799	5.951759	6.005025	7.478663
	10^{-4}	5.947417	5.947800	5.951769	6.005145	7.478663
M4	10^{-1}	-	-	-	-	-
	10^{-2}	5.947417	5.947799	5.951758	6.005021	7.478874
	10^{-3}	5.947417	5.947799	5.951758	6.005015	7.478665
	5×10^{-4}	5.947416	5.947799	5.951759	6.005025	7.478663
	10^{-4}	5.947417	5.947800	5.951769	6.005142	7.478663

Table 5.10: Convergence of Drag Factor, D^*, with refinement in timestep and at $N = 16$ for uniform Newtonian flow past a fixed sphere.

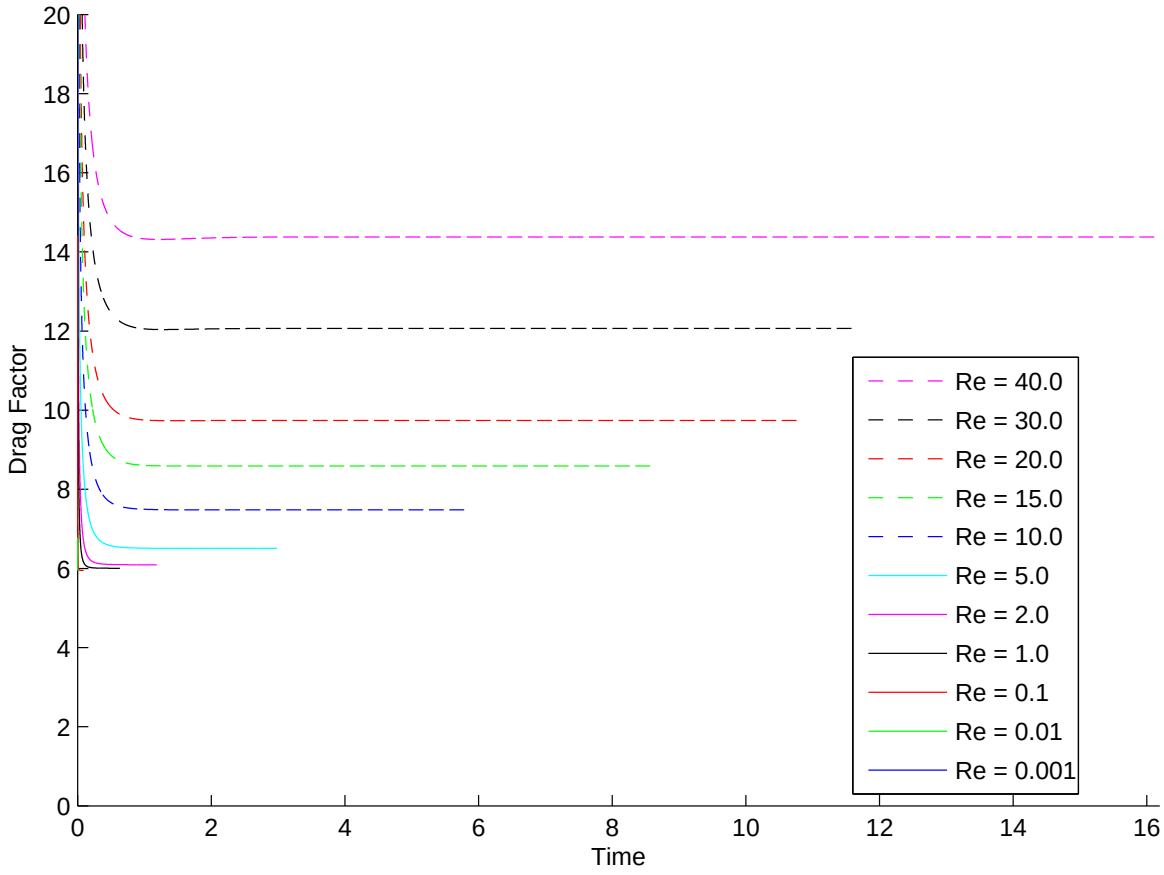

Figure 5.5: Evolution of the drag factor for Newtonian flow past a fixed sphere in a cylinder. Calculations performed on mesh $M4$ with $N = 16$ and timestep $\Delta t = 10^{-4}$.

convergence with timestep refinement is not being demonstrated. However, it is only at the 5^{th} decimal place. Furthermore the time when the simulation had been terminated for these results was different for different timesteps. This is beccause the simulation met the stopping criteria (notably that set on the L^2-norm of the difference between the field variables between consecutive timesteps) in fewer time units, in fact the $\Delta t = 10^{-4}$ took around half the time units to complete as $\Delta t = 10^{-2}$ at $Re = 1$. The reason for this is an oversight in setting a fixed value of the tolerance on a quantity which is essentially a rate of change. We note that by forcing the simulation to terminate after a set number of timesteps that convergence to a drag value certainly improves these results. We conclude that the numerical scheme has been demonstrated to converge with decreasing timestep for the sphere benchmark. In future simulations we make a change so that the threshold is set using $\frac{\text{tol}}{\Delta t}$, where tol is a chosen tolerance, to take the difference in timesteps into account.

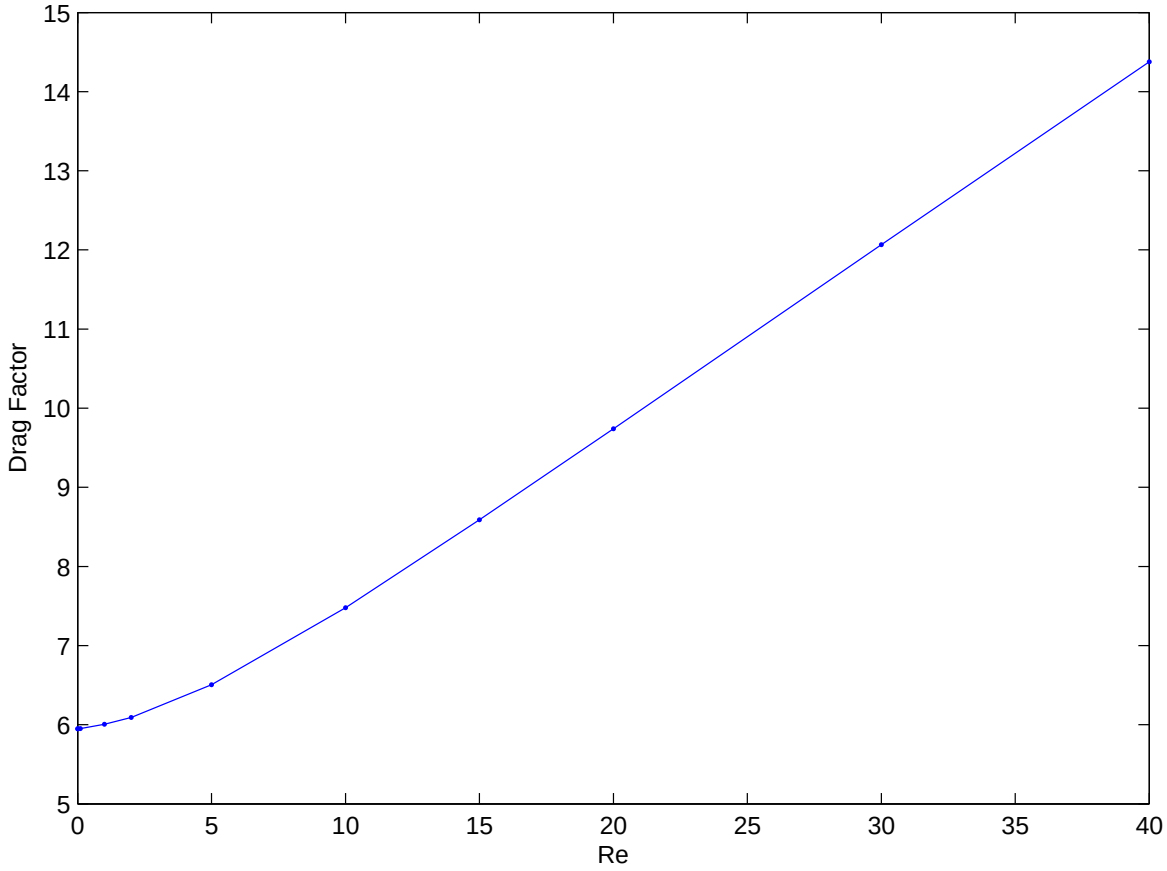

Figure 5.6: Dependence of the drag factor on Re for Newtonian flow past a fixed sphere in a cylinder. Calculations performed on mesh $M4$ with $N = 16$ and timestep $\Delta t = 10^{-4}$.

Figure 5.5 shows the evolution of the drag factor in time for each calculation performed at the highest refinement in all numerical parameters for a wider range of Reynolds numbers than considered above. As with the cylinder benchmark, the simulations are stopped according to our stopping criteria, so higher Re simulations take long to reach convergence in terms of the field variables and the drag. Unlike the cylinder benchmark there are no indications of instability in the evolution of the drag.

After reviewing some of the literature on Newtonian flow past a sphere we find that this behaviour is to be expected as detailed, for example, in the paper by Johnson and Patel [26]. There is a subtle difference between the wake behind the sphere and

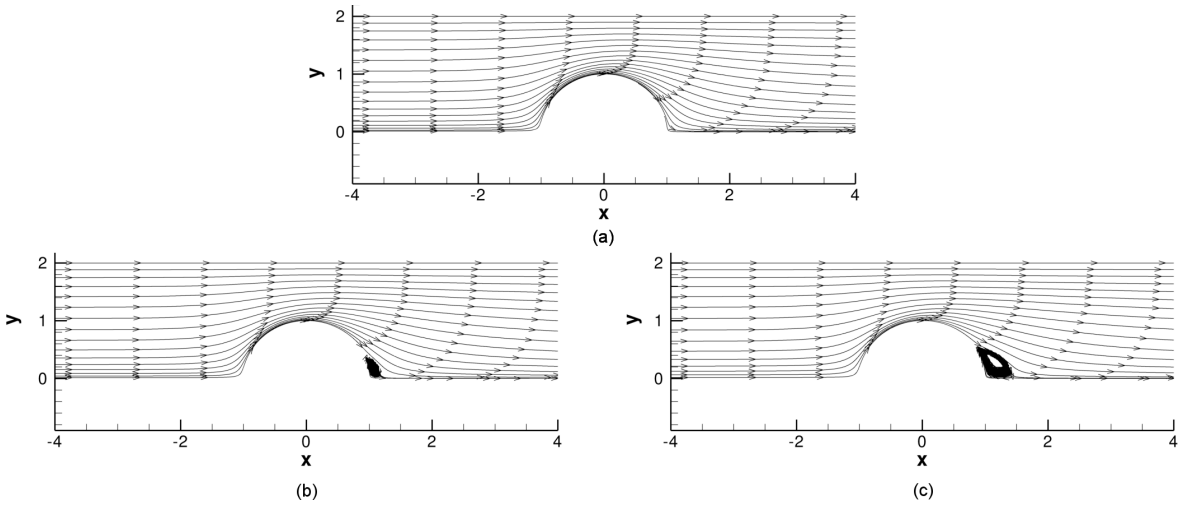

Figure 5.7: Streamlines for uniform Newtonian flow past a fixed sphere at (a) $Re = 20$ (b) $Re = 30$ (c) $Re = 40$. Calculation performed on mesh $M4$, $N = 16$ and $\Delta t = 10^{-4}$

the cylinder. For a sphere, while there is still a separation from the boundary layer, it remains a steady flow to Reynolds numbers upwards of 200, therefore our results up to $Re = 40$ should be expected to be stable and reach a steady drag value. This is exactly what we observe, which serves as some validation of the results obtained. Figure 5.7 shows the streamlines for the sphere benchmark at 3 different Reynolds numbers. Figure 5.7(c) clearly shows the separation from the boundary layer at $Re = 40$. Further the separation in the wake of the sphere happens between $Re = 20$ in Figure 5.7(a) and $Re = 30$ in Figure 5.7(b), which agrees well with the $Re = 24$ value found numerically and experimentally in the literature.

Finally, Figure 5.6 shows the steady drag factor value computed at all Reynolds numbers tested using the numerical scheme. As with the cylinder benchmark, we see a general trend of increasing drag factor with Re, which makes intuitive sense due to the increased flow rate.

5.3.3 Summary

As for the cylinder benchmark problem, while moderate Reynolds numbers are not the main focus of this thesis we have demonstrated that the 2^{nd}-order OIFS scheme performs well for moderate values of the Reynolds number and produces convergent

results with refinement for the parameter values tested. Additionally, our results match observed phenomena found in the literature on the topic.

Chapter 6

Viscoelastic Flows

Following the successful validation of our numerical scheme for a Newtonian fluid at low Reynolds number in Chapter 5, we now consider the viscoelastic flow of an Oldroyd B model fluid. The model was described in Section 2.2.1. We again use the start-up of Poiseuille flow in order to gauge the error incurred by our numerical scheme using the analytical solution for planar channel flow [62] and axisymmetric pipe flow [63]. These may be found in Sections 6.1.1 and 6.1.2, respectively.

We also continue to benchmark using the flow past a cylinder in an infinite channel for the planar geometry and flow past a fixed sphere in a cylinder for the cylindrical axisymmetric geometry, which may be found in Sections 6.2 and 6.3.

6.1 Start-up Poiseuille Flow for an Oldroyd B Fluid

6.1.1 Planar Geometry

We may validate our scheme for an Oldroyd B fluid using the analytical solution for start-up Poiseuille flow derived by Waters and King [62]. The non-trivial component

of velocity at time t is given by,

$$u(\mathbf{x},t) = A(y) - 32\sum_{n=1}^{\infty} \frac{\sin(\nu y/H)}{\nu^3} \exp\left(\frac{-\alpha_\nu t}{2El}\right) G_\nu(t), \tag{6.1}$$

with $\nu = \nu(n) = (2n-1)\pi$, $A(y) = -4y(y-1)$ and where,

$$G_\nu(t) = \begin{cases} \frac{1}{2}\left(a_\nu \exp(p_\nu t) + b_\nu \exp(q_\nu)\right) & \text{if} \quad \beta_\nu \geq 0 \\ \exp\left(\frac{-\alpha_\nu}{2El}\right)\left(\cos\left(\frac{\beta_\nu}{2El}\right) + \frac{\gamma_\nu}{\beta_\nu}\sin\left(\frac{\beta_\nu t}{2El}\right)\right) & \text{if} \quad \beta_\nu < 0 \end{cases} \tag{6.2}$$

with,

$$\begin{aligned} A(y) &= -4y(y-1), \quad \nu = (2n-1)\pi, \quad El = \frac{We}{Re}, \\ \alpha_\nu &= 1 + \beta El\nu^2, \quad \beta_\nu = \alpha_\nu^2 - 4El\nu^2, \quad \gamma_\nu = 1 + \nu^2 El(\beta - 2), \\ a_\nu &= 1 + \frac{\gamma_\nu}{\beta_\nu}, \quad b_\nu = 1 - \frac{\gamma_\nu}{\beta_\nu}, \quad p_\nu = -\frac{\alpha_\nu}{2El} + \frac{\beta_\nu}{2El}, \quad q_\nu = -\left(\frac{\alpha_\nu}{2El} + \frac{\beta_\nu}{2El}\right). \end{aligned} \tag{6.3}$$

Analytical expressions for the components of stress may be found in detail within the appendix of the 1992 paper by Carew, Townsend and Webster[9] or in the 2004 paper of Van Os and Phillips[59] with whom we draw comparisons.

Care must be taken with the infinite sums when implementing this solution in code. Following Van Os and Phillips, we choose to include a fixed number of terms, typically chosen to be 20 in our computations. Choosing more terms can have a negative impact on the performance of our solver, with the analytical solution taking longer to compute than that produced by our numerical scheme, although this is something we wish to address in the future.

We impose zero initial conditions for stress and velocity and apply the known analytical solution for velocity at both inflow and outflow and for stress only at inflow. No-slip and no-penetration conditions are imposed on the walls at the top and bottom of the channel.

In order to push the limits of our scheme we consider a fixed value of $Re = 1.0$ and, with the ratio of We to Re being an important factor, we vary We. The viscosity ratio is fixed at $\beta = \frac{1}{9}$ and we consider $We = 1, 10, 100$. We note that the original solution is valid for creeping flow (i.e. small Re). However, we wish to compare directly to the work of Van Os and Phillips[59], so we match their choice of parameter and hence use $Re = 1$.

Domain, Mesh and Timestepping

We choose the same domain, of length L and fixed height $H = 1$ as for the Newtonian counterpart to this problem. Similarly, meshes $T1$-$T4$ shown in Figure 3.3 are used. However, contrary to the Newtonian fluid, we vary the value of L for this model. Values $L = 8, 16, 32, 64$ are used in order to investigate dependence of L on the temporal stability of our scheme. Timesteps ranging from $\Delta t = 10^{-1}$ to $\Delta t = 10^{-4}$ are considered. A time limit of 40 time units is imposed, assuming the simulation has not already diverged, at which point the simulation is terminated.

Results

We use the same test points as in the Newtonian simulation, marked in Figure 3.3, with the velocity measured at the penultimate GLL-node in the centre of the channel (point B in the figure) and the stress measured on the penultimate GLL point on the lower wall (point C in the figure). We begin by considering the maximum channel length, $L = 64$ where we expect the most stability for our numerical scheme.

Figures 6.2(a)- 6.2(c) show the non-zero velocity and stress values at their respective test points for a moderate choice of Δt, K and N for $We = 1$. We see an almost indistinguishable difference between the computed and analytical for velocity, but slight over- and under-shoots for τ_{xx}, as well as small visual disagreement with the solution for τ_{xy}. The differences at the first peak, where our solution overshoots, are 3.056×10^{-4} (0.011%) for u_x, 0.7511 (2.3631%) for τ_{xx} and 0.0174 (0.3875%) for τ_{xy}. These results match closely with those of Van Os and Phillips.

We note that the analytical expression for the τ_{xx} component of elastic stress contains multiple infinite sums, so one would expect this to differ most from the true solution when the infinite sum is truncated. Further, those sums dominate the solution at lower values of t as seen in Figure 6.1 which shows the difference between the τ_{xx} solution using 20 terms against using 100 at the stress test point. We can see that it is clear that the largest difference is to be seen in the first 5-10 time units, peaking at a difference of almost 0.09. Since the stress is prescribed only at inflow, this could be a possible cause of instability or additional numerical error, particularly during the

transient stage of the flow, due to a mismatch with the error-prone solution set at inflow and that computed by the scheme at outflow which may be closer to the true solution. This may warrant further investigation at a later time, but we continue to investigate the error and stability of our solutions.

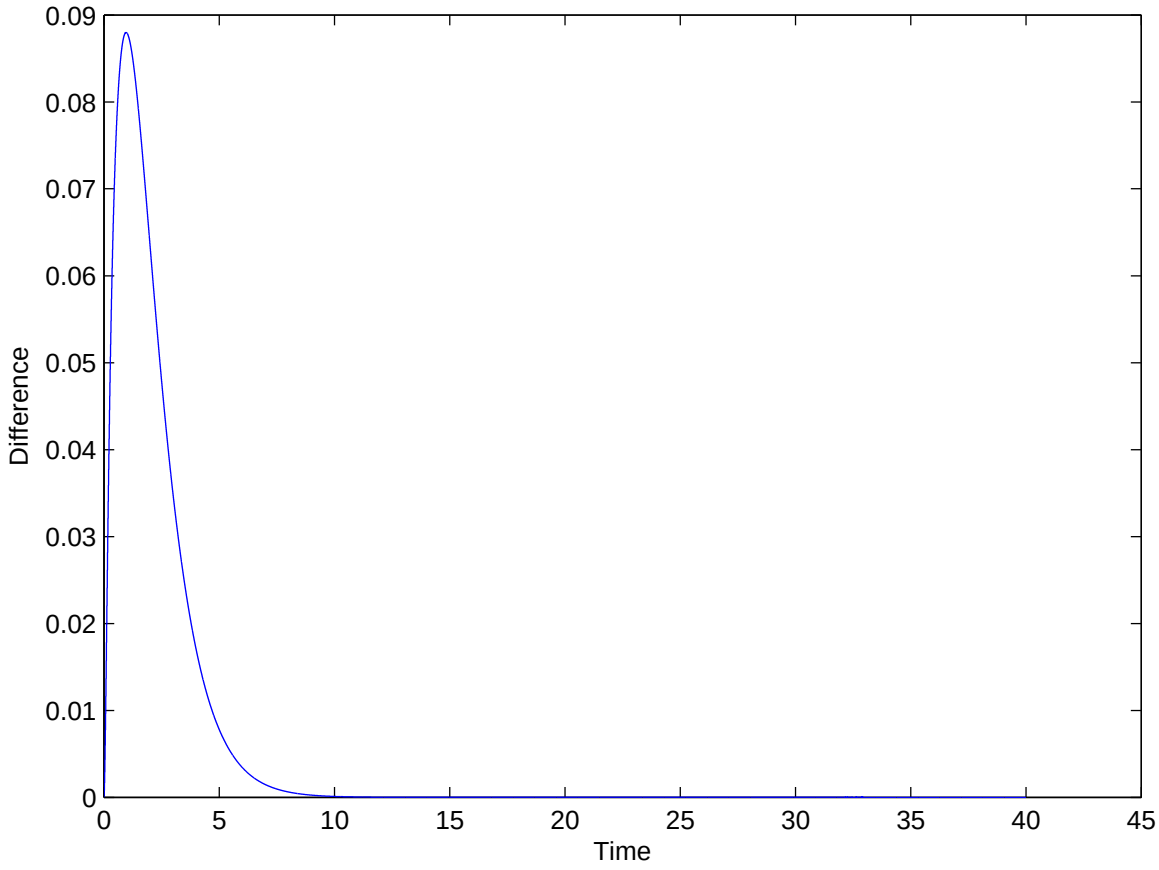

Figure 6.1: Difference of the value of analytical τ_{xx} using a truncated sum of 20 terms from that computed using 100 terms at the stress test point. Performed at $We = 1$, $\beta = \frac{1}{9}$, $Re = 1.0$.

Following the narrative from the Newtonian results, we investigate the error in more detail by looking at the instantaneous error in the H^1-norm at particular points in time and time-averaged error defined in (5.4). Concentrating on the effect of temporal refinement, Table 6.1 shows the velocity error at 4 points in time for $We = 1$ for varying Δt. We see improvement up to $\Delta t = 10^{-3}$ for each time point and a reduction in the

error as the flow nears its steady state, with the more refined mesh performing slightly better. However, the convergence to the analytical solution appears to stagnate at $\Delta t = 10^{-4}$. We consider $N = 16$ in Table 6.2 with the intention of eliminating spatial error as the dominating contribution. Unfortunately, the results are very similar showing minimal improvements in places which indicates that temporal discretisation error is the culprit. However, the error is consistently worse for values of $\Delta t \leq 10^{-3}$ on $T4$.

This makes it difficult to obtain the 2^{nd}-order accuracy of our numerical scheme although we may observe some positives in Table 6.3 which shows the time-averaged errors. Mesh $T1$ shows improvement with 2^{nd}-order convergence to the solution from a timestep of 10^{-1} to 10^{-3} for sufficiently refined values of N. However, the problem of reaching a limit of error convergence around an order of 10^{-7} is still present.

When considering spatial refinement, keeping focus on Table 6.3, we see a similar picture. The improvement from $N = 4$ to $N = 8$ is clear for all values of Δt, but we quickly hit the same wall in error. The mesh plays a role in what this limit may be, for example, fixing $\Delta t = 10^{-4}$ for meshes with refinement in the x-direction, T3 and T4, we see a vast improvement from $N = 4$ to $N = 8$ to an order of 10^{-6}, but any further polynomial refinement results in growth of the error. This behaviour is not seen with T1 and T2, which features no additional elements in the x-direction, although it also appears to be nearing a limit at an order of 10^{-7}. We assume that these observations are related to the inherent instability of the solution, particularly with refinement in the x-direction as mentioned by Van Os and Phillips. They did not present any errors with which we can directly compare.

We can, however, compare with work in the thesis of Lind [30] who obtained results for these fluid parameters using a 2×2 (T4) mesh with $N = 6$ and $\Delta t = 10^{-2}$ with an implicit Euler scheme. His E_u values were 1.44×10^{-4} for $L = 16$ and 3.92×10^{-4} for $L = 8$. While we did not obtain results for $N = 6$ for our tables, we did match these parameters and got $E_u = 1.34 \times 10^{-4}$ for $L = 16$, although the solution diverged for $L = 8$. Using $N = 4$ we got $E_u = 1.058 \times 10^{-4}$ for $L = 8$ and 1.37×10^{-4} for $L = 16$. The rise in error is slightly unexpected, but it is a small amount, and with increasing L, it reduces below the $L = 8$ value. Overall though, these results match well with those of Lind, with the 1^{st}-order scheme providing slightly more stability than our 2^{nd}-order

scheme.

Van Os and Phillips also looked at the sensitivity of the length of the channel, as well as the number of downstream elements. Table 6.4 shows the approximate time at which our solution diverged for each numerical parameter at $We = 1$. Van Os and Phillips did not consider values of $N > 6$ and used a fixed value of $\Delta t = 10^{-2}$, whereas we consider up to $N = 16$ and $\Delta t = 10^{-4}$ which is due to the additional computing power available today. Discounting the $\Delta t = 10^{-1}$ results, which are arguably under-refined in time, we see that there is little difference in the stability of the solution with increasing temporal refinement, with very small gains to be found for those which diverged and no gains in terms of convergence.

For a single element, we don't see the onset of divergence until the higher values of $N > 12$, and only for the $L = 8$ and $L = 16$ cases, which suggests that there is more to the instability than transmission across spectral element boundaries. Van Os and Phillips suggested that there was a weak influence on divergence from refinement in the cross-stream direction, and our results do support that. Firstly, with twice as many cross-stream points in T2 than T1 for any value of N, we see that the onset of instability occurred earlier for T2. Further, comparing T2 against T3 in the cases of divergence we see that the onset of instability occurred later on for T2 than T3. In comparison to Van Os and Phillips' scheme, we see that the use of the DG method appears to offer some gains, which is expected if the spectral element interfaces are the primary cause of instability. For example, for $N = 6$, they see divergence on mesh T4 at $t \approx 4.1$ at $L = 8$ and $t \approx 10.8$ at $L = 16$ whereas for the same values of L, using $N = 8$, we reach $t \approx 12.6$ and reach convergence, respectively. Note that, while our values of N are different, we'd expect using a larger value to cause diverge in a shorter timespan.

For $We > 1.0$, Figures 6.3 and 6.4 show solutions computed for $We = 10$ and $We = 100$. For $We = 10$, we see excellent agreement for velocity and τ_{xy}, but there is a clear difference for τ_{xx}. Comparing to the same result from Van Os and Phillips, we see a similar discrepancy. Interestingly, Lind's results match far better using the implicit Euler scheme, which leads us to believe that keeping the numerical method as implicit as possible is important at higher We in terms of accuracy of the computed solution. The $We = 100$ result looks to be an improvement on the $We = 10$ result,

although the solution is far from steady by the time the simulation was terminated. It is quite possible that it would diverge given a longer time limit. However, these results demonstrate that our scheme is capable of reaching high values of We. The time of divergence for these values of We are provided in Tables 6.5 and 6.6 and will be used to compare the performance of the DEVSS-G stabilisation.

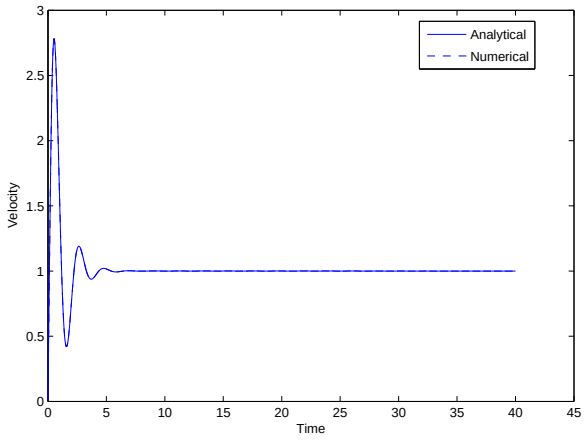

(a) u_x

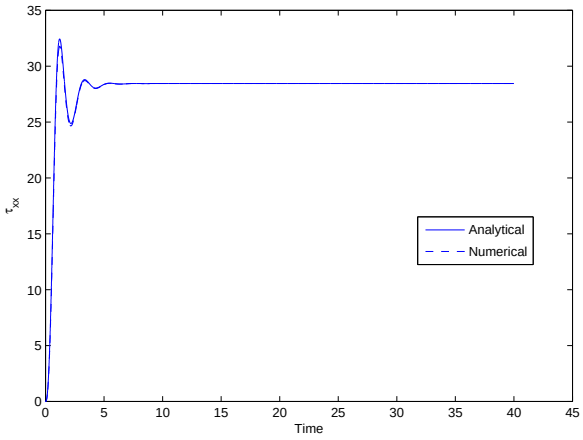

(b) τ_{xx}

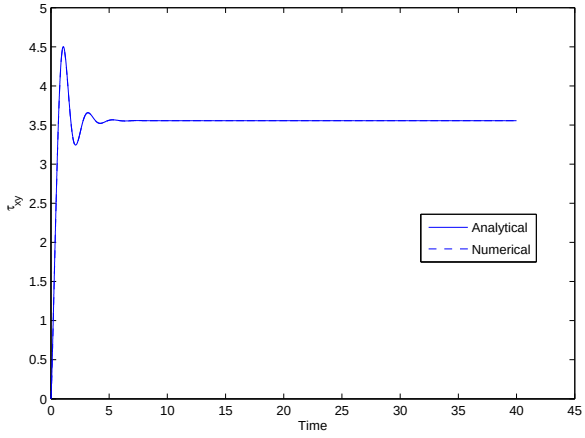

(c) τ_{xy}

Figure 6.2: Comparison of numerical and analytical solutions at the chosen test points for planar Oldroyd B start-up of Poiseuille flow for $\beta = \frac{1}{9}$, $Re = 1.0$, $We = 1$. Parameters used are $\Delta t = 10^{-3}$, mesh $T1$, $L = 64$, $N = 8$.

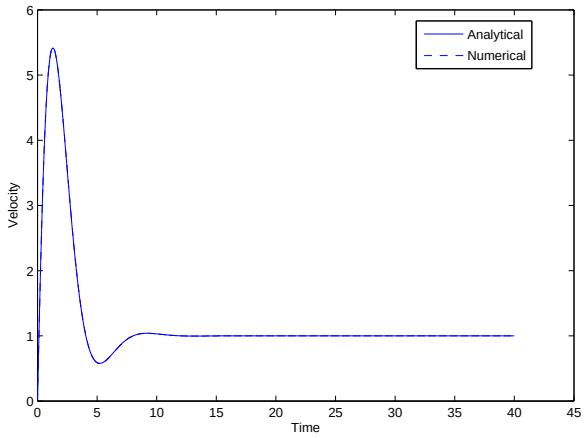

(a) u_x

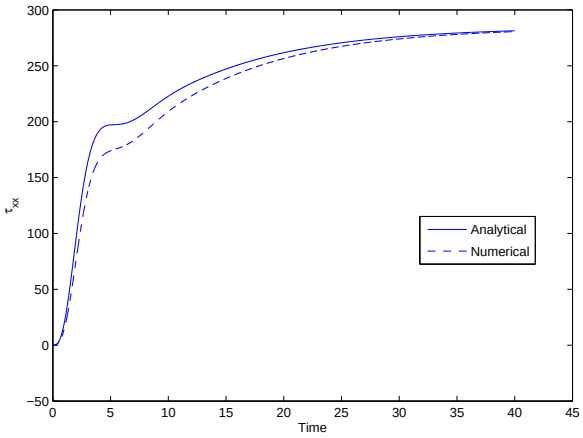

(b) τ_{xx}

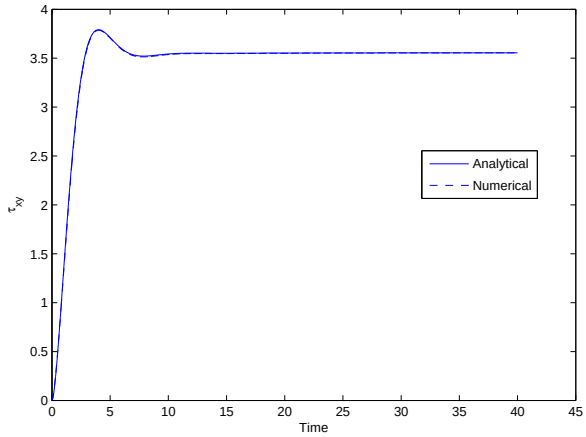

(c) τ_{xy}

Figure 6.3: Comparison of numerical and analytical solutions at the chosen test points for planar Oldroyd B start-up of Poiseuille flow for $\beta = \frac{1}{9}$, $Re = 1.0$, $We = 10$. Parameters used are $\Delta t = 10^{-3}$, mesh $T1$, $L = 64$, $N = 4$.

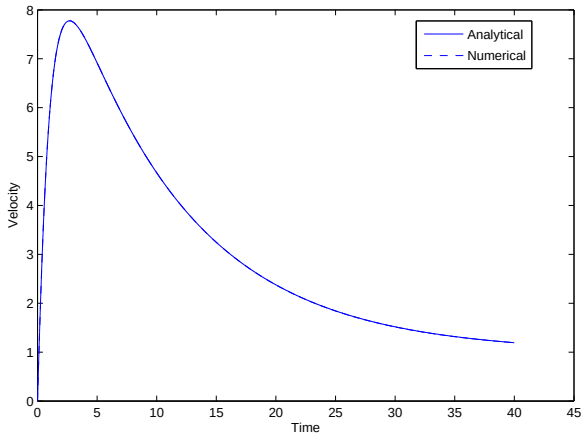

(a) u_x

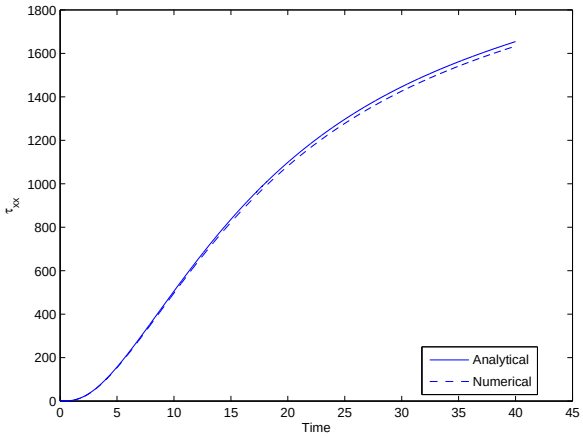

(b) τ_{xx}

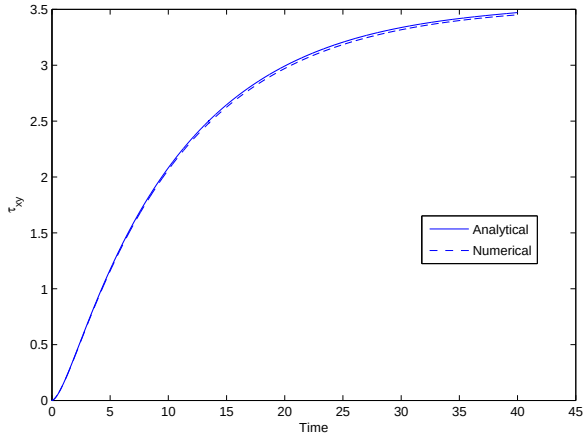

(c) τ_{xy}

Figure 6.4: Comparison of numerical and analytical solutions at the chosen test points for planar Oldroyd B start-up of Poiseuille flow for $\beta = \frac{1}{9}$, $Re = 1.0$, $We = 100$. Parameters used are $\Delta t = 10^{-3}$, mesh $T1$, $L = 64$, $N = 4$.

Mesh	Δt	time = 0.5	time = 1	time = 2.5	time = 5
T1	0.1	1.9234e+00	5.4556×10^{-1}	5.8893×10^{-2}	8.6976×10^{-3}
	0.01	1.4328×10^{-2}	1.3427×10^{-2}	5.1813×10^{-3}	8.7647×10^{-4}
	0.001	5.5575×10^{-3}	2.2255×10^{-3}	4.9186×10^{-4}	9.6148×10^{-5}
	0.0001	5.3467×10^{-3}	1.9444×10^{-3}	4.6784×10^{-5}	1.8231×10^{-5}
T4	0.1	-	-	-	-
	0.01	1.7814×10^{-2}	1.4254×10^{-2}	9.0536×10^{-3}	3.2135×10^{-4}
	0.001	6.8002×10^{-3}	1.9647×10^{-3}	9.8241×10^{-4}	3.0958×10^{-5}
	0.0001	6.4042×10^{-3}	2.1602×10^{-3}	2.2386×10^{-4}	1.8125×10^{-5}

Table 6.1: Dependence of the H^1-norm of velocity error at select points in time for planar start-up Poiseuille flow of an Oldroyd B fluid, $We = 1$, $\beta = \frac{1}{9}$, $Re = 1.0$, on Δt on the meshes T1 and T4, $L = 64$, and $N = 8$.

Mesh	Δt	time = 0.5	time = 1	time = 2.5	time = 5
T1	0.1	1.9388e+00	5.4622×10^{-1}	8.6683×10^{-2}	2.7280×10^{-3}
	0.01	1.7233×10^{-2}	1.2979×10^{-2}	8.1965×10^{-3}	1.3048×10^{-4}
	0.001	7.4869×10^{-3}	3.7036×10^{-3}	8.4833×10^{-4}	6.3372×10^{-5}
	0.0001	7.1595×10^{-3}	4.1586×10^{-3}	4.4874×10^{-4}	6.5569×10^{-5}
T4	0.1	-	-	-	-
	0.01	2.0090×10^{-2}	1.4643×10^{-2}	4.8301×10^{-3}	1.2055×10^{-3}
	0.001	9.5687×10^{-3}	8.3320×10^{-3}	1.8916×10^{-3}	5.1125×10^{-4}
	0.0001	9.0707×10^{-3}	8.3535×10^{-3}	1.9071×10^{-3}	4.8524×10^{-4}

Table 6.2: Dependence of the H^1-norm of velocity error at select points in time for planar start-up Poiseuille flow of an Oldroyd B fluid, $We = 1$, $\beta = \frac{1}{9}$, $Re = 1.0$, on Δt on the meshes T1 and T4, $L = 64$, and $N = 16$.

Mesh	Δt	N = 4	N = 8	N = 12	N = 16
T1	0.1	1.6674×10^{-3}	1.4122×10^{-3}	1.3808×10^{-3}	1.3622×10^{-3}
	0.01	6.5458×10^{-4}	2.8546×10^{-5}	1.8176×10^{-5}	1.7107×10^{-5}
	0.001	6.8430×10^{-4}	4.6869×10^{-6}	1.6276×10^{-6}	9.2953×10^{-7}
	0.0001	6.8792×10^{-4}	3.5243×10^{-6}	1.2631×10^{-6}	7.0806×10^{-7}
T2	0.1	1.7092×10^{-3}	1.4213×10^{-3}	-	-
	0.01	7.7812×10^{-5}	2.8622×10^{-5}	1.8334×10^{-5}	1.6965×10^{-5}
	0.001	2.1108×10^{-5}	3.0018×10^{-6}	1.3423×10^{-6}	8.8657×10^{-7}
	0.0001	1.6373×10^{-5}	1.6347×10^{-6}	9.6615×10^{-7}	8.4297×10^{-7}
T3	0.1	2.0271×10^{-3}	1.4068×10^{-3}	-	-
	0.01	6.6418×10^{-4}	3.5897×10^{-5}	1.8356×10^{-5}	2.3833×10^{-5}
	0.001	6.6918×10^{-4}	5.7246×10^{-6}	3.7385×10^{-6}	7.7544×10^{-6}
	0.0001	6.7599×10^{-4}	3.6682×10^{-6}	3.7231×10^{-6}	7.4788×10^{-6}
T4	0.1	2.0985×10^{-3}	-	-	-
	0.01	1.2460×10^{-4}	3.5864×10^{-5}	1.8104×10^{-5}	2.4329×10^{-5}
	0.001	2.6861×10^{-5}	4.3832×10^{-6}	3.3609×10^{-6}	8.2395×10^{-6}
	0.0001	1.7959×10^{-5}	2.4162×10^{-6}	3.3652×10^{-6}	7.9071×10^{-6}

Table 6.3: Time-averaged velocity error, E_u, at the test point for planar start-up flow of an Oldroyd B fluid, $We = 1$, $\beta = \frac{1}{9}$, $Re = 1.0$, $L = 64$.

		N for $L = 8$				N for $L = 16$				N for $L = 32$				N for $L = 64$			
Mesh	Δt	4	8	12	16	4	8	12	16	4	8	12	16	4	8	12	16
T1	10^{-1}	C	C	6.0	0.4	C	C	C	24.3	C	C	C	C	C	C	C	C
	10^{-2}	C	C	23.3	11.2	C	C	C	34.6	C	C	C	C	C	C	C	C
	10^{-3}	C	C	25.3	13.9	C	C	C	38.2	C	C	C	C	C	C	C	C
	10^{-4}	C	C	25.6	15.2	C	C	C	38.6	C	C	C	C	C	C	C	C
T2	10^{-1}	C	C	6.3	0.4	C	C	11.4	6.4	C	C	14.5	7.1	C	C	16.3	7.6
	10^{-2}	C	C	15.9	11.0	C	C	C	23.9	C	C	C	C	C	C	C	C
	10^{-3}	C	C	17.7	14.3	C	C	C	26.1	C	C	C	C	C	C	C	C
	10^{-4}	C	C	18.2	13.7	C	C	C	26.6	C	C	C	C	C	C	C	C
T3	10^{-1}	34.9	1.2	0.4	0.2	C	4.6	1.4	0.4	C	C	5.2	1.9	C	C	8.0	4.0
	10^{-2}	C	14.1	6.3	5.5	C	C	15.7	9.8	C	C	C	29.0	C	C	C	C
	10^{-3}	C	14.2	7.3	6.1	C	C	16.9	11.8	C	C	C	31.8	C	C	C	C
	10^{-4}	C	14.2	7.6	5.7	C	C	17.1	12.5	C	C	C	32.1	C	C	C	C
T4	10^{-1}	C	1.3	0.4	0.2	C	2.9	1.4	0.4	C	6.2	3.2	1.8	C	8.7	3.9	3.6
	10^{-2}	C	12.6	7.7	6.0	C	C	14.2	9.7	C	C	C	18.8	C	C	C	C
	10^{-3}	C	13.5	10.4	5.6	C	C	15.7	12.1	C	C	C	20.7	C	C	C	C
	10^{-4}	C	13.7	10.8	5.4	C	C	16.0	13.3	C	C	C	21.1	C	C	C	C

Table 6.4: Convergence of simulation for planar start-up of Poiseuille flow for an Oldroyd B fluid, $We = 1$, $\beta = \frac{1}{9}$, $Re = 1.0$. If the simulation completed it is marked with a "C", otherwise the approximate time the simulation diverged is shown

		N for $L = 8$				N for $L = 16$				N for $L = 32$				N for $L = 64$			
Mesh	Δt	4	8	12	16	4	8	12	16	4	8	12	16	4	8	12	16
T1	10^{-1}	7.0	2.4	0.7	0.4	C	5.1	2.2	0.9	C	23.2	5.2	2.9	C	C	19.3	7.1
	10^{-2}	8.8	2.9	2.0	1.7	C	5.5	2.7	2.1	C	23.4	5.4	3.1	C	C	20.7	7.4
	10^{-3}	8.8	2.9	2.0	1.7	C	5.6	2.7	2.1	C	23.4	5.5	3.1	C	C	21.0	7.5
	10^{-4}	8.8	2.9	2.0	1.7	C	5.6	2.7	2.2	C	23.4	5.5	3.1	C	C	21.0	7.5
T2	10^{-1}	14.6	2.2	0.7	0.4	C	6.3	1.9	0.9	C	13.7	4.4	1.8	C	C	12.1	4.4
	10^{-2}	14.1	2.7	2.0	1.8	C	5.2	2.6	2.1	C	12.2	4.5	2.9	C	C	10.6	5.1
	10^{-3}	13.9	2.7	2.0	1.8	C	5.2	2.6	2.1	C	12.0	4.5	3.0	C	C	10.3	5.1
	10^{-4}	13.9	2.7	2.0	1.8	C	5.2	2.6	2.1	C	11.9	4.5	3.0	C	C	10.3	5.1
T3	10^{-1}	2.1	0.7	0.3	0.2	6.2	2.2	0.7	0.4	16.8	3.3	2.2	0.9	C	11.7	3.8	2.5
	10^{-2}	3.1	1.8	1.6	1.5	5.7	2.6	1.9	1.7	23.1	4.0	2.5	2.1	C	10.8	4.1	2.8
	10^{-3}	3.2	1.8	1.6	1.6	5.3	2.6	2.0	1.7	24.3	4.0	2.6	2.1	C	10.7	4.1	2.8
	10^{-4}	3.2	1.8	1.6	1.6	5.3	2.6	2.0	1.7	24.4	4.0	2.6	2.1	C	10.7	4.1	2.8
T4	10^{-1}	3.7	0.7	0.3	0.2	11.2	2.2	0.7	0.4	39.8	4.2	1.6	0.9	C	16.2	3.9	1.5
	10^{-2}	5.0	1.9	1.6	1.5	11.1	2.6	2.0	1.8	C	4.6	2.5	2.1	C	10.8	4.2	2.8
	10^{-3}	4.9	1.9	1.6	1.5	11.1	2.6	2.0	1.8	C	4.6	2.5	2.1	C	10.6	4.2	2.8
	10^{-4}	4.9	1.9	1.6	1.5	11.1	2.6	2.0	1.8	C	4.6	2.5	2.1	C	10.6	4.2	2.8

Table 6.5: Convergence of simulation for planar start-up of Poiseuille flow for an Oldroyd B fluid, $We = 10$, $\beta = \frac{1}{9}$, $Re = 1.0$. If the simulation completed it is marked with a "C", otherwise the approximate time the simulation diverged is shown

		N for $L = 8$				N for $L = 16$				N for $L = 32$				N for $L = 64$			
Mesh	Δt	4	8	12	16	4	8	12	16	4	8	12	16	4	8	12	16
T1	10^{-1}	7.8	2.1	0.7	0.4	10.3	6.0	1.7	0.9	24.5	8.3	5.9	2.2	C	14.6	10.4	6.9
	10^{-2}	9.1	5.2	3.8	3.3	13.2	7.5	5.2	3.8	28.1	10.1	6.6	4.9	C	20.7	9.7	7.0
	10^{-3}	8.8	5.5	3.9	3.3	14.7	6.9	5.0	3.8	28.2	12.5	6.7	4.9	C	20.3	9.5	6.9
	10^{-4}	8.8	5.3	3.9	3.3	16.2	6.8	5.0	3.9	27.7	12.4	6.7	4.9	C	20.3	9.5	6.9
T2	10^{-1}	7.5	1.8	0.7	0.4	19.3	4.9	1.6	0.9	38.9	7.3	4.4	2.0	C	12.0	6.4	4.3
	10^{-2}	9.2	4.8	3.5	3.4	22.1	6.2	4.5	4.0	C	9.2	5.8	5.1	C	14.8	8.2	5.9
	10^{-3}	9.9	4.8	3.6	3.5	21.5	6.2	4.8	4.0	C	8.8	5.9	5.1	C	15.0	8.3	6.5
	10^{-4}	9.7	4.8	3.6	3.5	21.5	6.1	4.8	4.0	C	8.7	5.9	5.1	C	14.9	8.2	6.4
T3	10^{-1}	4.1	0.7	0.3	0.2	5.4	1.8	0.7	0.4	9.2	5.7	1.7	0.9	17.6	7.6	5.5	2.1
	10^{-2}	4.9	3.3	3.0	1.6	6.8	4.6	3.7	3.5	10.9	6.4	4.4	4.0	20.0	9.5	5.8	4.9
	10^{-3}	4.8	3.5	3.5	3.1	6.6	5.0	3.7	3.5	10.6	6.6	4.5	4.0	18.8	9.2	5.8	4.9
	10^{-4}	4.8	3.5	3.4	3.1	6.6	5.1	3.7	3.6	10.6	6.7	4.5	4.0	17.9	9.2	5.8	4.9
T4	10^{-1}	4.5	0.7	0.3	0.2	8.6	1.7	0.7	0.4	13.1	4.7	1.5	0.9	27.3	6.7	4.4	1.6
	10^{-2}	6.0	3.6	3.2	1.6	10.4	4.4	3.6	3.3	17.0	5.8	4.5	3.9	37.6	8.2	5.9	4.9
	10^{-3}	6.8	3.6	3.2	3.0	10.0	4.5	3.6	3.3	16.6	5.9	4.5	3.9	39.7	8.3	6.0	5.1
	10^{-4}	6.6	3.6	3.2	3.0	10.0	4.5	3.6	3.3	16.4	5.9	4.5	3.9	38.7	8.4	6.0	5.1

Table 6.6: Convergence of simulation for planar start-up of Poiseuille flow for an Oldroyd B fluid, $We = 100$, $\beta = \frac{1}{9}$, $Re = 1.0$. If the simulation completed it is marked with a "C", otherwise the approximate time the simulation diverged is shown

DEVSS-G Results

Now that we have investigated the performance of our numerical scheme using DG, we look at the effect of stabilisation using the DEVSS-G scheme. We consider two values of the stabilisation parameter, $\beta_s = 0.5, 1.0$. Tables 6.7 and 6.8 show the time-averaged errors, E_u, which can be directly compared to the DG-only results in Table 6.3. At $\beta_s = 0.5$ we can see clearly that there is a fairly consistent rise in the error of order 10 in each result, particularly at lower values of N where the issue of the analytical solution being under resolved is not present. Increasing to $\beta_s = 1.0$, the error increases slightly, but only at the trailing digit. This is in line with the results of Fiétier and Deville [16] who employed a DEVSS method for start-up of Poiseuille flow (folllowed by a decay), and found an error increase during the transient phase of their simulations.

We are now interested in any improvement in stability through the use of the DEVSS-G method. Tables 6.9 and 6.10 show the approximate time of divergence for $We = 1$ for $\beta_s = 0.5$ and $\beta_s = 1.0$ respectively. These should be directly compared with Table 6.4. In both cases we see a vast improvement in the time taken before the approximation diverges as well as reaching a converged solution for higher values of N and lower values of L which we interpret as additional stability. Using $\beta_s = 1.0$ instead of 0.5 gives additional stability in all cases except $\Delta t = 10^{-1}$(which we have previously discounted as insufficient). On mesh T4, where we saw the most instability in the DG-only results, we are able to reach convergence for all values of N up to 16 above $L = 32$ using $\beta_s = 1.0$, although for $\beta_s = 0.5$, we are unable to reach convergence for $L = 32$ at $N = 16$. This again agrees with the results of Fiétier and Deville[16].

Mesh	Δt	N = 4	N = 8	N = 12	N = 16
T1	0.1	3.2766×10^{-3}	-	-	-
	0.01	3.9348×10^{-3}	1.2778×10^{-4}	1.0007×10^{-4}	9.2719×10^{-5}
	0.001	3.9239×10^{-3}	4.2070×10^{-5}	2.5716×10^{-6}	1.7565×10^{-6}
	0.0001	3.9223×10^{-3}	4.1317×10^{-5}	1.7292×10^{-6}	1.1060×10^{-6}
T2	0.1	-	-	-	-
	0.01	2.3421×10^{-4}	1.0084×10^{-4}	1.0005×10^{-4}	9.2866×10^{-5}
	0.001	1.2309×10^{-4}	2.1952×10^{-6}	1.7103×10^{-6}	2.0865×10^{-6}
	0.0001	1.2279×10^{-4}	1.2682×10^{-6}	8.9690×10^{-7}	1.6561×10^{-6}
T3	0.1	3.4935×10^{-3}	-	-	-
	0.01	3.9371×10^{-3}	1.4151×10^{-4}	1.0502×10^{-4}	1.0965×10^{-4}
	0.001	3.9080×10^{-3}	4.1836×10^{-5}	3.8382×10^{-6}	9.6380×10^{-6}
	0.0001	3.9047×10^{-3}	4.0678×10^{-5}	3.5824×10^{-6}	8.9456×10^{-6}
T4	0.1	-	-	-	-
	0.01	3.0139×10^{-4}	1.1343×10^{-4}	1.0465×10^{-4}	1.1031×10^{-4}
	0.001	1.4774×10^{-4}	2.8551×10^{-6}	3.0706×10^{-6}	1.0666×10^{-5}
	0.0001	1.4733×10^{-4}	1.7071×10^{-6}	2.8276×10^{-6}	9.9305×10^{-6}

Table 6.7: Time-averaged velocity error, E_u, at the test point using DEVSS-G, $\beta_s = 0.5$, for planar start-up flow of an Oldroyd B fluid, $We = 1$, $\beta = \frac{1}{9}$, $Re = 1.0$, $L = 64$.

Mesh	Δt	N = 4	N = 8	N = 12	N = 16
T1	0.1	3.9655×10^{-3}	-	-	-
	0.01	4.7237×10^{-3}	2.4111×10^{-4}	2.1382×10^{-4}	1.8631×10^{-4}
	0.001	4.7195×10^{-3}	4.8280×10^{-5}	3.5762×10^{-6}	2.7629×10^{-6}
	0.0001	4.7184×10^{-3}	4.7202×10^{-5}	1.9020×10^{-6}	1.5647×10^{-6}
T2	0.1	-	-	-	-
	0.01	3.4911×10^{-4}	2.1343×10^{-4}	2.1324×10^{-4}	1.8637×10^{-4}
	0.001	1.3382×10^{-4}	2.8955×10^{-6}	2.7163×10^{-6}	3.4120×10^{-6}
	0.0001	1.3222×10^{-4}	1.1926×10^{-6}	9.2307×10^{-7}	2.4785×10^{-6}
T3	0.1	4.0972×10^{-3}	-	-	-
	0.01	4.7230×10^{-3}	2.7323×10^{-4}	2.3756×10^{-4}	2.4209×10^{-4}
	0.001	4.7063×10^{-3}	4.7841×10^{-5}	4.8958×10^{-6}	1.3980×10^{-5}
	0.0001	4.7040×10^{-3}	4.6498×10^{-5}	3.7612×10^{-6}	1.2540×10^{-5}
T4	0.1	-	-	-	-
	0.01	4.6785×10^{-4}	2.4211×10^{-4}	2.3610×10^{-4}	2.4255×10^{-4}
	0.001	1.7187×10^{-4}	3.4428×10^{-6}	4.1322×10^{-6}	1.5402×10^{-5}
	0.0001	1.7003×10^{-4}	1.5661×10^{-6}	2.7697×10^{-6}	1.4043×10^{-5}

Table 6.8: Time-averaged velocity error, E_u, at the test point using DEVSS-G, $\beta_s = 1.0$, for planar start-up flow of an Oldroyd B fluid, $We = 1$, $\beta = \frac{1}{9}$, $Re = 1.0$, $L = 64$.

		N for $L = 8$				N for $L = 16$				N for $L = 32$				N for $L = 64$			
Mesh	Δt	4	8	12	16	4	8	12	16	4	8	12	16	4	8	12	16
T1	10^{-1}	C	8.7	5.5	0.4	C	9.7	7.3	6.2	C	12.9	9.1	6.9	C	14.4	9.8	8.9
	10^{-2}	C	C	36.4	15.2	C	C	C	C	C	C	C	C	C	C	C	C
	10^{-3}	C	C	C	20.2	C	C	C	C	C	C	C	C	C	C	C	C
	10^{-4}	C	C	C	20.4	C	C	C	C	C	C	C	C	C	C	C	C
T2	10^{-1}	10.9	7.5	5.0	0.3	11.8	9.2	6.7	5.8	13.3	10.1	8.5	6.9	15.1	11.1	9.5	8.6
	10^{-2}	C	C	23.8	14.8	C	C	C	32.0	C	C	C	C	C	C	C	C
	10^{-3}	C	C	26.0	16.5	C	C	C	34.5	C	C	C	C	C	C	C	C
	10^{-4}	C	C	26.5	14.5	C	C	C	35.0	C	C	C	C	C	C	C	C
T3	10^{-1}	C	6.4	0.3	0.2	C	8.7	4.9	0.4	C	10.2	7.3	5.8	C	11.3	8.4	6.9
	10^{-2}	C	30.2	10.6	9.5	C	C	33.0	13.6	C	C	C	C	C	C	C	C
	10^{-3}	C	23.0	12.5	8.5	C	C	33.0	16.9	C	C	C	C	C	C	C	C
	10^{-4}	C	22.6	12.9	7.9	C	C	32.9	18.4	C	C	C	C	C	C	C	C
T4	10^{-1}	8.6	4.5	0.3	0.2	10.4	7.1	4.6	0.3	12.0	9.0	6.8	4.7	13.7	9.9	8.6	6.9
	10^{-2}	C	19.3	11.4	9.5	C	C	20.2	13.2	C	C	C	26.7	C	C	C	C
	10^{-3}	C	21.2	17.8	8.0	C	C	22.1	18.1	C	C	C	28.8	C	C	C	C
	10^{-4}	C	21.5	12.1	7.6	C	C	22.5	15.2	C	C	C	29.2	C	C	C	C

Table 6.9: Convergence of simulation using DEVSS-G, $\beta_s = 0.5$, for planar start-up of Poiseuille flow for an Oldroyd B fluid, $We = 1$, $\beta = \frac{1}{9}$, $Re = 1.0$. If the simulation completed successfully it is marked with a "C", otherwise the approximate time the simulation diverged is shown

		N for $L = 8$				N for $L = 16$				N for $L = 32$				N for $L = 64$			
Mesh	Δt	4	8	12	16	4	8	12	16	4	8	12	16	4	8	12	16
T1	10^{-1}	C	5.3	4.1	0.4	C	6.7	5.3	4.4	C	7.3	6.1	5.1	C	8.8	6.8	6.0
	10^{-2}	C	C	C	24.1	C	C	C	C	C	C	C	C	C	C	C	C
	10^{-3}	C	C	C	22.3	C	C	C	C	C	C	C	C	C	C	C	C
	10^{-4}	C	C	C	20.7	C	C	C	C	C	C	C	C	C	C	C	C
T2	10^{-1}	7.4	5.3	4.5	0.3	8.6	6.2	5.1	4.1	9.3	7.0	5.5	5.2	9.7	7.5	6.3	5.5
	10^{-2}	C	C	C	26.9	C	C	C	C	C	C	C	C	C	C	C	C
	10^{-3}	C	C	C	19.6	C	C	C	C	C	C	C	C	C	C	C	C
	10^{-4}	C	C	C	18.8	C	C	C	C	C	C	C	C	C	C	C	C
T3	10^{-1}	37.8	3.6	0.4	0.2	C	4.8	3.5	0.4	C	5.7	5.3	4.1	C	6.5	6.1	5.2
	10^{-2}	C	C	14.3	3.6	C	C	C	20.6	C	C	C	C	C	C	C	C
	10^{-3}	C	C	17.4	11.1	C	C	C	27.6	C	C	C	C	C	C	C	C
	10^{-4}	C	C	18.2	10.4	C	C	C	20.6	C	C	C	C	C	C	C	C
T4	10^{-1}	6.1	4.0	0.3	0.2	7.2	5.2	3.5	0.3	8.4	6.3	5.1	3.5	8.9	7.0	5.6	5.1
	10^{-2}	C	38.0	17.4	3.6	C	C	33.1	20.8	C	C	C	C	C	C	C	C
	10^{-3}	C	39.8	16.6	10.6	C	C	35.8	19.4	C	C	C	C	C	C	C	C
	10^{-4}	C	40.0	15.7	10.1	C	C	36.3	18.3	C	C	C	C	C	C	C	C

Table 6.10: Convergence of simulation using DEVSS-G, $\beta_s = 1.0$, for planar start-up of Poiseuille flow for an Oldroyd B fluid, $We = 1$, $\beta = \frac{1}{9}$, $Re = 1.0$. If the simulation completed successfully it is marked with a "C", otherwise the approximate time the simulation diverged is shown

Further evidence of the improvement in stability using DEVSS-G can be observed in the results for $We = 10$ and $We = 100$, which can seen in Tables 6.11 and 6.12, respectively, for $\beta_s = 0.5$ and in Tables 6.13 and 6.14, respectively, for $\beta_s = 1.0$. These are to be compared with the DG-only results in Tables 6.5 and 6.6, respectively. Starting from $We = 10$, with DG-only attempting to reach convergence for any values beyond $N = 4, 8$ was fairly fruitless and times taken for the approximation to diverge are all fairly low, even when increasing L. Using $\beta_s = 0.5$ we see a small improvement in some of the $N = 4, 8$ results, but little gain elsewhere. Similarly, $\beta_s = 1.0$ provides a small improvement on top of those already seen, and allows us to reach convergence for $N = 4$ on mesh T3. The $We = 100$ results tell a similar story, with further convergence reached for $N = 4$, $L = 32$ for both values of β_s over the DG-only scheme, as well as pushing the T4 mesh for $N = 4$, $L = 64$ over the 40 time limit. Although, it is quite possible these would diverge if left to run longer given that the steady state has not been reached, even for the velocity as seen in Figure 6.4.

These results appear disheartening for the DEVSS-G stabilsation scheme but the solution is known to suffer from the problem of spurious oscillations. This is noted by Van Os and Phillips[59] where attention is drawn to the thesis of Fiétier[15] who showed that mesh discretisation has a strong impact on the location of the eigenvalues of the associated generalised eigenvalue problem, which can cause numerical instability. They further note that this fits well with other points made in the literature about the generation of spurious oscillations due to inadequate spatial resolution of the continuous spectrum. Despite these problems, we certainly achieved some improvement in terms of additional stability for the scheme, and the trade-off in error is certainly manageable.

		N for $L = 8$				N for $L = 16$				N for $L = 32$				N for $L = 64$			
Mesh	Δt	4	8	12	16	4	8	12	16	4	8	12	16	4	8	12	16
T1	10^{-1}	15.4	3.5	0.6	0.4	C	7.0	2.9	1.1	C	21.4	5.9	3.1	C	C	19.0	8.3
	10^{-2}	15.7	3.3	2.2	1.9	C	7.4	2.9	2.3	C	22.5	5.6	3.0	C	C	19.6	7.6
	10^{-3}	15.4	3.2	2.2	1.9	C	7.3	2.9	2.3	C	22.6	5.7	3.0	C	C	19.7	7.6
	10^{-4}	15.3	3.2	2.2	1.9	C	7.3	2.9	2.3	C	22.6	5.7	3.1	C	C	19.8	7.6
T2	10^{-1}	18.3	3.2	0.5	0.4	C	6.8	2.6	0.6	C	14.6	5.5	2.4	C	C	13.6	6.5
	10^{-2}	20.9	3.1	2.2	1.9	C	7.5	2.9	2.4	C	22.4	5.7	3.1	C	C	19.7	6.9
	10^{-3}	20.8	3.1	2.2	1.9	C	7.5	2.9	2.4	C	22.1	5.7	3.1	C	C	18.8	7.0
	10^{-4}	20.8	3.1	2.2	1.9	C	7.5	2.9	2.4	C	22.0	5.7	3.1	C	C	18.7	7.0
T3	10^{-1}	3.2	0.7	0.3	0.2	11.5	3.1	0.6	0.4	28.2	5.8	2.9	1.1	C	20.7	6.1	3.2
	10^{-2}	3.4	2.3	1.9	1.8	13.3	3.2	2.2	1.9	30.1	5.6	2.9	2.3	C	21.7	6.1	3.0
	10^{-3}	3.4	2.3	1.9	1.7	13.7	3.2	2.2	1.9	30.5	5.6	2.9	2.3	C	21.8	6.2	3.1
	10^{-4}	3.4	2.3	1.9	1.7	13.8	3.2	2.2	1.9	30.5	5.6	2.9	2.3	C	21.8	6.2	3.1
T4	10^{-1}	7.7	0.7	0.2	0.1	17.9	2.9	0.6	0.4	C	6.9	2.7	0.6	C	16.1	5.8	2.7
	10^{-2}	7.1	2.3	1.8	1.6	16.7	3.2	2.2	1.9	C	6.8	3.0	2.4	C	17.1	5.8	3.1
	10^{-3}	7.1	2.3	1.8	1.6	16.6	3.2	2.2	1.9	C	6.7	3.0	2.4	C	16.5	5.8	3.1
	10^{-4}	7.1	2.3	1.8	1.6	16.6	3.2	2.2	1.9	C	6.7	3.0	2.4	C	16.5	5.7	3.1

Table 6.11: Convergence of simulation using DEVSS-G, $\beta_s = 0.5$, for planar start-up of Poiseuille flow for an Oldroyd B fluid, $We = 10$, $\beta = \frac{1}{9}$, $Re = 1.0$. If the simulation completed successfully it is marked with a "C", otherwise the approximate time the simulation diverged is shown

		N for $L = 8$				N for $L = 16$				N for $L = 32$				N for $L = 64$			
Mesh	Δt	4	8	12	16	4	8	12	16	4	8	12	16	4	8	12	16
T1	10^{-1}	10.1	2.9	0.6	0.4	20.8	7.6	2.8	0.7	C	11.0	6.6	3.9	C	18.5	11.6	8.2
	10^{-2}	10.6	5.9	4.3	4.1	22.4	8.7	6.0	4.4	C	13.3	7.3	5.5	C	32.5	11.3	7.5
	10^{-3}	10.6	6.6	5.2	4.2	22.9	9.5	6.1	4.5	C	15.2	8.1	5.4	C	31.7	10.8	7.5
	10^{-4}	10.6	6.7	5.1	4.2	22.9	8.9	6.2	4.5	C	15.4	9.0	5.4	C	31.6	10.8	7.5
T2	10^{-1}	9.3	2.7	0.6	0.2	18.6	5.6	2.4	0.6	C	9.4	5.1	2.6	C	17.6	8.0	5.6
	10^{-2}	10.9	5.9	4.3	4.0	21.8	7.8	5.2	4.9	C	11.6	7.0	5.6	C	20.3	9.6	6.8
	10^{-3}	10.6	6.0	4.5	4.1	21.4	7.4	5.3	4.8	C	10.8	7.2	5.9	C	18.9	9.8	7.6
	10^{-4}	10.6	5.9	4.5	4.1	21.4	7.4	5.3	4.8	C	10.8	7.2	5.9	C	18.9	9.8	7.8
T3	10^{-1}	5.0	0.7	0.3	0.2	7.6	3.1	0.6	0.4	12.3	7.2	2.8	0.8	22.5	11.1	6.5	4.2
	10^{-2}	5.9	4.6	3.8	3.5	7.8	5.4	4.4	4.1	12.4	7.6	5.7	4.8	22.5	12.5	7.3	5.8
	10^{-3}	5.9	4.5	4.2	4.0	7.8	6.0	4.7	4.5	12.5	8.0	5.7	5.0	22.5	12.5	7.4	5.8
	10^{-4}	5.9	4.5	4.2	4.1	7.8	6.3	4.7	4.6	12.5	8.0	5.7	5.0	22.5	12.5	7.5	5.8
T4	10^{-1}	5.3	0.7	0.2	0.1	9.3	2.7	0.6	0.2	18.2	6.4	1.8	0.6	C	8.9	5.3	1.9
	10^{-2}	6.3	4.5	4.1	3.6	10.4	5.5	4.7	4.3	19.4	7.6	5.6	4.8	C	10.6	6.5	5.8
	10^{-3}	6.3	4.6	4.4	4.1	10.2	5.6	4.7	4.4	19.5	7.3	5.5	4.8	C	12.4	6.9	5.9
	10^{-4}	6.3	4.7	4.3	4.1	10.2	5.6	4.7	4.4	19.6	7.3	5.5	4.8	C	11.8	6.9	5.9

Table 6.12: Convergence of simulation using DEVSS-G, $\beta_s = 0.5$, for planar start-up of Poiseuille flow for an Oldroyd B fluid, $We = 100$, $\beta = \frac{1}{9}$, $Re = 1.0$. If the simulation completed successfully it is marked with a "C", otherwise the approximate time the simulation diverged is shown

		N for $L = 8$				N for $L = 16$				N for $L = 32$				N for $L = 64$			
Mesh	Δt	4	8	12	16	4	8	12	16	4	8	12	16	4	8	12	16
T1	10^{-1}	22.2	3.8	0.6	0.2	C	7.9	3.4	0.7	C	22.2	6.6	3.4	C	C	18.4	8.2
	10^{-2}	22.9	3.5	2.4	2.0	C	8.0	3.0	2.4	C	23.5	6.0	3.1	C	C	18.2	7.7
	10^{-3}	23.9	3.4	2.4	2.0	C	8.0	3.0	2.4	C	23.6	6.0	3.2	C	C	18.3	7.7
	10^{-4}	24.0	3.4	2.4	2.0	C	8.0	3.0	2.4	C	23.6	6.0	3.2	C	C	18.3	7.7
T2	10^{-1}	20.8	3.6	0.5	0.2	C	7.2	2.8	0.6	C	15.8	5.9	2.9	C	C	16.4	6.5
	10^{-2}	26.8	3.4	2.3	2.0	C	8.4	3.0	2.5	C	24.4	5.8	3.2	C	C	18.9	7.2
	10^{-3}	26.8	3.4	2.3	2.0	C	8.4	3.1	2.5	C	24.4	5.8	3.2	C	C	19.0	7.2
	10^{-4}	26.8	3.4	2.3	2.0	C	8.4	3.1	2.5	C	24.3	5.9	3.2	C	C	19.0	7.2
T3	10^{-1}	3.9	0.7	0.2	0.2	16.0	3.9	0.6	0.3	C	8.6	3.3	0.7	C	22.6	7.2	3.4
	10^{-2}	3.9	2.5	2.0	1.9	15.3	3.6	2.4	2.0	C	8.3	3.1	2.4	C	24.6	5.6	3.1
	10^{-3}	4.0	2.5	2.0	1.8	14.3	3.6	2.4	2.0	C	8.3	3.1	2.4	C	24.7	5.6	3.1
	10^{-4}	4.0	2.5	2.0	1.8	14.2	3.6	2.4	2.0	C	8.3	3.1	2.4	C	24.8	5.6	3.1
T4	10^{-1}	8.4	0.7	0.2	0.1	19.3	3.6	0.6	0.2	C	8.5	3.0	0.6	C	19.2	6.7	2.9
	10^{-2}	8.5	2.6	1.9	1.7	22.3	3.6	2.3	2.0	C	8.4	3.0	2.5	C	18.8	5.7	3.2
	10^{-3}	8.5	2.6	2.0	1.7	22.3	3.6	2.3	2.0	C	8.3	3.1	2.5	C	19.0	5.7	3.2
	10^{-4}	8.5	2.6	2.0	1.7	22.3	3.6	2.3	2.0	C	8.3	3.1	2.5	C	19.0	5.7	3.2

Table 6.13: Convergence of simulation using DEVSS-G, $\beta_s = 1.0$, for planar start-up of Poiseuille flow for an Oldroyd B fluid, $We = 10$, $\beta = \frac{1}{9}$, $Re = 1.0$. If the simulation completed successfully it is marked with a "C", otherwise the approximate time the simulation diverged is shown

		N for $L = 8$				N for $L = 16$				N for $L = 32$				N for $L = 64$			
Mesh	Δt	4	8	12	16	4	8	12	16	4	8	12	16	4	8	12	16
T1	10^{-1}	11.8	3.2	0.6	0.2	26.8	5.3	1.9	0.7	C	12.2	6.5	3.9	C	21.0	12.0	7.7
	10^{-2}	12.5	6.3	4.5	4.4	26.6	10.1	6.4	4.8	C	15.1	7.6	5.8	C	33.8	12.1	8.1
	10^{-3}	12.5	6.9	5.6	4.6	26.7	10.3	6.3	4.9	C	16.8	8.2	5.8	C	34.0	11.4	8.0
	10^{-4}	12.5	7.2	5.5	4.6	26.7	10.4	6.2	4.9	C	17.0	8.5	5.8	C	34.0	11.4	8.0
T2	10^{-1}	11.1	2.7	0.6	0.2	23.0	5.9	1.7	0.6	C	10.4	5.6	2.2	C	19.1	8.5	5.6
	10^{-2}	12.8	6.1	4.9	4.3	26.8	8.1	5.7	5.1	C	12.6	7.9	6.1	C	23.2	10.5	7.5
	10^{-3}	12.5	6.7	5.0	4.6	26.4	8.6	5.7	5.1	C	12.4	7.8	6.4	C	22.8	10.7	8.0
	10^{-4}	12.4	6.7	5.0	4.6	26.4	8.9	5.7	5.1	C	12.3	7.8	6.4	C	22.6	10.7	8.1
T3	10^{-1}	6.1	0.7	0.2	0.2	9.2	3.4	0.6	0.2	16.4	7.1	2.8	0.7	30.0	12.3	6.5	4.1
	10^{-2}	6.5	4.9	3.9	3.1	9.5	6.0	4.5	4.4	16.2	8.0	6.3	5.0	30.4	14.8	7.8	6.3
	10^{-3}	6.5	5.7	4.7	4.4	9.5	6.4	5.3	4.9	16.2	9.0	6.6	5.2	30.4	14.1	8.0	6.2
	10^{-4}	6.5	5.3	4.7	4.2	9.5	6.5	5.4	4.8	16.2	9.6	6.6	5.2	30.5	14.0	8.0	6.2
T4	10^{-1}	5.5	0.7	0.2	0.1	9.9	2.1	0.6	0.2	23.0	6.1	1.7	0.6	C	9.4	5.6	1.6
	10^{-2}	6.9	4.9	4.3	2.1	13.3	6.3	5.4	4.6	25.7	8.2	6.3	4.9	C	12.0	7.0	6.2
	10^{-3}	7.2	5.4	4.7	4.1	12.1	6.8	5.4	4.8	25.8	8.6	6.2	4.9	C	12.2	7.3	6.1
	10^{-4}	7.2	5.9	4.7	4.2	12.0	6.9	5.4	4.8	25.8	8.8	6.2	4.9	C	12.2	7.3	6.1

Table 6.14: Convergence of simulation using DEVSS-G, $\beta_s = 1.0$, for planar start-up of Poiseuille flow for an Oldroyd B fluid, $We = 100$, $\beta = \frac{1}{9}$, $Re = 1.0$. If the simulation completed successfully it is marked with a "C", otherwise the approximate time the simulation diverged is shown

6.1.2 Axisymmetric Geometry

As for the planar case, there is an analytical solution for the analogous axisymmetric problem, start-up Poiseuille flow in a straight pipe of circular cross-section. Therefore we consider an Oldroyd B fluid using the analytical solution for start-up Poiseuille flow derived by Waters and King [63]. The non-trivial component of velocity at time t is given (in our non-dimensionalisation, adapted from [65]) by,

$$u_z(r,t) = A(r) - 8\sum_{n=1}^{\infty} \frac{J_0\left(rN_n\right)}{J_1\left(Z_n\right) Z_n^3} \exp\left(-\frac{\alpha_n t}{2El}\right) G_n\left(t\right), \tag{6.4}$$

where Z_n the n^{th} real and positive root of the Bessel function of zero order, J_0, $El = \frac{We}{Re}$ is the elasticity number, $A(r) = 1 - r^2$,

$$G_N(t) = \cosh\left(\frac{\beta_n t}{2El}\right) + \left[\frac{1 + Z_n^2 El\left(\beta - 2\right)}{\beta_n}\right] \sinh\left(\frac{\beta_n t}{2El}\right) \tag{6.5}$$

and,

$$\alpha_n = 1 + El\beta Z_n^2, \qquad \beta_n = \left[\left(1 + El\beta Z_n\right)^2 - 4El Z_n^2\right]^{1/2}. \tag{6.6}$$

While the planar solution to this problem has been widely used as a validation tool for numerical schemes, the axisymmetric version has received less attention with the only statement of the stress components of the problem to be found in the 1981 paper by Ryan and Dutta [51] who derived the shear stress. The solution may be derived in a similar fashion to that for the planar case. However, the solution is equally complicated and challenging to implement numerically so we instead choose to compute the velocity and its non-zero gradient component directly using the truncated sum of 20 terms, but approximate the constitutive equation using a BDF2 treatment of the temporal derivative in order to avoid having to compute the multiple infinite sums involved in the stress components.

At timestep t^{n+1}, assuming that we know u_z^{n+1} and $\frac{\partial u_z}{\partial r}^{n+1}$, we have,

$$\left(1 + \frac{We\gamma_0}{\Delta t}\right) \tau_{rz}^{n+1} = \left(1 - \beta\right) \frac{\partial u_z}{\partial r}^{n+1} + \frac{We}{\Delta t} \sum_{q=0}^{J-1} \alpha_q \tau_{rz}^{n-q}, \tag{6.7}$$

$$\left(1 + \frac{We\gamma_0}{\Delta t}\right) \tau_{zz}^{n+1} = 2We \frac{\partial u_z}{\partial r}^{n+1} \tau_{rz}^{n+1} + \frac{We}{\Delta t} \sum_{q=0}^{J-1} \alpha_q \tau_{zz}^{n-q}. \tag{6.8}$$

We compare our approximated analytical solution to that of Bodart and Crochet [4], who provide profiles of velocity and stress components, and get excellent agreement. Our approximated solution for τ_{zz} at the wall has been overlayed on their solution at the same point in Figure 6.5 to demonstrate this.

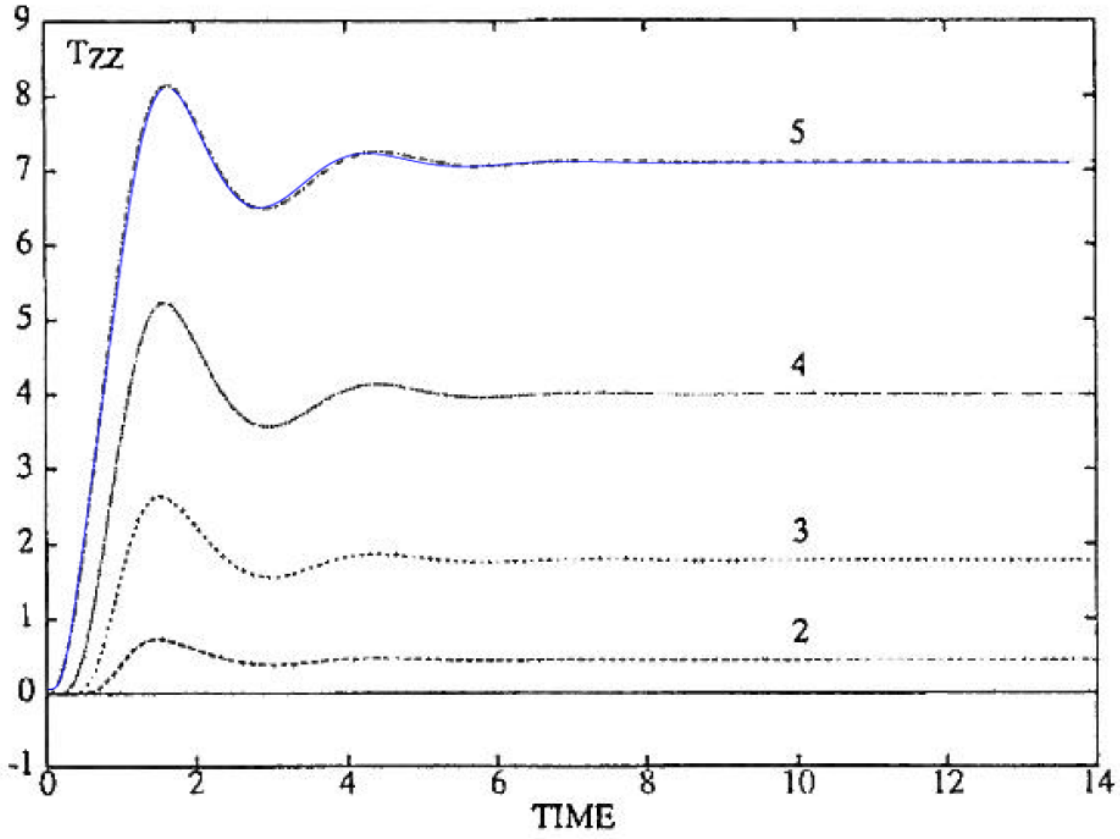

Figure 6.5: Overlay of our analytical approximation of τ_{zz}, in blue, on that of Bodart and Crochet [4]. The slight discrepancy is most likely due to the scan of the original paper rather than differences in the solution itself.

We proceed with confidence that our analytical solution is correct. We impose zero initial coniditions for stress and velocity and apply the analytical solution for velocity at inflow and outflow and for stress only at inflow. No-slip and no-penetration conditions are imposed on the wall at the top of the cylinder and symmetry wall conditions are applied at the centre of the cylinder, which is the bottom of our domain.

We fix the values of $Re = 1.0$ and $\beta = \frac{1}{9}$ and use values $We = 1, 10.0, 100.0$ in order to investigate the stability of our scheme for this flow.

Domain, Mesh and Timestepping

We use the same domain of length L and height $H = 2$ as used in the Newtonian counterpart to this problem in Section 5.1.2 although we vary the length of the cylinder, using $L = 8, 16, 32, 64$ as we did in the planar Oldroyd B study in Section 6.1.1. Timesteps ranging from $\Delta t = 10^{-1}$ to $\Delta t = 10^{-4}$ are considered and a time limit of 40 time units is imposed at which point the simulation is terminated if it has not already diverged.

Results

We measure the values of velocity and stress at the test points marked in Figure 3.3 using C (centre of cylinder) and A (top wall) respectively. Figure 6.6 shows the computed non-zero values of velocity and stress at their respective test point at $We = 1$. As with the planar case, there is excellent agreement at $We = 1$ and while the computed value of τ_{zz} still overshoots the analytical solution, it is less pronounced than the planar solution seen in Section 6.1.1, although the value of the stress is comparatively lower due to the diameter of the cylinder being twice that of the height of the channel considered in the planar case. On a single element, mesh T1, with $N = 8$, $L = 16$ and $\Delta t = 10^{-3}$ the difference between our solution and the computed analytical solution at the first peak is -3.7764×10^{-5} (-0.00154%) for velocity, 0.0708 (0.88%) for τ_{zz} and 0.0086 (0.4%). This compares very well with our planar results with τ_{xy} having roughly the same percentage error and a reduction in the magnitude of the percentage error for both velocity and τ_{zz} when compared to their planar counterparts. This difference may be due to the calculation of the analytical solution being more accurate using the BDF2 approximation over the truncation of the sums used in the planar version of the problem, although to confirm it would require comparison using the same method, or increasing the number of terms in the truncated sums. In terms of looking at the errors, we generally see a very similar picture to that seen in the planar case in Section 6.1.1. Tables 6.15 and 6.16 show the velocity in the H^1-norm at the same points in time as

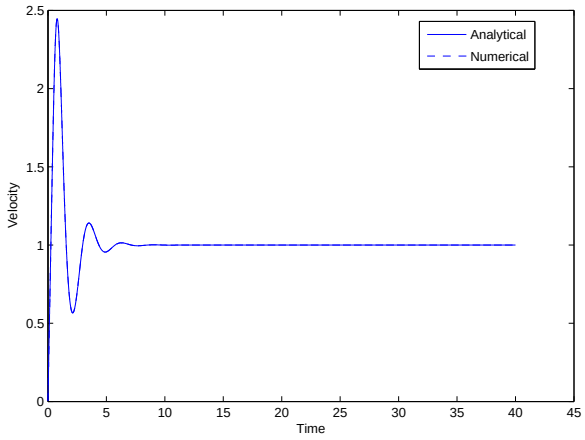

(a) u_z

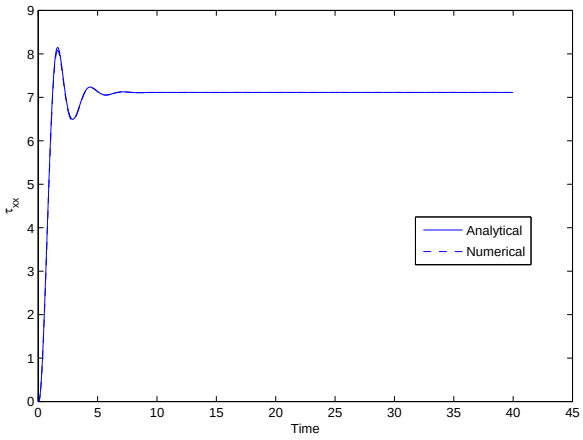

(b) τ_{zz}

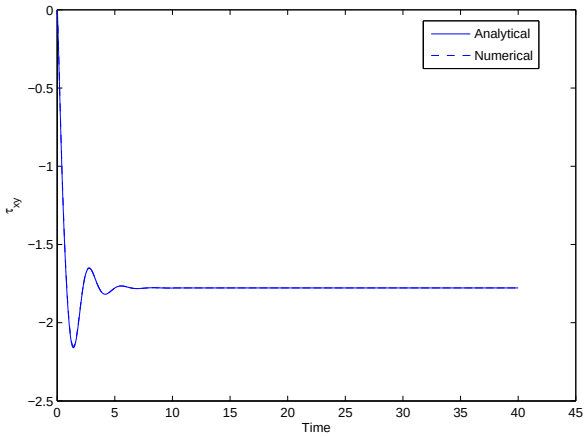

(c) τ_{rz}

Figure 6.6: Comparison of numerical and analytical solutions at the chosen test point for start-up of axisymmetric Poiseuille flow of an Oldroyd B fluid with $\beta = \frac{1}{9}$, $Re = 1.0$, $We = 1$. Parameters used are $\Delta t = 10^{-3}$, mesh $T1$, $L = 64$, $N = 8$.

we considered in the planar error analysis. We can observe a hint at 2^{nd}-order convergence with temporal discretisation, but we generally see the same problem as before, with a limit being quickly reached in terms of accuracy. We do note, however, that the error at time $t = 0.5$ is lower than was seen in the planar case. We note that the peak in the velocity value occurs later in the axisymmetric solution, but this does not fully explain the difference. Figure 6.7 shows the percentage errors for the velocity and τ_{zz} solutions for the planar and axisymmetric cases. We see that there is a large decrease in the velocity error just before $t = 0.5$ for u_z, so this difference seen in the table is not as important as it may first appear and we can see that both suffer from increased error for both velocity and stress in the transient stage of the flow. We also observe the same issue with refinement past a certain point in the downstream direction as seen in the planar version, although it appears to occur at higher levels of refinement. For example, using mesh T4, $\Delta t = 10^{-4}$ has a slightly smaller error at $t = 5$ using $N = 8$ compared to $N = 16$, whereas the same change in N results in a slight improvement in the error on mesh T1. The difference in H may explain this.

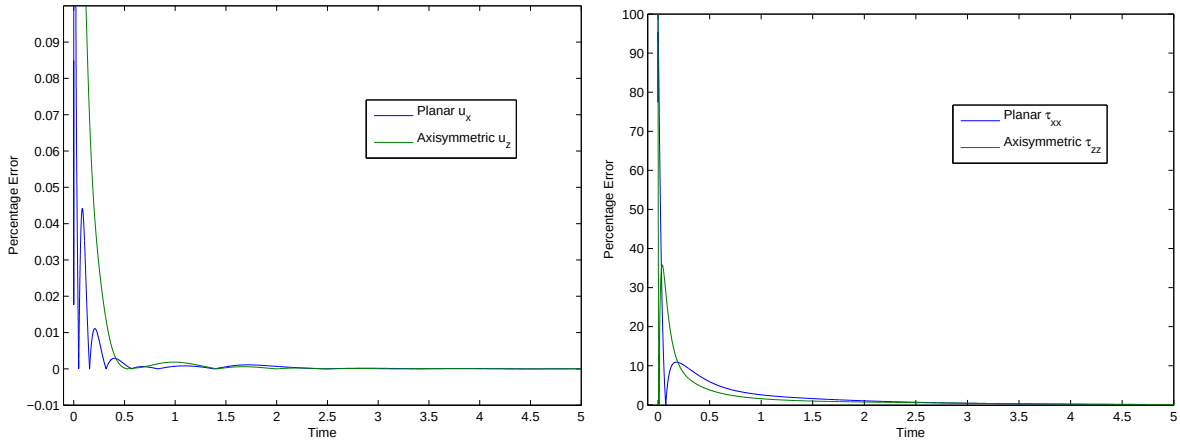

(a) u_x vs. u_z (b) τ_{zz} vs. τ_{zz}

Figure 6.7: Comparison of percentage error between the solutions produced by our numerical scheme for the planar and axisymmetric versions of start-up Poiseuille flow of an Oldroyd B fluid.

Table 6.17 shows the time-averaged error where we again see a clear limit in the error of order 10^{-6}. With this in mind, we see that refinement in the cross-stream direction improves the error with meshes T1-2 an order of magnitude behind T3-4 at $N = 4, 8$. For all meshes, $\Delta t = 10^{-3}$ is sufficient to reach the error limit, and we see a hint of

Mesh	Δt	time = 0.5	time = 1	time = 2.5	time = 5
T1	0.1	4.2402×10^{-2}	3.4836×10^{-2}	5.3466×10^{-3}	1.2472×10^{-3}
	0.01	4.6637×10^{-4}	7.5318×10^{-4}	4.5947×10^{-4}	1.2513×10^{-4}
	0.001	8.0499×10^{-5}	8.5364×10^{-5}	5.0167×10^{-5}	1.2970×10^{-5}
	0.0001	6.9789×10^{-5}	3.5814×10^{-5}	9.0072×10^{-6}	1.7281×10^{-6}
T4	0.1	-	-	-	-
	0.01	6.6074×10^{-4}	1.0691×10^{-3}	5.1508×10^{-4}	1.5676×10^{-4}
	0.001	6.2744×10^{-5}	1.0026×10^{-4}	4.7249×10^{-5}	1.4903×10^{-5}
	0.0001	5.7232×10^{-5}	3.9113×10^{-5}	2.3235×10^{-6}	6.5977×10^{-7}

Table 6.15: Dependence of velocity error in the H^1-norm of the numerical solution at points in time of axisymmetric start-up Poiseuille flow of an Oldroyd B. fluid, $We = 1$, $\beta = \frac{1}{9}$, $Re = 1.0$, on Δt on the meshes T1 and T4, length $L = 64$, and $N = 8$.

Mesh	Δt	time = 0.5	time = 1	time = 2.5	time = 5
T1	0.1	4.8281×10^{-2}	2.9312×10^{-2}	3.9284×10^{-3}	2.4587×10^{-4}
	0.01	5.3062×10^{-4}	8.4458×10^{-4}	9.2086×10^{-5}	3.1260×10^{-5}
	0.001	7.2432×10^{-5}	1.0501×10^{-4}	7.3388×10^{-6}	2.2486×10^{-6}
	0.0001	7.6528×10^{-5}	5.7313×10^{-5}	4.7334×10^{-6}	1.0801×10^{-6}
T4	0.1	-	-	-	-
	0.01	5.2440×10^{-4}	7.2511×10^{-4}	3.4853×10^{-4}	1.8653×10^{-5}
	0.001	4.8364×10^{-5}	8.5291×10^{-5}	3.2412×10^{-5}	2.7098×10^{-6}
	0.0001	4.9336×10^{-5}	3.3508×10^{-5}	2.6067×10^{-6}	1.5069×10^{-6}

Table 6.16: Dependence of velocity error in the H^1-norm of the numerical solution at points in time of axisymmetric start-up Poiseuille flow of an Oldroyd B. fluid, $We = 1$, $\beta = \frac{1}{9}$, $Re = 1.0$, on Δt on the meshes T1 and T4, length $L = 64$, and $N = 16$.

Mesh	Δt	N = 4	N = 8	N = 12	N = 16
T1	0.1	3.3430×10^{-3}	2.7823×10^{-3}	2.7930×10^{-3}	2.5022×10^{-3}
	0.01	5.8104×10^{-4}	3.2769×10^{-5}	2.8758×10^{-5}	2.9895×10^{-5}
	0.001	5.6018×10^{-4}	1.0696×10^{-5}	7.9993×10^{-6}	7.0197×10^{-6}
	0.0001	5.6073×10^{-4}	1.0002×10^{-5}	7.8672×10^{-6}	6.8087×10^{-6}
T2	0.1	2.7517×10^{-3}	2.7583×10^{-3}	-	-
	0.01	5.7401×10^{-5}	3.2894×10^{-5}	2.8496×10^{-5}	3.0387×10^{-5}
	0.001	1.5475×10^{-5}	8.6948×10^{-6}	6.5359×10^{-6}	7.0126×10^{-6}
	0.0001	1.3921×10^{-5}	7.9267×10^{-6}	6.4594×10^{-6}	6.5222×10^{-6}
T3	0.1	3.3579×10^{-3}	2.5572×10^{-3}	-	-
	0.01	5.7927×10^{-4}	3.0557×10^{-5}	2.6619×10^{-5}	2.1289×10^{-5}
	0.001	5.5076×10^{-4}	1.0779×10^{-5}	8.7400×10^{-6}	6.7602×10^{-6}
	0.0001	5.5198×10^{-4}	9.7969×10^{-6}	7.9539×10^{-6}	6.3403×10^{-6}
T4	0.1	2.8533×10^{-3}	-	-	-
	0.01	8.5332×10^{-5}	2.9977×10^{-5}	2.6037×10^{-5}	2.1398×10^{-5}
	0.001	1.7493×10^{-5}	8.9277×10^{-6}	7.2045×10^{-6}	7.3109×10^{-6}
	0.0001	1.4020×10^{-5}	8.2697×10^{-6}	6.4914×10^{-6}	6.4838×10^{-6}

Table 6.17: Time-averaged velocity error, E_u, at the test point for axisymmetric start-up flow of an Oldroyd B. Fluid, $We = 1$, $\beta = \frac{1}{9}$, $Re = 1.0$, $L = 64$.

2^{nd}-order convergence from $\Delta t = 10^{-1}$ to 10^{-2}. This is very much in line with the planar results.

Results for $We > 1$ are shown in Figures 6.8 and 6.9. We are able to compute the solution at $We = 10$ to a fairly high degree of accuracy with some visual differences from the solution, although the solution has not yet fully converged to the steady state within the time limit set. We also demonstrate the ability to compute a solution at $We = 100$ where the simulation has clearly not converged to the steady state, although it has reached the time limit set. It is possible the scheme would diverge from the analytical solution if we were to increase this time limit, however it demonstrates that our scheme is, at least, capable of simulating such values of We in both the planar and axisymmetric cases.

In terms of stability At $We = 1$, for $\Delta t \geq 10^{-2}$ the solution was stable up to the

specified time limit for all values of L and N on every mesh, which can be seen in Table 6.18. For the larger values of We, this was not the case so we will discuss the improvements using the DEVSS-G scheme at $We = 10, 100$ in the following section.

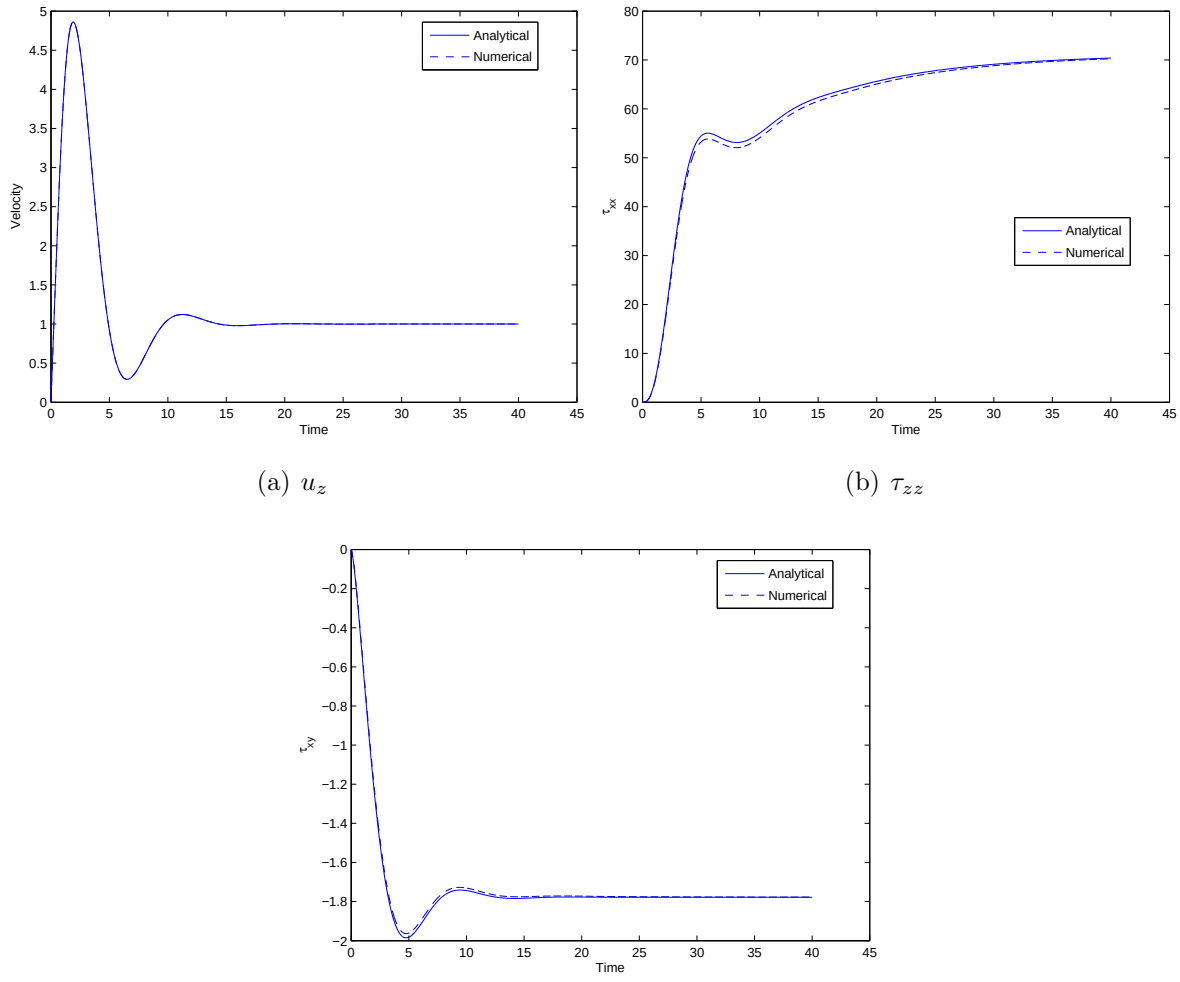

(a) u_z

(b) τ_{zz}

(c) τ_{rz}

Figure 6.8: Comparison of numerical and analytical solutions at the chosen test point for start-up of axisymmetric Poiseuille flow of an Oldroyd B fluid with $\beta = \frac{1}{9}$, $Re = 1.0$, $We = 10$. Parameters used are $\Delta t = 10^{-3}$, mesh $T1$, $L = 64$, $N = 8$.

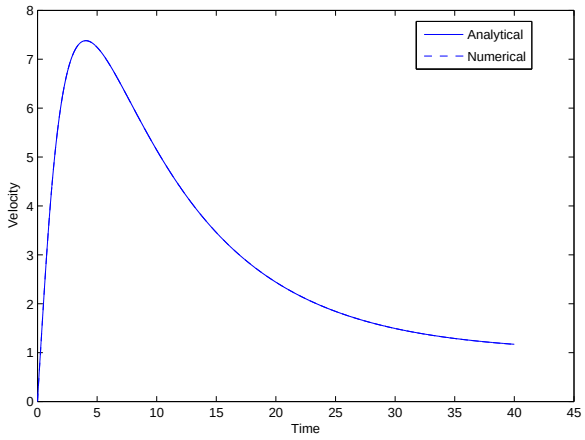

(a) u_z

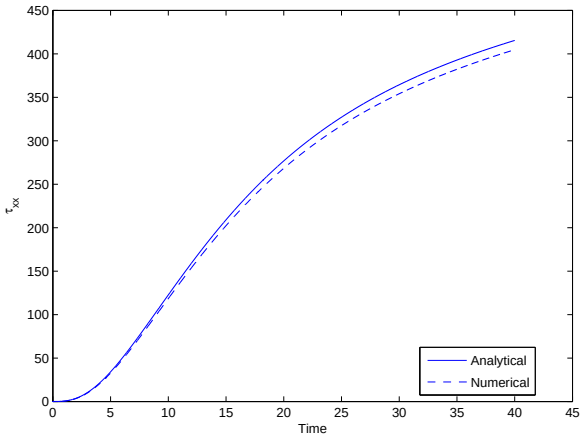

(b) τ_{zz}

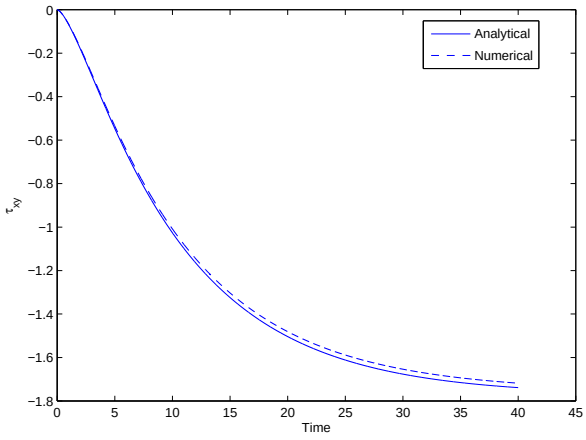

(c) τ_{rz}

Figure 6.9: Comparison of numerical and analytical solutions at the chosen test point for start-up of axisymmetric Poiseuille flow of an Oldroyd B fluid with $\beta = \frac{1}{9}$, $Re = 1.0$, $We = 100$. Parameters used are $\Delta t = 10^{-3}$, mesh $T1$, $L = 64$, $N = 4$.

		N for $L = 8$				N for $L = 16$				N for $L = 32$				N for $L = 64$			
Mesh	Δt	4	8	12	16	4	8	12	16	4	8	12	16	4	8	12	16
T1	10^{-1}	C	C	C	1.0	C	C	C	C	C	C	C	C	C	C	C	C
	10^{-2}	C	C	C	C	C	C	C	C	C	C	C	C	C	C	C	C
	10^{-3}	C	C	C	C	C	C	C	C	C	C	C	C	C	C	C	C
	10^{-4}	C	C	C	C	C	C	C	C	C	C	C	C	C	C	C	C
T2	10^{-1}	C	C	6.5	0.8	C	C	7.8	5.7	C	C	7.7	6.2	C	C	8.6	6.5
	10^{-2}	C	C	C	C	C	C	C	C	C	C	C	C	C	C	C	C
	10^{-3}	C	C	C	C	C	C	C	C	C	C	C	C	C	C	C	C
	10^{-4}	C	C	C	C	C	C	C	C	C	C	C	C	C	C	C	C
T3	10^{-1}	C	2.3	0.7	0.4	C	C	2.9	1.0	C	C	7.0	3.6	C	C	8.4	4.5
	10^{-2}	C	C	C	C	C	C	C	C	C	C	C	C	C	C	C	C
	10^{-3}	C	C	C	C	C	C	C	C	C	C	C	C	C	C	C	C
	10^{-4}	C	C	C	C	C	C	C	C	C	C	C	C	C	C	C	C
T4	10^{-1}	C	2.7	0.7	0.4	C	5.1	3.2	0.8	C	6.6	3.8	3.6	C	6.8	4.2	4.1
	10^{-2}	C	C	C	C	C	C	C	C	C	C	C	C	C	C	C	C
	10^{-3}	C	C	C	C	C	C	C	C	C	C	C	C	C	C	C	C
	10^{-4}	C	C	C	C	C	C	C	C	C	C	C	C	C	C	C	C

Table 6.18: Convergence of simulation for axisymmetric start-up of Poiseuille flow for an Oldroyd B. fluid, $We = 1$, $\beta = \frac{1}{9}$, $Re = 1.0$. If the simulation completed it is marked with a "C", otherwise the approximate time the simulation diverged is shown

DG/DEVSS-G Scheme

We now consider the same simulation when using the DEVSS-G scheme. Tables 6.19 and 6.20 show the time-averaged errors for velocity using $\beta_s = 0.5$ and $\beta_s = 1$, respectively. As with the planar case we see a small increase in error which is more exaggerated as N decreases, this is in line with what we would expect since the approximation space for $\mathbf{G}$ is of order $N-2$ whereas the velocity is N, so at low levels of refinement the error caused by using DEVSS-G grows particularly large, especially in areas of high velocity gradient. A good example of this can be seen on meshes T1 and T3 for $N = 4$ where the refinement in the cross-stream direction is particularly low and the error is a full order of magnitude larger than the DG-only scheme. Doubling the number of cross-stream elements or the polynomial order counteracts this although the requirement of $\Delta t = 10^{-3}$ to reach sufficient temporal accuracy becomes more important, with the $\Delta t = 10^{-2}$ errors being an order of magnitude larger than their DG-only equivalents. This is also present in the planar results, although not noted in the discussion. The EX2 treatment of the DEVSS-G terms is most likely the cause of this. Coupling the gradient projection equation with the momentum equation would likely improve this, although there would be a deterioration in performance for the linear solver. This is an option we will consider in the future as it may further improve stability.

Turning our attention to improvements in the stability of our scheme, Table 6.21 shows the times of divergence for the DG-only scheme at $We = 10.0$ where we see similar issues as encountered in the planar case, with the length of the cylinder as well as refinement in the downstream direction playing a crucial role. Tables 6.22 and 6.23 show the results using $\beta_s = 0.5$ and $\beta_s = 1.0$. A small improvement in the time to divergence is generally observed and it allows us to reach a converged solution at higher values of N on meshes T3 and T4 which feature additional downstream elements for $L = 64$ and $L = 16$. Using $\beta_s = 1$ instead of 0.5 brings about a small improvement in stability. Results for $We = 100$ are shown in Tables 6.24- 6.26, which show similar, albeit smaller, improvements. These results are very much in line with what was observed for the planar case and demonstrate that the scheme works equally well for both co-ordinate systems. The scheme is certainly not a remedy for overcoming these stability problems, but can push the results further along in terms of time to diverge

Mesh	Δt	N = 4	N = 8	N = 12	N = 16
T1	0.1	1.1834×10^{-1}	-	-	-
	0.01	2.5692×10^{-3}	1.8626×10^{-4}	1.3495×10^{-4}	1.1368×10^{-4}
	0.001	2.3904×10^{-3}	4.1372×10^{-5}	7.9518×10^{-6}	7.0379×10^{-6}
	0.0001	2.3883×10^{-3}	4.0193×10^{-5}	7.6029×10^{-6}	6.2258×10^{-6}
T2	0.1	-	-	-	-
	0.01	1.4313×10^{-4}	1.3454×10^{-4}	1.3364×10^{-4}	1.1369×10^{-4}
	0.001	8.3276×10^{-5}	8.0613×10^{-6}	7.0577×10^{-6}	7.1768×10^{-6}
	0.0001	8.2314×10^{-5}	7.6079×10^{-6}	6.0154×10^{-6}	6.1471×10^{-6}
T3	0.1	1.5132×10^{-1}	-	-	-
	0.01	2.7630×10^{-3}	2.0162×10^{-4}	1.4110×10^{-4}	1.3909×10^{-4}
	0.001	2.5366×10^{-3}	4.2423×10^{-5}	8.2835×10^{-6}	7.6572×10^{-6}
	0.0001	2.5336×10^{-3}	4.1126×10^{-5}	8.0250×10^{-6}	6.8868×10^{-6}
T4	0.1	-	-	-	-
	0.01	1.9478×10^{-4}	1.4267×10^{-4}	1.4014×10^{-4}	1.3908×10^{-4}
	0.001	8.8710×10^{-5}	8.8425×10^{-6}	7.4089×10^{-6}	7.7155×10^{-6}
	0.0001	8.6186×10^{-5}	8.2366×10^{-6}	6.6584×10^{-6}	7.1156×10^{-6}

Table 6.19: Time-averaged velocity error, E_u, at the test point using DEVSS-G, $\beta_s = 0.5$, for axisymmetric start-up flow of an Oldroyd B. Fluid, $We = 1$, $\beta = \frac{1}{9}$, $Re = 1.0$, $L = 64$.

Mesh	Δt	N = 4	N = 8	N = 12	N = 16
T1	0.1	-	-	-	-
	0.01	3.0658×10^{-3}	3.8300×10^{-4}	2.6086×10^{-4}	2.0473×10^{-4}
	0.001	2.6895×10^{-3}	4.8375×10^{-5}	9.3640×10^{-6}	7.6030×10^{-6}
	0.0001	2.6857×10^{-3}	4.6010×10^{-5}	7.4053×10^{-6}	6.1005×10^{-6}
T2	0.1	-	-	-	-
	0.01	2.5098×10^{-4}	2.7530×10^{-4}	2.6250×10^{-4}	2.0469×10^{-4}
	0.001	1.0347×10^{-4}	8.7187×10^{-6}	8.0995×10^{-6}	7.7975×10^{-6}
	0.0001	1.0297×10^{-4}	7.3983×10^{-6}	5.8806×10^{-6}	6.1266×10^{-6}
T3	0.1	-	-	-	-
	0.01	3.4506×10^{-3}	4.2757×10^{-4}	3.0421×10^{-4}	3.0489×10^{-4}
	0.001	2.9456×10^{-3}	5.0135×10^{-5}	1.0230×10^{-5}	9.5129×10^{-6}
	0.0001	2.9402×10^{-3}	4.7455×10^{-5}	8.0047×10^{-6}	7.3162×10^{-6}
T4	0.1	-	-	-	-
	0.01	3.4725×10^{-4}	3.0445×10^{-4}	3.0533×10^{-4}	3.0443×10^{-4}
	0.001	1.0810×10^{-4}	9.7587×10^{-6}	9.0657×10^{-6}	9.2622×10^{-6}
	0.0001	1.0637×10^{-4}	8.2214×10^{-6}	6.8879×10^{-6}	7.7592×10^{-6}

Table 6.20: Time-averaged velocity error, E_u, at the test point using DEVSS-G, $\beta_s = 1.0$, for axisymmetric start-up flow of an Oldroyd B. Fluid, $We = 1$, $\beta = \frac{1}{9}$, $Re = 1.0$, $L = 64$.

which can be beneficial for our simulations.

		N for $L = 8$				N for $L = 16$				N for $L = 32$				N for $L = 64$			
Mesh	Δt	4	8	12	16	4	8	12	16	4	8	12	16	4	8	12	16
T1	10^{-1}	34.8	4.4	1.3	0.7	C	11.2	4.5	1.6	C	C	9.5	5.1	C	C	C	23.4
	10^{-2}	C	5.6	4.0	3.6	C	11.4	6.3	4.8	C	C	14.8	7.5	C	C	C	22.4
	10^{-3}	C	5.9	4.4	3.6	C	11.3	6.5	4.7	C	C	14.7	7.5	C	C	C	22.4
	10^{-4}	C	6.0	4.4	3.6	C	11.3	6.5	4.6	C	C	14.7	8.6	C	C	C	22.4
T2	10^{-1}	C	4.0	1.3	0.7	C	10.4	3.7	1.6	C	C	7.8	3.7	C	C	C	13.3
	10^{-2}	C	6.8	5.3	4.2	C	18.3	6.9	5.3	C	C	16.4	7.8	C	C	C	23.3
	10^{-3}	C	9.8	5.0	4.0	C	17.9	7.1	5.1	C	C	15.9	8.0	C	C	C	23.2
	10^{-4}	C	9.8	5.0	4.0	C	17.9	7.1	5.1	C	C	15.8	8.0	C	C	C	23.2
T3	10^{-1}	10.3	1.3	0.6	0.4	19.6	3.5	1.3	0.7	C	7.2	3.9	1.6	C	39.6	7.3	4.5
	10^{-2}	14.8	3.6	3.2	3.1	28.3	4.5	3.9	3.8	C	9.1	6.4	4.5	C	38.7	11.4	7.9
	10^{-3}	16.8	3.7	3.4	3.0	29.1	4.8	4.8	3.7	C	9.4	6.1	4.5	C	34.5	11.3	8.1
	10^{-4}	17.1	3.7	3.4	3.0	29.2	4.9	4.8	3.7	C	9.4	6.0	4.5	C	34.2	11.2	8.1
T4	10^{-1}	14.3	1.3	0.6	0.4	25.3	4.2	1.3	0.7	C	11.9	3.7	1.6	C	38.9	7.1	3.8
	10^{-2}	14.8	4.0	3.8	3.6	35.6	7.4	4.9	4.0	C	12.1	7.1	5.1	C	C	12.0	8.2
	10^{-3}	14.7	4.3	3.8	3.5	34.7	7.9	4.7	3.9	C	12.3	7.1	5.0	C	C	12.1	8.1
	10^{-4}	14.7	4.4	3.8	3.5	34.6	7.9	4.7	3.9	C	12.3	7.1	5.0	C	C	12.1	8.1

Table 6.21: Convergence of simulation for axisymmetric start-up of Poiseuille flow for an Oldroyd B. fluid, $We = 10$, $\beta = \frac{1}{9}$, $Re = 1.0$. If the simulation completed it is marked with a "C", otherwise the approximate time the simulation diverged is shown

		N for $L = 8$				N for $L = 16$				N for $L = 32$				N for $L = 64$			
Mesh	Δt	4	8	12	16	4	8	12	16	4	8	12	16	4	8	12	16
T1	10^{-1}	C	6.9	1.4	0.7	C	13.3	5.3	2.0	C	C	10.2	5.6	C	C	C	10.8
	10^{-2}	C	8.8	5.5	5.0	C	14.0	8.3	7.7	C	C	21.9	10.3	C	C	C	14.2
	10^{-3}	C	9.4	6.0	4.8	C	14.0	7.7	6.8	C	C	20.2	11.4	C	C	C	15.7
	10^{-4}	C	9.5	6.1	4.8	C	14.0	7.7	6.6	C	C	20.0	11.4	C	C	C	16.0
T2	10^{-1}	C	5.7	0.8	0.5	C	12.2	4.4	0.8	C	C	7.5	4.1	C	C	C	7.9
	10^{-2}	C	9.9	7.7	5.2	C	24.5	10.8	7.7	C	C	21.4	12.4	C	C	C	25.7
	10^{-3}	C	10.6	7.3	5.0	C	24.2	9.4	6.4	C	C	21.6	11.0	C	C	C	20.3
	10^{-4}	C	10.8	7.4	5.0	C	24.1	9.4	6.4	C	C	21.4	10.8	C	C	C	20.3
T3	10^{-1}	16.2	1.3	0.6	0.4	C	5.7	1.4	0.7	C	11.9	4.9	2.1	C	C	10.0	5.5
	10^{-2}	19.2	5.1	4.8	5.1	C	7.3	5.6	5.1	C	13.4	8.0	6.6	C	C	15.5	10.1
	10^{-3}	20.6	5.4	5.1	4.6	C	7.5	6.2	5.1	C	13.3	9.4	7.0	C	C	15.4	11.3
	10^{-4}	20.8	5.5	5.2	4.6	C	7.6	6.2	5.1	C	13.3	9.3	6.9	C	C	15.4	11.2
T4	10^{-1}	14.7	1.3	0.6	0.3	32.1	5.8	0.8	0.6	C	12.7	4.7	0.8	C	C	8.0	4.3
	10^{-2}	16.9	6.2	5.7	5.0	C	10.2	8.2	5.4	C	17.6	9.6	7.1	C	C	19.4	11.7
	10^{-3}	16.9	6.6	5.6	5.0	C	10.7	7.4	5.3	C	17.8	10.6	7.5	C	C	18.5	11.6
	10^{-4}	16.9	6.6	5.6	5.0	C	10.7	7.3	5.3	C	17.8	10.2	7.5	C	C	18.5	11.4

Table 6.22: Convergence of simulation using DEVSS-G, $\beta_s = 0.5$, for axisymmetric start-up of Poiseuille flow for an Oldroyd B. fluid, $We = 10$, $\beta = \frac{1}{9}$, $Re = 1.0$. If the simulation completed successfully it is marked with a "C", otherwise the approximate time the simulation diverged is shown

		N for $L = 8$				N for $L = 16$				N for $L = 32$				N for $L = 64$			
Mesh	Δt	4	8	12	16	4	8	12	16	4	8	12	16	4	8	12	16
T1	10^{-1}	C	9.1	1.1	0.7	C	15.7	6.2	1.2	C	C	11.0	6.2	C	C	C	11.1
	10^{-2}	C	10.8	7.0	6.2	C	17.1	9.5	9.5	C	C	18.3	10.7	C	C	C	15.1
	10^{-3}	C	12.5	7.6	6.0	C	17.0	9.3	8.5	C	C	24.2	12.9	C	C	C	16.2
	10^{-4}	C	12.8	7.6	6.0	C	17.0	9.4	8.5	C	C	24.0	12.9	C	C	C	16.3
T2	10^{-1}	C	7.6	0.7	0.3	C	14.2	5.4	0.7	C	C	8.2	5.5	C	C	C	7.9
	10^{-2}	C	12.0	8.7	6.2	C	28.9	10.8	9.1	C	C	24.2	13.1	C	C	C	16.9
	10^{-3}	C	12.8	9.4	6.3	C	28.7	11.0	7.9	C	C	26.1	12.9	C	C	C	22.8
	10^{-4}	C	12.8	9.5	6.3	C	28.7	10.8	7.9	C	C	25.3	12.7	C	C	C	22.4
T3	10^{-1}	17.8	1.3	0.6	0.3	C	7.5	1.1	0.7	C	15.2	6.2	1.2	C	C	11.5	6.4
	10^{-2}	19.9	6.8	6.2	4.9	C	9.8	7.5	6.3	C	17.2	9.8	8.4	C	C	18.9	10.9
	10^{-3}	21.4	7.3	6.7	6.5	C	10.4	8.5	6.5	C	16.7	11.4	8.6	C	C	18.5	13.3
	10^{-4}	21.6	7.4	6.7	6.4	C	10.5	8.7	6.5	C	16.7	11.2	8.7	C	C	18.5	13.4
T4	10^{-1}	17.0	0.9	0.4	0.2	C	8.0	0.7	0.4	C	13.7	1.5	0.7	C	C	8.7	1.4
	10^{-2}	19.0	8.9	7.0	5.0	C	13.2	9.8	6.6	C	21.1	10.9	9.6	C	C	27.9	11.7
	10^{-3}	19.3	8.9	6.9	6.1	C	12.9	9.4	6.4	C	21.4	12.6	9.4	C	C	22.5	13.5
	10^{-4}	19.3	9.0	6.9	6.1	C	12.8	9.4	6.4	C	21.4	12.4	9.3	C	C	22.3	13.3

Table 6.23: Convergence of simulation using DEVSS-G, $\beta_s = 1.0$, for axisymmetric start-up of Poiseuille flow for an Oldroyd B. fluid, $We = 10$, $\beta = \frac{1}{9}$, $Re = 1.0$. If the simulation completed successfully it is marked with a "C", otherwise the approximate time the simulation diverged is shown

		N for $L = 8$				N for $L = 16$				N for $L = 32$				N for $L = 64$			
Mesh	Δt	4	8	12	16	4	8	12	16	4	8	12	16	4	8	12	16
T1	10^{-1}	13.1	2.9	1.3	0.7	29.7	8.0	2.7	1.5	C	12.3	10.0	3.8	C	33.7	13.7	10.0
	10^{-2}	14.2	7.1	5.1	4.7	39.4	10.2	6.4	6.1	C	13.7	9.0	7.3	C	22.1	13.8	10.0
	10^{-3}	14.5	7.2	5.2	4.9	C	9.8	6.4	6.1	C	13.9	9.0	7.3	C	21.9	13.8	10.0
	10^{-4}	14.5	7.2	5.2	4.9	C	9.8	6.4	6.1	C	13.9	9.0	7.3	C	21.9	13.8	10.0
T2	10^{-1}	14.6	2.9	1.3	0.7	29.2	8.2	2.7	1.5	C	15.8	7.6	3.6	C	27.7	11.5	7.4
	10^{-2}	15.7	6.5	6.0	5.0	30.4	9.0	7.1	5.6	C	15.7	9.3	7.4	C	28.7	13.5	9.8
	10^{-3}	15.9	6.6	6.0	5.0	30.6	9.0	7.1	5.9	C	15.7	9.3	7.5	C	28.8	13.5	9.9
	10^{-4}	15.9	6.6	6.0	5.0	30.6	9.0	7.1	5.9	C	15.7	9.3	7.5	C	28.8	13.5	9.9
T3	10^{-1}	6.0	1.2	0.6	0.4	8.2	2.9	1.2	0.7	19.5	7.4	2.7	1.5	C	10.6	8.3	3.5
	10^{-2}	6.9	5.5	4.8	2.9	12.1	6.7	5.5	4.8	23.6	8.2	6.5	5.4	C	11.3	8.4	6.8
	10^{-3}	8.0	5.9	5.0	4.4	12.2	6.6	5.4	4.8	23.6	8.2	6.5	5.4	C	11.4	8.4	6.9
	10^{-4}	7.8	5.8	5.1	4.4	12.1	6.6	5.4	4.8	23.5	8.3	6.5	5.4	C	11.4	8.4	6.9
T4	10^{-1}	9.1	1.2	0.6	0.4	12.0	2.8	1.3	0.7	18.7	8.8	2.7	1.5	38.3	12.3	7.8	3.5
	10^{-2}	10.3	5.6	4.7	2.9	14.4	6.7	5.2	4.9	24.2	9.0	6.5	5.5	C	12.9	9.5	7.0
	10^{-3}	10.6	5.5	4.7	4.6	14.2	6.7	5.2	4.9	24.0	9.0	6.5	5.6	C	12.9	9.6	7.0
	10^{-4}	10.6	5.5	4.7	4.6	14.2	6.7	5.2	4.9	24.0	9.0	6.5	5.6	C	12.9	9.6	7.0

Table 6.24: Convergence of simulation for axisymmetric start-up of Poiseuille flow for an Oldroyd B. fluid, $We = 100$, $\beta = \frac{1}{9}$, $Re = 1.0$. If the simulation completed it is marked with a "C", otherwise the approximate time the simulation diverged is shown

		N for $L = 8$				N for $L = 16$				N for $L = 32$				N for $L = 64$			
Mesh	Δt	4	8	12	16	4	8	12	16	4	8	12	16	4	8	12	16
T1	10^{-1}	14.9	4.2	1.3	0.7	30.0	9.2	4.2	1.6	C	14.8	10.8	7.4	C	C	17.3	11.7
	10^{-2}	14.7	8.7	6.4	6.3	C	12.3	7.3	6.9	C	17.4	9.6	8.6	C	28.1	18.4	12.6
	10^{-3}	14.3	9.5	6.3	6.4	35.8	12.1	7.3	6.9	C	21.3	9.5	8.6	C	27.6	18.6	12.6
	10^{-4}	14.3	9.2	6.3	6.4	35.5	12.0	7.3	6.9	C	21.0	9.5	8.6	C	27.6	18.6	12.6
T2	10^{-1}	16.4	4.2	0.9	0.6	37.8	10.8	4.1	0.9	C	18.7	8.9	6.2	C	38.5	13.9	8.4
	10^{-2}	18.9	7.7	6.7	6.6	37.4	10.2	8.0	6.4	C	21.0	10.4	7.8	C	39.5	17.5	12.9
	10^{-3}	19.5	7.8	6.8	6.6	37.4	10.2	8.4	6.7	C	19.3	10.4	8.5	C	39.6	17.5	13.2
	10^{-4}	19.5	7.8	6.8	6.6	37.4	10.2	8.4	6.7	C	19.3	10.4	8.5	C	39.7	17.5	13.2
T3	10^{-1}	7.5	1.2	0.6	0.3	11.0	4.2	1.2	0.7	22.5	9.3	4.2	1.6	C	13.1	9.4	8.0
	10^{-2}	8.0	7.5	6.2	5.5	12.4	8.0	7.1	6.2	23.7	10.2	8.3	7.0	C	14.9	10.8	8.2
	10^{-3}	8.1	7.3	6.4	5.6	12.2	8.0	7.2	6.2	23.8	10.3	8.3	7.1	C	15.0	10.6	8.2
	10^{-4}	8.1	7.3	6.4	5.7	12.2	8.0	7.2	6.2	23.8	10.3	8.3	7.1	C	15.0	10.6	8.2
T4	10^{-1}	10.2	1.2	0.6	0.3	14.8	4.2	0.9	0.6	30.5	9.2	4.1	0.9	C	16.5	9.1	6.2
	10^{-2}	11.1	7.2	6.2	6.1	16.6	8.2	6.8	6.2	30.9	10.7	9.2	7.3	C	17.6	10.3	8.1
	10^{-3}	10.7	7.3	6.3	6.1	16.9	8.3	6.8	6.3	31.0	10.6	9.3	7.3	C	18.0	10.4	8.3
	10^{-4}	10.6	7.3	6.3	6.1	17.0	8.3	6.8	6.3	31.0	10.6	9.3	7.3	C	18.0	10.4	8.3

Table 6.25: Convergence of simulation using DEVSS-G, $\beta_s = 0.5$, for axisymmetric start-up of Poiseuille flow for an Oldroyd B. fluid, $We = 100$, $\beta = \frac{1}{9}$, $Re = 1.0$. If the simulation completed successfully it is marked with a "C", otherwise the approximate time the simulation diverged is shown

		N for $L = 8$				N for $L = 16$				N for $L = 32$				N for $L = 64$			
Mesh	Δt	4	8	12	16	4	8	12	16	4	8	12	16	4	8	12	16
T1	10^{-1}	16.1	5.0	1.1	0.6	35.5	9.2	4.7	1.2	C	15.3	10.5	7.9	C	C	16.4	12.7
	10^{-2}	16.6	10.9	7.2	7.1	C	15.5	7.9	7.7	C	25.2	10.3	8.7	C	34.3	15.8	12.7
	10^{-3}	16.3	10.1	7.0	7.2	C	13.6	7.9	7.7	C	23.7	10.3	8.7	C	33.7	15.7	12.6
	10^{-4}	16.3	10.2	7.0	7.2	C	13.7	7.9	7.7	C	23.6	10.3	8.7	C	33.6	15.7	12.6
T2	10^{-1}	18.1	4.6	0.8	0.3	C	12.3	5.3	0.8	C	22.9	10.5	6.6	C	C	16.3	9.3
	10^{-2}	22.5	8.8	7.6	6.8	C	11.2	9.0	7.3	C	18.8	10.8	8.6	C	C	17.1	11.6
	10^{-3}	24.7	8.8	7.7	6.8	C	11.3	9.0	7.6	C	18.7	10.9	8.7	C	C	17.0	11.7
	10^{-4}	25.0	8.8	7.7	6.8	C	11.3	9.0	7.6	C	18.7	10.9	8.7	C	C	17.0	11.7
T3	10^{-1}	8.1	1.2	0.5	0.3	11.5	4.8	1.1	0.6	29.7	11.1	4.7	1.2	C	14.9	10.1	7.8
	10^{-2}	9.2	8.0	7.0	3.5	15.0	8.9	7.5	7.3	30.2	12.0	9.0	7.7	C	17.9	11.2	8.4
	10^{-3}	9.0	8.4	7.2	6.7	14.5	9.3	7.5	7.2	30.1	12.3	9.2	7.7	C	18.2	11.3	8.4
	10^{-4}	9.0	8.5	7.3	6.7	14.4	9.3	7.5	7.2	30.1	12.4	9.2	7.7	C	18.2	11.3	8.4
T4	10^{-1}	9.8	0.9	0.4	0.2	16.3	4.5	0.8	0.4	34.4	10.0	1.5	0.8	C	16.1	10.0	1.4
	10^{-2}	13.6	8.2	7.3	3.6	20.0	9.3	8.1	6.6	38.2	11.9	8.7	7.9	C	16.6	11.0	8.4
	10^{-3}	11.6	8.2	7.4	6.8	23.1	9.4	8.1	6.7	38.7	11.8	8.7	7.9	C	16.7	11.0	8.5
	10^{-4}	11.6	8.2	7.4	6.8	26.0	9.4	8.1	6.7	38.8	11.8	8.7	7.9	C	16.7	11.0	8.5

Table 6.26: Convergence of simulation using DEVSS-G, $\beta_s = 1.0$, for axisymmetric start-up of Poiseuille flow for an Oldroyd B. fluid, $We = 100$, $\beta = \frac{1}{9}$, $Re = 1.0$. If the simulation completed successfully it is marked with a "C", otherwise the approximate time the simulation diverged is shown

6.1.3 Summary

We have shown that our DG-SEM scheme is capable of a high level of accuracy for the Oldroyd B model, and is capable of handling transient flows with a small amount of error. We have validated our results with other work and matched their accuracy or improved upon it in some cases. Further, the DEVSS-G scheme has been demonstrated to provide additional stability for flows which are known to cause divergence problems when solved numerically. While it does not remedy the problems, it can provide the means to run a simulation for a longer time period and can certainly be used to obtain a solution which is convergent to the degree of accuracy we require.

6.2 Flow past a Fixed Cylinder

We consider the planar geometry benchmark of flow past a fixed cylinder in an infinite cylinder for an Oldroyd B fluid, continuing from the Newtonian fluid in section 5.2. Following the majority of the literature we fix $Re = 0$ and $\beta = 0.59$ in order to draw direct comparison.

We prescribe the velocity given in (4.4), with $H_C = 4$ and $U_{av} = 1$, at inflow and outflow and prescribe the elastic stress at inflow given by,

$$\tau_{xx} = 2We\,(1-\beta)\left(\frac{\partial u_x}{\partial y}\right)^2, \tag{6.9}$$

$$\tau_{xy} = (1-\beta)\,\frac{\partial u_x}{\partial y}, \tag{6.10}$$

$$\tau_{yy} = 0 \tag{6.11}$$

where $\frac{\partial u_x}{\partial y} = -\frac{3}{4}y$ for the chosen velocity profile. No-slip and no penetration conditions are set at the channel walls and symmetry boundary conditions are set on the axis of symmetry. Zero initial conditions are set for all variables.

The value of We will be increased as high as possible using our numerical scheme.

Timestep	Drag
10^{-2}	123.19613707
10^{-3}	123.19613634
10^{-4}	123.19613628
10^{-5}	123.19613627

Table 6.27: Temporal convergence of drag for flow past a fixed cylinder in an infinite channel of an Oldroyd B fluid with $Re = 0.0$, $\beta = 0.59$, $We = 0.3$. Peformed on mesh M3 with $N = 8$.

6.2.1 Domain, Mesh and Timestepping

We use the same meshes as seen in the Newtonian fluid benchmark, shown in Figure 3.4, but also include mesh M5 which features additional refinement in the wake of the cylinder. The length of the mesh is again fixed at 40 radii and the height fixed at 2 radii, with $R_C = 1$.

We consider timesteps $\Delta t = 10^{-1}, 10^{-2}, 10^{-3}, 10^{-4}$ and impose a time limit of 50 time units, at which point the simulation is terminated if it has not met our convergence criteria or otherwise diverged.

6.2.2 Results

The main results for the drag are presented in Table 6.33, but we first confirm that we see convergence with respect to temporal and spatial refinement. Starting with temporal refinement, Table 6.27 shows the computed drag (using the DG-only scheme) for a moderate value of $We = 0.3$ for a moderate spatial refinement, to a high number of decimal places. We see that there is little variance of the drag for any of these timesteps, although we do see convergence at 7 decimal places with increasing timestep. We checked that this was also true for a more refined mesh and larger N, and found the same result. We choose to use $\Delta t = 10^{-4}$ for our main simulations.

Table 6.28 shows the computed drag for the DG-only scheme at $We = 0.3$ using $\Delta t = 10^{-4}$. We observe a steady convergence with mesh refinement at fixed N, which suggests

Mesh	N = 4	N = 8	N = 12	N = 16
M1	123.374545	123.014923	123.194371	123.185684
M2	121.079170*	123.197103	123.192201	123.191168
M3	122.757546	123.196136	123.190978	123.191207
M4	123.078513	123.191297	123.191216	123.191247
M5	123.078626	123.191294	123.191216	123.191246

Table 6.28: Spatial convergence of drag for flow past a fixed cylinder in an infinite channel of an Oldroyd B fluid with $Re = 0.0$, $\beta = 0.59$, $We = 0.3$. Performed with timestep $\Delta t = 10^{-4}$. Results which had not met the convergence criteria are marked with an asterisk.

that mesh dependence is minimal, at least for this value of We. Refinement in N yields convergence of the drag by $N = 12$ where we are satisfied with agreement up to 5 decimal places in the computed drag.

	Mesh M4				Mesh M5			
We	N = 15	N = 16	N = 17	N = 18	N = 13	N = 14	N = 15	N = 16
0.1	130.362671	130.362671	130.362671	130.362671	130.362671	130.362671	130.362671	130.362671
0.2	126.625216	126.625216	126.625216	126.625216	126.625217	126.625216	126.625216	126.625216
0.3	123.191247	123.191247	123.191245	123.191243	123.191233	123.191242	123.191246	123.191246
0.4	120.591218	120.591234	120.591238	120.591234	120.591150	120.591190	120.591219	120.591234
0.5	118.825951	118.825977	118.826007	118.826030	118.825814	118.825939	118.825967	118.825992
0.6	117.774382*	117.774649*	117.775198*	-	117.774274	117.774914	117.775155*	117.775112*

Table 6.29: Drag for flow past a fixed cylinder in an infinite channel of an Oldroyd B fluid with $Re = 0.0$, $\beta = 0.59$. Performed with timestep $\Delta t = 10^{-4}$. Results which had not met the convergence criteria are marked with an asterisk.

Timestep	Drag
10^{-2}	123.19531615
10^{-3}	123.19531543
10^{-4}	123.19531535
10^{-5}	123.19531534

Table 6.30: Temporal convergence of drag for flow past a fixed cylinder in an infinite channel of an Oldroyd B fluid with $Re = 0.0$, $\beta = 0.59$, $We = 0.3$. Peformed on mesh M3 with $N = 8$ using DEVSS-G, $\beta_s = 1.0$.

Table 6.29 shows the computed drag with increasing We using our DG-only scheme on our most refined meshes at the highest attainable values of N. We see excellent convergence of the drag with increasing N up to $We = 0.5$. At $We = 0.6$ there is an issue with the numerical scheme reaching a fully converged steady-state solution. While the simulation does not diverge, the time limit was reached before the field variables had reached threshold set with regard to their change over time, although the change in drag over time does appear to have reached the required threshold. At values higher than $We = 0.6$ we find that the drag may appear to have converged, but the simulation later diverges and does not reach the steady state.

Table 6.32 shows the computed drag factor when employing the DEVSS-G scheme to stabilise our results. We only consider $\beta_s = 1$, as using anything below the value of $\beta = 0.59$ would not be expected to stabilise the simulation (θ would become negative, see (3.191)). Table 6.30 shows the convergence of the drag with temporal refinement, which shows a similar rate of convergence to the DG-only scheme.

The values for the drag in Table 6.30 differ at the 3^{rd} decimal place when compared to those for the DG-only scheme (Table 6.27), which is a slight cause for concern. Table 6.31 shows the computed drag factor with spatial refinement which brings the drag values back into line with the DG-only scheme with increased refinement in N. We note the additional error introduced by the DEVSS-G scheme impacts on the computed drag, although additional spatial refinement appears to alleviate this. This is fairly intuitive given that we only calculate the value of $\mathbf{G}$ on the internal nodes and then extrapolate the value onto a mesh boundary node. Given that the drag is computed along element boundaries on the surface of the cylinder we would expect to

Mesh	N = 4	N = 8	N = 12	N = 16
M1	125.647513	123.118874	123.197836	123.185491
M2	123.947735	123.197671	123.192282	123.191161
M3	122.882292	123.195315	123.190915	123.191211
M4	123.145048	123.191222	123.191220	123.191247
M5	123.144690	123.191218	123.191219	123.191246

Table 6.31: Spatial convergence of drag for flow past a fixed cylinder in an infinite channel of an Oldroyd B fluid with $Re = 0.0$, $\beta = 0.59$, $We = 0.3$. Performed with timestep $\Delta t = 10^{-4}$ using DEVSS-G, $\beta_s = 1.0$.

see any error introduced by the DEVSS-G scheme exaggerated.

	Mesh M4				Mesh M5			
We	N = 15	N = 16	N = 17	N = 18	N = 13	N = 14	N = 15	N = 16
0.1	130.362671	130.362671	130.362671	130.362671	130.362670	130.362671	130.362671	130.362671
0.2	126.625216	126.625216	126.625215	126.625215	126.625215	126.625216	126.625216	126.625215
0.3	123.191247	123.191247	123.191245	123.191243	123.191235	123.191243	123.191246	123.191246
0.4	120.591220	120.591235	120.591238	120.591234	120.591154	120.591192	120.591220	120.591234
0.5	118.825957	118.825984	118.826012	118.826032	118.825816	118.825933	118.825964	118.825991
0.6	117.774730	117.774916	117.775000	117.775059	117.774236	117.774927	117.775169	117.775180
0.7	117.186297*	117.205605*	-	-	117.312688*	117.313787*	117.320522*	117.306286*

Table 6.32: Drag for flow past a fixed cylinder in an infinite channel of an Oldroyd B fluid with $Re = 0.0$, $\beta = 0.59$. Performed with timestep $\Delta t = 10^{-4}$ using DEVSS-G, $\beta_s = 1.0$.Results which had not met the convergence criteria are marked with an asterisk.

We	Present Work	Claus et al.[12]	Alves et al.[1]	Fan et al.[14]	Owens et al.[43]
0.1	130.363	130.364	130.355	130.36	-
0.2	126.625	126.626	126.320	126.62	-
0.3	123.191	123.192	123.210	123.19	-
0.4	120.591	120.593	120.607	120.59	-
0.5	118.826	118.826	118.838	118.83	118.827
0.6	117.775	117.776	117.787	117.77	117.775
0.7	117.306*	117.316	117.323	117.32	117.291
0.8	-	117.352	117.357	117.36	117.237

Table 6.33: Comparison of computed drag for flow of an Oldroyd B fluid past a fixed cylinder in an infinite cylinder at $Re = 0$, $\beta = 0.59$ against those found in the literature. Results which had not met the convergence criteria are marked with an asterisk.

The computed drag for increasing We is shown in Table 6.32. We are able to achieve converged results for $We = 0.6$ and reach the time limit without convergence of the field variables at $We = 0.7$. This is a small improvement, but a search of the literature reveals that others have encountered problems reaching steady-state solutions at $We > 0.6$. For example, Sahin et al. [52] experienced the same issue, although they were able to compute solutions above $We = 0.7$. Additionally, recent work by Claus and Phillips [12], who also employ a SEM DG/DEVSS-G scheme but using a modal, rather than nodal, basis conclude the same. This serves as excellent validation of our results and gives us confidence that our solver is performing well. We provide a comparison of our results with a selection found in the literature in Table 6.33, which shows excellent agreement for our computed drag values. A plot of the data is shown in Figure 6.10, which suggest that our computations are accurate as well as capturing observed phenomena.

Contour plots at various values of We are shown in Figures 6.12- 6.14 which are able to compare directly with Claus and Phillips [12], where we see excellent agreement with our maximum and minimum velocity and stress values at $We = 0.1$ and $We = 0.5$, although we see slight disagreement for the maximum axial stress value at $We = 0.7$. Given that our results were not fully converged for this We value, this is not surprising. Our contour plots show an increasingly thin boundary layer forming on the surface of the cylinder with increasing We, with the axial stress growing in magnitude

considerably.

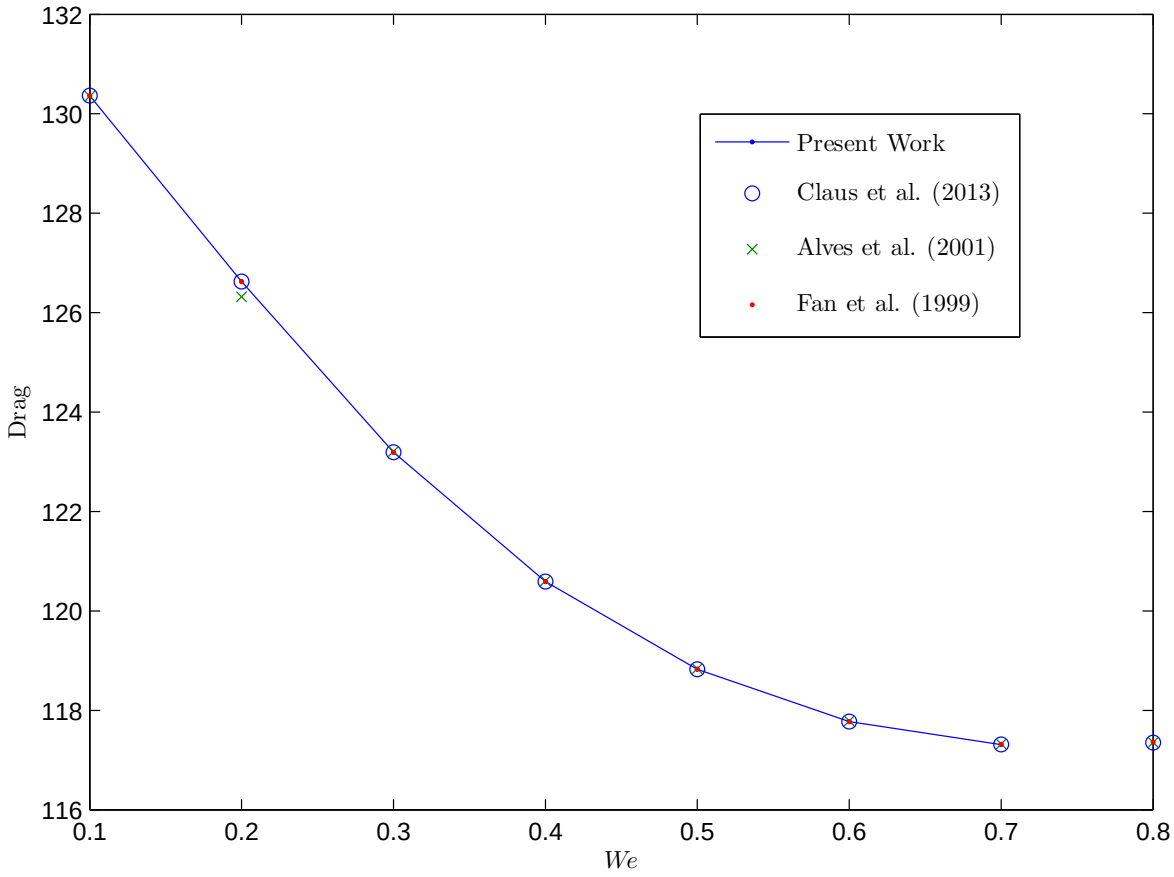

Figure 6.10: Comparison of drag predictions for the flow past a fixed cylinder in an infinite channel benchmark for an Oldroyd B fluid with other results in the literature. Values taken from Table 6.33

Plots of the stress along the central axis and along the surface of the cylinder are provided in Figure 6.11, which show a large growth of normal stress (and 1^{st} normal stress difference) in the wake of the cylinder with increasing We, as seen in the contour plots. This provides a possible explanation of the breakdown of the simulations. Claus and Phillips [12] suggest that this growth cannot be captured by a polynomial basis alone, and that an improvement may be found by using the log conformation approach. Our results support this.

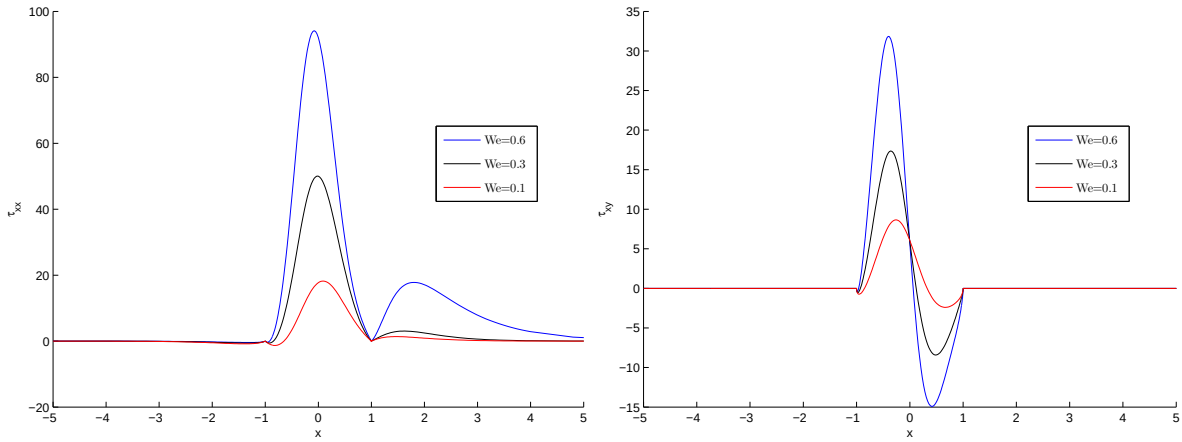

(a) τ_{xx} (b) τ_{xy}

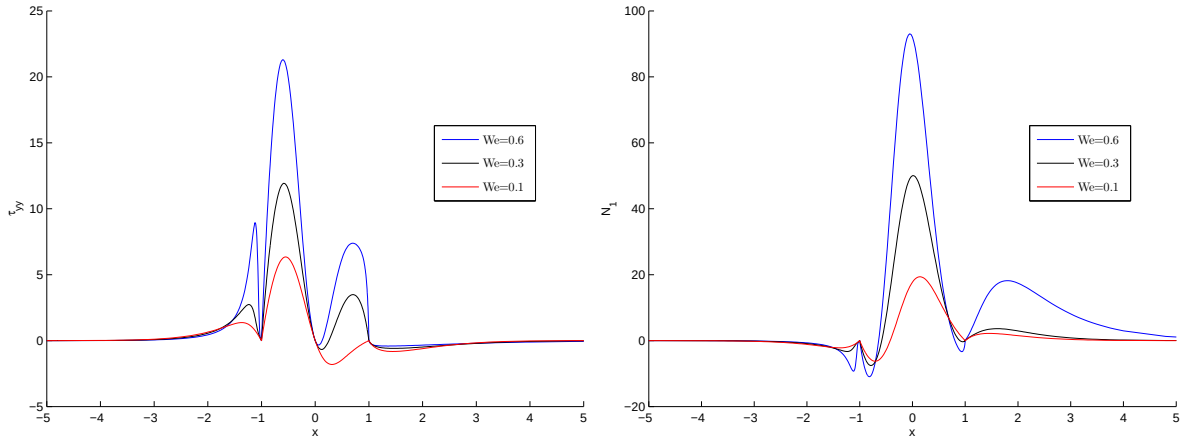

(c) τ_{yy} (d) $N_1 = \tau_{xx} - \tau_{yy}$

Figure 6.11: Components of elastic stress along the axis of symmetry for flow of an Oldroyd B fluid past a fixed cylinder in an infinite channel. Model parameters $\beta = 0.59$, $Re = 0.0$. Numerical parameters, $\Delta t = 10^{-4}$, $N = 16$ on mesh M5 using DEVSS-G with $\beta_s = 1.0$.

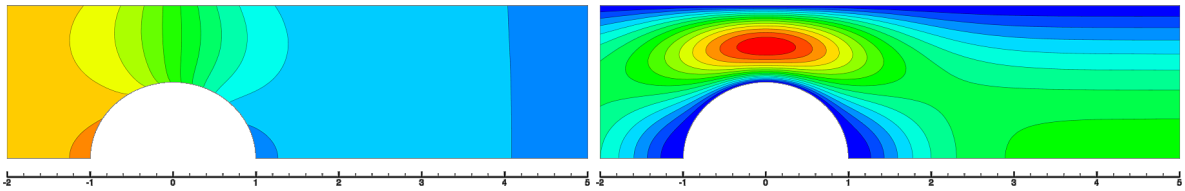

(a) p $We = 0.1$ min: -36.9475 max: 36.815

(b) u_x $We = 0.1$ min:0 max: 2.95473

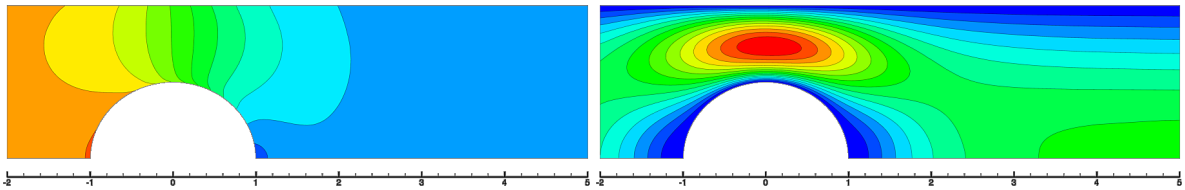

(c) p $We = 0.5$ min:-35.5411 max: 35.05

(d) u_x $We = 0.5$ min:0 max: 2.98041

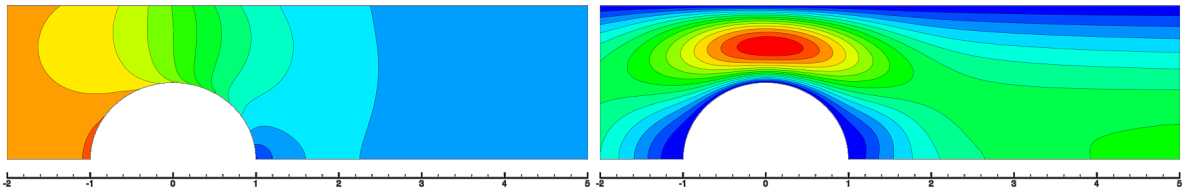

(e) p $We = 0.7$ min:-35.4732 max: 34.7949

(f) u_x $We = 0.7$ min:0 max: 2.98829

Figure 6.12: Contours of pressure and velocity for flow past a fixed cylinder in an infinite channel of an Oldroyd B fluid, $Re = 0$, $\beta = 0.59$.

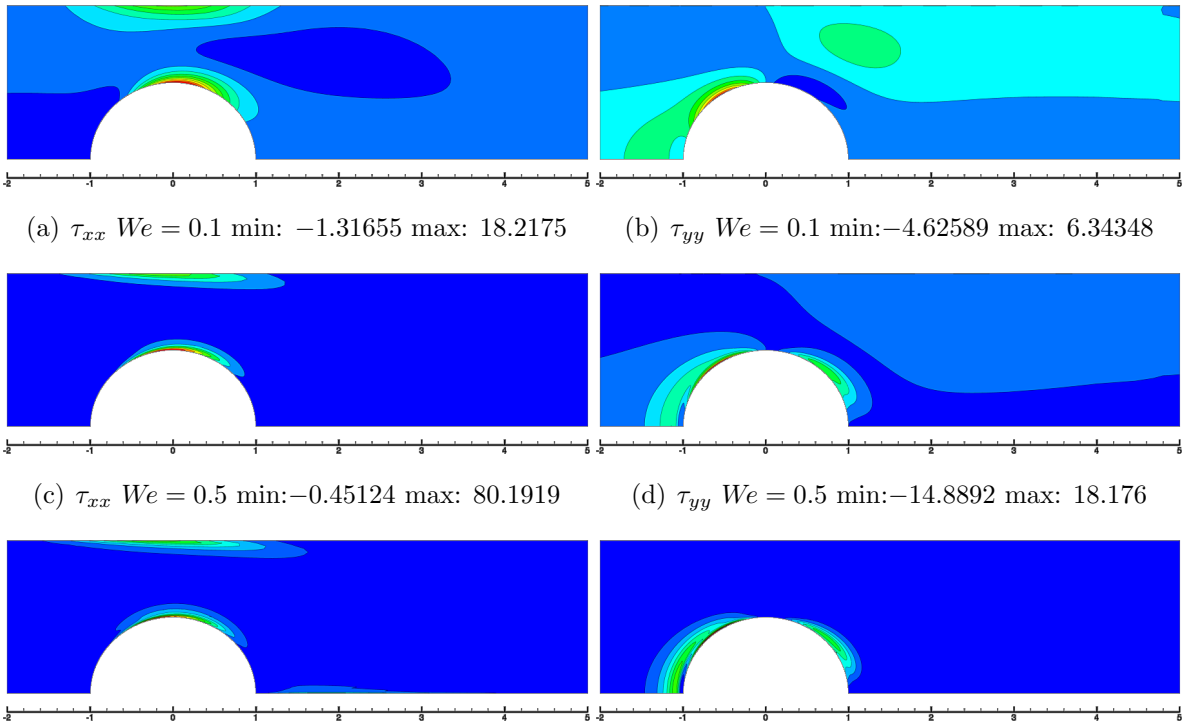

(a) τ_{xx} $We = 0.1$ min: -1.31655 max: 18.2175

(b) τ_{yy} $We = 0.1$ min:-4.62589 max: 6.34348

(c) τ_{xx} $We = 0.5$ min:-0.45124 max: 80.1919

(d) τ_{yy} $We = 0.5$ min:-14.8892 max: 18.176

(e) τ_{xx} $We = 0.7$ min:-0.367768 max: 115.8

(f) τ_{yy} $We = 0.7$ min:-21.0719 max: 24.5473

Figure 6.13: Contours of normal stress components for flow past a fixed cylinder in an infinite channel of an Oldroyd B fluid, $Re = 0$, $\beta = 0.59$.

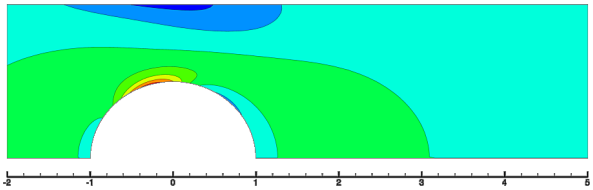

(a) τ_{xy} $We = 0.1$ min: -4.62589 max: 8.65696

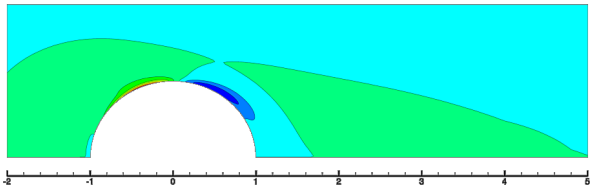

(b) τ_{xy} $We = 0.5$ min:-14.8892 max: 26.9793

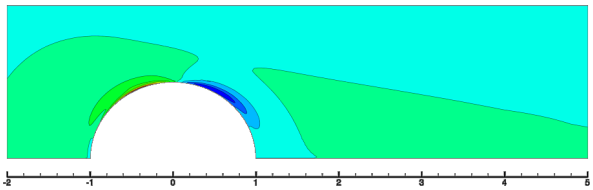

(c) τ_{xy} $We = 0.7$ min:-21.0719 max: 37.0622

Figure 6.14: Contours of shear stress for flow past a fixed cylinder in an infinite channel of an Oldroyd B fluid, $Re = 0$, $\beta = 0.59$.

6.2.3 Summary

We have performed the flow past a cylinder benchmark widely used in the literature to validate our numerical scheme for the Oldbroyd B fluid and have found excellent agreements with the results found in the literature. We agree with recent work on the benchmark that there is a limit around $We = 0.7$ where the flow appears to have some kind of inherent instability. Further work is certainly warranted, and is ongoing by others. Although the focus of this thesis is on the sedimentation of a sphere, this has piqued our interest and provided a stern test of our numerical scheme. This serves as an excellent validation of our scheme's ability to handle viscoelastic flows in a planar geometry.

6.3 Flow past a Fixed Sphere

We now consider the benchmark of uniform flow past a fixed sphere on the central axis of cylinder for an Oldroyd B fluid, continuing from the Newtonian fluid in section 5.3. We set $Re = 0.01$, in order to draw direct comparison with Bodart and Crochet [5]. Two prominent values of β have been considered in the literature, $\beta = \frac{1}{9}$ and $\beta = \frac{1}{2}$. We consider these two values as well as $\beta = \frac{8}{9}$ and increase We as high as possible using our numerical scheme.

We set zero initial conditions and apply the uniform velocity profile at inflow, outflow and along the wall of the cylinder. No-slip and no penetration conditions are prescribed on the surface of the sphere and axisymmetric boundary conditions are applied along the axis of symmetry.

6.3.1 Domain, Mesh and Timestepping

We use the same meshes as seen in the Newtonian fluid benchmark, shown in Figure 3.4, but also include mesh M5 which features additional refinement in the wake of the sphere. The length of the mesh is fixed at 40 radii and the radius of the cylinder is fixed at 2 radii, with $R_S = 1$. This gives a blockage ratio of 0.5, we do not consider

Timestep	$\beta = \frac{1}{9}$	$\beta = \frac{1}{2}$	$\beta = \frac{8}{9}$
10^{-2}	-	5.69440080	5.89271973
10^{-3}	5.48345697	5.69440069	5.89271963
10^{-4}	5.48345697	5.69440068	5.89271963
10^{-5}	5.48345697	5.69440065	5.89271958

Table 6.34: Temporal convergence of drag factor for flow past a fixed sphere in a cylinder of an Oldroyd B fluid with $Re = 0.01$ and $We = 0.3$. Performed on mesh M3 with $N = 8$.

other blockage ratios in the present work.

We consider timesteps $\Delta t = 10^{-1}, 10^{-2}, 10^{-3}, 10^{-4}$ and impose a time limit of 50 time units, at which point the simulation is terminated if it has not met our convergence criteria or otherwise diverged.

6.3.2 Results

Our collected results of the computed drag factor for each value of β are shown in Table 6.47, with comparison to results found in the literature shown in Tables 6.45 and 6.46 for $\beta = \frac{1}{9}$ and $\beta = \frac{1}{2}$, respectively.

We begin by considering the DG-only scheme. Convergence with temporal refinement at each value of β for $We = 0.3$ is shown in Table 6.34 with agreement in the drag factor to 7 decimal places demonstrated, noting that the simulation diverged at for insufficient temporal refinement at $\beta = \frac{1}{9}$. We choose to fix $\Delta t = 10^{-4}$ for all simulations. Convergence of the drag factor with spatial refinement is shown in Table 6.35, again at $We = 0.3$. We see excellent convergence for $\beta = \frac{8}{9}$ but problems with divergence appear for $\beta = \frac{1}{2}$ with mesh M3 being required for any meaningful results and additional refinement in N required to reach agreement with meshes M4 and M5. For $\beta = \frac{1}{9}$ we have poor results at this moderate value of We, with only mesh M5 providing a converged value of the drag with sufficient N. This highlights the importance of mesh refinement at low values of β where the additional refinement in the wake appears to yield some success in mesh M5.

	$\beta = \frac{1}{9}$				$\beta = \frac{1}{2}$				$\beta = \frac{8}{9}$			
Mesh	N = 4	N = 8	N = 12	N = 16	N = 4	N = 8	N = 12	N = 16	N = 4	N = 8	N = 12	N = 16
M1	-	-	-	-	-	-	-	5.694446	5.899683	5.894394	5.892594	5.892698
M2	-	-	-	-	-	-	5.694341	-	-	5.892733	5.892718	5.892718
M3	-	5.483457	-	-	5.676612	5.694401	5.694337	5.694340	5.891668	5.892720	5.892717	5.892718
M4	-	-	-	-	5.689055	5.694338	5.694340	5.694340	5.891209	5.892717	5.892718	5.892718
M5	5.470330	5.483256	5.483275	5.483275	5.689064	5.694338	5.694340	5.694340	5.891228	5.892717	5.892718	5.892718

Table 6.35: Spatial convergence of drag for uniform flow of an Oldroyd B fluid past a fixed sphere in a cylinder with $Re = 0.01$ and $We = 0.3$. Performed with timestep, $\Delta t = 10^{-4}$.

	Mesh M4				Mesh M5			
We	N = 15	N = 16	N = 17	N = 18	N = 13	N = 14	N = 15	N = 16
0.1	5.872271	5.872271	5.872271	5.872271	5.872271	5.872271	5.872271	5.872271
0.2	5.693800	5.693800	5.693800	5.693800	5.693800	5.693800	5.693800	5.693800
0.3	-	-	-	-	5.483275	5.483275	5.483275	5.483275
0.4	-	-	-	-	5.280605	5.280605	5.280604	5.280604
0.5	-	-	-	-	5.101475	-	-	-

Table 6.36: Drag for uniform flow of an Oldroyd B fluid past a fixed sphere in a cylinder with $Re = 0.01$ and $\beta = \frac{1}{9}$. Performed with timestep, $\Delta t = 10^{-4}$.

The disappointing results with the DG-only scheme at $\beta = \frac{1}{9}$ are continued in Table 6.36. Convergence of the drag factor is reached on mesh M4 up to $We = 0.2$, with M5 providing results up to $We = 0.4$, although the convergence of the value is excellent for those computed. Increasing to $\beta = \frac{1}{2}$, Table 6.37 shows similar mesh dependence suggesting that capturing the behaviour of the flow in the wake is still a cause of instability for the simulations. Convergence up to $We = 0.9$ can be reached on mesh M5 compared to $We = 0.5$ for M4, although convergence with refinement in N remains excellent for all results. Finally, Table 6.38 shows results for $\beta = \frac{8}{9}$ with a reduction in the dependence on the mesh, suggesting that flow behaviour in the wake is no longer dominating to the extreme it was for lower values of β. We reach convergence up to $We = 0.9$ for M4 and $We = 1$ for M5 as well as computing some unconverged (with respect to the stopping criteria) values at slightly higher We which do not diverge.

We now consider the DEVSS-G scheme and attempt to increase the attainable We for each value of β. We begin by considering $\beta = \frac{1}{9}$ with $\beta_s = 0.5$, which we would expect to roughly match the attainable We reached by the DG-only scheme with $\beta = \frac{1}{2}$, with the computed drag factor shown in Table 6.39. We see a small increase on mesh M4, although not quite matching the attainable We of $\beta = \frac{1}{2}$, further suggesting that the wake is an important factor to account for when attempting to reach higher We at this value of β. However, we see a dramatic improvement for the results on mesh M5, with convergence in the drag factor up to $We = 0.8$ as well as a converged result at $We = 0.9$ although we cannot verify it with further refinement in N.

With this success in mind, we increase the stabilisation parameter to $\beta_s = 1$. Conver-

	Mesh M4				Mesh M5			
We	N = 15	N = 16	N = 17	N = 18	N = 13	N = 14	N = 15	N = 16
0.1	5.906026	5.906027	5.906027	5.906026	5.906026	5.906027	5.906026	5.906027
0.2	5.808245	5.808245	5.808245	5.808245	5.808245	5.808245	5.808245	5.808245
0.3	5.694340	5.694340	5.694340	5.694340	5.694340	5.694340	5.694340	5.694340
0.4	5.586113	5.586113	5.586113	5.586113	5.586113	5.586113	5.586113	5.586113
0.5	5.491800	5.491800	5.491800	5.491800	5.491800	5.491801	5.491800	5.491800
0.6	-	-	-	-	5.413131	5.413133	5.413134	5.413133
0.7	-	-	-	-	5.349202	5.349210	5.349213	5.349213
0.8	-	-	-	-	5.298235	5.298250	5.298258	5.298261
0.9	-	-	-	-	5.258298	5.258318	5.258334	5.258343

Table 6.37: Drag for uniform flow of an Oldroyd B fluid past a fixed sphere in a cylinder with $Re = 0.01$ and $\beta = \frac{1}{2}$. Performed with timestep, $\Delta t = 10^{-4}$.

	Mesh M4				Mesh M5			
We	N = 15	N = 16	N = 17	N = 18	N = 13	N = 14	N = 15	N = 16
0.1	5.938663	5.938663	5.938663	5.938663	5.938663	5.938663	5.938663	5.938663
0.2	5.917382	5.917382	5.917382	5.917382	5.917382	5.917382	5.917382	5.917382
0.3	5.892718	5.892718	5.892718	5.892718	5.892718	5.892718	5.892718	5.892718
0.4	5.869454	5.869454	5.869454	5.869454	5.869454	5.869454	5.869454	5.869454
0.5	5.849474	5.849474	5.849474	5.849474	5.849474	5.849474	5.849474	5.849474
0.6	5.833280	5.833280	5.833280	5.833280	5.833279	5.833280	5.833280	5.833280
0.7	5.820817	5.820817	5.820817	5.820817	5.820816	5.820817	5.820817	5.820817
0.8	5.811850	5.811851	5.811851	5.811851	5.811847	5.811849	5.811850	5.811851
0.9	5.806112	5.806115	5.806116	5.806117	5.806110	5.806113	5.806115	5.806117
1	5.802177*	-	-	-	5.803367	5.803369	5.803373	5.803375
1.1	-	-	-	-	5.803401*	5.803407	-	-

Table 6.38: Drag factor for uniform flow of an Oldroyd B fluid past a fixed sphere in a cylinder with $Re = 0.01$ and $\beta = \frac{8}{9}$. Performed with timestep, $\Delta t = 10^{-4}$. Results which had not met the convergence criteria are marked with an asterisk.

	Mesh M4				Mesh M5			
We	N = 15	N = 16	N = 17	N = 18	N = 13	N = 14	N = 15	N = 16
0.1	5.872271	5.872271	5.872271	5.872271	5.872271	5.872271	5.872271	5.872271
0.2	5.693800	5.693800	5.693800	5.693800	5.693800	5.693800	5.693800	5.693800
0.3	5.483275	5.483275	5.483275	5.483275	5.483275	5.483275	5.483275	5.483275
0.4	-	5.280604	-	5.280604	5.280605	5.280604	5.280604	5.280604
0.5	-	-	-	-	5.101474	5.101473	5.101472	5.101471
0.6	-	-	-	-	4.949510	4.949508	4.949505	4.949504
0.7	-	-	-	-	4.823299	4.823296	4.823292	4.823289
0.8	-	-	-	-	4.719717	4.719712	4.719705	4.719700
0.9	-	-	-	-	4.635265*	4.635348	-	-

Table 6.39: Drag factor for uniform flow of an Oldroyd B fluid past a fixed sphere in a cylinder with $Re = 0.01$ and $\beta = \frac{1}{9}$. Performed with timestep, $\Delta t = 10^{-4}$ using DEVSS-G, $\beta_s = 0.5$. Results which had not met the convergence criteria are marked with an asterisk.

gence of the drag factor with temporal refinement at each value of β for $We = 0.3$ is shown in Table 6.40, where we see excellent convergence by $\Delta = 10^{-3}$, although we note that the converged value at this spatial refinement does not agree perfectly with the DG-only scheme in Table 6.34, which was also observed in the flow past a cylinder benchmark in Section 6.2. However, when considering convergence of the drag factor with spatial refinement in Table 6.41 we see that with sufficient refinement in space, the computed drag factor does agree with that found by the DG-only scheme shown in Table 6.35. Spatial convergence at $\beta = \frac{1}{9}$ is also demonstrated from mesh M3 onwards with increasing N, which is a vast improvement on the DG-only scheme. In terms of mesh refinement it is clear that meshes M1 and M2 are not suitable for this benchmark even with the additional stabilisation provided by DEVSS-G.

Timestep	$\beta = \frac{1}{9}$	$\beta = \frac{1}{2}$	$\beta = \frac{8}{9}$
10^{-2}	-	5.69436872	5.89271937
10^{-3}	5.48335220	5.69436861	5.89271927
10^{-4}	5.48335220	5.69436861	5.89271926
10^{-5}	5.48335218	5.69436857	5.89271922

Table 6.40: Temporal convergence of drag factor for flow past a fixed sphere in a cylinder of an Oldroyd B fluid with $Re = 0.01$ and $We = 0.3$. Performed on mesh M3 with $N = 8$ using DEVSS-G, $\beta_s = 1.0$.

	$\beta = \frac{1}{9}$				$\beta = \frac{1}{2}$				$\beta = \frac{8}{9}$			
Mesh	N = 4	N = 8	N = 12	N = 16	N = 4	N = 8	N = 12	N = 16	N = 4	N = 8	N = 12	N = 16
M1	-	-	-	-	-	5.693303	5.693861	5.694332	5.925820	5.894727	5.892601	5.892696
M2	-	-	5.483269	-	-	5.694405	5.694341	5.694340	-	5.892738	5.892718	5.892718
M3	5.456118	5.483352	5.483272	5.483276	5.686380	5.694369	5.694338	5.694340	5.893470	5.892719	5.892717	5.892718
M4	5.480210	5.483270	5.483275	5.483275	5.693262	5.694338	5.694340	5.694340	5.891969	5.892717	5.892718	5.892718
M5	5.480188	5.483270	5.483275	5.483275	5.693255	5.694338	5.694340	5.694340	5.891987	5.892717	5.892718	5.892718

Table 6.41: Spatial convergence of drag factor for uniform flow of an Oldroyd B fluid past a fixed sphere in a cylinder with $Re = 0.01$ and $We = 0.3$. Performed with timestep, $\Delta t = 10^{-4}$ using DEVSS-G, $\beta_s = 1.0$.

Table 6.42 shows the drag factor computed for attainable We with $\beta = \frac{1}{9}$. We again see mesh dependence with M5 still vastly outperforming M4 and are able to obtain converged results up to $We = 0.9$ with convergence with refinement in N and additional unconverged results up to $We = 1.1$. Drag factors for $\beta = \frac{1}{2}$ are shown in Table 6.43 where we are able to obtain converged results up to $We = 1$ and unconverged results at $We = 1.1$. Once again, the additional refinement in the wake for mesh M5 is shown to produce a vast improvement in the attainable We. Finally, the computed drag factor at $\beta = \frac{8}{9}$ is shown in Table 6.44, where we are able to obtain results up to $We = 1.0$ and some additonal results at $We = 1.1$. There is an improvement in the attainable We value for mesh M4 as observed in the DG-only scheme.

Table 6.47 shows the collected results from the DEVSS-G scheme using $\beta_s = 1$. In terms of the behaviour of the drag, we see a drag reduction with increasing We. With decreasing β we observe an increase in the rate of drag reduction with We. This is consistent with the literature. Tables 6.45 and 6.45 show some comparison against those found in the literature and Figure 6.15. We see excellent agreement at $\beta = \frac{1}{9}$ with Bodart and Crochet [5] as well as at $\beta = \frac{1}{2}$ with both Lunsmann et al. [33] and Chauvière and Owens [10], although we fail to attain the values of We obtained by any of these studies. We suspect this may be due to the strict convergence criteria applied to the drag and field variables with respect to their change between timesteps. In many cases the drag appeared to have converged without the field variables meeting the stopping criterion followed by divergence of the solution at some point in time before the set time limit. Additional investigation would be warranted and we may be able to match the drag factor values found by these authors by relaxing the stopping criterion applied to the field variables. There are no available results in the literature at $\beta = \frac{8}{9}$ although Tamaddon-Jahromi et al. [58] provide results at $\beta = 0.9$ which we may compare with. While they do not provide the full data set in the paper, we see a similar trend to our results up to about $We = 0.8$ where they predict a larger reduction in the drag factor. We do not predict this reduction, which could be due to insufficient mesh refinement in the wake of the sphere, although their results at $\beta = \frac{1}{9}$ also predict a reduction in the drag factor which disagrees with the results of Bodart and Crochet [5].

	Mesh M4				Mesh M5			
We	N = 15	N = 16	N = 17	N = 18	N = 13	N = 14	N = 15	N = 16
0.1	5.872271	5.872271	5.872271	5.872271	5.872271	5.872271	5.872271	5.872271
0.2	5.693800	5.693800	5.693800	5.693800	5.693800	5.693800	5.693800	5.693800
0.3	5.483275	5.483275	5.483275	5.483275	5.483275	5.483275	5.483275	5.483275
0.4	5.280604	5.280604	5.280604	5.280604	5.280605	5.280604	5.280604	5.280604
0.5	5.101432*	-	5.101471	5.101471	5.101474	5.101472	5.101471	5.101471
0.6	-	-	-	-	4.949510	4.949507	4.949505	4.949504
0.7	-	-	-	-	4.823299	4.823296	4.823292	4.823289
0.8	-	-	-	-	4.719717	4.719711	4.719705	4.719700
0.9	-	-	-	-	4.635359	4.635348	4.635335	4.635326
1	-	-	-	-	4.567070*	4.567052*	-	-
1.1	-	-	-	-	4.519212*	4.502012*	-	-

Table 6.42: Drag factor for uniform flow of an Oldroyd B fluid past a fixed sphere in a cylinder with $Re = 0.01$ and $\beta = \frac{1}{9}$. Performed with timestep, $\Delta t = 10^{-4}$ using DEVSS-G, $\beta_s = 1.0$. Results which had not met the convergence criteria are marked with an asterisk.

	Mesh M4				Mesh M5			
We	N = 15	N = 16	N = 17	N = 18	N = 13	N = 14	N = 15	N = 16
0.1	5.906026	5.906027	5.906027	5.906027	5.906026	5.906027	5.906027	5.906027
0.2	5.808245	5.808245	5.808245	5.808245	5.808245	5.808245	5.808245	5.808245
0.3	5.694340	5.694340	5.694340	5.694340	5.694340	5.694340	5.694340	5.694340
0.4	5.586113	5.586113	5.586113	5.586113	5.586113	5.586113	5.586113	5.586113
0.5	5.491800	5.491800	5.491800	5.491800	5.491801	5.491801	5.491800	5.491800
0.6	5.413134	5.413133	5.413133	5.413132	5.413131	5.413134	5.413134	5.413133
0.7	5.349204*	5.349213	5.349213	5.349212	5.349203	5.349211	5.349213	5.349213
0.8	-	-	-	-	5.298236	5.298250	5.298259	5.298262
0.9	-	-	-	-	5.258296	5.258318	5.258334	5.258343
1	-	-	-	-	5.227584	5.227611	5.227635	-
1.1	-	-	-	-	5.204528*	5.204543*	-	-

Table 6.43: Drag factor for uniform flow of an Oldroyd B fluid past a fixed sphere in a cylinder with $Re = 0.01$ and $\beta = \frac{1}{2}$. Performed with timestep, $\Delta t = 10^{-4}$ using DEVSS-G, $\beta_s = 1.0$. Results which had not met the convergence criteria are marked with an asterisk.

	Mesh M4				Mesh M5			
We	N = 15	N = 16	N = 17	N = 18	N = 13	N = 14	N = 15	N = 16
0.1	5.938663	5.938663	5.938663	5.938663	5.938663	5.938663	5.938663	5.938663
0.2	5.917382	5.917382	5.917382	5.917382	5.917382	5.917382	5.917382	5.917382
0.3	5.892718	5.892718	5.892718	5.892718	5.892718	5.892718	5.892718	5.892718
0.4	5.869454	5.869454	5.869454	5.869454	5.869454	5.869454	5.869454	5.869454
0.5	5.849474	5.849474	5.849474	5.849474	5.849474	5.849474	5.849474	5.849474
0.6	5.833280	5.833280	5.833280	5.833280	5.833279	5.833280	5.833280	5.833280
0.7	5.820817	5.820817	5.820817	5.820817	5.820816	5.820817	5.820817	5.820817
0.8	5.811850	5.811851	5.811851	5.811851	5.811847	5.811849	5.811850	5.811851
0.9	5.806113	5.806116	5.806117	5.806117	5.806110	5.806113	5.806115	5.806117
1	5.800868*	-	-	-	5.803367	5.803369	5.803373	5.803375
1.1	-	-	-	-	5.803404*	5.803408	-	-

Table 6.44: Drag factor for uniform flow of an Oldroyd B fluid past a fixed sphere in a cylinder with $Re = 0.01$ and $\beta = \frac{8}{9}$. Performed with timestep, $\Delta t = 10^{-4}$ using DEVSS-G, $\beta_s = 1.0$. Results which had not met the convergence criteria are marked with an asterisk.

Present Work		Bodart & Crochet (1994)[5]	
We	Drag Factor	We	Drag Factor
0	5.9478	0	5.9475
0.1	5.8723	0.131875	5.8224
0.2	5.6938	0.2078125	5.6775
0.3	5.4833	0.3078125	5.4666
0.4	5.2806	0.4078125	5.2655
0.5	5.1015	0.5078125	5.0885
0.6	4.9495	0.6078125	4.9388
0.7	4.8233	0.7078125	4.8147
0.8	4.7197	0.8078125	4.7131
0.9	4.6353	0.9078125	4.6306
1	4.5671*	1.0078125	4.5642
1.1	4.5192*	1.1078125	4.5112
1.2	–	1.2078125	4.4697

Table 6.45: Drag factor for uniform flow of an Oldroyd B fluid past a fixed sphere in a cylinder with $Re = 0.01$, $\beta = \frac{1}{9}$. Comparison of best results taken from Table 6.42. Results which had not met the convergence criteria are marked with an asterisk.

We	Present work	Chauviere & Owens (2000)[10]	Lunnsmann et al. (1993)[33]
0	5.9478	5.9475	5.94716
0.1	5.906	–	–
0.2	5.8082	–	–
0.3	5.6943	–	5.69368
0.4	5.5861	–	–
0.5	5.4918	5.4852	–
0.6	5.4131	5.4009	5.41225
0.7	5.3492	5.3411	–
0.8	5.2983	5.2945	–
0.9	5.2583	5.2518	5.25717
1	5.2276	5.224	–
1.1	5.2045	5.2029	–
1.2	–	5.1842	5.18648
1.3	–	5.1421^a	–
1.4	–	5.1240^a	–
1.5	–	–	5.15293

Table 6.46: Drag factor for uniform flow of an Oldroyd B fluid past a fixed sphere in a cylinder with $Re = 0.01$, $\beta = \frac{1}{2}$. Best results taken from Table 6.43.

We	$\beta = \frac{8}{9}$	$\beta = \frac{1}{2}$	$\beta = \frac{1}{9}$
0	5.9478	5.9478	5.9478
0.1	5.9387	5.9060	5.8723
0.2	5.9174	5.8082	5.6938
0.3	5.8927	5.6943	5.4833
0.4	5.8695	5.5861	5.2806
0.5	5.8495	5.4918	5.1015
0.6	5.8333	5.4131	4.9495
0.7	5.8208	5.3492	4.8233
0.8	5.8119	5.2983	4.7197
0.9	5.8061	5.2583	4.6353
1	5.8034	5.2276	4.5671*
1.1	5.8034	5.2045*	4.5192*

Table 6.47: Collected results for uniform flow of an Oldroyd B fluid past a fixed sphere in a cylinder showing the drag factor. All results computed at $Re = 0.01$ using the DG/DEVSS-G scheme with $\beta_s = 1.0$, using $\Delta t = 10^{-4}$. Results which had not met the convergence criteria are marked with an asterisk.

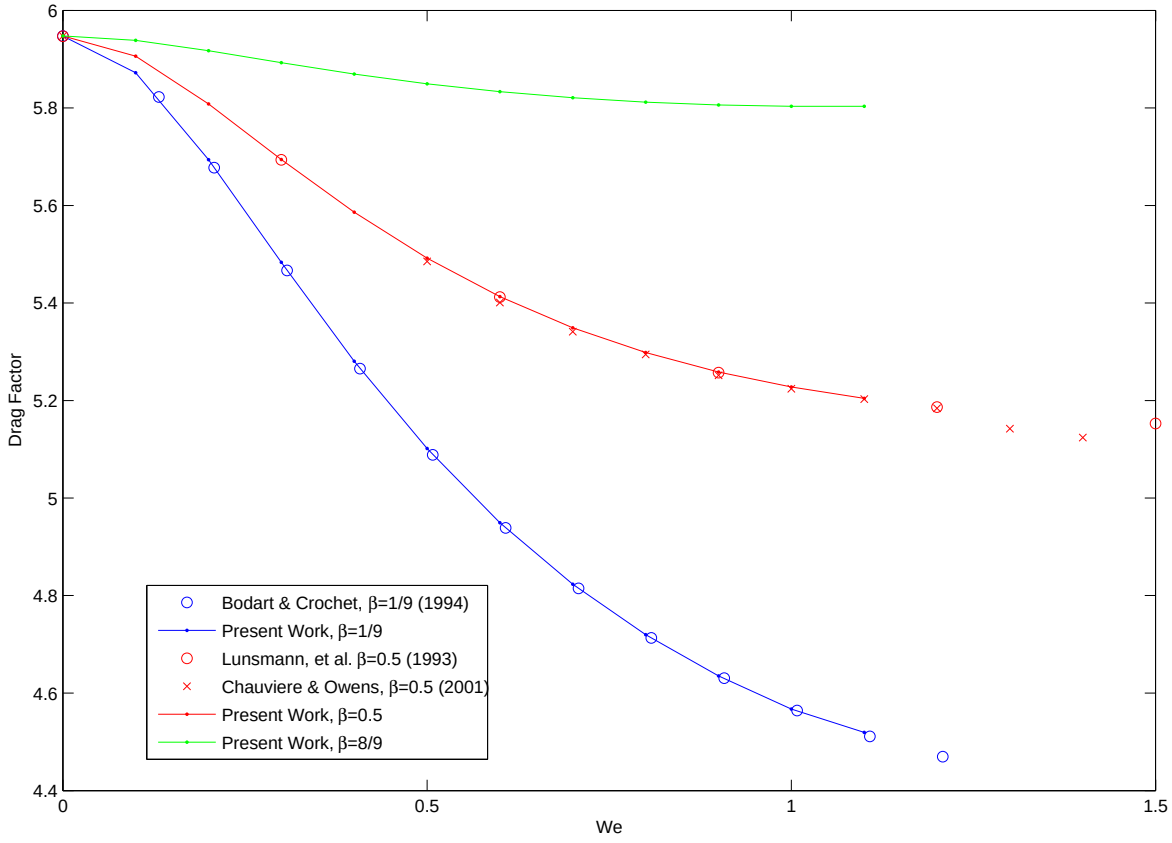

Figure 6.15: Collected results for the benchmark of flow past a fixed sphere in a cylinder for an Oldroyd B fluid comparing the present study against values found in the literature. Values taken from Table 6.47

Figures 6.16- 6.17 show the stress along the axis of symmetry and along the surface of the sphere at $\beta = \frac{1}{2}$. We indeed see a large increase in the axial stress in the wake of the sphere with increasing We, which supports the observations with mesh refinement. As well as an increase in magnitude, we also see that the length which the stress rise propagates downstream is increased with rising We. All of our meshes had a central mesh extending to a length of 4 in each direction from the centre of the sphere, at which point a single long element makes up the rest of the channel. The fact the the axial stress has not fully relaxed beyond $z = 5$ is a good reason to extend the central mesh beyond $z = 4$ when attempting to obtain solutions at higher values of We. There is also a significant growth in both the radial and shear stress on the surface of the sphere with increasing We, with a slight shift downstream of the second peak on the surface of the sphere for the radial stress seen at $We = 1$. The value of $\tau_{\theta\theta}$ grows in the stagnation zone in front of the sphere with increasing We and we predict a decrease in magnitude in the wake as We increases but with a propagation downstream before relaxing fully. Finally, a growth of the N_1 on the surface of the sphere and the wake with increasing We is predicted, with a significant increase in the wake in comparison to that on the surface as well as an increase in magnitude in the stagnation zone in front of the sphere.

We provide contour plots of pressure, velocity and stress at $\beta = \frac{1}{2}$ in Figures 6.18-6.20. With increasing We we predict an increasing pressure reduction in the wake of the sphere closest to the surface. While the maximum velocity of the fluid remains fairly constant, there is a clear reduction in velocity in the wake of the sphere, with its influence on the flow downstream becoming greater as We increases. The axial stress contour shows an increasingly thin boundary layer developing on the surface of the sphere and in the wake with increasing We Another notable feature is the propagation of $\tau_{\theta\theta}$ downstream and near to the surface of the sphere with increasing We.

Figures 6.21- 6.22 show the stress along the axis of symmetry and along the surface of the sphere at $We = 1$ with increasing β. The growth in axial stress on the surface and in the wake of the sphere is not as dramatic when compared with increasing We and we predict a reduction in axial stress and N_1 in the wake when decreasing β from $\frac{1}{2}$ to $\frac{1}{9}$. It is possible this is a spurious result and we predict the opposite at $We = 0.9$,

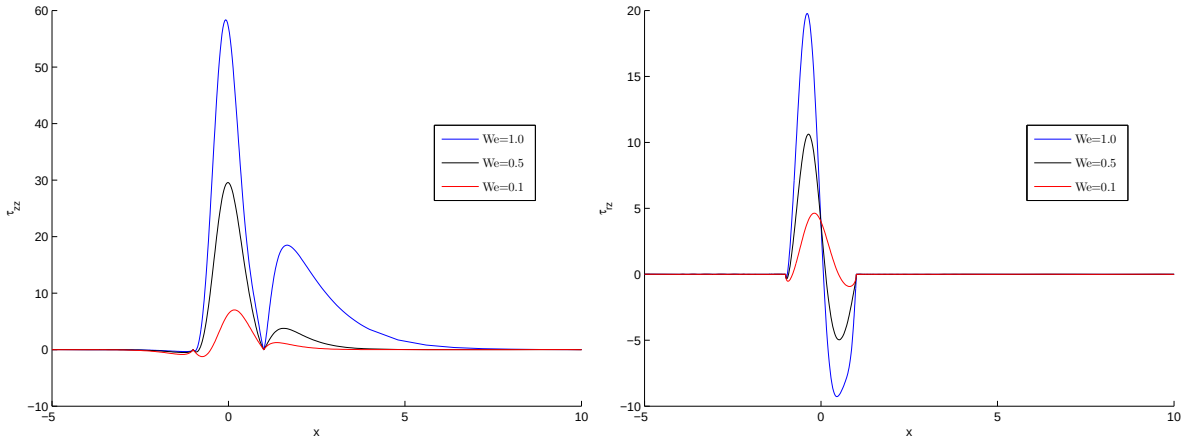

(a) τ_{zz} (b) τ_{rz}

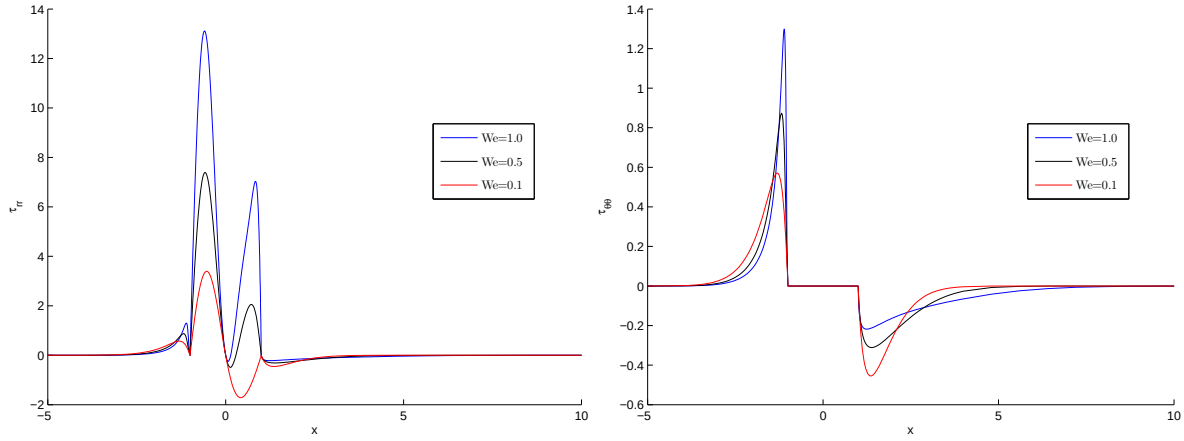

(c) τ_{rr} (d) $\tau_{\theta\theta}$

Figure 6.16: Components of elastic stress along the axis of symmetry for uniform flow of an Oldroyd B fluid past a fixed sphere in a cylinder. Model parameters $\beta = 0.5$, $Re = 0.01$.

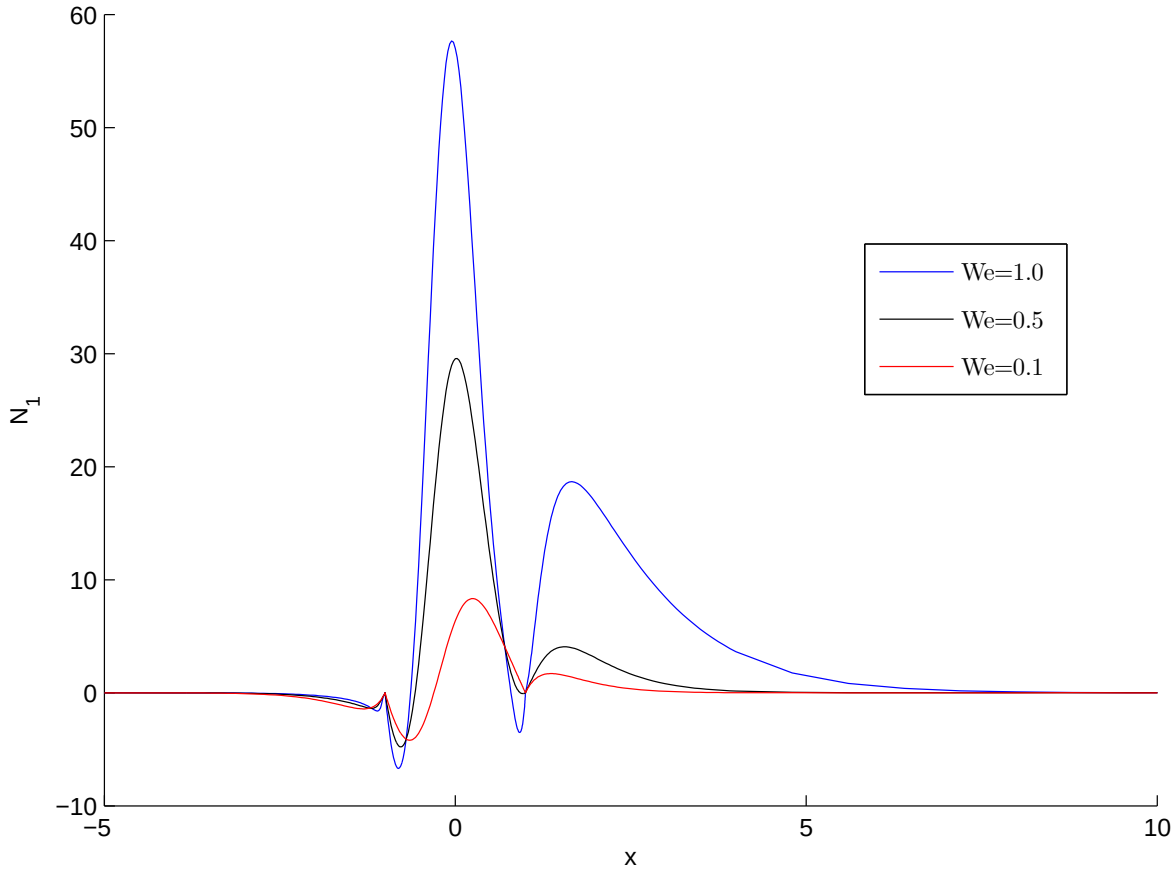

Figure 6.17: First normal stress difference, $N_1 = \tau_{zz} - \tau_{rr}$, along the axis of symmetry for uniform flow of an Oldroyd B fluid past a fixed sphere in a cylinder. Model parameters $\beta = 0.5$, $Re = 0.01$.

shown in Figure 6.23. Contrary to the less dramatic axial stress growth, we predict a large growth in radial stress, shear stress and $\tau_{\theta\theta}$ with decreasing β which may be a cause of the instabilities above $We = 1$.

Figures 6.24- 6.26 show the contour plots at $We = 1$ with decreasing β. As observed with increasing We, there is a pressure drop in the wake, close to the sphere when increasing from $\beta = \frac{8}{9}$ to $\beta = \frac{1}{2}$. There is a slight increase at $\beta = \frac{1}{9}$, although this could be spurious as noted above in relation to the difference between $We = 0.9$ and $We = 1$ at this viscosity ratio. Looking at the axial velocity, the maximum value is slightly increasing with decreasing β and we observe an increase with respect to the

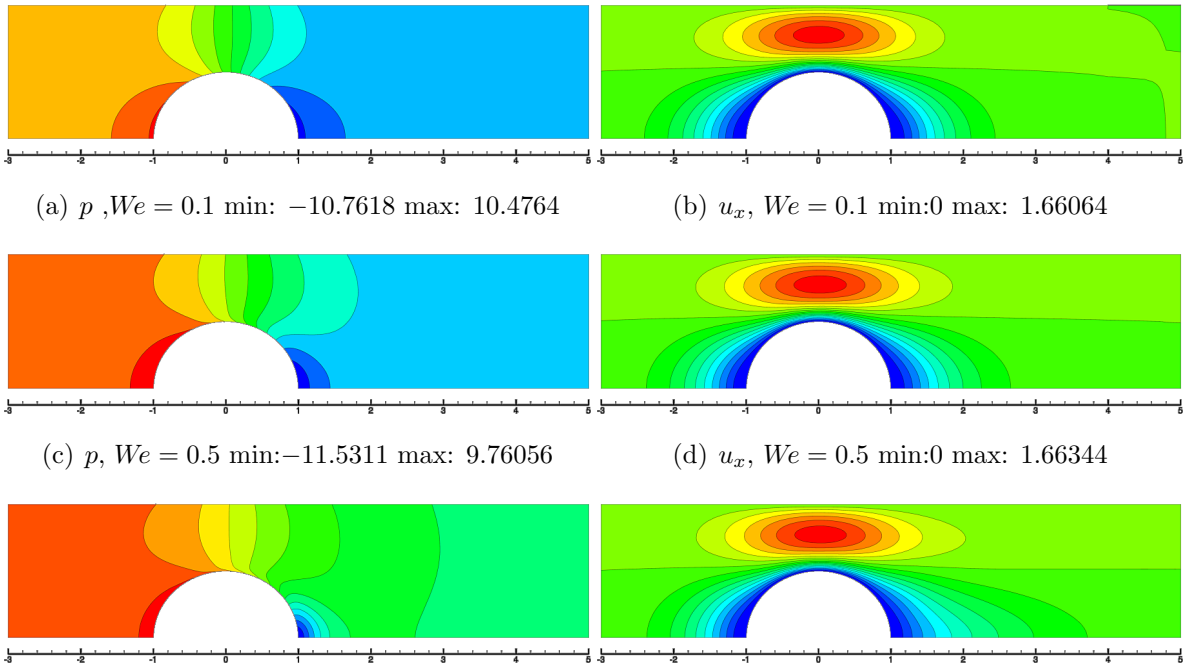

(a) p ,$We = 0.1$ min: -10.7618 max: 10.4764

(b) u_x, $We = 0.1$ min:0 max: 1.66064

(c) p, $We = 0.5$ min:-11.5311 max: 9.76056

(d) u_x, $We = 0.5$ min:0 max: 1.66344

(e) p, $We = 1.0$ min:-17.7909 max: 9.3244

(f) u_x, $We = 1.0$ min:0 max: 1.66116

Figure 6.18: Contours of pressure and velocity for uniform flow of an Oldroyd B fluid past a fixed sphere in a cylinder, $Re = 0.01$, $\beta = 0.5$.

influence of the sphere, downstream. We observe a large increase in the axial and radial stress boundary layer on the surface of and in the wake of the sphere as β decreases, which is similar in effect to an increase in We. While the magnitude of the shear stress certainly increases with decreasing β we see very little change in the thickness of the boundary layer, with a small growth in thickness as β decreases. This differs from the effect of increasing We. This suggests that shearing effects are minimal with increasing polymeric viscosity. Similarly, the value of We appears to be more important than β for the $\tau_{\theta\theta}$ component of elastic stress too, with only subtle thinning of the boundary layer around the surface of the sphere with decreasing β.

6.3.3 Summary

We have performed the flow past a fixed sphere benchmark for an Oldroyd B fluid which has been widely used in the literature and found excellent agreement for the attainable values of We in terms of the computed drag factor. The usage of DEVSS-G

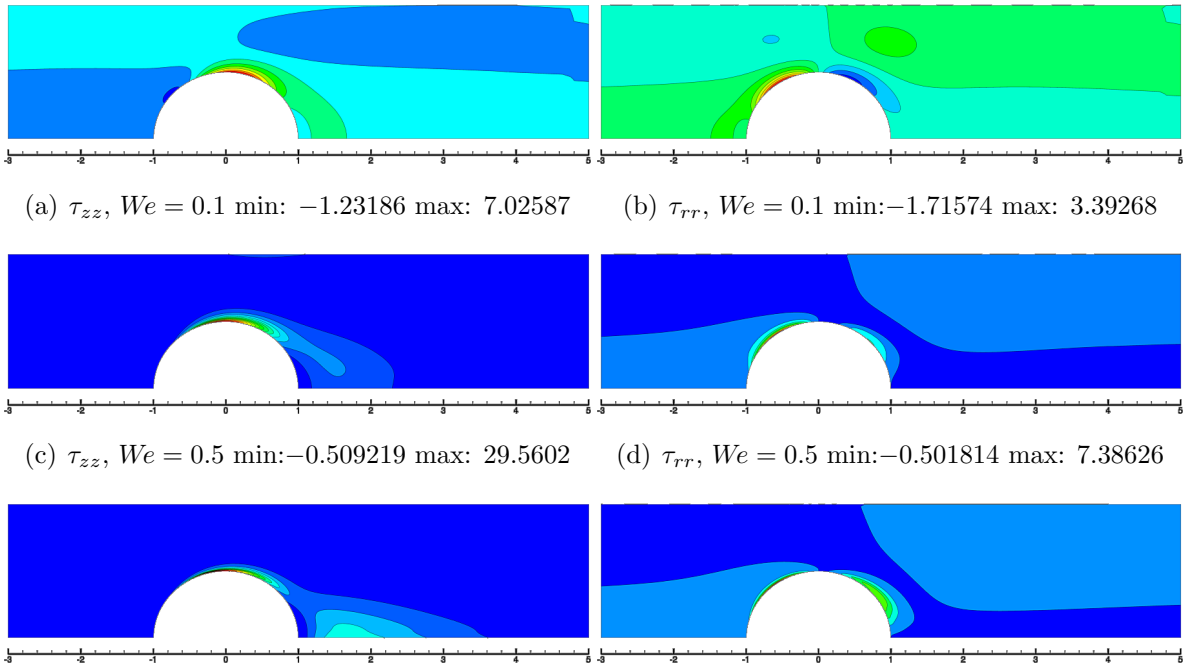

(a) τ_{zz}, $We = 0.1$ min: -1.23186 max: 7.02587

(b) τ_{rr}, $We = 0.1$ min:-1.71574 max: 3.39268

(c) τ_{zz}, $We = 0.5$ min:-0.509219 max: 29.5602

(d) τ_{rr}, $We = 0.5$ min:-0.501814 max: 7.38626

(e) τ_{zz}, $We = 1.0$ min:-0.33593 max: 58.3747

(f) τ_{rr}, $We = 1.0$ min:-0.30457 max: 13.1167

Figure 6.19: Contours of stress components for uniform flow of an Oldroyd B fluid past a fixed sphere in a cylinder, $Re = 0.01$, $\beta = 0.5$.

as a stabilisation scheme appears to be very successful in increasing the attainable We, particularly as β decreases with little loss in the apparent accuracy of our results. However, a limit of $We = 1.1$ was found for all values of β, although it is increasingly difficult to find a steady solution as β decreases.

It's possible that our meshes are responsible for this relatively low limiting value of We and that refinement in the wake of the sphere may allow us to reach higher values. We intend to perform additional simulations in order to investigate further, and hope to attain values in line with those of Chauvière and Owens [10] who reach a value in excess of $We = 1.3$ at $\beta = 0.5$. However, they postulate that the large growth of the axial stress in the wake of the sphere above $We = 1.3$ means results above this value are highly susceptible to error. This limiting value of $We = 1.3$ was also reported by Fan [13]. Our results support this claim with a strong growth in the axial stress in the wake with increasing We and comparatively little influence with decreasing β.

It would also be interesting to compare the extension rate in the wake of the sphere. This is a region of pure (although not steady) elongation meaning the infinite exten-

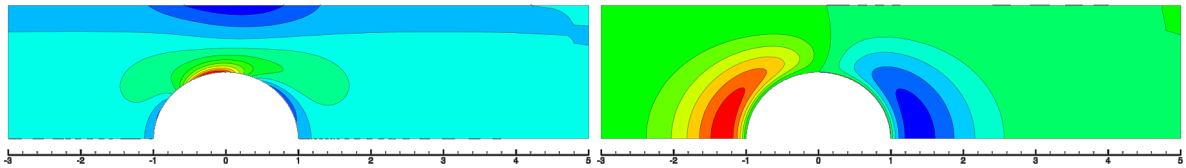

(a) τ_{rz}, $We = 0.1$ min: -1.47365 max: 4.63417 (b) $\tau_{\theta\theta}$, $We = 0.1$ min: -0.454302 max: 0.570813

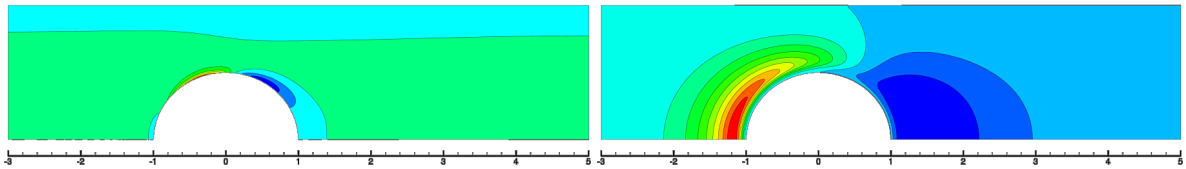

(c) τ_{rz}, $We = 0.5$ min:-4.98889 max: 10.6292 (d) $\tau_{\theta\theta}$, $We = 0.5$ min: -0.310987 max: 0.873459

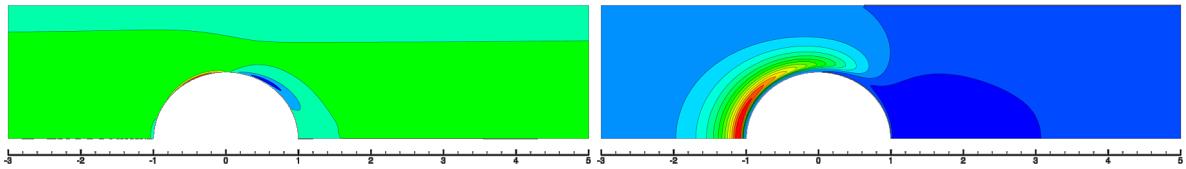

(e) τ_{rz}, $We = 1.0$ min:-11.6732 max: 19.7696 (f) $\tau_{\theta\theta}$, $We = 1.0$ min: -0.22202 max: 1.29901

Figure 6.20: Contours of stress components for uniform flow of an Oldroyd B fluid past a fixed sphere in a cylinder, $Re = 0.01$, $\beta = 0.5$.

sional viscosity associated with the Oldroyd B model is likely to be a cause of the breakdown of our numerical scheme. The reason being that a node being placed on or near a region where the elongation rate is close to the finite value causing the infinite extensional velocity then this would cause serious problems for our numerical scheme. This is an issue that we shall consider in the future when investigating the mesh refinement.

Tamaddon-Jahromi et al. [58] predict a local minimum of the drag factor between $We = 1$ and $We = 1.1$ at $\beta = 0.9$. Our results at $\beta = \frac{1}{9}$ also hint at the presence of a local minimum around this value although we are unable to confirm it due to not being able to attain a converged solution at high enough We.

In summary, this serves as a strong validation of our DG/DEVSS-G scheme on what is widely considered to be a testing benchmark, despite its deceptive simplicity in terms of geometry.

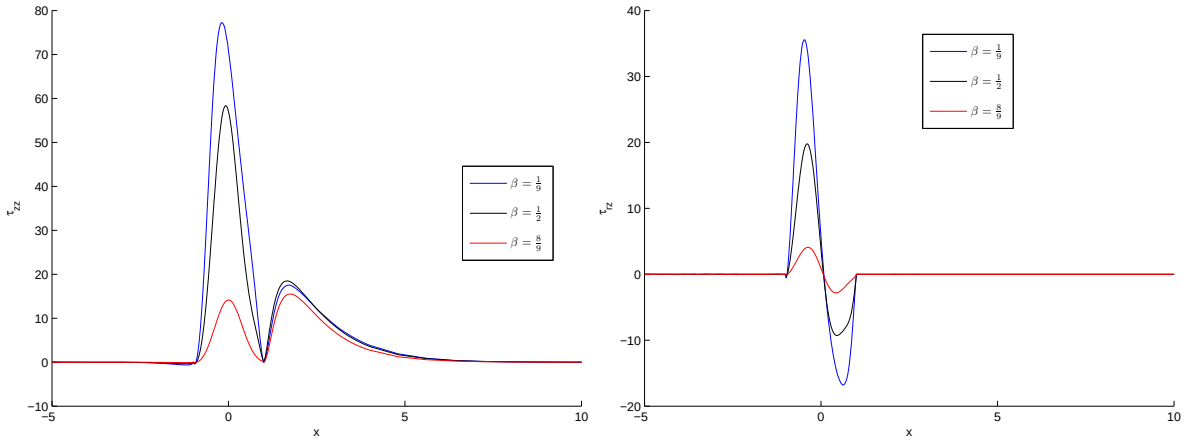

(a) τ_{zz}

(b) τ_{rz}

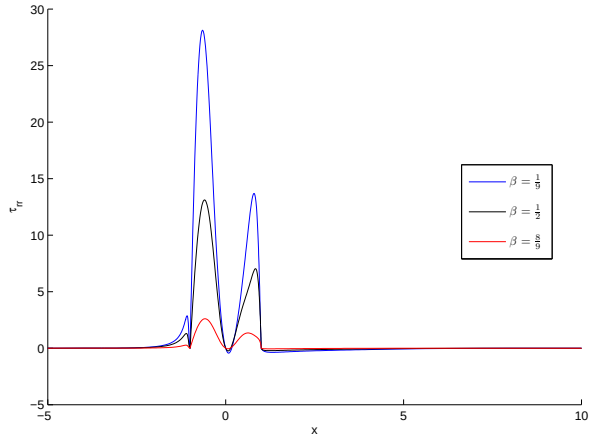

(c) τ_{rr}

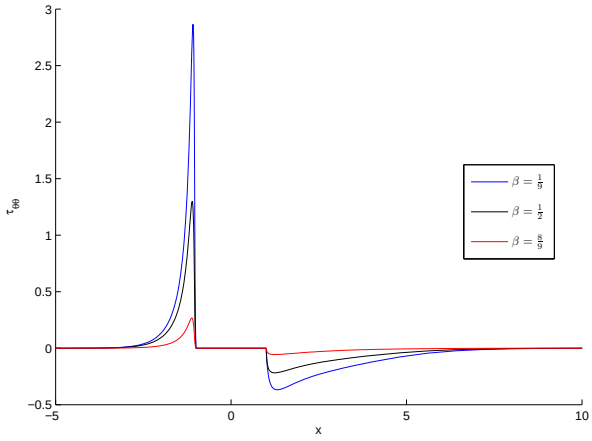

(d) $\tau_{\theta\theta}$

Figure 6.21: Components of elastic stress along the axis of symmetry for uniform flow of an Oldroyd B fluid past a fixed sphere in a cylinder. Model parameters $We = 1$, $Re = 0.01$.

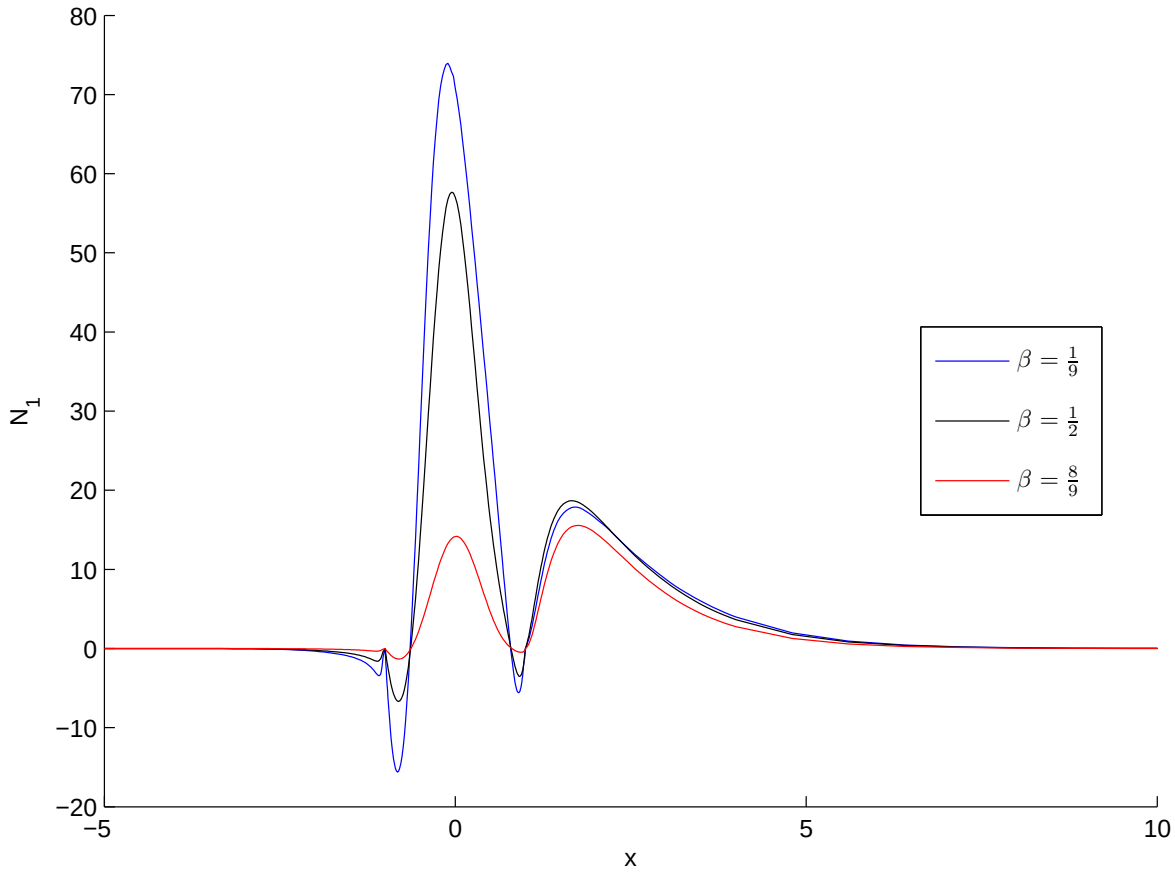

Figure 6.22: $N_1 = \tau_{zz} - \tau_{rr}$, along the axis of symmetry for uniform flow of an Oldroyd B fluid past a fixed sphere in a cylinder. Model parameters $We = 1$, $Re = 0.01$.

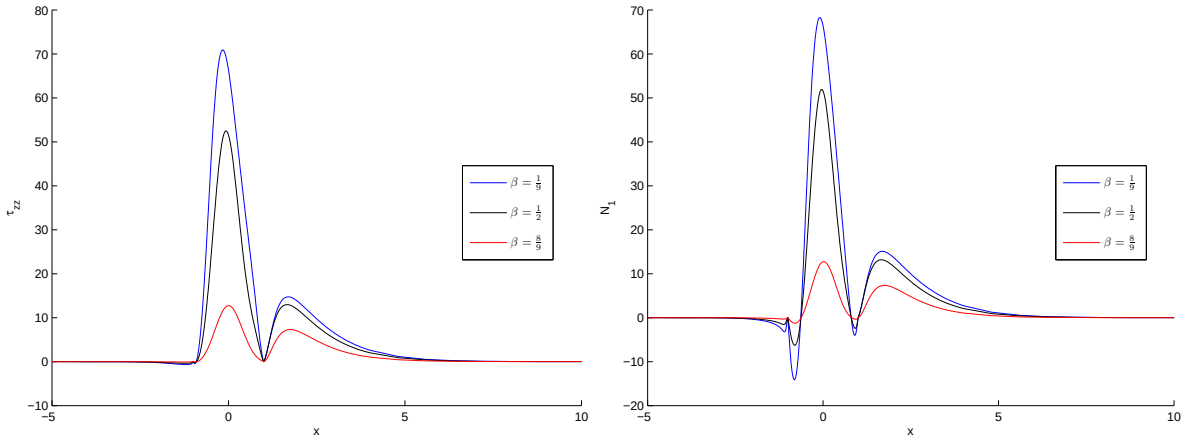

(a) τ_{zz} (b) $N_1 = \tau_{zz} - \tau_{rr}$

Figure 6.23: Axial stress and first normal stress difference along the axis of symmetry for uniform flow of an Oldroyd B fluid past a fixed sphere in a cylinder. Model parameters $We = 0.9$, $Re = 0.01$.

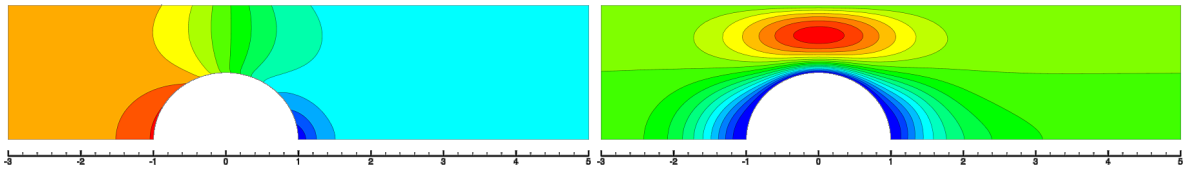

(a) p, $\beta = \frac{8}{9}$ min: -13.8022 max: 10.3799

(b) u_x, $\beta = \frac{8}{9}$ min:0 max: 1.65954

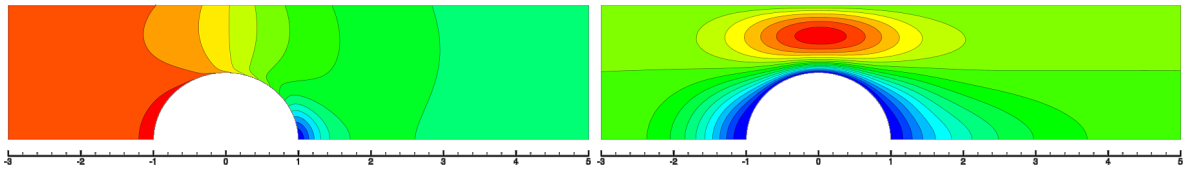

(c) p, $\beta = \frac{1}{2}$ min:-17.7909 max: 9.3244

(d) u_x, $\beta = \frac{1}{2}$ min:0 max: 1.66116

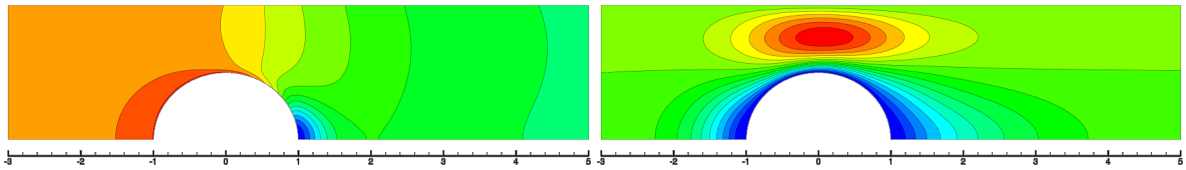

(e) p, $\beta = \frac{1}{9}$ min:-17.3712 max: 8.96045

(f) u_x, $\beta = \frac{1}{9}$ min:0 max: 1.67972

Figure 6.24: Contours of pressure and velocity for uniform flow of an Oldroyd B fluid past a fixed sphere in a cylinder, $Re = 0.01$, $We = 1.0$.

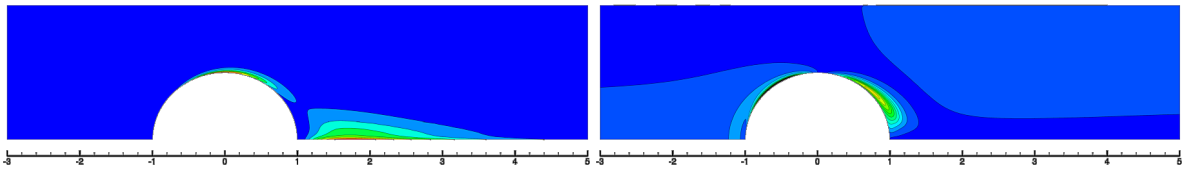

(a) τ_{zz}, $\beta = \frac{8}{9}$ min: -0.0736256 max: 15.5234

(b) τ_{rr}, $\beta = \frac{8}{9}$ min:-0.0678164 max: 2.60096

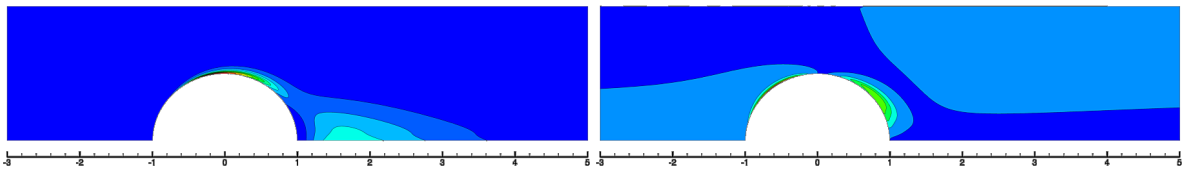

(c) τ_{zz}, $\beta = \frac{1}{2}$ min:-0.33593 max: 58.3747

(d) τ_{rr}, $\beta = \frac{1}{2}$ min:-0.30457 max: 13.1167

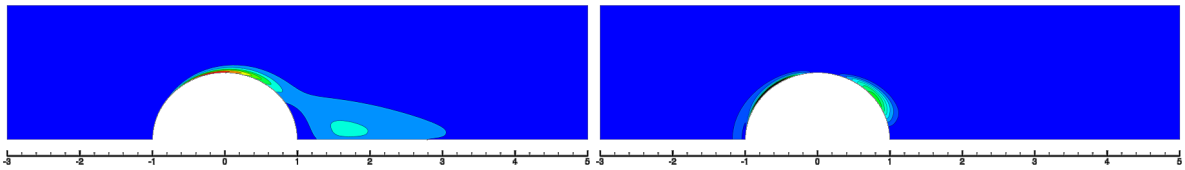

(e) τ_{zz}, $\beta = \frac{1}{9}$ min:-0.620205 max: 77.2469

(f) τ_{rr},$\beta = \frac{1}{9}$ min:-0.538143 max: 28.127

Figure 6.25: Contours of stress components for uniform flow of an Oldroyd B fluid past a fixed sphere in a cylinder, $Re = 0.01$, $We = 1.0$.

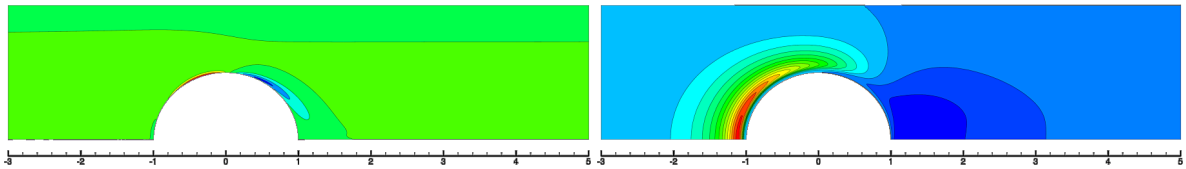

(a) τ_{rz}, $\beta = \frac{8}{9}$ min: -3.24058 max: 4.09651

(b) $\tau_{\theta\theta}$, $\beta = \frac{8}{9}$ min: -0.0562914 max: 0.267076

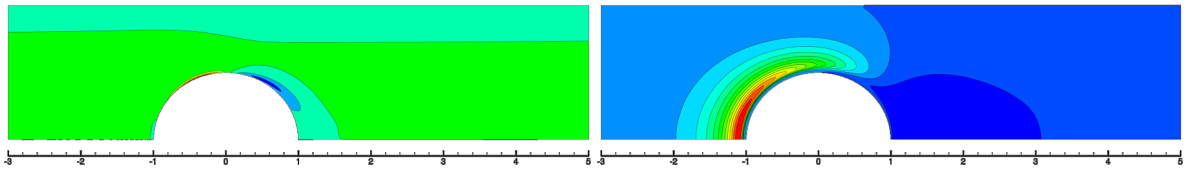

(c) τ_{rz}, $\beta = \frac{1}{2}$ min:-11.6732 max: 19.7696

(d) $\tau_{\theta\theta}$, $\beta = \frac{1}{2}$ min:-0.22202 max:1.29901

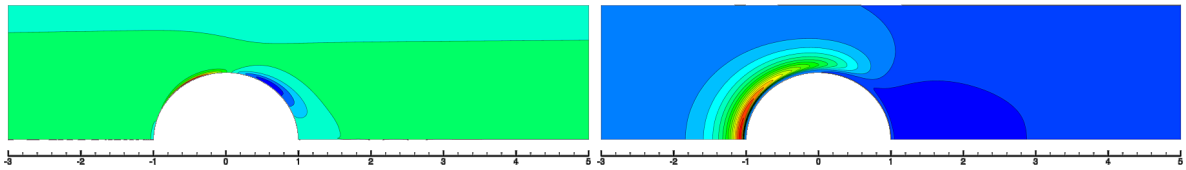

(e) τ_{rz}, $\beta = \frac{1}{9}$ min:-17.4909 max: 35.5741

(f) $\tau_{\theta\theta}$, $\beta = \frac{1}{9}$ min: -0.372593 max: 2.86695

Figure 6.26: Contours of stress components for uniform flow of an Oldroyd B fluid past a fixed sphere in a cylinder, $Re = 0.01$, $We = 1.0$.

6.3.4 Giesekus Model

For the fixed sphere benchmark we also consider the Giesekus model as described in Section 2.2.2. We use the same meshes, timestep and initial and boundary conditions as the Oldroyd B fluid and only consider the DG/DEVSS-G scheme with $\beta_s = 1$. We consider values $\alpha = 0.001, 0.01$ and 0.1 and investigate the effect on the drag factor and flow properties.

Table 6.48 shows the collected results from Tables 6.49- 6.57, which show the spatial convergence for each set of parameters, with increasing We.

	$\beta = \frac{1}{9}$			$\beta = \frac{1}{2}$			$\beta = \frac{8}{9}$		
We	$\alpha = 0.001$	$\alpha = 0.01$	$\alpha = 0.1$	$\alpha = 0.001$	$\alpha = 0.01$	$\alpha = 0.1$	$\alpha = 0.001$	$\alpha = 0.01$	$\alpha = 0.1$
0.1	5.854544	5.719759	5.203281	5.895991	5.821879	5.604715	5.93642	5.920253	5.876479
0.2	5.662541	5.435936	4.585723	5.790225	5.666142	5.243307	5.913297	5.886227	5.796995
0.3	5.442417	5.160942	4.201197	5.670226	5.515299	5.027768	5.887168	5.853158	5.748641
0.4	5.232558	4.915557	3.918241	5.557056	5.380966	4.866674	5.862658	5.823647	5.712294
0.5	5.047523	4.70415	3.692446	5.458406	5.265572	4.73752	5.841519	5.798275	5.683145
0.6	4.890276	4.524466	3.504897	5.375678	5.167812	4.630335	5.824153	5.776795	5.658991
0.7	4.759029	4.372133	3.345381	5.307771	5.0852	4.539481	5.81042	5.758697	5.638558
0.8	4.650437	4.242539	3.207566	5.252766	5.015114	4.461321	5.799998	5.743438	5.621015
0.9	4.560957	4.131536	3.087155	5.208626	4.955194	4.393316	5.79252	5.730518	5.605777
1	4.487404*	4.035642	2.981045	5.17347	4.903463	4.333597	5.787616	5.719512	5.592415
1.1	4.428358*	3.952021*	2.886881	5.145677*	4.858335	4.280744	5.784901	5.710063	5.580602
1.2	-	-	2.802819	5.123866*	4.818544	4.233647	5.783934*	5.701884	5.570086
1.3	-	-	2.727382*	-	4.783137	4.191423	-	5.694743	5.560666
1.4	-	-	2.659361*	-	4.751331*	4.153361	-	5.688455	5.552181
1.5	-	-	-	-	4.722584*	4.118878	-	5.682875	5.5445
1.6	-	-	-	-	-	4.087495	-	5.677873	5.537517
1.7	-	-	-	-	-	4.058814	-	5.673378	5.53114
1.8	-	-	-	-	-	4.0325	-	5.669313	5.525297
1.9	-	-	-	-	-	4.00827	-	-	5.519923
2	-	-	-	-	-	3.985884	-	-	5.514965

Table 6.48: Drag factor for flow past a fixed sphere in a cylinder for a Giesekus fluid at $Re = 0.01$. Performed with timestep, $\Delta t = 10^{-4}$ using DEVSS-G, $\beta_s = 1.0$. Collected from Tables of results within Section 6.3.4

In general we see an improvement on the Oldroyd B fluid in terms of attainable We with increasing α. A comparison may be seen in Figure 6.29. We also see a vast decrease in the drag factor with increasing α. The shear-thinning property of the Giesekus model is the dominating factor for this decrease. Figure 6.27 shows the influence on the axial component of elastic stress of α at fixed $We = 1$ and $\beta = \frac{1}{2}$. We observe a large decrease in axial stress on the surface of the sphere and, interestingly, a decrease in the axial stress in the wake. The peak of the stress in the wake and on the surface of the sphere at $\alpha = 0.1$ are almost equivalent, which is quite different to the values at lower values of α and for the Oldroyd B fluid. There is a similar decrease for the radial stress, with the peaks on the surface of the sphere becoming closer in magnitude, and for the shear stress. The effect on $\tau_{\theta\theta}$ is less dramatic, however. Figure 6.28 shows the normal stress differences with a reduction in N_1 at the stagnation point in front of the sphere with increasing α. The main mechanism for the drag reduction with increasing α appears to be the decrease in the axial and shear stress, with the axial stress undergoing the largest reduction.

Figure 6.30 shows a plot of the drag factor for Giesekus fluid model parameters considered. There is little sign of a local minimum for the drag factor at $\beta = \frac{1}{9}$ for any value of α. However, for the other two values of β the drag factor is showing signs of nearing a minimum, although further investigation would be required. When running the simulations we only considered values up to $We = 2$ and it would clearly be possible to increase this for $\beta = \frac{1}{2}$ and $\beta = \frac{8}{9}$. This will be left as future work, although it is important that we first compare the current results with those available in the literature in order to validate the scheme for the Giesekus model.

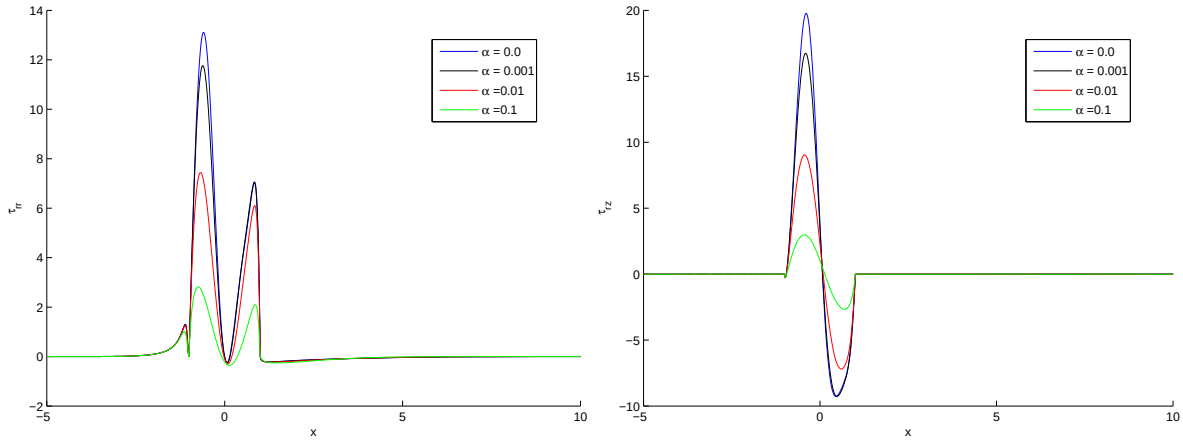

(a) τ_{rr} (b) τ_{rz}

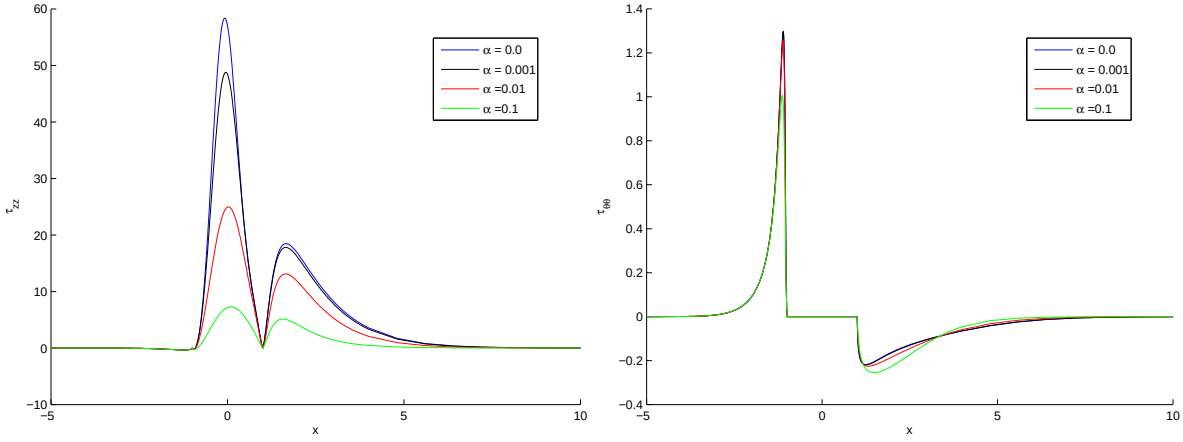

(c) τ_{zz} (d) $\tau_{\theta\theta}$

Figure 6.27: Components of elastic stress along the axis of symmetry for Giesekus fluid flow past a fixed sphere in a cylinder. Model parameters $\beta = 0.5$, $Re = 0.01$ and $We = 1$. Numerical parameters, $\Delta t = 10^{-4}$, $N = 15$ on mesh M5 using DEVSS-G with $\beta_s = 1.0$.

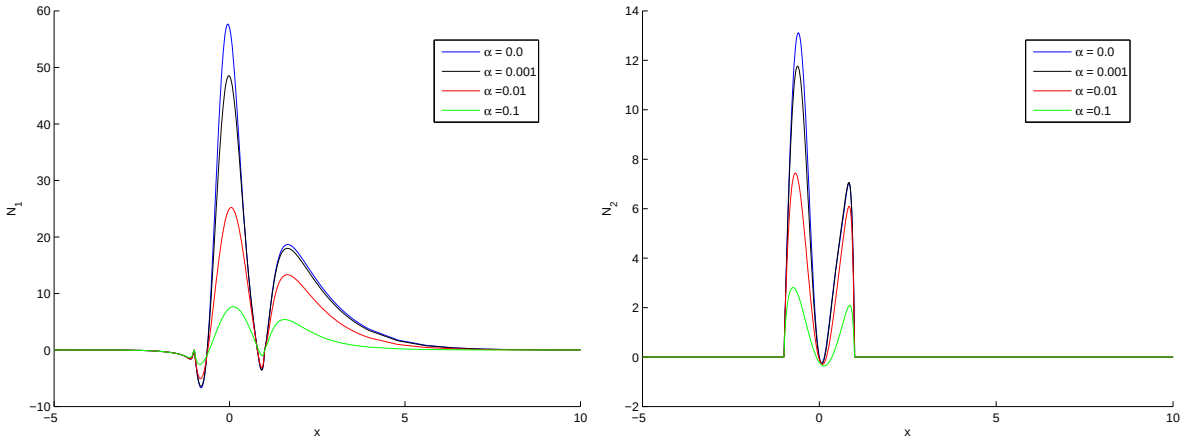

(a) $N_1 = \tau_{zz} - \tau_{rr}$ (b) $N_2 = \tau_{rr} - \tau_{\theta\theta}$

Figure 6.28: Normal stress differences along the axis of symmetry for Giesekus fluid flow past a fixed sphere in a cylinder. Model parameters $\beta = 0.5$, $Re = 0.01$ and $We = 1$. Numerical parameters, $\Delta t = 10^{-4}$, $N = 15$ on mesh M5 using DEVSS-G with $\beta_s = 1.0$.

	Mesh M4				Mesh M5			
We	N = 15	N = 16	N = 17	N = 18	N = 13	N = 14	N = 15	N = 16
0.1	5.854544	5.854544	5.854544	5.854544	5.854544	5.854544	5.854544	5.854544
0.2	5.662541	5.662541	5.662541	5.662541	5.662541	5.662541	5.662541	5.662541
0.3	5.442417	5.442417	5.442417	5.442417	5.442417	5.442417	5.442417	5.442417
0.4	5.232558	5.232558	5.232558	5.232558	5.232558	5.232558	5.232558	5.232558
0.5	5.047486*	5.047523	5.047524	5.047524	5.047524	5.047524	5.047523	5.047523
0.6	-	-	-	-	4.890278	4.890277	4.890277	4.890276
0.7	-	-	-	-	4.759031	4.759029	4.759029	4.759029
0.8	-	-	-	-	4.650445	4.650436	4.650435	4.650437
0.9	-	-	-	-	4.560987	4.560963	4.560955	4.560957
1	-	-	-	-	4.487441*	4.487404*	-	-
1.1	-	-	-	-	4.426899*	4.428358*	-	-

Table 6.49: Drag for flow past a fixed sphere in a cylinder for a Giesekus fluid with $Re = 0.01$, $\beta = \frac{1}{9}$, $\alpha = 0.001$. Performed with timestep, $\Delta t = 10^{-4}$ using DEVSS-G, $\beta_s = 1.0$.

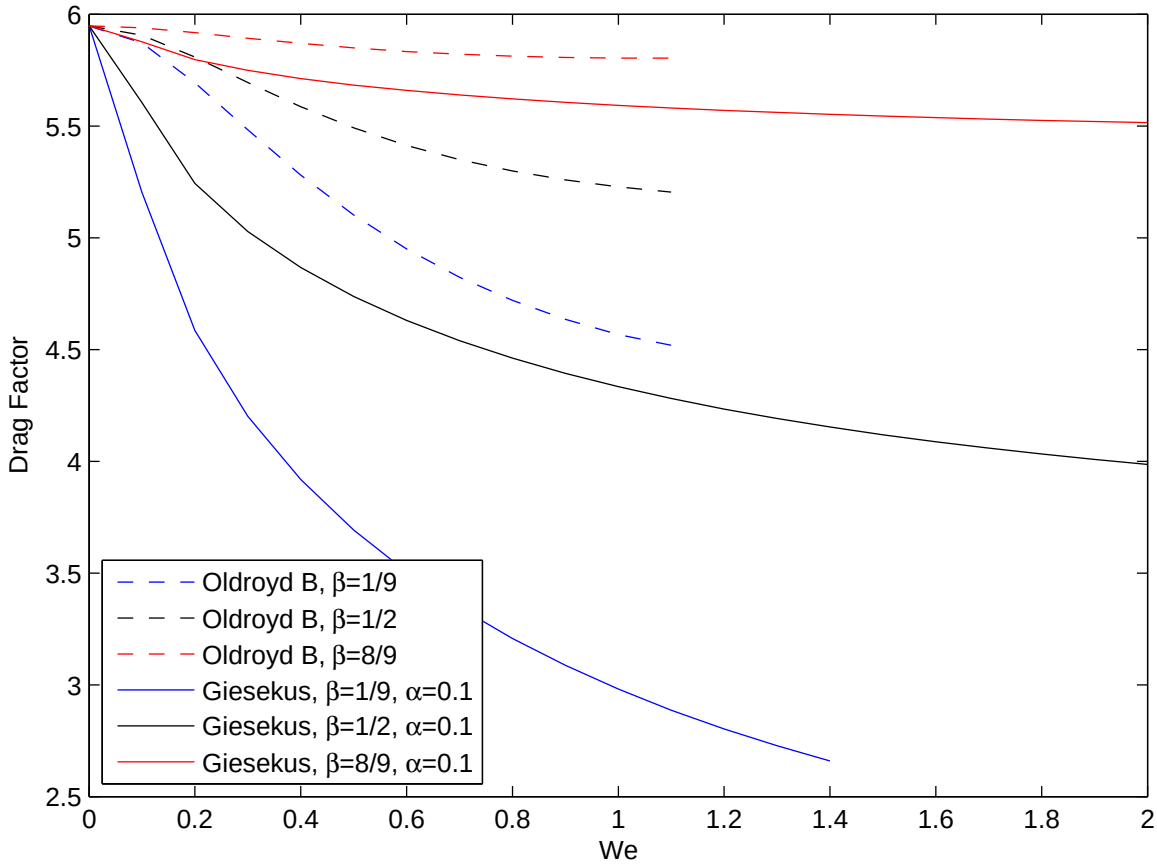

Figure 6.29: Comparison of drag factor for an Oldroyd B fluid and a Giesekus fluid with $\alpha = 0.1$ for flow past a fixed sphere in a cylinder.

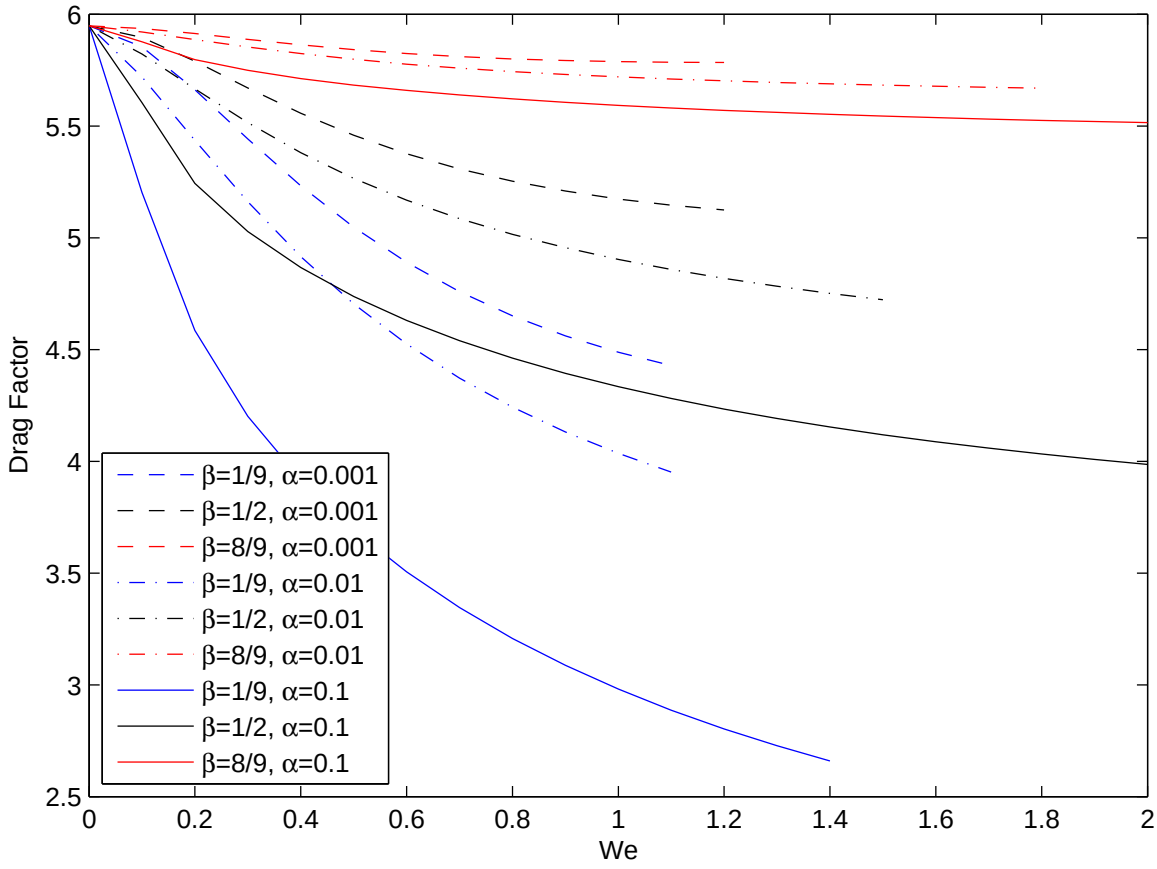

Figure 6.30: Drag factor for all parameters considered for Giesekus fluid flow past a fixed sphere in a cylinder.

	Mesh M4				Mesh M5			
We	N = 15	N = 16	N = 17	N = 18	N = 13	N = 14	N = 15	N = 16
0.1	5.895991	5.895991	5.895991	5.895991	5.895991	5.895991	5.895991	5.895991
0.2	5.790225	5.790225	5.790225	5.790225	5.790225	5.790225	5.790225	5.790225
0.3	5.670226	5.670226	5.670226	5.670226	5.670226	5.670226	5.670226	5.670226
0.4	5.557056	5.557056	5.557056	5.557056	5.557056	5.557056	5.557056	5.557056
0.5	5.458406	5.458406	5.458406	5.458406	5.458407	5.458406	5.458406	5.458406
0.6	5.375679	5.375678	5.375678	5.375678	5.375680	5.375679	5.375679	5.375678
0.7	5.307763*	5.307771	5.307770	5.307770	5.307772	5.307772	5.307771	5.307771
0.8	-	-	-	-	5.252767	5.252767	5.252766	5.252766
0.9	-	-	-	-	5.208631	5.208628	5.208627	5.208626
1	-	-	-	-	5.173485	5.173475	5.173470	5.173470
1.1	-	-	-	-	5.145696*	5.145677*	-	-
1.2	-	-	-	-	5.123895*	5.123866*	-	-

Table 6.50: Drag for flow past a fixed sphere in a cylinder for a Giesekus fluid with $Re = 0.01$, $\beta = \frac{1}{2}$, $\alpha = 0.001$. Performed with timestep, $\Delta t = 10^{-4}$ using DEVSS-G, $\beta_s = 1.0$.

	Mesh M4				Mesh M5			
We	N = 15	N = 16	N = 17	N = 18	N = 13	N = 14	N = 15	N = 16
0.1	5.936420	5.936420	5.936420	5.936420	5.936420	5.936420	5.936420	5.936420
0.2	5.913297	5.913297	5.913297	5.913297	5.913297	5.913297	5.913297	5.913297
0.3	5.887168	5.887168	5.887168	5.887168	5.887168	5.887168	5.887168	5.887168
0.4	5.862658	5.862658	5.862658	5.862658	5.862658	5.862658	5.862658	5.862658
0.5	5.841519	5.841519	5.841519	5.841519	5.841519	5.841519	5.841519	5.841519
0.6	5.824153	5.824153	5.824153	5.824153	5.824153	5.824153	5.824153	5.824153
0.7	5.810420	5.810420	5.810420	5.810420	5.810420	5.810420	5.810420	5.810420
0.8	5.799998	5.799998	5.799998	5.799998	5.799998	5.799998	5.799998	5.799998
0.9	5.792519	5.792520	5.792520	5.792520	5.792521	5.792520	5.792520	5.792520
1	-	5.787449*	-	-	5.787618	5.787616	5.787615	5.787616
1.1	-	-	-	-	5.784906	5.784902	5.784901	-
1.2	-	-	-	-	-	5.783934*	-	-

Table 6.51: Drag for flow past a fixed sphere in a cylinder for a Giesekus fluid with $Re = 0.01$, $\beta = \frac{8}{9}$, $\alpha = 0.001$. Performed with timestep, $\Delta t = 10^{-4}$ using DEVSS-G, $\beta_s = 1.0$.

	Mesh M4				Mesh M5			
We	N = 15	N = 16	N = 17	N = 18	N = 13	N = 14	N = 15	N = 16
0.1	5.719759	5.719759	5.719759	5.719759	5.719759	5.719759	5.719759	5.719759
0.2	5.435936	5.435936	5.435936	5.435936	5.435936	5.435936	5.435936	5.435936
0.3	5.160942	5.160942	5.160942	5.160942	5.160942	5.160942	5.160942	5.160942
0.4	4.915557	4.915557	4.915557	4.915557	4.915557	4.915557	4.915557	4.915557
0.5	4.704150	4.704150	4.704150	4.704150	4.704150	4.704150	4.704150	4.704150
0.6	-	-	-	-	4.524464	4.524466	4.524467	4.524466
0.7	-	-	-	-	4.372123	4.372131	4.372134	4.372133
0.8	-	-	-	-	4.242519	4.242529	4.242536	4.242539
0.9	-	-	-	-	4.131514	4.131517	4.131529	4.131536
1	-	-	-	-	4.035636*	-	-	4.035642
1.1	-	-	-	-	3.952059*	3.952021*	-	-

Table 6.52: Drag for flow past a fixed sphere in a cylinder for a Giesekus fluid with $Re = 0.01$, $\beta = \frac{1}{9}$, $\alpha = 0.01$. Performed with timestep, $\Delta t = 10^{-4}$ using DEVSS-G, $\beta_s = 1.0$.

	Mesh M4				Mesh M5			
We	N = 15	N = 16	N = 17	N = 18	N = 13	N = 14	N = 15	N = 16
0.1	5.821879	5.821879	5.821879	5.821879	5.821879	5.821879	5.821879	5.821879
0.2	5.666142	5.666142	5.666142	5.666142	5.666142	5.666142	5.666142	5.666142
0.3	5.515299	5.515299	5.515299	5.515299	5.515299	5.515299	5.515299	5.515299
0.4	5.380966	5.380966	5.380966	5.380966	5.380966	5.380966	5.380966	5.380966
0.5	5.265572	5.265572	5.265572	5.265572	5.265572	5.265572	5.265572	5.265572
0.6	5.167812	5.167812	5.167812	5.167812	5.167813	5.167813	5.167812	5.167812
0.7	5.085201	5.085200	5.085200	5.085200	5.085199	5.085202	5.085201	5.085200
0.8	-	-	-	-	5.015107	5.015115	5.015116	5.015114
0.9	-	-	-	-	4.955176	4.955189	4.955195	4.955194
1	-	-	-	-	4.903433	4.903450	4.903462	4.903463
1.1	-	-	-	-	4.858294	4.858309	4.858328	4.858335
1.2	-	-	-	-	4.818513	4.818520	4.818544	-
1.3	-	-	-	-	4.783122	4.783112	4.783137	-
1.4	-	-	-	-	4.751367*	4.751331*	-	-
1.5	-	-	-	-	4.722632*	4.722584*	-	-

Table 6.53: Drag for flow past a fixed sphere in a cylinder for a Giesekus fluid with $Re = 0.01$, $\beta = \frac{1}{2}$, $\alpha = 0.01$. Performed with timestep, $\Delta t = 10^{-4}$ using DEVSS-G, $\beta_s = 1.0$.

	Mesh M4				Mesh M5			
We	N = 15	N = 16	N = 17	N = 18	N = 13	N = 14	N = 15	N = 16
0.1	5.920253	5.920253	5.920253	5.920253	5.920253	5.920253	5.920253	5.920253
0.2	5.886227	5.886227	5.886227	5.886227	5.886227	5.886227	5.886227	5.886227
0.3	5.853158	5.853158	5.853158	5.853158	5.853158	5.853158	5.853158	5.853158
0.4	5.823647	5.823647	5.823647	5.823647	5.823647	5.823647	5.823647	5.823647
0.5	5.798275	5.798275	5.798275	5.798275	5.798275	5.798275	5.798275	5.798275
0.6	5.776795	5.776795	5.776795	5.776795	5.776795	5.776795	5.776795	5.776795
0.7	5.758697	5.758697	5.758697	5.758697	5.758697	5.758698	5.758697	5.758697
0.8	5.743438	5.743438	5.743437	5.743437	5.743437	5.743438	5.743438	5.743438
0.9	5.730519	5.730518	5.730518	5.730517	5.730515	5.730518	5.730519	5.730518
1	5.719512	5.719512	5.719510	5.719510	5.719504	5.719510	5.719512	5.719512
1.1	5.710061	5.710062	5.710061	5.710060	5.710051	5.710058	5.710062	5.710063
1.2	5.701852*	5.701876	5.701879	5.701879	5.701868	5.701874	5.701881	5.701884
1.3	5.694574*	-	-	-	5.694724	5.694728	5.694737	5.694743
1.4	-	-	-	-	5.688438	5.688437	5.688447	5.688455
1.5	-	-	-	-	5.682864	5.682855	5.682864	5.682875
1.6	-	-	-	-	5.677886	5.677866	5.677873	-
1.7	-	-	-	-	5.673408	5.673378	-	-
1.8	-	-	-	-	5.669367*	5.669322*	5.669313	-

Table 6.54: Drag for flow past a fixed sphere in a cylinder for a Giesekus fluid with $Re = 0.01$, $\beta = \frac{8}{9}$, $\alpha = 0.01$. Performed with timestep, $\Delta t = 10^{-4}$ using DEVSS-G, $\beta_s = 1.0$.

	Mesh M4				Mesh M5			
We	N = 15	N = 16	N = 17	N = 18	N = 13	N = 14	N = 15	N = 16
0.1	5.204770	5.203281	5.201625	5.200093	5.205620	5.205684	5.204770	5.203281
0.2	4.585723	4.585723	4.585723	4.585723	4.585723	4.585723	4.585723	4.585723
0.3	4.201197	4.201197	4.201197	4.201197	4.201197	4.201197	4.201197	4.201197
0.4	3.918241	3.918241	3.918241	3.918241	3.918241	3.918241	3.918241	3.918241
0.5	3.692446	3.692446	3.692446	3.692446	3.692446	3.692446	3.692446	3.692446
0.6	-	3.504897	3.504897	-	3.504897	3.504897	3.504897	3.504897
0.7	-	-	-	-	3.345382	3.345381	3.345381	3.345381
0.8	-	-	-	-	3.207566	3.207566	3.207566	3.207566
0.9	-	-	-	-	3.087154	3.087156	3.087156	3.087155
1	-	-	-	-	2.981042	2.981044	2.981045	2.981045
1.1	-	-	-	-	2.886877	2.886879	2.886881	2.886881
1.2	-	-	-	-	2.802817	2.802819	-	-
1.3	-	-	-	-	2.727382*	-	-	-
1.4	-	-	-	-	2.659361*	-	-	-

Table 6.55: Drag for flow past a fixed sphere in a cylinder for a Giesekus fluid with $Re = 0.01$, $\beta = \frac{1}{9}$, $\alpha = 0.1$. Performed with timestep, $\Delta t = 10^{-4}$ using DEVSS-G, $\beta_s = 1.0$.

	Mesh M4				Mesh M5			
We	N = 15	N = 16	N = 17	N = 18	N = 13	N = 14	N = 15	N = 16
0.1	5.604715	5.604715	5.604715	5.604715	5.604715	5.604715	5.604715	5.604715
0.2	5.243307	5.243307	5.243307	5.243307	5.243307	5.243307	5.243307	5.243307
0.3	5.027768	5.027768	5.027768	5.027768	5.027768	5.027768	5.027768	5.027768
0.4	4.866674	4.866674	4.866674	4.866674	4.866674	4.866674	4.866674	4.866674
0.5	4.737520	4.737520	4.737520	4.737520	4.737520	4.737520	4.737520	4.737520
0.6	4.630335	4.630335	4.630335	4.630335	4.630335	4.630335	4.630335	4.630335
0.7	4.539481	4.539481	4.539481	4.539481	4.539482	4.539482	4.539481	4.539481
0.8	4.461322	4.461321	4.461321	4.461322	4.461322	4.461322	4.461322	4.461321
0.9	4.393316	4.393316	4.393316	4.393316	4.393316	4.393316	4.393316	4.393316
1	4.333598	4.333597	4.333597	4.333597	4.333597	4.333597	4.333598	4.333597
1.1	4.280744	4.280744	4.280744	4.280743	4.280744	4.280744	4.280744	4.280744
1.2	4.233647	4.233647	4.233647	4.233646	4.233648	4.233647	4.233647	4.233647
1.3	4.191423	4.191423	4.191424	4.191423	4.191424	4.191424	4.191423	4.191423
1.4	4.153361	4.153361	4.153361	4.153361	4.153362	4.153363	4.153361	4.153361
1.5	4.118879	4.118878	4.118878	4.118878	4.118878	4.118881	4.118879	4.118878
1.6	4.087496	4.087495	4.087495	4.087495	4.087493	4.087499	4.087497	4.087495
1.7	-	4.058812	4.058812	-	4.058807	4.058817	4.058816	4.058814
1.8	-	-	4.032496	-	4.032487	4.032500	4.032502	4.032500
1.9	-	-	-	-	4.008251	4.008266	4.008272	4.008270
2	-	-	-	-	3.985858	3.985876	3.985885	3.985884

Table 6.56: Drag for flow past a fixed sphere in a cylinder for a Giesekus fluid with $Re = 0.01$, $\beta = \frac{1}{2}$, $\alpha = 0.1$. Performed with timestep, $\Delta t = 10^{-4}$ using DEVSS-G, $\beta_s = 1.0$.

	Mesh M4				Mesh M5			
We	N = 15	N = 16	N = 17	N = 18	N = 13	N = 14	N = 15	N = 16
0.1	5.876479	5.876479	5.876479	5.876479	5.876479	5.876479	5.876479	5.876479
0.2	5.796995	5.796995	5.796995	5.796995	5.796995	5.796995	5.796995	5.796995
0.3	5.748641	5.748641	5.748641	5.748641	5.748641	5.748641	5.748641	5.748641
0.4	5.712294	5.712294	5.712294	5.712294	5.712294	5.712294	5.712294	5.712294
0.5	5.683145	5.683145	5.683145	5.683145	5.683145	5.683145	5.683145	5.683145
0.6	5.658991	5.658991	5.658991	5.658991	5.658991	5.658991	5.658991	5.658991
0.7	5.638558	5.638558	5.638558	5.638559	5.638559	5.638559	5.638558	5.638558
0.8	5.621015	5.621015	5.621015	5.621015	5.621015	5.621016	5.621015	5.621015
0.9	5.605777	5.605777	5.605777	5.605777	5.605777	5.605777	5.605777	5.605777
1	5.592415	5.592415	5.592415	5.592415	5.592415	5.592415	5.592415	5.592415
1.1	5.580602	5.580602	5.580602	5.580602	5.580602	5.580602	5.580602	5.580602
1.2	5.570086	5.570086	5.570086	5.570086	5.570086	5.570086	5.570086	5.570086
1.3	5.560666	5.560666	5.560666	5.560666	5.560667	5.560666	5.560666	5.560666
1.4	5.552181	5.552181	5.552181	5.552181	5.552182	5.552182	5.552181	5.552181
1.5	5.544501	5.544500	5.544500	5.544500	5.544501	5.544502	5.544501	5.544500
1.6	5.537517	5.537517	5.537516	5.537516	5.537517	5.537518	5.537517	5.537517
1.7	5.531141	5.531140	5.531140	5.531140	5.531139	5.531142	5.531142	5.531140
1.8	5.525298	5.525297	5.525296	5.525296	5.525294	5.525298	5.525298	5.525297
1.9	5.519924	5.519923	5.519922	5.519921	5.519918	5.519923	5.519924	5.519923
2	5.514965	5.514965	5.514963	5.514963	5.514957	5.514963	5.514966	5.514965

Table 6.57: Drag for flow past a fixed sphere in a cylinder for a Giesekus fluid with $Re = 0.01$, $\beta = \frac{8}{9}$, $\alpha = 0.1$. Performed with timestep, $\Delta t = 10^{-4}$ using DEVSS-G, $\beta_s = 1.0$.

Chapter 7

Motion of Sphere Falling in Viscoelastic flow

In this chapter we extend the numerical scheme described earlier in this thesis to the situation where the sphere is moving or sedimenting in a viscoelastic fluid.

7.1 Equation of Motion for Falling Sphere

In the case of a falling sphere, we require an additional governing equation for its motion. We consider the axisymmetric case of a sphere falling along the centreline of a cylinder, so the sphere will only have a non-zero velocity component in the axial direction of the cylinder. We assume that there is no rotation of the sphere. Using Newton's 2^{nd} Law, we obtain an equation of motion for a sphere of radius R_S falling under gravity through fluid within a cylinder

$$\frac{4\pi}{3}R_S^3\rho_S\frac{\partial \mathbf{V}_S}{\partial t}\mathbf{e}_z = \frac{4\pi}{3}R_S^3\left(\rho_S - \rho_F\right)\mathbf{g} + \mathbf{D} \tag{7.1}$$

where $\mathbf{V}_S$ is the velocity of the sphere, ρ_S is the density of the sphere, $\mathbf{g}$ is the acceleration due to gravity and $\mathbf{D}$ is the drag on the sphere. As we have presented all of our equations in non-dimensional form, we apply the same dimensionless scaling to

this equation of motion. The resulting dimensionless equation is

$$\frac{\partial \mathbf{V_S}}{\partial t}\mathbf{e}_z = \left(1 - \frac{\rho_F}{\rho_S}\right)\mathbf{g} + \left(\frac{L}{R_S}\right)^3 \frac{3}{4\pi}\frac{\rho_F}{\rho_S}\frac{1}{Re}\mathbf{D}. \tag{7.2}$$

The term in front of the drag, $\mathbf{D}$, provides motivation for the choice of the characteristic length, L. In the case of a falling sphere we choose $L = R_S$ so that (7.2) depends on only two dimensionless groups, the Reynolds number, and the ratio of fluid-to-sphere density. Our final non-dimensionalised equation of motion for the falling sphere is then

$$\frac{\partial \mathbf{V_S}}{\partial t}\mathbf{e}_z = \left(1 - \frac{\rho_F}{\rho_S}\right)\mathbf{g} + \frac{3}{4\pi}\frac{\rho_F}{\rho_S}\frac{1}{Re}\mathbf{D}. \tag{7.3}$$

where $\mathbf{e}_z$ is the unit vector in the vertically downwards direction. Thus we consider a falling (rather than rising) sphere to have positive velocity.

7.2 Solution of the Equation of Motion of a Falling Sphere

The current sphere velocity, $\mathbf{V}_S$, is found by solving the equation of motion for the sphere, which depends on the drag at the current time. The drag is calculated from the solution of the conservation and constitutive equations. We employ a J^{th}-order Adams-Bashforth (AB) numerical scheme to calculate $\mathbf{V}_S$. At time t^{n+1}, the sphere velocity is approximated by

$$\mathbf{V}_S^{n+1} = \mathbf{V}_S^n + \Delta t\left(\gamma_0 \mathbf{f}^S\left(t^n\right) - \sum_{q=1}^{J} \alpha_{q-1}\mathbf{f}^S\left(t^{n-q}\right)\right) \tag{7.4}$$

where γ_0 and $\{\alpha_q\}_{q=0}^{J-1}$ are given in Table 3.1 and $\mathbf{f}^S\left(t^i\right)$ is the RHS expression in the equation of motion of the sphere evaluated at the i^{th} timestep, given by

$$\mathbf{f}^S\left(t\right) = \left(1 - \frac{\rho_F}{\rho_S}\right)\mathbf{g} - \frac{3}{4\pi Re}\frac{\rho_F}{\rho_S}\mathbf{D}\left(t\right) \tag{7.5}$$

where $\mathbf{D}\left(t\right)$ is the non-dimensional drag computed at time t.

7.3 Mesh Deformation

In the field of fluid dynamics, the ability to accurately model the interaction between a fluid and a solid boundary is very important. In the case of a fixed boundary, this is accomplished through the imposition of boundary conditions. If the boundary can also move or react to the fluid in some way then handling the boundary can prove to be difficult. Numerical methods for solving moving boundary problems may be broadly classified into two categories, moving mesh methods, or fixed mesh methods. There are advantages and disadvantages for each.

In the case of a fixed grid method, there are many different techniques that can be employed to deal with moving boundaries. For example, there are methods which track the surface of the boundary, such as marker particle methods and the level-set method [42]. There are also methods which track volume, for example the volume of fluid method [23]. These methods are capable of modelling very complex interfaces and motion. However, they require careful treatment of boundary conditions because one cannot guarantee that the boundaries will be accurately resolved. This is due to the boundaries not necessarily lying on the numerical grid, meaning their position can be subject to numerical error.

In the case of moving mesh methods it is usual to have the boundary fitted to the mesh which then moves with it. This means that enforcement of the boundary conditions is no different to a stationary boundary from timestep to timestep. The downside in this method is that the geometry of the problem changes regularly which usually requires remeshing. Dealing with remeshing and the resulting change in the linear system from the geometry-related terms can mean a large amount of additional computational effort if not handled carefully.

Due to the simplicity of the geometry, the current work will focus on moving mesh methods. In the case of the sphere falling along the central axis of a cylinder, we will only see a change in the z-coordinates of the mesh points, which may be exploited to avoid computational effort in recalculating geometry-related terms in the weak formulation.

Moving the mesh accurately with the movement of the sphere is an important element

in the numerical simulation of the flow. We employ various schemes to achieve this. Firstly, we must calculate the speed of the sphere by solving equation (7.3), which will require the computed drag on the sphere at each timestep. Secondly, we must adjust the mesh to follow the location of the sphere. The fact that the mesh may not be fixed from one timestep to the next must be taken into account.

From this point on we assume that the sphere velocity is of the form $\mathbf{V}_S(t) = (0, V_S(t))$ with V_S being the velocity in the z-direction.

7.3.1 Accordion Mesh Scheme

As we are modelling a solid sphere we assume that the spherical boundary does not deform, so we wish to ensure that the mesh around the sphere does not change. This requires a method which imposes this rigidity from one timestep to the next. Following Bodart and Crochet [5], we decompose the mesh into three main sections. We set up a sliding central section of elements which follows the sphere and moves as a rigid body translation, without deformation. This section is connected at each end to two deformable sections which compress and elongate, respectively, as the central portion of the mesh moves towards or away from them at the velocity of the sphere. One may liken this to the deformation of an accordion as it is played. See Figure 7.1 for a schematic of the evolution of the mesh.

There are, of course, alternatives to dealing with a mesh which tracks the sphere. Rasmussen and Hassager [48] employed a Lagrangian approach and a finite element method on a deforming mesh. In their work the sphere moves (deforming the mesh around it) for certain periods of time, depending on the density of the sphere, before remeshing is performed. Another example is the deformation field approach adopted by Hulsen et al. [47]. These works have been applied to integral constitutive equations rather than the differential constitutive equations used in the current work, although in former case, it would be applicable to our equations. However, we shall focus on and adapt the technique described by Bodart and Crochet [5] who fix the position of the sphere and translate the mesh around it.

The sphere velocity is used to move the central section of our accordion mesh.

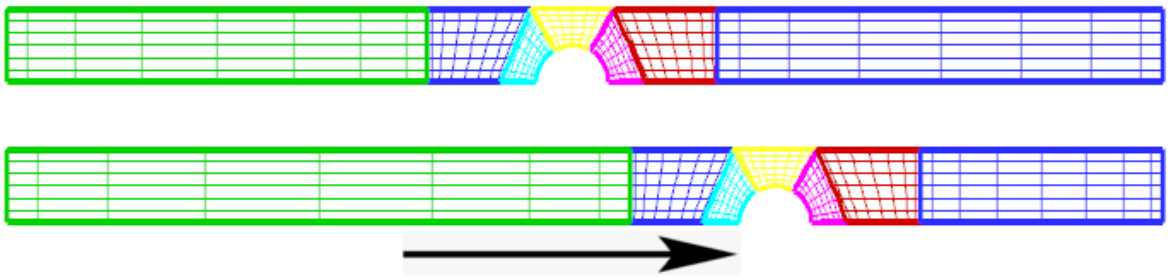

Figure 7.1: Simple schematic diagram of an accordion mesh, showing a single element undergoing elongation on the left, the rigid central mesh around the sphere, and a single element undergoing compression on the right.

Mesh Velocity

We move the central portion of the mesh using the calculated sphere velocity, $\mathbf{V}_S^{n+1}$. Each of the four vertex nodes of each central mesh element is moved according to a 2^{nd}-order Adams-Bashforth scheme

$$\mathbf{X}_i^{n+1} = \mathbf{X}_i^n + \frac{\Delta t}{2}\left(3\mathbf{V}_S^n - \mathbf{V}_S^{n-1}\right) \tag{7.6}$$

This also gives us the axial extent of the two accordion zones, respectively, and the quantitative information required to expand and compress the zones.

When each accordion zone is made up of more than one element in the z-direction, we may distribute the deformation either equally, or according to some prescribed weighting. This may be done at chosen ratios. For example, we may have 2 elements in each of the two accordion sections and we may want the elements which are closer to the central section to deform less than those further away. Alternatively, we may wish the extended section to account for more of the deformation of the meshes than the compressing section.

Once the accordion element vertex nodes have been moved according to the criteria set, we have the positions of the elements for the next time step. This means that the Gauss-Lobatto grid may be generated on each element, and we may now calculate the mesh velocity for each node point in our grid using

$$\mathbf{v}_i^{n+1} = \frac{1}{\Delta t}\left(\gamma_0 \mathbf{X}_i^{n+1} - \sum_{q=0}^{J-1} \alpha_q \mathbf{X}_i^{n-q}\right). \tag{7.7}$$

7.3.2 Arbitrary Lagrangian Eulerian Scheme

In the case of a deforming mesh containing a moving boundary we combine our OIFS scheme with the Arbitrary Lagrangian Eulerian (ALE) technique [22]. This accounts for the inertia introduced to the system by the moving nodal points.

Modification to Convective Derivatives

We account for the movement of the mesh points by modifying the convective derivative contained within the material derivative. A general material derivative of some arbitrary function, $\mathbf{G}$, previously defined in (2.6) becomes

$$\frac{D\mathbf{G}}{Dt} = \frac{\partial \mathbf{G}}{\partial t} + (\mathbf{u} - \mathbf{v}) \cdot \nabla \mathbf{G}. \tag{7.8}$$

This is reflected in both the DG treatment of convective terms in the constitutive equations as well as within OIFS treatment of the material derivative in the momentum equation.

Modification to OIFS Problems

The OIFS approximation, at time $t = t^{n+1}$, of the material derivative, of some general function $\mathbf{G}$, given by (3.9) does not change itself. However, the pure advection problems, to which $\left\{\widetilde{\mathbf{G}}_q\right\}_{q=0}^{J-1}$ are the solutions, previously given in equation (3.10) now reflect that the mesh is moving

$$\frac{\partial \widetilde{\mathbf{G}}_q}{\partial t} = -\left(\mathbf{u}^* - \mathbf{v}^n\right) \cdot \nabla \widetilde{\mathbf{G}}_q, \qquad t \in \left[t^{n-q}, t^{n+1}\right], \qquad \widetilde{\mathbf{G}}\left(\mathbf{x}, t^{n-q}\right) = \mathbf{G}^{n-q}\left(\mathbf{x}\right). \tag{7.9}$$

7.4 Boundary and Initial Conditions

Figure 7.2 shows a simple schematic of the domain we consider. In the case of a fixed sphere in space with a flow moving past it, we apply no-slip and no penetration conditions on the surface of the sphere. However, when the sphere is moving through

the fluid we make a new assumption. Under our assumption of no slip on stationary walls, it is reasonable to assume that the thin layer of fluid touching the sphere's surface will move with it. Therefore, the boundary condition on the surface of a fixed sphere $\mathbf{u} = 0$ is replaced by $\mathbf{u} = \mathbf{V}_S$ on the surface of a moving sphere. We also consider the sphere to be fully enclosed within the cylinder, so we set zero inflow and outflow conditions and no-slip and no-penetration conditions on the walls. Figure 7.3 shows a schematic of the boundary conditions for the falling sphere problem.

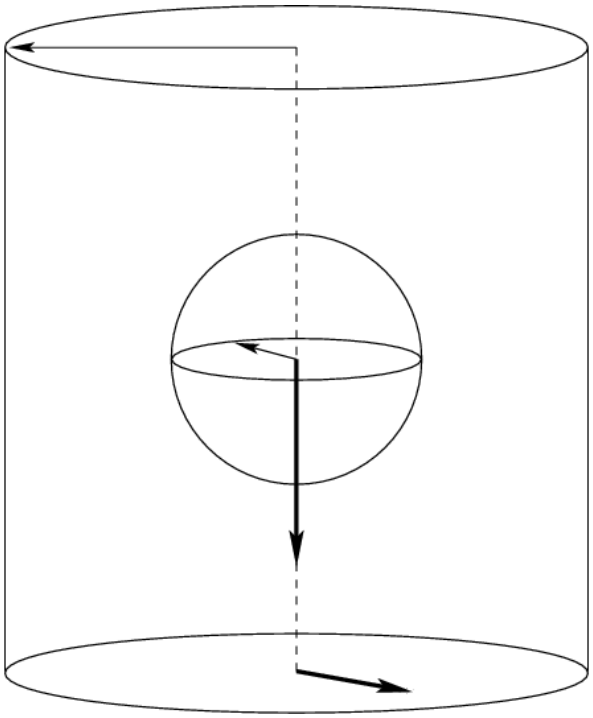

Figure 7.2: Schematic of the 3-dimensional domain.

Even though we consider a sphere starting from rest, we apply a very small initial velocity for the sphere typically $V_S^0 = 10^{-6}$, while setting zero initial conditions for the fluid. This is done in order to avoid problems experienced with zero boundary conditions at our first timestep. The sphere starts at the centre of our domain, at position $(0, 0)$, while the cylinder extends 20 radii in each axial direction. We fix the radius of sphere, $R_S = 1$ and the cylinder, $R_C = 2$. Blockage ratios other than 0.5 are not currently considered.

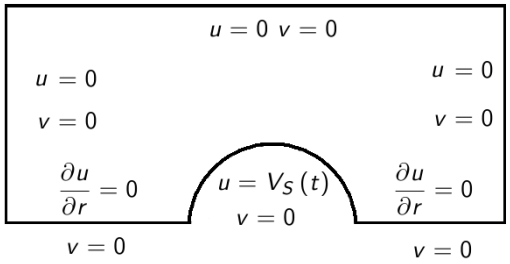

Figure 7.3: Diagram showing axisymmetric boundary conditions for the case of a sphere falling along the central axis of a cylinder filled with fluid. Here u represents velocity in the axial direction and v represents velocity in the radial direction.

7.5 Results

As a test of our scheme we follow Bodart and Crochet [5] and choose a fluid density of $\rho_f = 0.868$ g cm^{-3} who chose properties similar to that of an M1 Boger fluid. In their test case, Bodart and Crochet chose a sphere of density $\rho_s = 3.581$ g cm^{-3}, which gives us a density ratio of $\frac{\rho_f}{\rho_s} = 0.2424$. We fix this value in all of our simulations. The gravity constant is set to be $g = 9.807$ ms^{-2} with gravity considered to be acting in the positive axial direction.

In all simulations we use a timestep of $\Delta t = 10^{-4}$ with a time limit of 20 and all are performed on either mesh M4 or M5 with the outer set of elements set to be of accordion type. The additional refinement in the wake of M5 is switched to the opposite side of the mesh in order to align with gravity acting in the positive axial direction. All simulations are performed at $N = 12$ or $N = 8$ when not possible.

During initial testing we found that matching the fluid parameters to the work of Bodart and Crochet caused a lot of stability problems with the scheme. This is most likely due to the differences in our choice of dimensionless form. This is something which we aim to improve upon in the future and hope to validate against their results directly. In the meantime, the fluid parameters considered are $Re = 0.01$ and 0.1, $\beta = \frac{1}{9}$ and $\frac{1}{2}$ and $\alpha = 0$ (Oldroyd B) and 0.1 (Giesekus).

During the simulation we keep track of the sphere velocity and stop the simulation

when the change between timesteps is less than a chosen threshold, S_{crit}. That is when,

$$S_{sphere} = \left| \frac{V_S^n - V_S^{n-1}}{V_S^n} \right| < S_{crit}, \tag{7.10}$$

the simulation is terminated. We typically set $S_{crit} = \frac{10^{-6}}{\Delta t}$.

All results presented were obtained with the DG-only scheme. We were unable to obtain results using the DEVSS-G scheme as all attempts resulted in divergence. We suspect this is due to the explicit treatment of the $\nabla \cdot \mathbf{G}$ terms in the momentum equation. It is likely that the moving mesh scheme possibly requires an implicit treatment to remain stable. It would be possible to include the velocity gradient projection into coupled system in order to solve this issue, although there would be a large penalty in terms of performance of the linear solver. Due to these issues, the DEVSS-G scheme was disabled for the following simulations.

We begin with results at $Re = 0.01$ showing results for an Oldroyd B fluid with $\beta = \frac{1}{9}$ in Figure 7.4 with the Newtonian result shown for comparison where we observe a monotonic increase to the settling velocity. At low We we see a large overshoot, followed by undershoots which dampen towards the final settling velocity. As We increases the initial overshoot increases but there is no observable undershoot. Figure 7.5 shows the results for $\beta = \frac{1}{2}$. We observe no undershoots after the initial overshoot at this value of β, which suggests that the effect is due to the polymeric viscosity. The overshoots are also smaller in magnitude in comparison to those at $\beta = \frac{1}{9}$ with the settling velocity being very similar. However the time taken to reach the settling velocity is significantly higher than for $\beta = \frac{1}{9}$. At this value of Re there is no visible difference between the results for the Oldroyd B model and the Giesekus model using $\alpha = 0.1$.

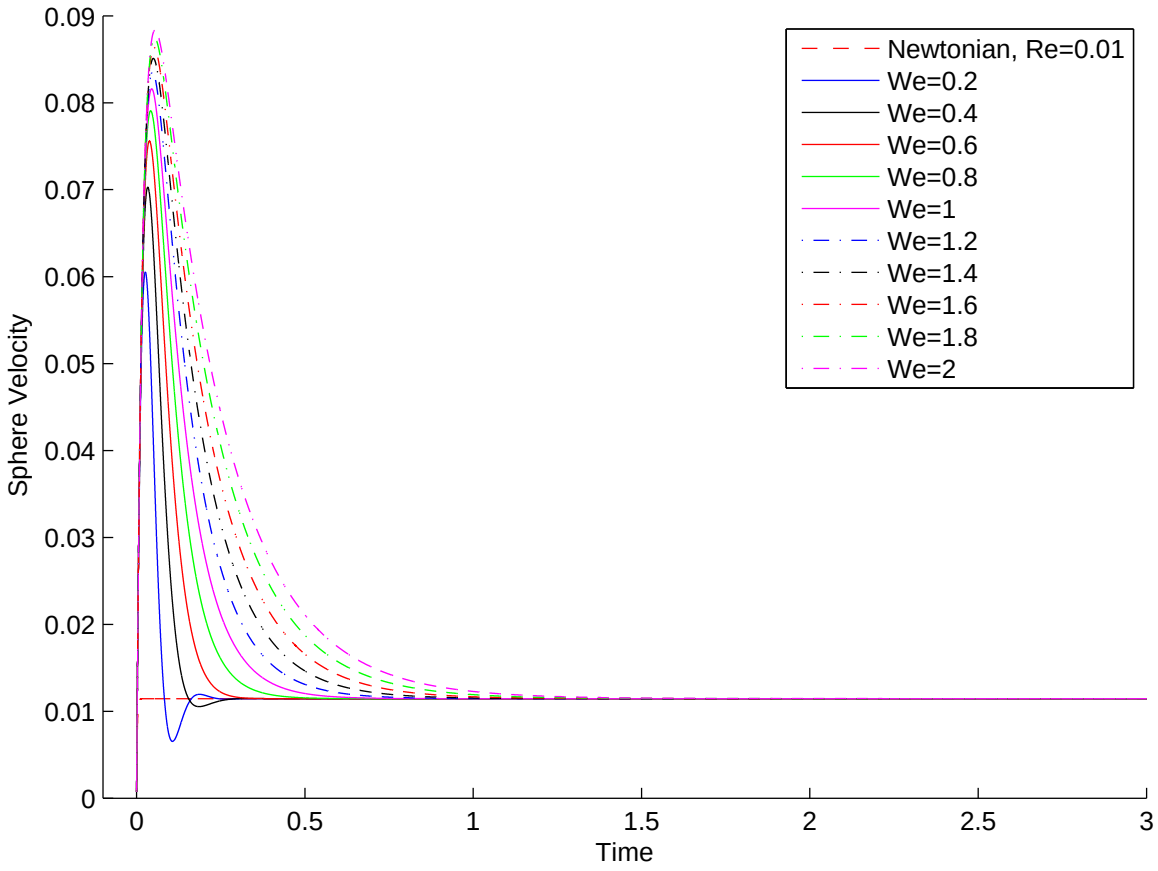

Figure 7.4: Evolution of velocity of a sphere falling in an Oldroyd B fluid with $Re = 0.01$ and $\beta = \frac{1}{9}$.

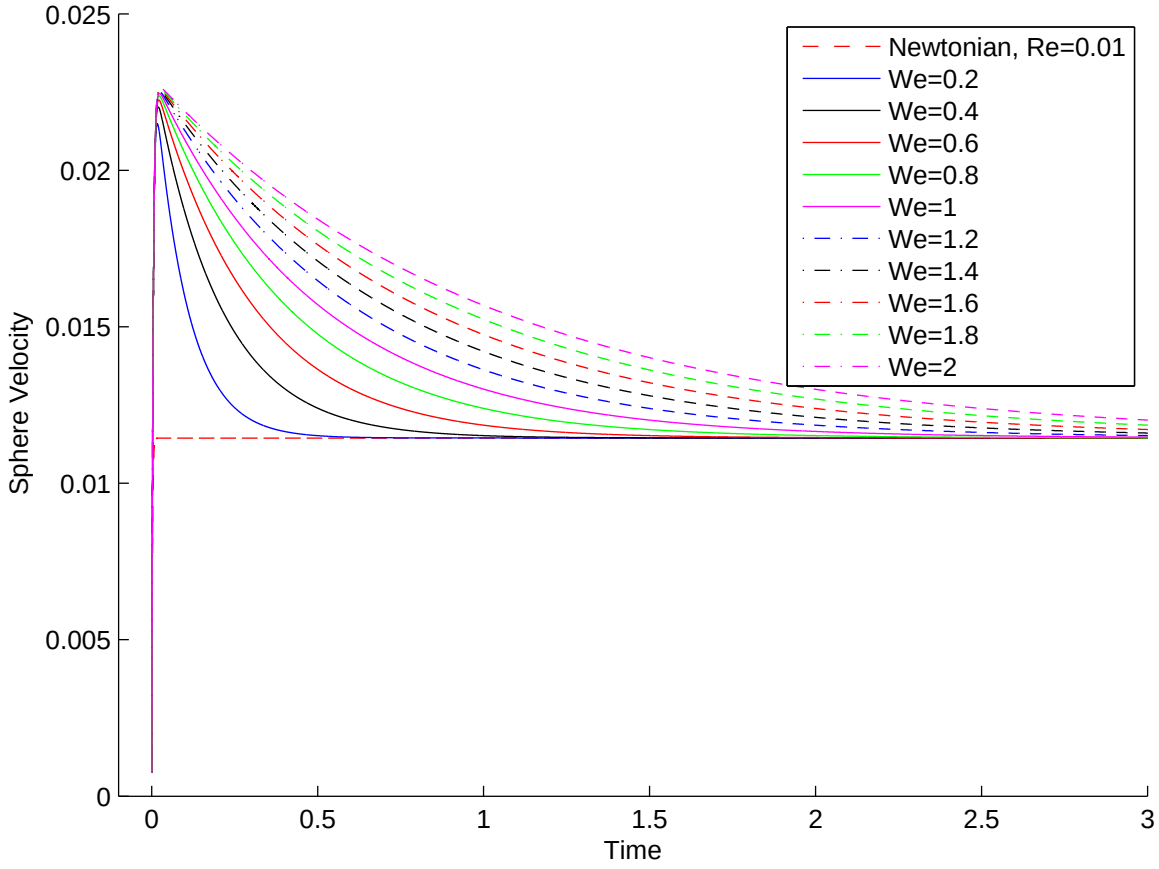

Figure 7.5: Evolution of velocity of a sphere falling in an Oldroyd B fluid with $Re = 0.01$ and $\beta = \frac{1}{2}$.

	Normalised V_S^F				$C_{overshoot}$			
	$\beta = \frac{1}{9}$		$\beta = \frac{1}{2}$		$\beta = \frac{1}{9}$		$\beta = \frac{1}{2}$	
We	$\alpha = 0$	$\alpha = 0.1$	$\alpha = 0$	$\alpha = 0.1$	$\alpha = 0$	$\alpha = 0.1$	$\alpha = 0$	$\alpha = 0.1$
0.2	1.00001159	1.00006475	1.00000409	1.0000356	5.28804891	5.28776799	1.87694961	1.87689047
0.4	1.00000281	1.00011022	1.00001614	1.00009486	6.14122305	6.14056362	1.92432842	1.92417694
0.6	1.00005296	1.00019414	1.00003613	1.00016202	6.60414985	6.60321777	1.94384187	1.94359719
0.8	1.00009693	1.00033065	1.00006414	1.00023711	6.90887646	6.90726233	1.95476346	1.95442543
1	1.00015292	1.00045462	1.00009999	1.00031995	7.12944223	7.12729229	1.96181479	1.96138339
1.2	1.00022091	1.00058879	1.00014354	1.00041057	7.29860848	7.29592509	1.96676184	1.96623687
1.4	1.00030086	1.00073384	1.00019402	1.00050862	7.43354922	7.43033305	1.97080962	1.96980774
1.6	1.00039271	1.00088998	1.00025465	1.00061566	7.54429507	7.54054687	1.97324527	1.97253334
1.8	1.00049644	1.00105733	1.00032083	1.00072853	7.63716965	7.63289062	1.97546998	1.97466517
2	1.00061213	1.00123599	1.00039528	1.00084914	7.71638329	7.71157532	1.97725984	1.9763632

Table 7.1: Overshoot coefficient and settling velocity for falling sphere in both an Oldroyd B fluid and a Giesekus fluid at $Re = 0.01$.

In considering the overshoots it is useful to look at the overshoot coefficient defined by

$$C_{overshoot} = \max_t \left(\frac{V_S(t)}{V_S^F} \right), \tag{7.11}$$

where V_S^F is the final settling velocity. In order to compare results at different values of Re we also present normalised V_S^F using the Newtonian value of V_S^F.

Table 7.1 show the values of the normalised settling velocity and overshoot coefficients for the $Re = 0.01$ results obtained up to $We = 2$. For both values of β we see a steady, if very subtle, increase in the settling velocity indicating drag reduction with increasing We. There is a large increase of the overshoot coefficient with We, but it appears to tend towards a local minimum as We increases towards 2. The influence of the viscosity ratio is also very much apparent in terms of the relative size of the overshoot with $\beta = \frac{1}{9}$ resulting in almost 4 times the size of the coefficient. This result supports the fairly intuitive idea that the overshoot is very much an elastic effect. We also observe a subtle difference for the Giesekus fluid, with a slightly increased settling velocity, resulting in a slightly smaller overshoot coefficient.

Finally at $Re = 0.01$, we note that we are able to obtain solutions up to $We = 2$ without divergence and so have not found a maximum attainable value for $Re = 0.01$ at this point. Higher values of We will be considered in the future in order to find a limiting value of We. We also note that we do not observe any suggestion of a negative wake in any of these results.

We now consider $Re = 0.1$ where we did find a limiting value of We as well as some small differences between the Oldroyd B and Giesekus fluid models. Results at $\beta = \frac{1}{9}$ proved particularly unstable and we can only assume that the problems in obtaining a solution in the fixed sphere benchmark which were improved using DEVSS-G are also present here. The Oldroyd B fluid was only stable up to $We = 0.1$ and the Giesekus fluid stable up to $We = 0.2$. Results at $\beta = \frac{1}{2}$ proved to be more stable with a limit of $We = 0.6$ reached for the Oldroyd B fluid and $We = 0.5$ for the Giesekus fluid, although in both cases we were only able to find a convergent solution by reducing N at the limiting values of We. The limited result for $\beta = \frac{1}{9}$, $\alpha = 0.1$ may be seen in Figure 7.6

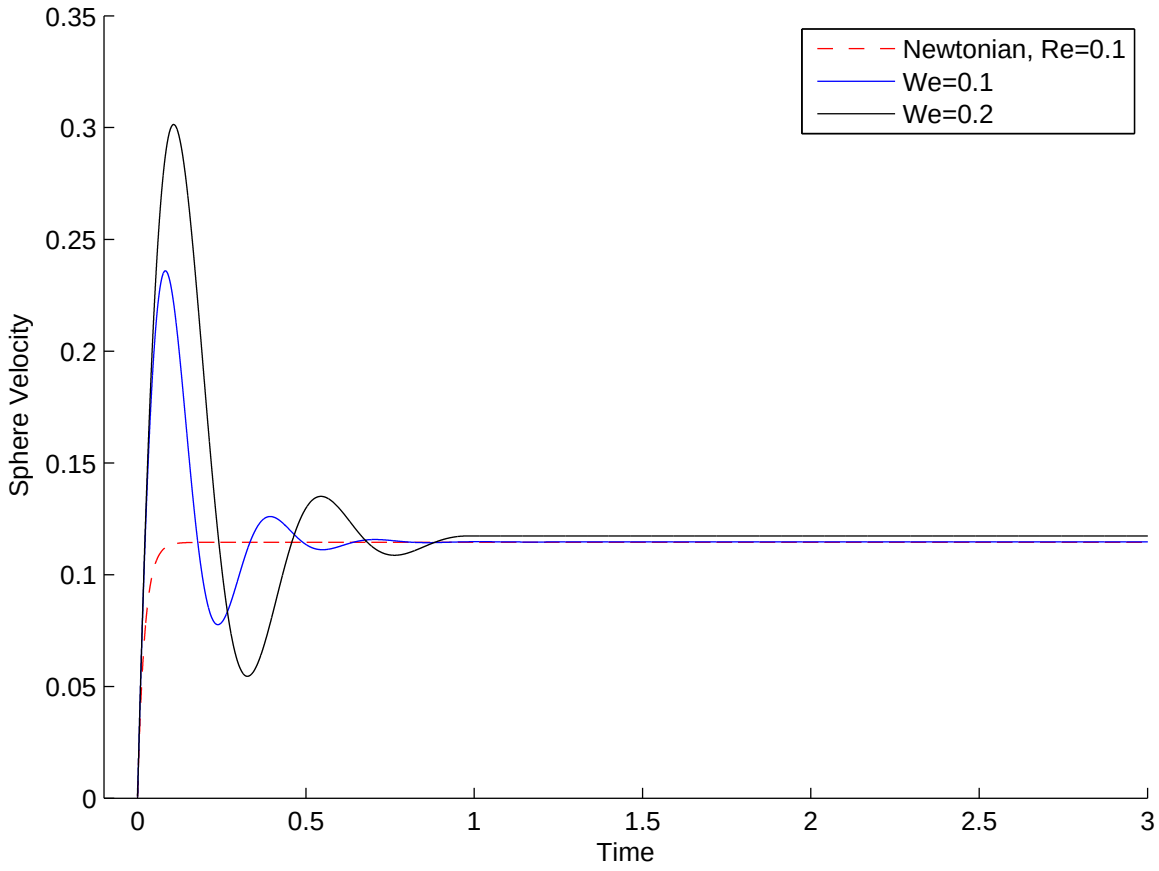

Figure 7.6: Evolution of velocity of a sphere falling in an Oldroyd B fluid with $Re = 0.1$, $\beta = \frac{1}{2}$.

with the $We = 0.1$ result for Oldroyd B being visually the same as that shown in the figure. The presence of large overshoots and undershoots is at least encouraging.

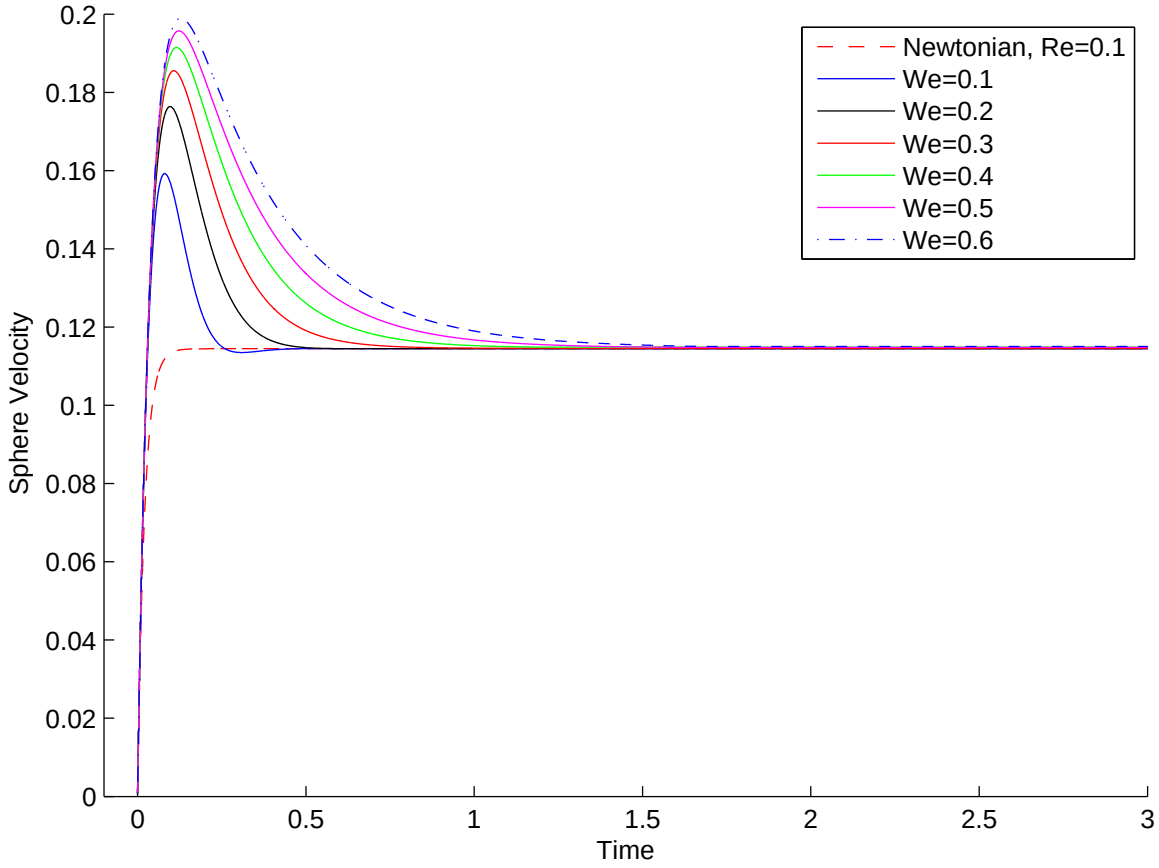

Figure 7.7: Evolution of velocity of a sphere falling in an Oldroyd B fluid with $Re = 0.1$, $\beta = \frac{1}{2}$.

Figure 7.7 shows the Oldroyd B results for $\beta = \frac{1}{2}$, with the Giesekus results being visually indistinguishable. The increase in β again leads to a vast reduction in the undershoot and increasing We appears to remove them entirely. The trend of increasing overshoot with increasing We is observed as was the case for $Re = 0.01$ as well as an increased settling time.

A comparison of overshoot coefficient and settling velocity values are presented in Table 7.2 which shows a fairly large reduction in the size of the overshoot when compared to the $Re = 0.01$ results. This suggests that Newtonian effects can limit the overshoot

phenomena. We also see some small differences for the Giesekus fluid which causes a reduction in overshoot for the considered value of α. When comparing the normalised settling velocity values with those for $Re = 0.01$ we see an increase of more than an order of magnitude. Further, the Giesekus model appears to have an effect on the settling velocity, with a large percentage increase compared to the Oldroyd B fluid at equivalent β. The increase in settling velocity again suggests drag reduction as viscoelastic effect.

	Normalised V_S^F				$C_{overshoot}$			
	$\beta = \frac{1}{9}$		$\beta = \frac{1}{2}$		$\beta = \frac{1}{9}$		$\beta = \frac{1}{2}$	
We	$\alpha = 0$	$\alpha = 0.1$	$\alpha = 0$	$\alpha = 0.1$	$\alpha = 0$	$\alpha = 0.1$	$\alpha = 0$	$\alpha = 0.1$
0.1	1.0001547482	1.00166766	1.00028896	1.00088394	2.06065784	2.0577201	1.39088158	1
0.2	–	1.02486422	1.00017199	1.00296857	–	2.56922591	1.54071653	1.39007891
0.3	–	–	1.00087356	1.00613298	–	–	1.61951554	1.53643552
0.4	–	–	1.00359172	1.00883589	–	–	1.66679031	1.61105605
0.5	–	–	1.00305462	1.01179861	–	–	1.70467246	1.65813707
0.6	–	–	1.00522506	–	–	–	1.72904052	1.68994613

Table 7.2: Overshoot coefficient and settling velocity for falling sphere in both an Oldroyd B fluid and a Giesekus fluid at $Re = 0.1$.

Due to the limited values of We we can reach at $Re = 0.1$, we compare the evolution of sphere velocity at $We = 0.1$ in Figure 7.8. We note the large oscillations with increasing Re and β, as well as the longer time to reach a settled velocity.

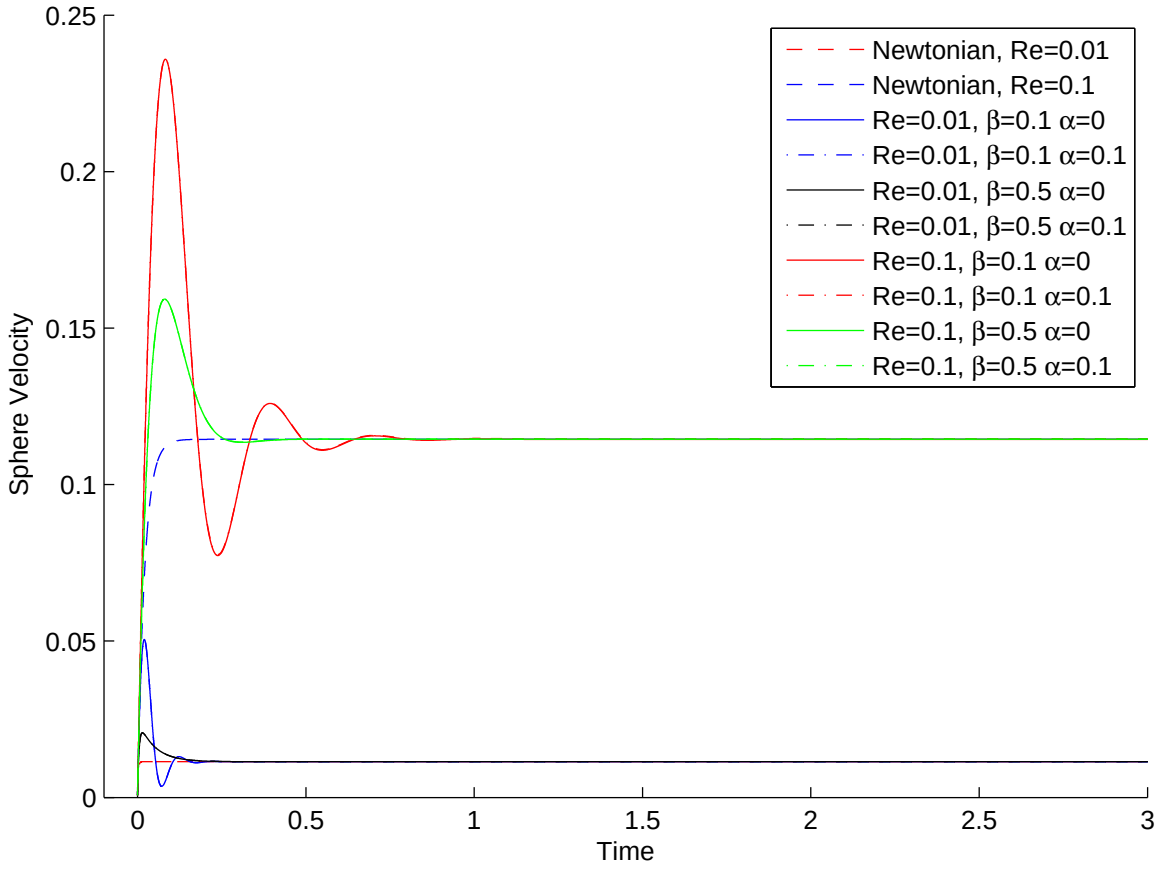

Figure 7.8: Evolution of velocity of a sphere falling in an Oldroyd B fluid and a Giesekus fluid at $We = 0.1$.

Figure 7.9 shows the axial stress at the point of convergence for all simulations at $We = 0.1$. where we see a large increase with Re as well as with decreasing β. The effect of the Giesekus mode on a reduction of the overall axial stress is also observed. This explains the increase in settling velocity for the Giesekus fluid to some degree because a decrease in the axial stress across the surface of the sphere will result in a drag reduction, as can be seen from the expression for the drag in (2.53).

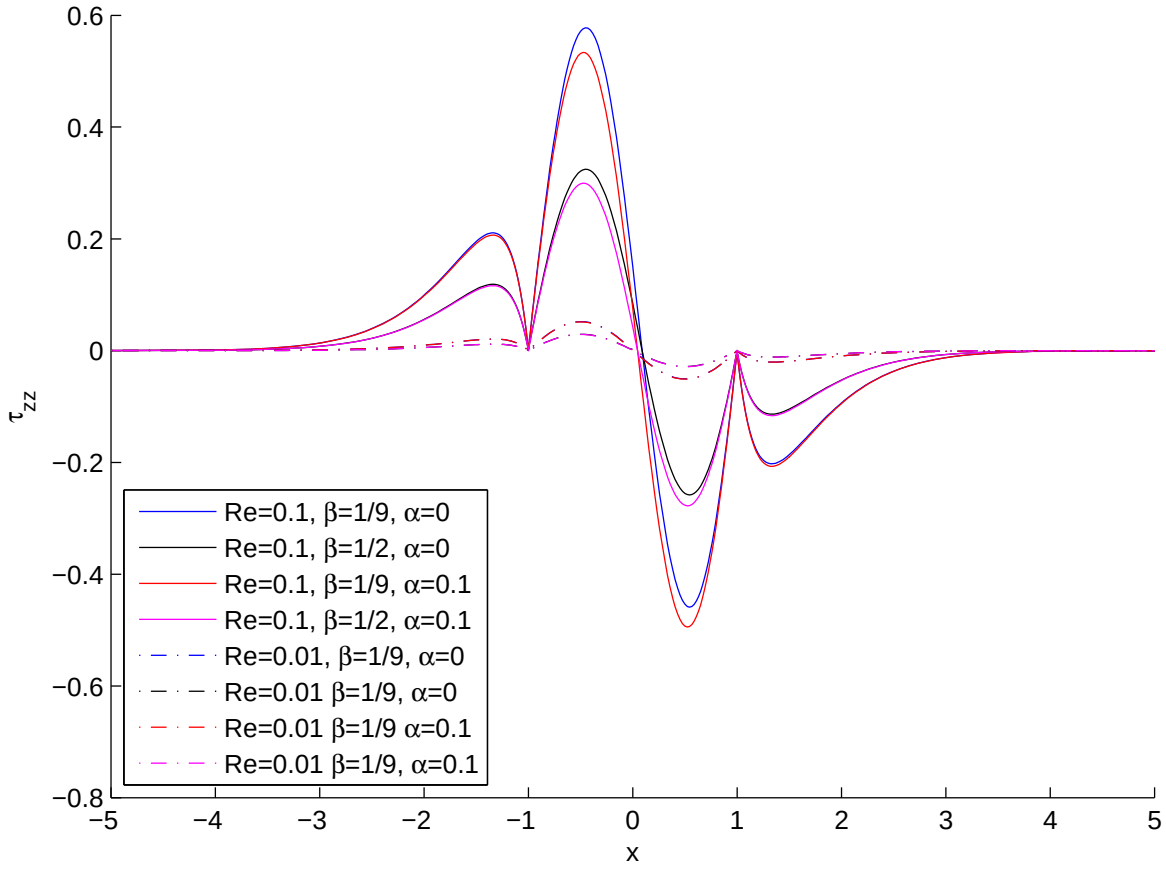

Figure 7.9: Axial stress at steady state for the falling sphere in an Oldroyd B fluid and a Giesekus fluid at $We = 0.1$.

For the choice of parameters there is little to compare the results with available in the literature. However, we may compare more generally with the results of Bodart and Crochet [5] who calculated overshoot coefficients. At $Re = 0.01053$, $We = 0.364$, $\beta = \frac{1}{9}$ and equivalent density ratio, they calculate a overshoot coefficient of 2.85, which compares to a value of 2.57 for $We = 0.2$ for the Giesekus fluid when we take into account that the Oldroyd B fluid has shown an increase in $C_{overshoot}$ compared to the Giesekus fluid and we expect an increase in the coefficient with increasing We. Further, at $Re = 0.000822$, $We = 0.071$, $\beta = 19$ they predict an $C_{overshoot} = 6.99$ at equivalent density ratio. From our results, this would appear to be in line with our prediction of at $Re = 0.01$. While this does not serve as full validation of the predictions of the current work it does add some confidence to their validity.

One criticism is the criteria we set on terminating the simulation, which only featured convergence of the sphere velocity. In most cases this meant that the simulation was thought to have converged at the bottom of the first shallow undershoot, while the drag had not yet reached a fully stable state. This was an oversight on our part and we intend to re-run the simulations with drag convergence in time taken into account. The result of this will likely be to increase the predicted settled velocity values, which would lower the predicted overshoot coefficient by a small amount.

7.6 Summary

We have presented results for a small range of Re for both Oldroyd B and Giesekus fluids and obtained results to a relatively high value of We for $Re = 0.01$. It remains to obtain a limiting value of We for this Re. At $Re = 0.1$ it is clear that additional stabilisation is required to obtain results for high and even moderate values of We. This may be achieved using the DEVSS-G scheme, although we believe it will require including the velocity gradient projection in the coupled section of our solver. This will lead to a decrease in performance due to the large number of extra degrees of freedom, but the reward in stability would be large if the fixed sphere benchmark results are an indication.

We have captured experimentally observed phenomena in velocity overshoot and un-

dershoot as well as drag reduction. However, we have not captured the negative wake. This may be achievable with improvements to our scheme and we intend to pursue this in the future. However, before this we must perform a more thorough validation of predictions by making direct comparisons with work in the literature such as that by Bodart and Crochet [5].

Chapter 8

Conclusions

With the aim of studying sedimentation in viscoelastic flow, we have successfully implemented a decoupled numerical scheme utilising SEM to perform spatial discretisation and a fixed timestep using a combination of OIFS and BDF at second order to perform temporal discretisation and have included an alternative formulation of the continuity equation. The constituitive equation has been handled using a DG treatment of convection and stabilisation of the momentum equation has been performed using DEVSS-G. We have also implemented the possibility of a moving mesh using an ALE scheme. This has been implemented into a numerical code using PARDISO from the Intel MKL library as the primary linear solver. The scheme is capable of handling both planar and axisymmetric cylindrical geometries.

In the construction of this numerical code we have attempted to validate each module at every step, beginning with the spatial discretisation of the Stokes problem in Chapter 4. We validated using a combination of a known model solution and benchmarks found in the literature which are relevant to sedimentation. The addition of the temporal scheme was first validated for a Newtonian fluid in Chapter 5 at low to moderate Re using a both a known analytical solution and a continution of popular benchmarks found in the literature. Excellent agreement was found at all levels.

In Chapter 6 we validate our implementation of the decoupled constuitive equation using the analytical solutions of Waters and King [62, 63] where we demonstrate similar agreement with those solutions as others using similar methods from the literature. We

performed benchmarks on both flow past a fixed cylinder and flow past a fixed sphere and for the attainable range of We achieve excellent agreement with authors from the literature. We also implemented an additional viscoelastic model in the Giesekus model in Section 6.3.4 where we performed an investigation of the effect of the additional parameter α which introduces shear-thinning and extension-thinning behaviour and allowed us to obtain results at higher We.

Finally in Chapter 7 we describe and implement a method for the falling sphere problem and were able to perform some initial numerical experiments. While the results do not match exactly with those that we found in the literature, they appear to offer reasonable predictions of known phenomena and give justifiable agreement with numerical simulations using parameters close to those used in our work. There is much improvement to be made on our results and the fact that the use of the explicit implementation of DEVSS-G results in divergence is one such area in which we could make a change.

Further work will involve additional validation of the Waters and King solution with more effort to investigate the inherent instability in the solution when using spectral methods. Additional mesh refinement and other methods of stabilisation shall be investigated for the fixed sphere benchmark, as well as a continuation of work on the Giesekus model and others which exhibit stable behaviour in extensional flow. Efforts to improve the results already attained for the falling sphere problem are a high priority and making parts of the scheme more implicit are one possible avenue to this. Additionally, the performance in terms of computational cost when using the moving mesh need to be optimised. It is possible that we may avoid recomputing the factorisation for the majority nodes which are within the central moving mesh, which could provide a vast improvement in computational speed. Iterative methods, which have traditionally been popular in computational fluid dynamics may also have been a better option, although there is computational performance to be found in the use of the sparse methods available through PARDISO.

Bibliography

[1] M. A. Alves, F. T. Pinho, and P. J. Oliveira. The flow of viscoelastic fluids past a cylinder: finite-volume high-resolution methods. *J. Non-Newtonian Fluid Mech.*, 97:207–232, 2001.

[2] F Belblidia, H Matallah, and MF Webster. Alternative subcell discretisations for viscoelastic flow: Velocity-gradient approximation. *Journal of Non-Newtonian Fluid Mechanics*, 151(1):69–88, 2008.

[3] A. N. Beris, R. C. Armstrong, and RA Brown. Finite element calculation of viscoelastic flow in a journal bearing: I. small eccentricities. *J. Non-Newtonian Fluid Mech.*, 16(1):141–172, 1984.

[4] C. Bodart and M. J. Crochet. Time-dependent numerical simulation of viscoelastic flow and stability. *Theoretical and Computational Fluid Dynamics*, 5(2-3):57–75, 1993.

[5] C. Bodart and M. J. Crochet. The time-dependent flow of a viscoelastic fluid around a sphere. *J. Non-Newtonian Fluid Mech.*, 54:303–329, August 1994.

[6] A. C. B. Bogaerds, A. M. Grillet, G. W. M. Peters, and F. Baaijens. Stability analysis of polymer shear flows using the extended pom–pom constitutive equations. *J. Non-Newtonian Fluid Mech.*, 108(1):187–208, 2002.

[7] Alexander N. Brooks and Thomas J.R. Hughes. Streamline upwind/petrov-galerkin formulations for convection dominated flows with particular emphasis on the incompressible navier-stokes equations. *Comp. Meth. App. Mech. Eng.*, 32(1):199–259, 1982.

[8] R. A. Brown, M. J. Szady, P. J. Northey, and R. C. Armstrong. On the numerical stability of mixed finite-element methods for viscoelastic flows governed by differential constitutive equations. *Theoretical and Computational Fluid Dynamics*, 5(2-3):77–106, 1993.

[9] E. O. Carew, P. Townsend, and M. F. Webster. Taylor-galerkin algorithms for viscoelastic flow: Application to a model problem. *Numerical Methods for Partial Differential Equations*, 10(2):171–190, 1994.

[10] Cédric Chauvière and Robert G Owens. How accurate is your solution?: Error indicators for viscoelastic flow calculations. *J. Non-Newtonian Fluid Mech.*, 95(1):1–33, 2000.

[11] J. -H. Chen, W. G. Pritchard, and S. J. Tavener. Bifurcation for flow past a cylinder between parallel planes. *J. Fluid Mech.*, 284:23–41, 1995.

[12] S. Claus and T.N. Phillips. Viscoelastic flow around a confined cylinder using spectral/hp element methods. *J. Non-Newtonian Fluid Mech.*, In press, 2013a.

[13] Y. Fan. Limiting behavior of the solutions of a falling sphere in a tube filled with viscoelastic fluids. *J. Non-Newtonian Fluid Mech.*, 110(2-3):77 – 102, 2003.

[14] Y. Fan, R. I. Tanner, and N. Phan Thien. Galerkin/least-square finite-element methods for steady viscoelastic flows. *J. Non-Newtonian Fluid Mech.*, 84:233–256, 1999.

[15] N. Fiétier. *Numerical Simulation of Viscoelastic Fluid Flows by Spectral Element Methods and Time-dependent Algorithms*. PhD thesis, Ecole Polytechnique Fédérale de Lausanne, Switzerland, 2002.

[16] N. Fiétier and M. O. Deville. Time-dependent algorithms for the simulation of viscoelastic flows with spectral element methods: applications and stability. *J. Comp. Phys.*, 186(1):93–121, 2003.

[17] Michel Fortin and André Fortin. A new approach for the fem simulation of viscoelastic flows. *J. non-newtonian fluid Mech.*, 32(3):295–310, 1989.

[18] H. Giesekus. A simple constitutive equation for polymer fluids based on the concept of deformation-dependent tensorial mobility. *J. Non-Newtonian Fluid Mech.*, 11:69–109, 1982.

[19] W. J. Gordon and C. A. Hall. Transfinite element methods: blending function interpolation over arbitrary curved element domains. *Numer. Math.*, 21:109–129, 1973.

[20] D. Gottlieb and S. A. Orszag. Numerical analysis of spectral methods siam. *Philadelphia, PA*, 1977.

[21] R. Guénette and M. Fortin. A new mixed finite element method for computing viscoelastic flows. *J. Non-Newtonian Fluid Mech.*, 60(1):27–52, 1995.

[22] C. W. Hirt, A. A. Amsden, and J. L. Cook. An Arbitrary Lagrangian-Eulerian computing method for all flow speeds. *J. Comput. Phys.*, 14:227–253, 1974.

[23] C. W. Hirt and B. D. Nichols. Volume of fluid (VOF) method for the dynamics of free boundaries. *J. Comput. Phys.*, 39:201–225, 1981.

[24] T. J.R. Hughes and A. Brooks. A multidimensional upwind scheme with no cross-wind diffusion. *Finite element methods for convection dominated flows, AMD*, 34:19–35, 1979.

[25] M. A. Hulsen, A. P. G van Heel, and B. H. A. A. van den Brule. Simulation of viscoelastic flows using Brownian configuration fields. *J. Non-Newtonian Fluid Mech.*, 70:79–101, 1997.

[26] T. A. Johnson and V. C. Patel. Flow past a sphere up to a Reynolds number of 300. *J. Fluid Mech.*, 378:19–70, 1999.

[27] G. E. Karniadakis, M. Israeli, and S. A. Orszag. High-order splitting methods for the incompressible navier-stokes equations. *J. Comp. Phys.*, 97(2):414–443, 1991.

[28] H. Lamb. On the uniform motion of a sphere in a viscous fluid. *Phil. Mag.*, 21:112–119, 1911.

[29] P. Lesaint and P-A. Raviart. *On a finite element method for solving the neutron transport equation*. Univ. Paris VI, Labo. Analyse Numérique, 1974.

[30] S. J. Lind. *A Numerical Study of The Effect of Viscoelasticity on Cavitation and Bubble Dynamics*. PhD thesis, Cardiff University, July 2010.

[31] E. R. Lindgren. The motion of a sphere in an incompressible viscous fluid at reynolds numbers considerably less than one. *Physica Scripta*, 60(2):97, 1999.

[32] A. W. Liu, D. E. Bornside, R. C. Armstrong, and R. A. Brown. Viscoelastic flow of polymer solutions around a periodic, linear array of cylinders: comparisons of predictions for microstructure and flow fields. *J. Non-Newtonian Fluid Mech.*, 77(3):153–190, 1998.

[33] W. J. Lunsmann, L. Genieser, R. C. Armstrong, and R. A. Brown. Finite element analysis of steady viscoelastic flow around a sphere in a tube: calculations with constant viscosity models. *J. Non-Newtonian Fluid Mech.*, 48:63–99, 1993.

[34] Y. Maday and A. T. Patera. Spectral element methods for the Incompressible Navier-Stokes equations. In A. K. Noor and J. T. Oden, editors, *State of the Art Surveys in Comp. Mech.*, pages 71–143. ASME, New York, 1989.

[35] Y. Maday, A. T. Patera, and M. Rønquist. An operator-integration-factor splitting method for time-dependent problems: application to incompressible fluid flow. *J. Sci. Comp.*, 5(4), 1990.

[36] H Matallah, MJ Banaai, KS Sujatha, and MF Webster. Modelling filament stretching flows with strain-hardening models and sub-cell approximations. *Journal of non-newtonian fluid mechanics*, 134(1):77–104, 2006.

[37] M. A. Mendelson, P-W. Yeh, R.A. Brown, and R.C. Armstrong. Approximation error in finite element calculation of viscoelastic fluid flows. *J. Non-Newtonian Fluid Mech.*, 10(1):31–54, 1982.

[38] F. Noether. On the validity of stokes' resistance formula. *Z. Math. Physik*, 62:1–38, 1913.

[39] J. G. Oldroyd. On the formulation of rheological equations of state. *Proc. R. Soc. Lond. A*, 200:523–541, 1950.

[40] C. W. Oseen. Über die Stokes'sche formel, und ber eine verwandte Aufgabe in der Hydrodynamik. *Arkiv. Matem. Astron. Fysik*, 6(3), 1910.

[41] C. W. Oseen. *Ueber den gueltigkeitsbereich der stokesschen widerstandsformel.* Friedländer, 1913.

[42] S. Osher and J. Sethian. Fronts propagating with curvature-dependent speed: Algorithms based on Hamilton-Jacobi formulations. *J. Comput. Phys.*, 79:12–49, 1988.

[43] R. G. Owens, C. Chauvière, and T. N. Phillips. A locally-upwinded spectral technique (LUST) for viscoelastic flows. *J. Non-Newtonian Fluid Mech.*, 108:49–71, 2002.

[44] R. G. Owens and T. N. Phillips. Steady viscoelastic flow past a sphere using spectral elements. *Int. J. Numer. Meth. Eng.*, 39:1517–1534, 1996.

[45] R. G. Owens and T. N. Phillips. *Computational Rheology.* Imperial College Press, 2002.

[46] M. G. N. Perera and K. Walters. Long-range memory effects in flows involving abrupt changes in geometry: Part i: flows associated with i-shaped and t-shaped geometries. *J. Non-Newtonian Fluid Mech.*, 2(1):49–81, 1977.

[47] E. A. J. F. Peters, M. A. Hulsen, and B. H. A. A. van den Brule. Instationary Eulerian viscoelastic flow simulations using time separable RivlinSawyers constitutive equations. *J. Non-Newtonian Fluid Mech.*, 89:209–228, 2000.

[48] H. K. Rasmussen and O. Hassager. On the sedimentation velocity of spheres in a polymeric liquid. *Chem. Eng. Sci.*, 51:1431–1440, 1996.

[49] M. Renardy. *Mathematical Analysis of Viscoelastic Flows.* SIAM, Philadelphi, 2000.

[50] D. Rh. Gwynllyw and T. N. Phillips. On the enforcement of the zero mean pressure condition in the spectral element approximation of the Stokes problem. *Comp. Meth. App Mech. Eng.*, 195:1027–1049, 2006.

[51] M. E. Ryan and A. Dutta. Analysis of the constant rate startup flow of a viscoelastic fluid in annular, cylindrical, and planar conduits. *J. Rheol.*, 25(2):193–212, 1981.

[52] M Sahin and H. J. Wilson. A semi-staggered dilation-free finite volume method for the numerical solution of viscoelastic fluid flows on all-hexahedral elements. *J.of Non-Newtonian Fluid Mech.*, 147(1):79–91, 2007.

[53] O. Schenk and K. Gärtner. Solving unsymmetric sparse systems of linear equations with pardiso. *Future Generation Computer Systems*, 20(3):475–487, 2004.

[54] C. Schneidesch and M. O. Deville. Chebyshev collocation method and multi-domain decomposition for Navier-Stokes equations in complex curved geometries. *J. Comput. Phys.*, 105:234–257, 1993.

[55] G. G. Stokes. On the theories of the internal friction of fluids in motion, and of the equilibrium and motion of elastic solids. *Trans. Camb. Phil. Soc.*, 8:287–305, 1845.

[56] G. G. Stokes. On the effect of the internal friction of fluids on pendulums. *Trans. Camb. Phil. Soc.*, 9:8–106, 1851.

[57] J. Sun, N. Phan-Thien, and R. I. Tanner. An adaptive viscoelastic stress splitting scheme and its applications: Avss/si and avss/supg. *J. Non-Newtonian Fluid Mech.*, 65(1):75–91, 1996.

[58] H.R. Tamaddon-Jahromi, M.F. Webster, and P.R. Williams. Excess pressure drop and drag calculations for strain-hardening fluids with mild shear-thinning: contraction and falling sphere problems. *J. Non-Newtonian Fluid Mech.*, 166(16):939–950, 2011.

[59] R. G. M. van Os and T. N. Phillips. The prediction of complex flows of polymer melts using spectral elements. *J. Non-Newtonian Fluid Mech.*, 122:287–301, 2004.

[60] R. O. Vargas, O. Manero, and T. N. Phillips. Viscoelastic flow past confined objects using a micro-macro approach. *Rheol. Acta.*, 49:373–395, 2009.

[61] G. J. Wagner, N. Moës, W. K. Liu, and T Belytschko. The extended finite element method for rigid particles in Stokes flow. *Int. J. Num. Meth. Eng.*, 51:293–313, 2001.

[62] N. D. Waters and M. J. King. Unsteady flow of an elastico-viscous liquid. *Rheol. Acta.*, 9:345–355, 1970.

[63] N. D. Waters and M. J. King. Unsteady flow of an elastico-viscous liquid in a straight pipe of circular cross section. *J. Phys. D: Appl. Phys.*, 4:204–211, 1971.

[64] J. L. White. Dynamics of viscoelastic fluids, melt fracture, and the rheology of fiber spinning. *J. App. Polym. Sci.*, 8:2339–2357, 1964.

[65] S. Xu, A. R. Davies, and T. N. Phillips. Pseudospectral method for transient viscoelastic flow in an axisymmetric channel. *Numerical Methods for Partial Differential Equations*, 9(6):691–710, 1993.